DEVELOPMENT OF NOVEL MAGNETIC NANOPARTICLES TO TRACK STEM CELLS IN TISSUE-ENGINEERED ORGANS

Roxanne Hachani

Supervisors

Professor Nguyễn T. K. Thanh

Professor Martin Birchall

A thesis submitted to the University College London for the degree of Doctor of Philosophy in the Faculty of Mathematical and Physical Sciences, Department of Physics and Astronomy, University College London, 2017.

DECLARATION

I, Roxanne Hachani, confirm that the work presented in this thesis is my own.

Where information has been derived from other sources, I confirm that this has been indicated in the thesis.

ABSTRACT

This overall aim of this thesis was to develop and optimise the synthesis of superparamagnetic iron oxide nanoparticles (IONPs) as potential magnetic resonance imaging (MRI) contrast agents. Indeed, these nanoparticles offer the possibility of multimodality, surface biofunctionalisation, and can offer better MRI sensitivity than conventional molecular-based contrast agents as long as their magnetic properties are adequate and that they are administered in a sufficient and safe dose.

In the initial phases of this project, IONPs were synthesised by the polyol method in various experimental conditions: under inert atmosphere using a Schlenk line, using a microwave reactor and in high pressure high temperature conditions. The impact of these synthetic methods and the reaction variables on the physical and chemical properties of nanoparticles were studied. Iron oxide nanoparticles with low polydispersity were obtained through the polyol synthesis in high pressure high temperature conditions. Iron oxide NPs with a diameter of *ca.* 8 nm could be obtained in a reproducible manner and with good crystallinity as evidenced by X-ray diffraction analysis and high saturation magnetisation value (84.5 emu/g). However, poor results were obtained for their stability in aqueous solution.

To overcome this, alternative surface functionalisation was investigated, using a variety of ligands in order to improve their stability. The surface of the IONPs could be modified post synthesis with the ligand 3,4-dihydroxyhydrocinnamic acid (DHCA) which provided functionality and long term stability in water and phosphate buffer saline (PBS). Their potential as MRI contrast agents was confirmed as they had an improved r_2/r_1 ratio by a factor of more than 3 in comparison to FDA-approved nanoparticles for MRI Resovist® and Endorem®, with relaxivity values of r_1 = 7.95 mM^{-1} s^{-1} and r_2 = 185.58 mM^{-1} s^{-1} measured at 1.4 T. To assess their biocompatibility, multiparametric high-content imaging analysis was carried out with human mesenchymal stem cells (hMSCs) to evaluate cell viability,

formation of reactive oxygen species, mitochondrial health, as well as cell morphology. Results demonstrated that hMSCs were minimally affected after labelling with IONP-DHCA. Their cellular uptake was confirmed by transmission electron microscope (TEM) and iron specific Prussian Blue staining and quantified using a colourimetric method. *In vivo*, IONPs were detected as hypointense regions in the liver by 9.4 T MRI up to two weeks after intravenous administration into six Swiss female mice.

These results demonstrate the successful development of novel iron oxide nanoparticles, their biocompatibility with hMSCs, and their potential as MRI contrast agents.

TABLE OF CONTENTS

ACKNOWLEDGEMENTS

Finally, I am especially grateful to my parents for their eternal and unconditional support and believing in my ability to finish this PhD. Even if you did not always understand all the technical challenges I had to overcome, you always listened to me and pushed me to persevere and find a solution.

PUBLICATIONS ARISING FROM THIS THESIS

R. Hachani, M. Lowdell, M. Birchall and N.T.K. Thanh. Tracking stem cells in tissue-engineered organs using magnetic nanoparticles. *Nanoscale*, **2013**, 5, 11362-11373, Advance Article.

R. Hachani, M. Lowdell, M. Birchall, A. Hervault, D. Mertz, S. Begin-Colin and N.T.K. Thanh, Polyol synthesis, functionalisation and biocompatibility studies of superparamagnetic iron oxide nanoparticles as potential MRI contrast agents. *Nanoscale*, **2016**, 8, 3278-3287.

R. Hachani, M. Birchall, M. Lowdell, G. Kasparis, L.D. Tung, B.B. Manshian, S.J. Soenen, W. Gsell, U. Himmelreich, C. A. Gharagouzloo, S. Sridhar, and N.T.K. Thanh. Assessing cell-nanoparticle interactions by high content imaging of biocompatible iron oxide nanoparticles as potential contrast agents for magnetic resonance imaging. *Scientific Reports*, **2017**, 7(1), 7840.

A.P. LaGrow, M.O. Besenhard, **R. Hachani** and N.T.K. Thanh. Experimental considerations for scalable magnetic nanoparticle synthesis and surface functionalisation for clinical applications. Book chapter in ""CLINICAL APPLICATIONS OF MAGNETIC NANOPARTICLES", CRC Press/Taylor and Francis, **2018,** *in press*.

LIST OF FIGURES

19

LIST OF TABLES

LIST OF EQUATIONS

ABBREVIATIONS

2-MPA   2-mercaptopropionic acid

3-MPA   3-mercaptopropionic acid

ATMP   Advanced therapy medicinal products

ATR   Attenuated total reflectance

BSA   Bovine serum albumin

cGMP   Current good manufacturing practice

CTAB   Cetyltrimethylammonium bromide

dH_2O Reverse osmosis water (Milli-Q®)

DEG   Diethylene glycol

D_H Hydrodynamic diameter

DLS   Dynamic light scattering

DMEM   Dulbecco's modified eagle's medium

DMSA   2,3-dimercaptosuccinic acid

DMSO   Dimethyl sulfoxide

DNA   Deoxyribonucleic acid

DOTA   1,4,7,10-tetraazacyclododecane-1,4,7,10-tetraacetic acid

D_{TEM} Diameter estimated by TEM

D_{XRD} Crystallite size estimated by XRD

EDC	N-ethyl-N'-(3-diethyl-aminopropyl)-carbodiimide
EDTA	Ethylenediaminetetraacetic acid
EPR	Enhanced permeability and retention
ESCs	Embryonic stem cells
FBS	Fetal bovine serum
FC	Field cooling
FC	Flow cytometry
Fcc	Face centred cubic
FDA	Food and drug administration
FITC	Fluorescein isothiocyanate
FOV	Field of view
FTIR	Fourier transform infrared spectroscopy
H	Magnetic field
HBSS	Hank's balanced salt solution
H_C	Coercive field
HEPES	(4-(2-hydroxyethyl)-1-piperazineethanesulfonic acid)
HOBt	Hydroxybenzotriazole
IONP	Iron oxide nanoparticle
IR	Infrared

ICP-AES	Inductively coupled plasma – atomic emission spectroscopy
MEM	Minimum essential media
MES	2-(4-morpholino)ethanesulphonic acid
MNP	Magnetic nanoparticle
M_r	Remanence
MRI	Magnetic resonance imaging
Ms	Saturation magnetisation
MSC	Mesenchymal stem cell
MTT	3-(4,5-Dimethylthiazol-2-yl)-2,5-diphenyltetrazolium
MTS	3-(4,5-dimethylthiazol-2-yl)-5-(3-carboxymethoxyphenyl)-2-(4-sulfophenyl)-2H-tetrazolium
M_w	Molecular weight
MW	Microwave
MWCO	Molecular weight cut-off
NHS	N-hydrosuccinimide
NMR	Nuclear magnetic resonance
NP	Nanoparticle
PAA	Poly(acrylic acid)
PBS	Phosphate buffered saline

pdf	Powder data file
PEG	Poly (ethylene glycol)
PES	Phenylethosulfate
PFA	Paraformaldehyde
PI	Propidium iodide
PLL	Poly (L-lysine)
PS	Phosphatidylserine
PTFE	Polytetrafluoroethylene
PVP	Poly(vinylpyrrolidone)
RES	Reticule endothelial system
RF	Radiofrequency
ROI	Region of interest
Rpm	Revolutions per minute
RT	Room temperature
SC	Stem cell
SQUID	Superconducting Quantum Interference Device
SQUID-VSM	Superconducting Quantum Interference Device Vibrating Sample Magnetometer
SSC	Side scatter channel
t	time

T_1	Longitudinal relaxation
T_2	Transverse relaxation
TE	Echo time
TEG	Tetraethylene glycol
TES	2-[tris(hydroxymethyl)-methylamino]-ethanesulfonic acid
TEM	Transmission electron microscope/microscopy
TGA	Thermogravimetric analysis
TR	Repetition time
TREG	Triethylene glycol
UV	Ultraviolet
XRD	X-Ray diffraction
ZFC	Zero field cooled

Chapter 1 INTRODUCTION

1.1 SUPERPARAMAGNETIC IRON OXIDE NANOPARTICLES

Magnetic IONPs have been the subject of great interest in recent years due to their various potential biomedical applications such as magnetic hyperthermia,[2] MRI,[3-5] drug delivery, or cell tracking for example.[6-9] Their unique physical and chemical properties which make them valuable are due to their size, biocompatibility, non-toxicity and non-immunogenicity in biological systems. Furthermore, Feridex© or Resovist© are example of IONPs which have been approved for clinical applications by the federal drug administration (FDA) in the 1980s and have since then been discontinued.[10, 11] These were developed as contrast agents for MRI of malignant diseases in organs associated with the reticuloendothelial system (e.g., liver, spleen)[12-14] and lymph nodes.[15]

Despite all these advantages, the *in vitro* and *in vivo* use of IONPs still faces some challenges. The lack of reproducibility in the synthesis methods that yield water-dispersible nanoparticles is a major setback that this project aims to address. The wide size distribution of nanoparticles synthesised and the lack of control of their aggregation are also current limitations to their use for biomedical applications. Indeed, while the co-precipitation of Fe(II) and Fe(III) ions in a basic solution is a widespread method in literature due to the high yields obtained,[16, 17] the reproducibility of this synthesis remains a limitation.[18] On the other hand, the main synthetic pathways which allow for better control of the size and shape of nanoparticles obtained involve the use of organic solvents. The nature of these solvents means post synthesis steps to render the nanoparticles hydrophilic and biocompatible are necessary, but these are difficult to monitor and control precisely in a quantitative manner.

1.1.1 *Magnetite and maghemite*

This thesis focused on the development of superparamagnetic IONPs as these have been previously FDA approved for clinical MRI. The most studied IONP materials for this biomedical application are magnetite (Fe_3O_4) and its oxidised form maghemite (γ-Fe_2O_3). This is because they possess ferrimagnetic properties, and are less toxic and less susceptible to oxidation than other magnetic nanoparticles (MNPs).

Ferrites are described by the structural formula $M^{II}Fe_2O_4$ where M represents a divalent metal ion such as Fe^{II}, Co^{II} or Ni^{II} for example, or a mixture of two metals. They are characterised by a spinel cubic crystal structure in the Fd3m space group. The crystal structure will be described as spinel or inverse spinel depending on whether the metallic divalent ions M^{2+} occupy the tetrahedral or octahedral sites of the face-centred cubic formed by the oxygen atoms.

Magnetite Fe_3O_4 is a black ferrimagnetic material containing both Fe^{2+} and Fe^{3+}. It has an inverse spinel structure which can be written as $B(AB)O_4$ with 32 oxygen anions O^{2-} forming a face-centred cubic crystal system, where B describes the tetrahedral sites and (AB) describes the octahedral sites.[19] As shown in Figure 1-1, all tetrahedral sites are
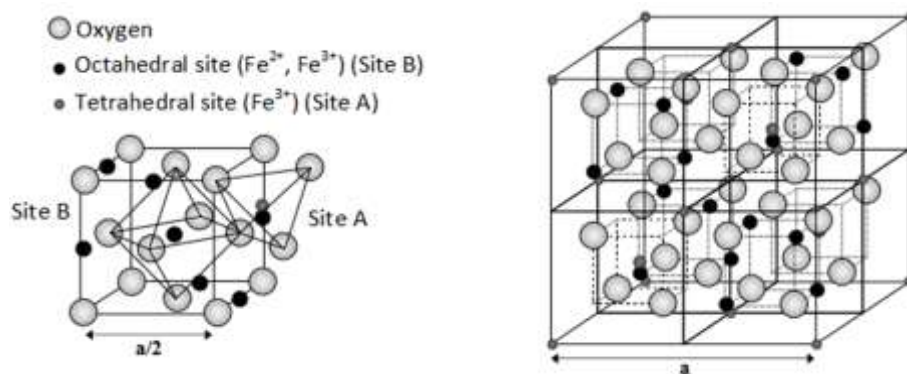
Figure 1-1 Scheme representing the inverse spinel structure of magnetite. Reproduced from Mornet S., Doctoral dissertation, 2002.

occupied by Fe^{3+} and octahedral sites are occupied by both Fe^{3+} and Fe^{2+} in equal amounts.[20] Magnetite exhibits the strongest magnetism in comparison to the other transition metal oxides,[21] this is mainly due to the occupancy of octahedral sites with Fe^{2+} ions.

Maghemite is a red brown ferrimagnetic material isostructural to magnetite but with cation deficient sites. It is characterised by all of the iron present being in the trivalent state (Fe^{3+}) and by the existence of cation vacancies in the octahedral sites. Spontaneous or provoked oxidation of magnetite to maghemite may occur through aerial oxidation, or under specific pH conditions in solution, or specific pressure and temperature conditions. For example, under acidic and anaerobic conditions, surface Fe^{2+} may be desorbed; under basic conditions, oxidation may occur at the surface of the NP. This explains the formation of vacancies in octahedral positions due to the oxidation of Fe^{2+} to Fe^{3+}. The oxidation model is based on the assumption that free oxygen at the surface of the crystal is adsorbed and ionized by Fe^{2+} atoms, according to the reaction: $Fe^{2+} + \frac{1}{2}zO \longrightarrow zFe^{3+} + (1-z)Fe^{2+} + \frac{1}{2}zO^{2-}$, where the degree of oxidation z is the ratio between the number per f.u. of oxidised Fe^{2+} ions and the initial number, Fe_0^{2+} ($0 \leq z \leq 1$).[22, 23] This is always accompanied by a migration of cations through the lattice, which creates vacancies, in order to maintain the charge balance.[24] These vacancies can be random, ordered or partially random and will lead to symmetry lowering. The degree of ordering in the distribution of the vacancies affects the magnetic properties, implying that magnetic moments in the interior of the particles can be significantly influenced by canting effects and may lead to lower saturation magnetisation in comparison to magnetite. Infrared spectroscopy and x-ray diffraction (XRD) studies have shown that vacancies are ordered in IONPs exceeding 5 nm in diameter.[25]

Magnetite and maghemite are often chosen for the development of magnetic IONPs for biomedical applications as they have the desired magnetic properties for these applications
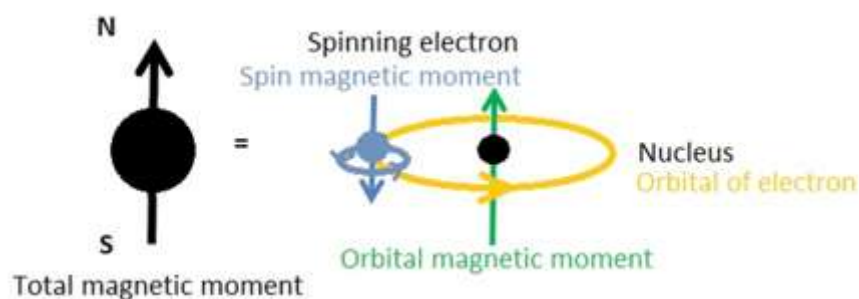
Figure 1-2 Scheme of different components of the magnetic moment of electrons in atoms.

and fulfil the requirements of non-toxicity and non-immunogenicity essential for pre-clinical and clinical use.

1.1.2   *Magnetic properties*

The change in size of certain materials from their bulk state to the nanoscale modifies their magnetic properties which may be interesting for different applications of these nanomaterials. A number of ferrite-based nanoparticles are studied for various applications such as their use as semiconductors, electrochemistry, or energy storage applications for example.[26] The choice of nanomaterial will depend on the desired application. In the case of biomedical applications, IONPs composed of magnetite and/or its oxidised form maghemite, are some of the most frequently investigated as they possess the desired magnetic properties, they have been previously FDA approved for clinical MRI and are deemed some of the safest in terms of cytotoxicity. For example, the use of hematite (α-Fe_2O_3) nanoparticles, a canted anti-ferromagnetic material would not be ideal when a high magnetic moment is needed as this is the case in MRI.

Magnetism originates from the magnetic moment of electrons. As illustrated in Figure 1-2, these charged particles experience a movement, which can be described by two components: an orbital angular momentum and a spin momentum. The electrons are magnetised by spinning on their own axis at a constant rate which causes the spin

magnetic moment; as well as by orbiting around the nucleus which is called the orbital magnetic moment.

Diamagnetism is a form of atomic magnetic effect which occurs in all materials as it is inherently due to the presence of paired electrons. If other magnetic effects are present, it may be 'masked' by stronger magnetic effects such as paramagnetism or ferromagnetism for example. Diamagnetic materials will contain paired opposing electron spins which cancel each other out, thus leading to a weak repulsion of the magnetic field. In the absence of an external magnetic field, these materials will not possess a magnetic moment.

Paramagnetism is another atomic magnetic effect. Unlike diamagnetism, this effect occurs when the atomic orbitals contain unpaired electrons. The Pauli exclusion principle infers that two electrons in an orbital spin must have opposite spins and thus cancel each other out. However, when dealing with unpaired electrons, these may have a random orientation. When an external magnetic field is applied, some of the unpaired spins may occupy a lower energy level and align with the applied field, thus leading to positive magnetisation and positive magnetic susceptibility. However, paramagnets will not retain magnetisation once the field is removed as thermal energy will dominate and electron spins will regain a random orientation.

In the case of paramagnets, the magnetic susceptibility is temperature dependent and follows the Curie-Weiss law (Equation 1-1):

$$\chi_m = \frac{C}{T - \theta}$$
(Equation 1-1)

where χ_m is the susceptibility, C is the Curie constant, T is the temperature and θ is the Weiss constant in units of temperature. θ is a measure of the interaction of atomic magnetic moments. If there are no interactions, then θ is negative and the moments are opposing the applied field.

Additional interactions between atoms can be extrapolated to the whole lattice by the following Hamiltonian (H) in Equation 1-2, initially described for the interaction between two atoms by Heisenberg:

$$\mathbf{H} = -2\sum_{ij} \mathbf{J_{ij}S_iS_j}$$

(Equation 1-2)

where i and j represent the position of the atoms within the crystal lattice and J is the exchange constant. The strength and nature of intermolecular interactions will be dependent upon the crystalline structure.

Ferromagnetic materials will have paramagnetic domains aligned parallel, thus J will be positive. Ferromagnetism appears below the Curie temperature, the latter being material dependent. Above the Curie temperature, the moments are randomly oriented resulting in no net magnetisation and the material behaves as a paramagnet. On the contrary, if J is negative, the spins are coupled in an anti-parallel manner. This is the case in ferrimagnets or anti-ferromagnets. Anti-ferromagnetic materials will have dipoles with equal moment but in opposing directions, thus resulting in the absence of magnetisation as they cancel each other out. Ferrimagnets will also have dipoles of opposing directions but these do not cancel each other out, thus resulting in a magnetic moment. All these magnetic behaviours are illustrated in Figure 1-3 below.
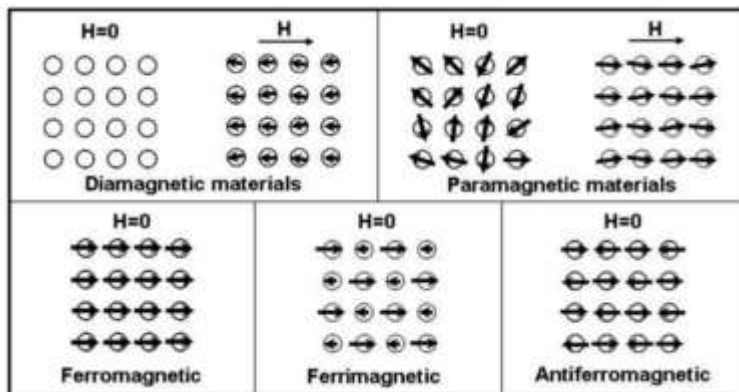
Figure 1-3 Scheme illustrating the arrangements of magnetic dipoles in one dimension for different types of magnetic materials in the absence or presence of an applied external magnetic field H. Reproduced from Jeong et al., Advanced Materials, 2006 with permission from John Wiley and Sons.
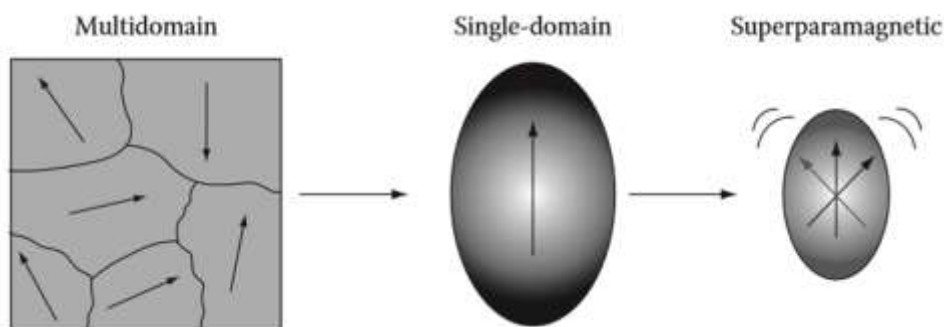
Figure 1-4 Magnetic behaviours derived from the scale reduction in magnetic materials. Reproduced from Ortega D., Chapter 1 in Magnetic Nanoparticles: From Fabrication to Clinical Applications, 2012, CRC Press.

As explained in the previous paragraph, some paramagnetic materials undergo a transition upon cooling to an ordered state in which there is local alignment of atomic moments. A critical temperature, named the Curie temperature for ferrimagnets and Néel temperature

for anti-ferromagnets, is the temperature above which thermal energy fluctuations will dominate and the magnetisation will drop to zero.

The internal structure of a bulk magnetic material is made of magnetic domains which have coupled magnetic moments, and which are separated by domain walls. These walls constitute a transition area between two magnetic domains where a gradual reorientation of the moments occurs, and where defects are usually found. Domain walls may be displaced gradually with the application of an external magnetic field. When magnetic materials, such as magnetite for example, are reduced in size there is a critical size below which it is more energetically favourable to split the magnetic domains into a single domain (Figure 1-4), and where the formation of a domain wall is energetically too costly.

This critical size R_c is also known as the "Weiss domain", which is when there is only a single domain and its magnetic moment is blocked at room temperature (RT). This critical size is determined by the following equation:

$$\mathbf{R_C} = \frac{36\sqrt{AK}}{\mu_0 \, M_S^2} \qquad\qquad \text{(Equation 1-3)}$$

where R_C is the critical domain size, A is the exchange stiffness (measure of the critical temperature for which this material is magnetically ordered), K is the magnetic anisotropy of the particle, μ_0 is the permeability of free space and M_s is the saturation magnetisation.
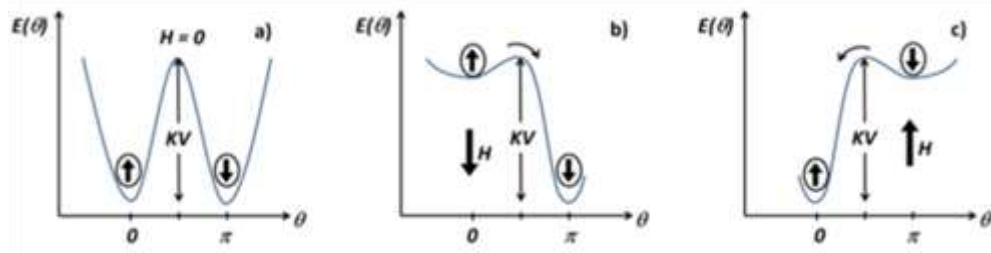
Figure 1-5 Switching of the magnetisation of a particle across the anisotropy barrier under a) no external magnetic field; b) external magnetic field pointing downwards; and c) external magnetic field pointing upwards. Reproduced from Nguyen, V.T.A., Doctoral dissertation, 2015.

The critical size will be material dependent (90-100 nm for maghemite and 80-90 nm for magnetite),[27, 28] but generally is a particle containing 10^{12} to 10^{18} atoms approximately.

As seen in Figure 1-4, for simplification purposes, a single domain will be represented as a single vector. In the absence of an external field, the latter will show a certain preference for an axis along which its magnetisation will align, this is referred to as the easy magnetisation axis or anisotropy axis. An energy barrier imposed by the anisotropy energy of the system will separate and limit the possible orientation states of the magnetisation. This energy will be dependent upon the angle between the magnetisation vector and the easy axis, and will also depend on the crystal structure of the material. This is described by the Stoner-Wohlfarth model (Figure 1-5)[29] and by the following equation:

$$E(\theta) = KVsin^2\theta \qquad \text{(Equation 1-4)}$$

where K is the anisotropy constant, V is the volume of the sample and θ the angle formed between the easy axis and the magnetic moment.

Both orientations of the magnetisation with minimum energy ($\theta = 0$ or $\theta = \pi$) are equally probable and are separated by the anisotropy energy barrier $E_a = KV$. When applying an external magnetic field H along the easy axis, the energy barrier is reduced, thus facilitating

the change of direction of the magnetisation from an energetically unfavourable state (opposed to H) to an energetically favourable state (same direction as H).

When the size of a particle is further reduced, there is a size below which the thermal energy will overcome the anisotropy energy barrier and the magnetisation will be able to flip easily between the two states. This is known as the superparamagnetic regime and starts at r < 17.5 nm for maghemite and r < 12.2 nm for magnetite.[30, 31]

Superparamagnetic NPs will demagnetise spontaneously after saturation magnetisation is reached. This is important for biomedical applications in order to minimise the risk of IONPs retaining any magnetic moment *in vivo* once an external field is removed.[32] Under the effect of thermal energy, NPs with uniaxial anisotropy can randomly flip the direction of their magnetisation. The average time to perform a flip is defined as the relaxation time τ, also known as Néel relaxation time which is defined in Equation 1-5:

$$\boldsymbol{\tau = \tau_0 e^{\frac{\Delta E}{k_B T}}}$$
(Equation 1-5)

where τ_0 is a length of time characteristic of the material (typical values for τ_0 are between 10^{-9} and 10^{-10} sec), ΔE is the energy barrier the magnetisation flip has to overcome by thermal energy, k_B is the Boltzmann constant and T is the temperature.

When characterising superparamagnetic IONPs, the measurement time τ_M is an essential parameter to consider. If $\tau_M > \tau$, then it will appear that the magnetisation will flip several times during the measurement, and so the magnetisation will average to zero. The NP is said to exhibit superparamagnetic behaviour. However if $\tau_M < \tau$, it will appear that the magnetisation has not flipped and is that of the NP at the beginning of the measurement. The NP is said to be "blocked". The transition between both states can occur when $\tau_M = \tau$, and this is generally done by keeping the measurement time constant and varying the temperature. The temperature at which the transition occurs is called the blocking temperature. The blocking temperature is routinely reported in scientific publications and

used to approximate the NP size and to gain information on the behaviour of a NP in a specific set of conditions (magnetic field applied field and temperature). However, this remains approximate as it assumes all NPs in the sample are perfectly spherical, and is defined by the measurement time which depends on the measurement tool used.

Unless an applied external magnetic field is applied, the superparamagnetic NPs will have paramagnetic behaviour: no net magnetisation is present. However, when applying a magnetic field the spins will align along the line of easy axis to provide a net magnetisation.

The response of a magnetic material to an applied field is described by:

$$\mathbf{M} = \chi \mathbf{H}$$ (Equation 1-6)

where M is the magnetisation, χ the susceptibility and H the applied field. The susceptibility will depend on the temperature and the magnetic field applied H. This can be observed when considering the sigmoidal shape of M-H plots as illustrated in Figure 1-6.

The initial curve, also known as the virgin curve, is characterised by an increase in the sample magnetisation following the application of an external magnetic field. This curve cannot be obtained twice with the same sample, as it is only obtained from a demagnetised sample which has not been previously exposed to a magnetic field. After all magnetic moments in the material are aligned with H, the maximum value of M obtained is defined as the saturation magnetisation (M_s) and is often used to characterise materials. When decreasing the applied field, the material will retain a certain amount of magnetisation, which is defined as the remanent magnetisation M_r when H = 0. In order to completely demagnetise the sample, the field to apply is defined as the coercive field H_c or coercivity.

In ferromagnetic materials, the plot will be characterised by hysteresis, a loop opening which is caused by magnetic pinning sites due to impurities, grain boundaries or
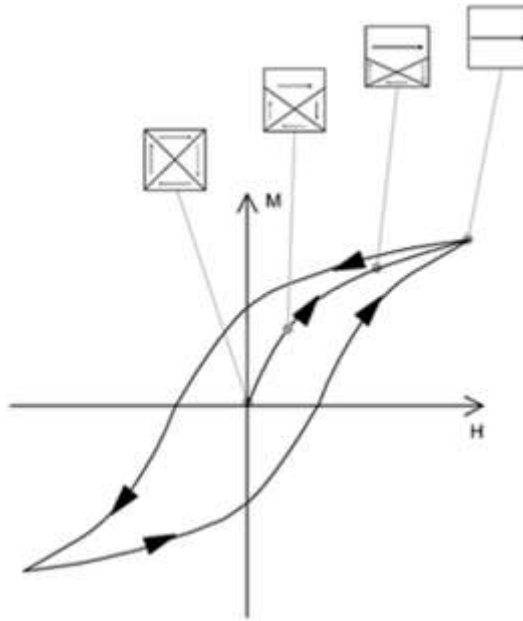
Figure 1-6 Hysteresis cycle of a multidomain magnetic material and domain wall displacements in such a material (squares symbolise multidomain material, with magnetisation of each domain; arrows on the cycle indicate the way the cycle is described when increasing or decreasing the field amplitude). Reproduced from S.Mornet et al., Journal of Materials Chemistry, 2004 with permission from the Centre National de la Recherche Scientifique (CNRS) and the Royal Society of Chemistry.

movements of domain walls, and which will vary with the size of the NPs. This hysteresis behaviour was first described by Pierre Weiss in 1907 with the assumption that ferromagnetic materials are made of magnetic domains.[33] The presence of pinning sites means a larger field will be necessary to displace domain walls, and this is why the M-H plot can be characterised by a hysteresis loop and remanence. Superparamagnetic NPs are characterised by the absence of coercivity and remanence. Due to an increased surface to volume ratio at the nanoscale, the presence of surface canted spins which are not aligned with the spins of the NP core, will lead to a decrease in the M_s in comparison to the bulk material (92 emu/g for Fe_3O_4 and 78 emu/g for γ-Fe_2O_3).[34-36]

1.1.3   Synthesis methods

Iron oxide nanoparticles used for MRI have been routinely synthesised by the alkaline co-precipitation of ferric Fe^{3+} and ferrous Fe^{2+} iron in ratio 2:1 in an aqueous solution[37, 38] and coated with hydrophilic molecules such as dextran,[39, 40] citrate,[7] chitosan,[41] heparin,[42, 43] and albumin.[44] More recently, the use of phosphonate ligands has been of interest[45-47] as they create dense and stable Fe-O-P bonds which have a pH dependent conformation and could enhance the magnetic properties of IONPs through the absence of surface spin canting, unlike carboxylate groups (Figure 1-7).[48, 49] Co-precipitation is a widespread method in literature due to the low reaction temperature, short reaction time and high yields obtained,[16] but does not generate nanoparticles in a reproducible manner.[18]

Different factors such as the pH, Fe(II)/Fe(III) ratio or ionic strength of the reaction medium will influence the growth of the IONPs.[10, 50, 51] For example, the use of a strong base such as ammonia will induce severe localised pH changes which lead to multiple bursts of nucleation and thus have an impact on the IONP size distribution.[52] The pH will affect the protonation and deprotonation process of surface hydroxyl groups which in turn will impact the electrostatic surface charge. To obtain monodisperse NPs, a short burst
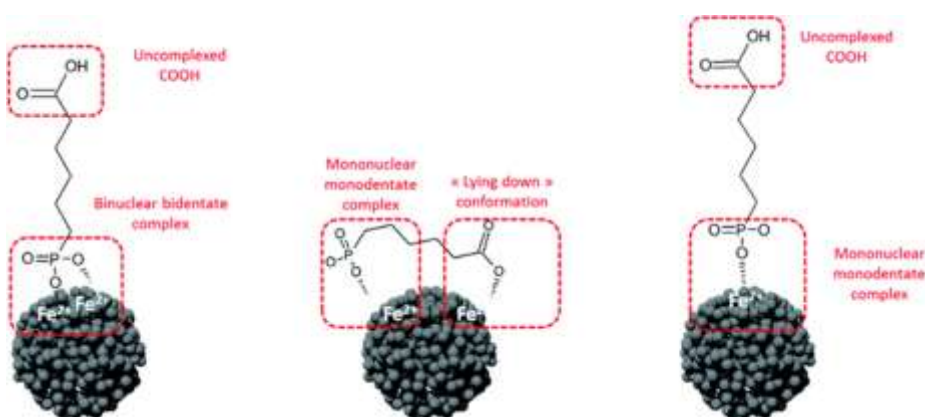
Figure 1-7 The most likely conformations of the 6-phosphonohexanoic acid (PHA) molecule at the NP surface. Reproduced from Thomas et al., Dalton Transactions, 2016 with permission from with permission from the Centre National de la Recherche Scientifique (CNRS) and the Royal Society of Chemistry.
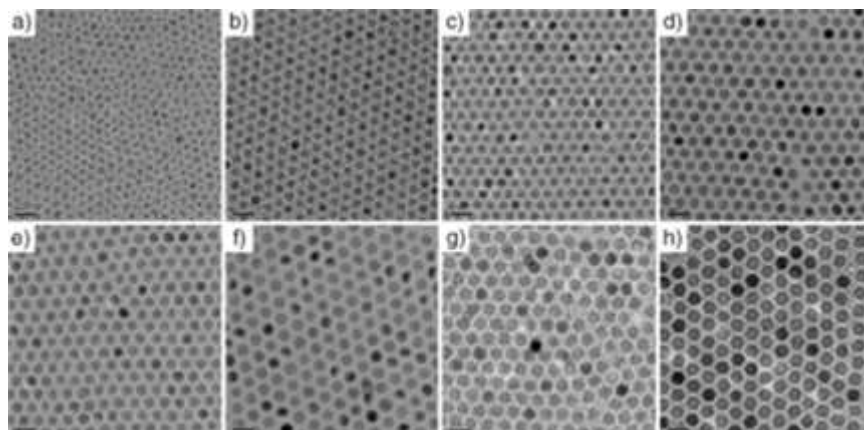
Figure 1-8 TEM images of a) 6-, b) 7-, c) 8-, d) 9-, e) 10-, f) 11-, g) 12-, and h) 13-nm-sized air-oxidised iron oxide nanoparticles showing the one nanometer level increments in diameter. Scale bar 20 nm. Reproduced from Park J. et al., Angewandte Chemie International Edition, 2005, with permission from John Wiley and Sons.

nucleation and slow controlled growth is required.

On the other hand, methods involving the use of organic solvents allow better control of the morphology of the IONPs and improved crystallinity. The synthesis of monodisperse crystalline NPs is essential to obtain a high magnetic moment and saturation magnetisation, and so a high relaxivity value for MRI. These methods involve the decomposition of organometallic complexes in organic solvents at high temperatures with the use of surfactants to tailor the nanoparticle's surface.

Sun *et al.* synthesised IONPs through the decomposition of iron (III) acetylacetonate in phenyl ether or benzyl ether with the addition of 1,2 hexadecylamine, oleic acid and oleylamine.[53] The particle size was tuned from 4 – 20 nm by first growing smaller seed particles and then adding more reagents. TEM images of the obtained NPs are reported in Figure 1-8. This method of synthesis yielded NPs of narrow size distribution and highly uniform shape.

A similar technique was used by Park *et al.*[54] to produce monodisperse IONPs using iron (III) chloride and sodium oleate, which are both inexpensive and non-toxic, to generate an iron oleate complex. The latter was then decomposed at high temperatures (240 – 320 °C) in different solvents to produce IONPs with diameters in the range of 5 – 22 nm depending on the temperature and aging period. The same group produced monodisperse iron NPs by the sequential decomposition of iron pentacarbonyl $Fe(CO)_5$ and the iron oleate complex at different temperatures.[55] The reaction is similar to a seed mediated growth process and allows very fine control over the particle size.

However, when considering NPs for biomedical applications, the main drawback of this synthesis method lies in the hydrophobic nature of the particles obtained. MNPs must be rendered water dispersible through a post synthesis step: phase transfer or ligand exchange, so that the NPs are coated with an alternative hydrophilic ligand. The new ligand should present a higher affinity for the NP than the hydrophobic one, and should confer the desired properties to the NP. Otherwise this may lead to a mixed organic shell (mixture of the hydrophobic and hydrophilic ligands) which could have an impact on the colloidal stability of NPs.[56] In most cases, an excess of the new ligand allows for the complete replacement of the original ligand. Another drawback is that the yield of the ligand exchange reaction will depend on the experimental conditions (i.e. pH, temperature, stirring/agitation, time, etc.) in which they are done.[57, 58] However, even though the ligand exchange process is frequently reported in publications reporting the synthesis and biomedical applications of NPs synthesised in research laboratories, this step often lacks characterisation. This is the main drawback as not only is aggregation of the NPs during the ligand exchange step possible, but the new organic shell is not defined in terms of composition and quantity of ligands present. To date, attempts to characterise this reaction have been scarce as IONP characterisation methods present technical limitations. The robustness and reproducibility of the analytical techniques chosen must initially be proven before addressing how this process affects the properties of the NPs. In 2014, Davis and colleagues were able to qualitatively and quantitatively assess the ligand exchange

reaction of IONPs in which radiolabeled oleic acid was replaced by poly (ethyleneglycol) with various terminal groups.[59] This research confirmed hierarchal binding of functional groups on the surface of magnetite NPs with catechol derived groups and phosphonate groups having higher binding affinity than amine and carboxylate derived PEG ligands. As Figure 1-9 illustrates, even with high affinity ligands such as catechol derived groups, oleic acid still remained on the surface of the NPs after ligand exchange.
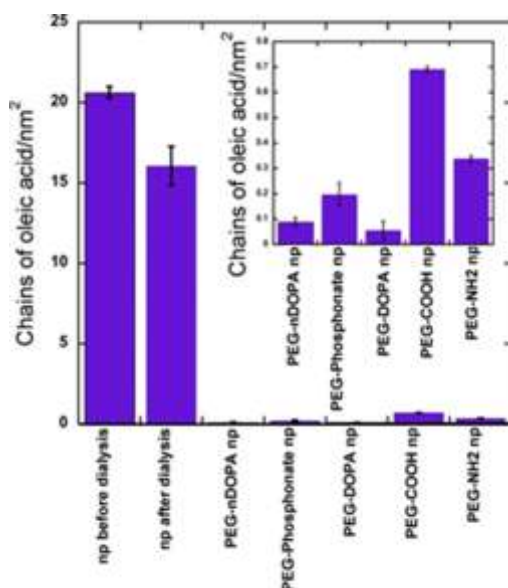
Figure 1-9 Chains of oleic acid remaining on the surface of the nanoparticles before and after ligand exchange determined by liquid scintillation counting (LSC). The data for the PEG-coated nanoparticles represent the amount of oleic acid remaining after dialysis. Reprinted from Davis et al., Langmuir, Copyright 2014 American Chemical Society.

In a more recent study by the same team, the higher affinity of catechol derived ligands for IONPs in comparison to other functional groups was demonstrated.[60] Bifunctional ligands were found to coat the NPs in a more efficient manner the monofunctional ligands.

More recently, hydrothermal synthesis of IONPs has been studied more intensely. This method is based on the crystallisation of a substance in a high temperature aqueous solution (130 to 250 °C) in a sealed container. The synthesis uses the dehydration and hydrolysing power of supercritical water to make metal oxides from their salts. The main advantages of this method lie in the use of non-organic solvents and the high crystallinity of the NPs obtained which should lead to a high M_s. While this method allows for good control of the shape and size of NPs obtained,[61-63] it is inconvenient because of the extremely high temperatures and pressures needed. For example, in terms of safety and scalability, this can be difficult to set up in an industrial or university research environment.

This project focused on the polyol method as it is a simple one-pot synthesis, which leads to water dispersible IONPs. One or more metal salts are dissolved in an alkaline polyalcohol and heated to obtain MNPs. The composition, size, and crystallinity of the particles are determined by the reaction rate of the polyol process.[64] The reaction rate in turn is a function of many experimental parameters such as polyol reduction potential, metal salt concentration, pH and reaction temperature. The synthesis of magnetite occurs by the decomposition of the iron precursor, iron (III) acetylacetonate $Fe(acac)_3$, at high temperature (180 - 190 °C). The polyol will act as a solvent as well as a reducing agent and surfactant to avoid the aggregation and control the growth of NPs. IONPs smaller than 10 nm have been obtained through the decomposition of $Fe(acac)_3$ in diethylene glycol (DEG).[65, 66] Other groups have also proven that the type of polyol and its length may influence the reaction conditions and shape of NPs obtained.[67, 68] The thermal decomposition of $Fe(acac)_3$ is initiated around 180 °C but is optimum at temperatures above 200 °C and manifests by a decrease in the iron metal – acetlyacetonate π interactions with the progressive removal of iron acetylacetonate groups. From the metal acetylacetonate/polyol mixture, several gaseous compounds will be eliminated during the thermal decomposition process such as acetaldehyde, carbon dioxide and carbon monoxide.[69-71] The formation of NPs by the polyol process has been recently studied and exact nature of the iron complexes formed has not been determined experimentally,
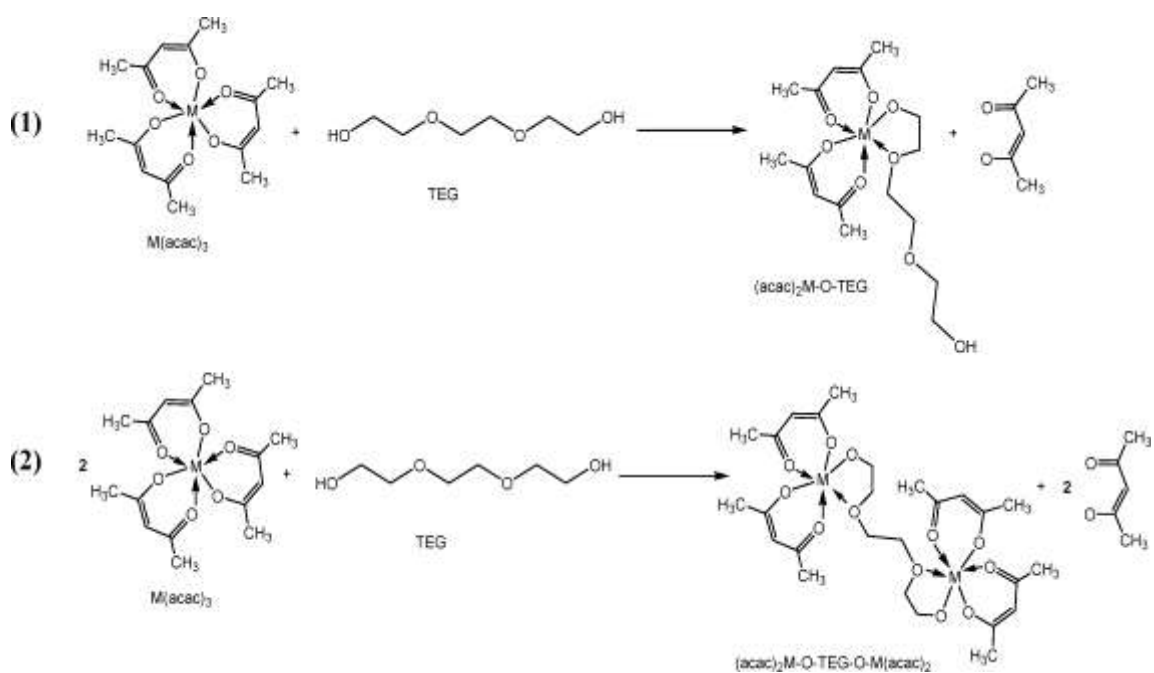
Figure 1-10 Illustration of the proposed reactions between Fe(acac)$_3$ and triethylene glycol (TEG) molecules. Reprinted with permission from Miguel-Sancho et al., Industrial & Engineering Chemistry Research, Copyright 2012 American Chemical Society.

several studies suggest that the polyol is coordinated to the iron centre.[69, 72, 73] This has led to the identification of the following phases which are represented in Figure 1-10: the heating of Fe(acac)$_3$ in a polyol solvent leads to the formation of an intermediate alkoxy-acetylacetonate-Fe^{3+} with the ferric iron being coordinated with both the polyol and the acetylacetonate ions. In turn, these complexes would assemble and form larger complexes with the polyol acting as a ligand.

The hydrophilic nature of the polyols on the surface of the NPs implies there is no need for a post synthesis ligand exchange process as they are water dispersible.[74]

During this project, water-dispersible magnetite NPs were synthesised as described by Cai and Wan with some modifications of the experimental conditions used detailed in chapter 3.[65, 75] Some reactions were initially carried out inside a microwave vessel and later on these reactions were conducted in an autoclave to meet high temperature and high

pressure conditions. The increased temperature led to increased solubility and reactivity of the metal precursor $Fe(acac)_3$ as well as a significant decrease in the viscosity of the solvent.[69] The latter has an essential role in determining the size of the NPs obtained. Indeed, the low viscosity of polyol at their boiling point, in conjunction with the increased diffusion coefficient, means a large number of iron species in solution may diffuse rapidly and lead to crystal growth by their addition onto previously formed crystals at lower temperatures. Furthermore, the high concentration of $Fe(acac)_3$ in the initial solution leads to a gradual release of iron species, which will be added onto growing crystals in solution.

Cheng *et al.* demonstrated the important of the reduction potential of the polyol solvent on the size and morphology of NPs obtained by polyol synthesis carried out in an autoclave.[76] Propylene glycol, which has a higher reduction potential than ethylene glycol, leads to a quicker formation and growth of NPs. The latter therefore do not have time to align correctly to minimise their surface energy and will instead form a cluster of misaligned crystals. During the second phase of the synthesis, the NPs continue to grow and since their surface energy is high, they disaggregate and the monomers attach onto the surface of larger NPs. With the solvent of lower redox potential, such as ethylene glycol, NPs aligned along the same crystal orientation and formed flower-like shaped clusters, which were maintained through the growth of the NPs because of low surface energy.

However, the coating of IONPs by polyol ligands may lead to a lack of biological compatibility and stability. In a recent study, triethylene glycol (TREG) was shown to have short-term stability on the surface of NPs and to degrade with time.[77] Ligand exchange of TREG with dimercaptosuccinic acid (DMSA) was necessary in order to provide better stability of the NPs both in water and PBS. The next section (1.1.4) will explain the importance of the surface ligands for interactions of IONPs with biological systems.

1.1.4   *Surface functionalisation of IONPs*

IONPs are more reactive when their size decreases due to a large surface area to volume ratio. For example, smaller NPs will be more rapidly degraded and excreted from the body once exposed to biological systems. IONPs with sizes smaller than 10 nm are essentially eliminated by renal clearance, whereas IONPs larger than 200 nm are taken up by phagocytic cells of the body such as macrophages, especially in the spleen and liver.[78, 79] IONPs within the size range of 10 to 100 nm are considered to be optimal for biomedical applications, as they allow for longer circulation times by avoiding rapid elimination by the reticuloendothelial system (RES).

The interaction of NPs with biological systems occurs in 2 phases. The first one is their recognition by circulating plasma proteins, opsonins, which will adsorb to their surface. The latter then initiate the second phase as they recognise cells of the RES (blood monocytes, macrophages and bone marrow progenitor cells), which will interact with the NPs through endocytosis or phagocytosis. The NPs can then be eliminated in organs of the RES, mostly in the liver, kidneys, spleen and lymph nodes. It has been reported in several studies that coating NPs with polysaccharides or polymers improves the adhesion of NPs to cell membranes.[80] Furthermore, the surface charge strongly impacts the biodistribution of NPs within cells and living organisms.[81] Positively charged NPs, with amino functions on their surface for example, will have a higher cellular uptake than those negatively charged, but this can be non-specific. This can be explained by an affinity between positively charged NPs and negatively charged cellular membranes.[82] This has been observed with most cell lines excluding certain macrophages and stem cells (SCs).[83, 84] Cationic particles interact with cells by penetrating the cell membrane, which may contribute to their cytotoxicity. On the other hand, phagocytic cells and SCs have been shown to preferentially internalise negatively charged particles. In phagocytic cells, this phenomenon has been suggested to be due to their inherent function: the uptake of bacteria, which is negatively charged.[85] The internalisation of negatively charged MNPs is believed to occur through nonspecific binding

and clustering of the NPs on the few positively charged sites on the plasma membrane followed by endocytosis.[86] In more recent studies, thiolated NPs had a higher level of tumour accumulation than non-thiolated NPs.[87] Also, they accumulated more significantly in the spleen. This could be due to aggregation of NPs by disulfide bond formation or reaction with thiolated proteins in the bloodstream.

The surface functionalisation of IONPs is a critical parameter when considering their interactions with cells or other biological systems. The isoelectric point of bare magnetite NPs is around pH 7, and can vary with the temperature or presence of ions in solution.[88] It is therefore necessary to modify the surface of the NPs to avoid their sedimentation or precipitation at physiological pH 7.4. Furthermore, they must be able to withstand environments of different pH. For example, tumour tissues are nearly neutral (pH 6 – 8) whereas certain intracellular organelles such as lysosomes are characterised by very acidic conditions (pH 4 - 5). There are two strategies for the stabilisation of NPs:

 - Electrostatic stabilisation, which will depend on the surface charge of the colloid, the ionic strength and pH of the solution in which it is dispersed. It relies on the repulsion of overlapping double layers of NPs with the same charge. The attractive van der Waals forces are counterbalanced by repulsive Coulomb forces. This strategy will however be pH sensitive, and there is a risk of aggregation when the pH is close to the isoelectric point of the NPs in solution.

 - Steric stabilisation, which uses sterically bulky molecules on the surface of NPs and which will depend on the grafting density of the coating and its molecular weight. This relies on molecules of polymer adsorbed to the surface of NPs in order to create a repulsive force between them.

It has been shown however, that magnetite requires both steric and electrostatic stability to prevent aggregation or precipitation across a wide range of pH.[89]

Coatings of IONPs frequently used are lipids, dendrimers,[90] carboxylic acids,[91] phosphonates,[45-47] carbohydrates or starch,[92] proteins or peptides,[29] various polymers such as polyethylene glycol (PEG) or poly(acrylic acid) (PAA).[93] PEG is commonly used to render IONPs stealth for biomedical applications as it provides steric hindrance and reduces protein adsorption.[94] Functionalised PEG may also provide free functional groups, which can be used for further functionalisation with various biomolecules.[95, 96] Coating the NPs with an inert silica shell is also another way of minimising interactions with biological environments and also adding functional groups on the surface for further biofunctionalisation for example. Most of the clinically approved IONPs for MRI are functionalised with dextran or its derivatives as it has proven to have a high affinity for iron oxide and they have also been efficiently used as plasma extenders.[97, 98]

1.2 MAGNETIC NANOPARTICLES AS CONTRAST AGENTS FOR MRI

The clinical potential of NPs has been the subject of a number of scientific studies, particularly for their use as MRI contrast agents.[11, 99] The use of NPs in a clinical setting requires specific properties which will be determined by their synthetic pathway as well as the application for which they are designed. For instance, the challenge remains of developing tools to specifically monitor and/or deliver drugs to cancer cells as well as to monitor the biodistribution and viability of SCs for tissue engineering applications. While there is an array of medical imaging techniques available in the clinic (see Table 1-1), choosing one for a specific application requires consideration of various factors such as: sensitivity, resolution, specificity and exposure of patients to secondary effects.[5] In this project the main focus was on the use of IONPs for MRI as it presents the following advantages:

- MRI is readily accessible in a clinical setting
- It is a non-invasive imaging modality
- The use of non ionising radiation

- With the exception of the use of NPs in microbubbles used as intravenous ultrasound enhancing agents, MRI is the only clinically available imaging technique for which IONPs have been FDA approved.

IONPs approved by the FDA for MRI, Feridex® or Resovist® for example, have now been discontinued by manufacturers. To overcome the unmet need of IONPs as MRI contrast agents in a clinical setting, more and more studies rely on the use of Ferumoxytol (Feraheme®) which is an FDA-approved iron replacement therapy for iron anaemia caused by chronic kidney disease.[100] Indeed, the majority of the clinical trials in which it is used focus on imaging of cancer or other pathologies (22 for imaging *vs* 6 for anaemia treatment).[11]

1.2.1 *Magnetic Resonance Imaging*

MRI is a powerful diagnostics tool which is based on the nuclear magnetic resonance (NMR) phenomena initially described by F.Bloch and E.Purcell in 1946.[101-103] The first MR image was published in 1973,[104] while the first MRI scan on a human was done in 1977.[105, 106] It has been developed over the past decades as a non-invasive method to obtain high resolution anatomical images.

1.2.2 *T_1 and T_2 relaxation*

MRI detects the signal emitted by the protons present, which will respond to a magnetic field in an environment-dependant manner (*i.e.* different tissues). Hydrogen protons are the predominant source of the MRI signal because of their high magnetic moment and high abundance in tissues such as water and fat. In the presence of an external magnetic field B_0 along the z axis, the nuclear spins will align with the applied field. The latter also causes a precession of the spins around the axis B_0 at a frequency ω, known as the Larmor frequency. When radiofrequency (RF) pulses are applied at the Larmor frequency, the nuclei become excited and transit between low and high energy levels.

Table 1-1 Comparison of several imaging modalities. Reproduced from Hachani R. et al., Nanoscale, 2013, Published by The Royal Society of Chemistry.

	Source of imaging	Spatial resolution	Tissue penetrating depth	Sensitivity	Types of probe
MRI	radiowave	25–100 μm	no limit	mM to μM (low)	para- (Gd^{3+}) or superparamagnetic (Fe_3O_4) materials
Positron emission tomography (PET)	γ-ray	1–2 mm	no limit	pM (high)	radionuclides ($^{18}F, ^{11}C, ^{13}N, ^{15}O, ^{124}I, ^{64}Cu$)
Computed tomography (CT)	X-ray	50–200 μm	no limit	not well characterised	high atomic number atoms (iodine, barium sulphate)
Optical fluorescence imaging	visible or near-infrared light	*in vivo*, 2–3 mm; *in vitro*, sub-μm	< 1 cm	nM to pM (medium)	fluorescent dyes, quantum dots

When switching off the RF pulse, the protons return to a state of equilibrium in alignment with B_0 through a phenomenon known as relaxation.[32, 107] Two different relaxation signals are generated:[108]

i) The T_1 relaxation (longitudinal, or spin-lattice relaxation) involves the release of the adsorbed energy to the surrounding lattice or dispersant; it is described by the decay

constant M_z (the parallel component of the nuclear spin vector M). The longitudinal relaxation time T_1 is the time it takes to recover 63% of the original magnetisation.

ii) The T_2 relaxation (transverse, or spin-spin relaxation) involves the exchange of energy between proton spins. This dephasing of spins is due to inhomogeneities in the magnetic field; it is described by the decay constant M_{xy} (the perpendicular component of the nuclear spin vector M). The transverse relaxation time T_2 is defined as the time required after excitation for the magnetisation to be reduced to 37% of the equilibrium magnetisation. When the magnetic field B_0 is not homogenous, there may be dephasing of the magnetisation of individual protons, thus leading to a more rapid loss of transverse relaxation and this is referred to as T_2^*. This T_2^* decay is what a coil receiver will actually detect immediately after application of the pulse and is of much greater magnitude than T_2 in tissues due to the inhomogeneities of the magnetic field. If the latter were perfectly uniform and the materials or tissue being visualised did not lead to any susceptibility effects, the T_2 and T_2^* would be equal. Although this was not used during our project, certain sequences described as "T_2^* weighted" can be used to accentuate local magnetic inhomogeneities in order to detect calcifications or haemorrhage for example.

These two relaxation phenomena are described by the following equations:

$$\mathbf{M_z(t) = M_{z,eq}\left(1 - e^{-\frac{T}{T_1}}\right)} \qquad \text{(Equation 1-7)}$$

$$\mathbf{M_{xy}(t) = M_{xy,eq}(0)e^{\frac{-T}{T_2}}} \qquad \text{(Equation 1-8)}$$
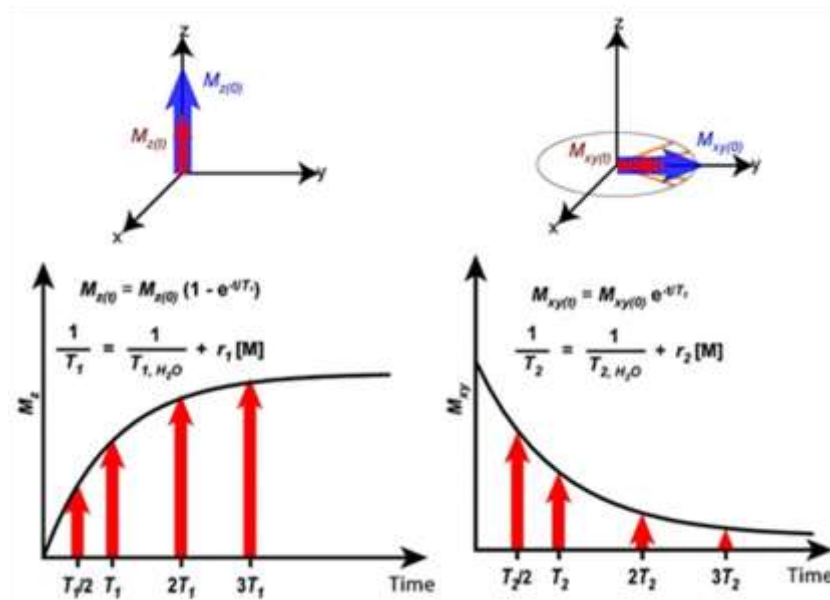
Figure 1-11 Representative T_1 and T_2 relaxation mechanism (top) and a representative Z-spectrum are illustrated (bottom). Adapted from C. Khemtong, et al., Chemical Communications, 2009, with permission from the Royal Society of Chemistry.

1.2.3 *MRI contrast agents (molecular-based and magnetic nanoparticles)*

Magnetic resonance imaging, without the use of contrast agents (CAs), allows one to distinguish between various tissues or anatomical structures. However, these can sometimes be difficult to discern and identify, and the use of CAs then helps increase the spatial resolution of the images obtained as well as to identify the nature of certain tissues such as tumours for example. CAs will act by influencing the relaxation times of the protons, T_1 or T_2, and will consequently be categorised as T_1 (positive) or T_2 (negative) CAs. They are commonly described and compared by their relaxivity values r_1 and r_2 (Figure 1-11). While a large r_1 is important for a T_1-weighted contrast agent, this criteria is not exclusive and it is also the ratio r_2/r_1 which determines the properties of a CA: the ratio

r_2/r_1 is generally between 1 and 3 for a T_1 CA, whereas T_2 CAs will generally have a ratio r_2/r_1 >10.

The properties of CAs approved for clinical applications can be found in Table 1-2. The increase in r_1 with increasing diameter is attributed to the decrease in rotation correlation time as the molecular weight or diameter increases.[109] Amongst the potential candidates for cellular paramagnetic labelling, gadolinium-based CAs offer efficient intracellular labelling, and certain Gd chelates present the advantage of having clinical FDA approval (Magnevist® or Omniscan® for example).[109, 110] The structures of the three most commonly used gadolinium-based CAs are shown in Figure 1-12. However, precaution must be taken when using CAs containing gadolinium because of the risk of development of nephrogenic systemic fibrosis (NSF) in patients with renal failure as this occurred following the administration of Omniscan®.[111] Indeed, free Gd^{3+} ions are able to bind to Ca^{2+} binding enzymes and voltage-gated Ca^{2+} channels, which can lead to adverse biological effects.[88] Therefore, as a preventive measure, Gd^{3+} cations are administered in a chelated form. Complexes of Gd^{3+} are now routinely used in MRI and can be conjugated with NPs to render the latter suitable for T_1 weighted MRI.[112]

The complexes which chelate Gd^{3+}: DOTA (1,4,7,10-tetraazacyclododecane-1,4,7,10-tetraacetic acid) and DTPA (diethylenetriaminepentaacetic dianhydride), are stable and soluble in physiological medium. Their chelation to Gd^{3+} can be seen in Figure 1-12 with the structures of these clinically approved CAs. They have a low osmotic potential and are rapidly eliminated from the body by renal excretion, so this confers the minimal biological impact desired. Although Gd-DTPA (Magnevist®) was the first chelate to be commercially available in 1988,[30] Gd-DOTA (Dotarem®) is preferentially used as it is more advantageous in terms of high relaxivity, blood clearance rate *in vivo*, higher binding coefficient to Gd^{3+} (more stable *in vivo* in terms of thermodynamics and kinetics) and for the same image quality a smaller dose is required than the DTPA chelate.[113] All these characteristics make it safer and more efficient in comparison to Gd-DTPA. The main drawback of using this CA is

that it must be administered in high concentrations to produce an effective contrast. This is because of diffusion, low relaxivity (the change in relaxation rate) per gadolinium ion and dilution phenomena *in vivo* after injection.
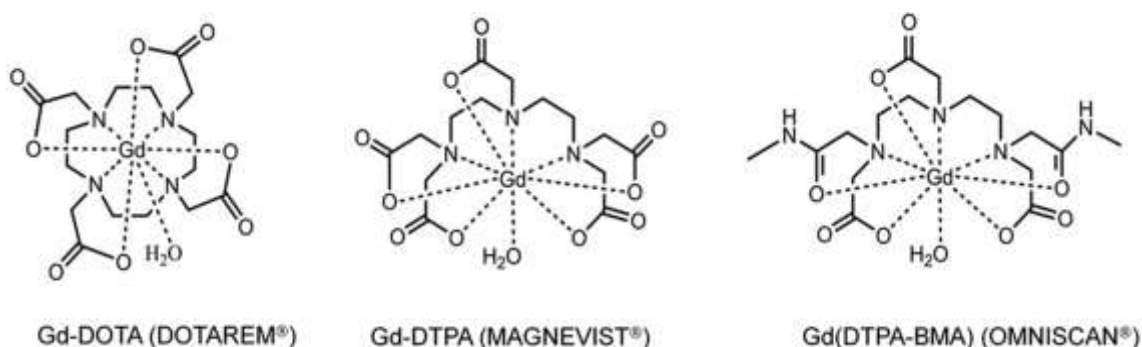
Figure 1-12 Structures of the Gd(III) based MRI contrast agents currently used in the clinical practice. Adapted from Zhou et al., Wiley Interdisciplinary Reviews: Nanomedicine and Nanotechnology, 2012 with permission.

In comparison to molecular-based CAs, NPs allow a higher concentration of CA to be administered with fewer risks, through binding of multiple complexes of Gd per NP. They can also potentially lead to improved targeting as it is the case in tumours with passive targeting by the enhanced permeability and retention (EPR) effect.[114-116] Indeed, tumour sites have a dense vasculature but lack lymphatic drainage, which allows the retention of molecules or NPs by the EPR effect.

Unlike molecular-based positive CAs, to this day, only superparamagnetic IONPs have been used as T_2 negative contrast agents. They are frequently used when investigating tumours or other abnormalities affecting the liver, spleen, lymph nodes and bone marrow as they are internalised non-specifically by the macrophages of the RES.[117, 118] IONPs clinically approved for such applications include ferumoxides Feridex® in the USA, Endorem® in Europe) functionalised with dextran; and Ferucarbotran (Resovist®), which is functionalised with carboxydextran. The main characteristics of these IONP based CAs are listed in Table

1-2. They are both comprised of a magnetite core 10-20 nm in size with a biocompatible polymer leading to a hydrodynamic diameter of approximately 60-250 nm. In the case of liver imaging, they usually undergo phagocytosis by macrophages of the RES. However, in the case of lesions lacking hepatocyte Kupffer cells this process does not occur.[15, 119-121]

FDA-approved IONPs such as Ferumoxides and Ferucarbotran were discontinued in 2008 and 2009. Since then, the only formulation remaining on the market is Ferumoxytol (Feraheme®), an ultrasmall IONP used in the treatment of iron deficiency anaemia, which has been investigated more recently in cellular labelling applications.[122, 123]

Table 1-2 Characteristics of clinically approved IONP colloids as MRI contrast agents, *adapted from Anselmo et. al, Bioengineering and Translational Medicine, 2016,***1**, 10-29.

Name	Company	Coating agent	Hydrodynamic size (nm)	Relaxivity at 1.5 T $(mM^{-1} s^{-1})$	Applications	Status
Ferumoxides (Feridex IV®, Endorem®)	Feridex IV® by Berlex Laboratories, Endorem® by AMAG Pharmaceuticals	Dextran	120 - 180 nm	$r_1 = 4.7$ $r_2 = 41$	Liver lesions imaging	FDA approved in 1996, discontinued in 2008
Ferucarbotran (Resovist®)	Ferucarbotran by Meito Sango, Resovist® by Schering	Carboxydextran	40 - 60 nm	$r_1 = 8.7$ $r_2 = 61$	Liver lesions imaging	EMA approved in 2001, discontinued in 2009
Lumirem®, Gastromark™	AMAG Pharmaceuticals	Silicone	50 nm	$r_1 = 10.7$ $r_2 = 38$	Bowel imaging	FDA approved in 1996, discontinued in 2012

When using MNPs as CAs, size is an important factor because the domain size and magnetic state (superparamagnetism or ferromagnetism) will determine the magnetic property.[124] Generally, smaller particles will have a smaller relaxivity r_2 due to a smaller magnetic moment. This has been observed in magnetite Fe_3O_4 NPs where the decrease in size from 12 nm to 4 nm was accompanied by a decrease in the saturation magnetisation from 102 to 25 emu/g as well as the r_2 relaxivity value.[125] In another recent study, the r_2 value of IONPs synthesised in organic solvents increased from 84 to 317 mM^{-1} s^{-1} as the particle size increased from 4 nm to 9 nm.[126] It has been frequently demonstrated that larger IONPs have higher r_2 relaxivity values due to higher saturation magnetisation values.[127, 128] With larger NPs, the interactions between NPs are very strong within aggregates formed in suspensions solidified by agar gel. These strong inter crystal interactions produce a high magnetic field gradient which leads to an enhanced r_2 effect by accelerating the loss of phase coherence of the spins contributing to the MR signal. This study also highlighted the importance of the crystallinity of the NPs synthesised as well as the effect of their aggregation on an increased r_2 relaxivity. This strategy has been used to encapsulate several IONPs in order to enhance their sensitivity for T_2-weighted MRI.[129, 130] Furthermore, it has been shown that when IONPs are small enough or coated with the right polymer, they may be used as T_1 contrast agents.[131, 132] This may be useful depending on the anatomical structures to be observed and to avoid potential long term toxicity in comparison to gadolinium-based CAs. Indeed, when decreasing the size of IONPs (5 nm diameter and below), the magnetic moment of the IONPs will also decrease due to the reduction in the volume magnetic anisotropy and spin disorders on the surface of the IONPs.[133, 134] The small IONPs can therefore potentially be used as T_1 CAs as their large surface area with 5 unpaired electrons enhances the T_1 relaxation process, and their small magnetic moment decreases the T_2 effect, thus leading to an overall increase in the r_1/r_2 ratio.[135]

Another factor to consider is the surface chemistry of the NPs used in MRI as this will impact the NP's environment and its interactions with it. For example, in the case of ultrasmall

Gd$_2$O$_3$ NPs, polyvinyl pyrrolidone (PVP) coated Gd$_2$O$_3$ NPs showed an enhanced longitudinal r$_1$ relaxivity in comparison to oleic acid and cetyl trimethylammonium bromide (CTAB) co-coated Gd$_2$O$_3$ NPs of identical size. The authors hypothesised that this phenomenon was due to better interaction of the NPs with surrounding water molecules.[136]

1.2.4   *Advantages and limits of MRI*

The use of contrast agents to monitor cells is recent, with the first studies taking place in 2000.[90, 137] More recently, labelling and monitoring of SCs by MRI for cellular therapy has been investigated more intensely.[138] However, a number of variables such as the cellular localisation of NPs for example, can influence the signal obtained. The cellular compartmentalisation into lysosomes strongly decreases the longitudinal relaxivity of Gd-based CAs, this is probably due to the limited accessibility of water protons to the surface of the spatially confined CAs.[139 140] This leads to a T$_2$ weighted MRI of labelled cells due to an increased r$_2$/r$_1$ ratio in a dose-dependent manner. Also, some technical constraints such as the inherent absence of signal in certain anatomical regions can make it difficult to interpret the negative contrast obtained with IONPs by T$_2$ weighted images. To overcome this, different MRI sequences have been developed which allow us to generate positive MRI signal from IONPs and to quantify the labelled cells.[141] As little as 120 000 cells could be visualised in a rat using a modified sequence with a conventional clinical MRI scanner operating at 1.5 T.[99]

Clinical MRI (1.5 T scanner with radiofrequency coils) is not ideal for imaging of single cells after systemic administration. The spatial resolution needed would require long scanning times, which is not realistic in clinical settings. They are however still adequate for visualising magnetically labelled cells administered locally (for example, in the case of an implanted scaffold). This requires a compromise between the minimum number of cells detectable and the concentration of NPs to ensure there is no effect on cell viability or proliferation. Schäfer *et al*. determined that at least 1000 IONP-labelled mesenchymal stem

cells (MSCs) could be visualised by MRI *in vitro* after exposition to a magnetic field.[142] Another recent study showed that a relatively high incubation concentration (10 µg ultrasmall IONPs per 10^5 cells) and a long incubation time (21 h) were needed to detect a minimum of 250 000 MSCs *in vivo*.[143] In comparison, the *in vitro* detection threshold of cells after incubation with gadolinium oxide NPs at a Gd concentration of 0.2 g per 5 x 10^5 cells for 2 h was estimated to be about 10 000 cells.[144] Yang *et al*. were able to compare the efficiency of MSC labelling with IONPs and paramagnetic chelates.[145] IONP labelling had a detection threshold of 12 500 cells *in vitro*, while gadolinium chelate labelling could be detected for at least 50 000 cells.[145]

New strategies have been explored to overcome the limits of clinical MRI when studying the biodistribution of a single cell. These include the use of high field MRI scanners (for example 9.4 T, 17.6 T),[146] cryogenic probes,[147] or high temperature superconducting coils[148] that can be mounted on clinical 1.5 T devices and which allow the resolution at a single cell level even after systemic administration. For example, a cryo cooled high temperature superconducting coil can increase the signal-to-noise ratio by decreasing the noise generated by the detection coil, thus allowing for the detection of 1.3 pg Fe/cell *in vitro* with lymphocytes.[148]

MRI is an imaging technique which produces anatomical images with good resolution (25–50 µm), but is limited by its low sensitivity. Current research focuses on its combination with other higher sensitivity-low resolution techniques such as Positron Emission Tomography (PET), Single Photon Emission Computed Tomography (SPECT) or Near Infrared Fluorescence (NIRF) imaging. Indeed, multimodal NPs incorporating several imaging probes on a single platform are being developed to overcome the limitations of a single modality by complementing it with another one.[149]

Biomedical applications of IONPs will require an efficient and sufficient uptake in cells. In terms of cell labelling, the main limitations of MRI are currently the loss of signal with time

and the lack of specificity. NPs can be internalised by non-specific cells *in vivo* after implanted SCs undergo apoptosis or degradation, or their exocytosis can occur under stress conditions.[6, 150-152] To overcome these limits, chitosan coated NPs have been studied as they allow an enhanced uptake and long term tracking of adult neural SCs through limited endo-lysosomal trafficking and exocytosis.[153] Recently, hydrophilic IONPs coated with glucosaminic acid were shown to selectively enhance cellular uptake of NPs in cancer cells but not in macrophages or fibroblast cells after 40 h of cell culture.[154] Furthermore, once SCs divide or differentiate the concentration of NPs decreases rapidly hence the MRI signal is lost with time. Encapsulation of IONPs in polymeric microparticles has been a strategy explored to help maintain a strong MRI signal and reduce exocytosis in order to enable the longitudinal tracking of SCs.[155]

Although this was not investigated during our project, it is worth mentioning that IONPs may potentially be used for dual purpose in MRI: not only as a contrast agent to visualise the cells, but also to label cells that can be then magnetically targeted by MRI. This has been recently demonstrated within clinical grade MRI scanners and MSCs.[156-158]

1.3 NANOPARTICLE-CELL INTERACTIONS

1.3.1   *Mechanisms of cellular uptake of nanoparticles*

As explained in section 1.2.4, a prerequisite in the use of IONPs for MRI is that a sufficient amount of NPs enter the cells. This will be dependent upon the cell type, cell culture conditions and some of the NPS properties such as their shape, size, coating, and surface charge. To label cells with NPs, the most simple and common method used is to label them *in vitro*. The NPs may enter cells by endocytosis through different pathways as illustrated in Figure 1-13.[159] Endocytosis is the process by which cells take in foreign materials by engulfing and fusing them with their plasma membrane. It will be dependent upon the NP's size, degree of aggregation and surface chemistry. It is reported in most scientific publications that NPs used in biomedical applications (< 100 nm) will be internalised by

endocytosis (clathrin or caveolae mediated), whereas larger particles (> 0.5 μm) will be internalised by phagocytosis or macropinocytosis.[160, 161] NP internalisation by receptor-mediated endocytosis may be visualised and characterised as small vesicles made of the NPs by TEM.[162]

A strategy commonly used to increase the labelling efficiency of cells by NPs is to functionalise the latter with transfection agents or cell penetrating peptides to enhance their endocytosis.[163, 164] These peptides are mostly cationic and include poly (l-lysine) (PLL),[165] lipofectamine,[166] and protamine sulphate.[167]

They will enhance the uptake of NPs through electrostatic interactions with negatively charged phospholipids of the cellular membrane. Another strategy is to use HIV derived Tat (Arginine rich) peptides, which avoid the endosomal endocytosis pathway and allow the uptake of NPs to the cytoplasm or nucleus.[137, 168] A lower number of labelled cells can then be visualised by MRI *in vivo* or labelled cells may be magnetically sorted after *in vivo* migration for further analysis.[137] However, these peptides may present a risk of toxicity if
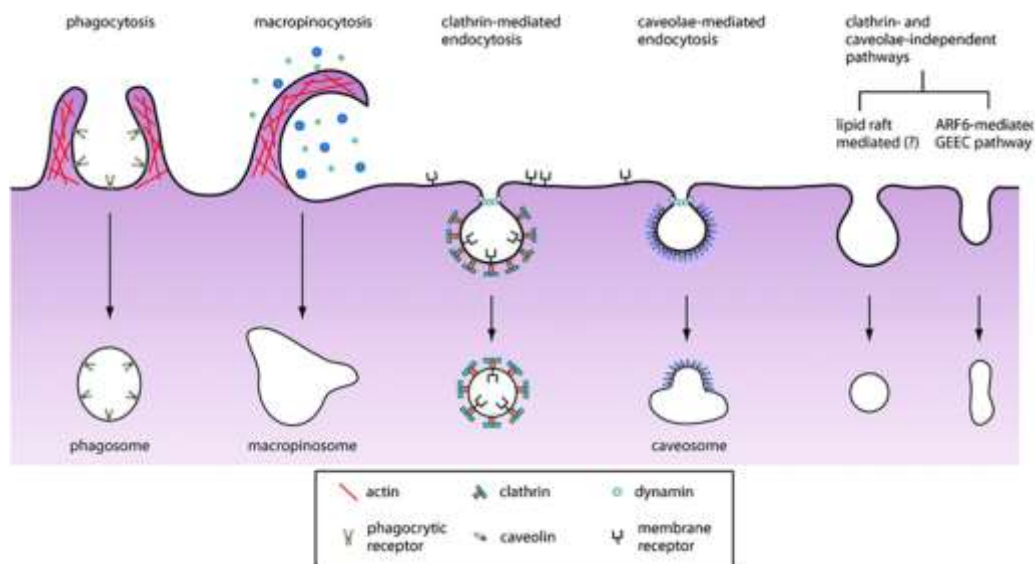
Figure 1-13 Pathways of entry into the cell. Reproduced from L. Y. T. Chou et al., Chem. Soc. Rev., 2011 with permission from The Royal Society of Chemistry.

their ratio is not controlled and if used on their own without NPs.[163, 169]

A new strategy has been recently investigated to label cells more efficiently with minimum invasiveness: *in vivo* labelling. Khurana *et. al* used the phagocytic capacity of MSCs to label them *in vivo* after intravenous injection. In comparison to the equivalent *ex vivo* labelling, the iron uptake was found to be significantly higher with fluorescence intensity of NPs being 3.2 times higher in the case of cells labelled *in vivo*. The labelled MSCs were then implanted into the knees of rats with an induced osteochondral defect, and could be visualised up to 4 weeks after transplantation by T_2 weighted MRI.[170] This strategy could only be implemented for cells that are phagocytic in nature such as MSCs, and there will always be the inherent inability to distinguish live from dead cells, or to know whether the labelling agent has been taken up specifically by MSCs or macrophages. However, this technique is clinically relevant to track the cells immediately post transplantation to monitor the cell engraftment in real time. Labelling *in vivo* aims to eliminate the risks of contamination and biologic alteration of SCs which may occur with *ex vivo* or *in vitro* methods.[171]

1.3.2   *Cell – iron oxide nanoparticle interactions*

One of the main reasons IONPs are considered advantageous in comparison to other nanomaterials is that in acidic conditions in the human body, iron oxide can be degraded into iron ions. Briefly, after cellular endocytosis, IONPs may be degraded in lysosomes into Fe^{2+} ions. These can potentially cross the nuclear or mitochondrial membrane, and if so, can react with hydrogen peroxide and oxygen produced by the mitochondria to produce highly reactive hydroxyl radicals and ferric ions (Fe^{3+}) via the Fenton reaction.[172] The Fe^{3+} ions resulting from this process may then be part of the biologically available iron storage which is approximately 3 to 5 g: approximately 2.5 g in haemoglobin and the rest in ferritin (bone marrow, liver and spleen).[27, 173] Considering that most applications will require a dose administered in the range of 0.5 – 5 mg of IONPs per kg of body weight, the resulting iron produced will be negligible.[15] Iron is considered safe as long as it is bound to a protein or

chelated, as this is the case in heme for the transport of O_2 in the blood. Otherwise, free iron can catalyse the conversion of H_2O_2 into free radicals such as: $H_2O_2 + Fe^{2+} \rightarrow Fe^{3+} + OH°$ + OH^-. More recently, safety concerns have risen regarding the use of IONPs as iron overload occurred in a cirrhosis model. Accumulation of iron in the liver over the course of several weeks induced oxidative stress and an increase in lipid peroxidation.[174] The impact of the nanomaterials on biological systems is an important factor to take into account when considering their biomedical applications. For example, copper-based NPs are inert in their bulk state, but numerous studies have demonstrated that they exhibit toxicity through DNA damage and oxidative stress at the nanoscale.[93, 175-177]

When administering NPs *in vivo*, one must avoid aggregation and adsorption of proteins or other macromolecules to their surface. To render them stealth, various polymers or surface functionalisation strategies can be investigated in order to ensure plasma proteins, such as opsonins, will not adsorb on the NP surface which would lead to their uptake by macrophages, monocytes and dendritic cells, thereby leading to their clearance from circulation. PEG is currently the most widespread polymer used to render the surface of the NPs stealth. It induces steric hindrance between NPs thus avoiding their agglomeration,[178] as well as decreasing the surface charge which could in turn decrease the cellular uptake in a dose and cell-type dependent manner.[179] Proteins exhibit less attractive van der Waals forces towards it due to its low refractive index, thus minimising interaction.[180] Briefly, the first approach to van der Waals interactions between two colloidal particles developed by Hamaker was called pair-wise addition. However, in the case of NPs, the alternative Lifshitz theory should be applied as this takes into account the many-body effect: the dipole field of one particle is influenced by its neighbouring particles. This theory considers each particle as a dielectric continuum characterised by a frequency/wavelength dependent refractive index.[181] As modelled by Jeon *et al*., the interaction between the protein and a polymer surface across water is van der Waals interaction.[180] The latter has been modelled and calculated by Jeon and colleagues. When increasing the surface density of the polymer, the volume fraction of the polymer increases, in turn leading to a higher refractive index while

the static dielectric constant decreases, thus resulting in an increase in the van der Waals free energy. Furthermore, the water molecules arranged around PEG minimise the interaction of the polymer chains with proteins in the local environment. However, whereas many publications have found PEG to be a non-toxic organic coating for NPs; a recent study has shown cytotoxicity of PEG-coated gold NPs through production of reactive oxygen species in comparison to a same intracellular concentration of polymer coated gold NPs.[179]

Conflicting results regarding the interaction of IONPs with cells *in vitro* or *in vivo* have been published in recent years. It is clear that parameters such as the size or coating will play a major role in determining the fate of the NPs.[182] It was found for example that 12 nm magnetite NPs coated with PEG circulated twice as long in the bloodstream as 2,3-dimercaptosuccinic acid coated NPs of the same size and material.[183] Also, studies have consistently demonstrated that smaller IONPs will tend to accumulate in the liver rather than the spleen.[95]

The interaction of NPs with living organisms poses several questions such as their internalisation pathway, biodistribution or their toxicity. The latter has been the subject of over 10 000 papers in the past 30 years however there is still a fundamental lack of standardisation for answers to this question.[184] Indeed, a recent review[175] found that most of these publications did not characterise their nanomaterials (no study was done to see whether there was any contamination of the engineered nanomaterials for example), or no reference or control samples were used. To date however, the scientific community regards iron oxides as being the safest material to investigate for biomedical applications. In comparison to gadolinium for example, IONPs have shown limited toxic effects and are considered safer as confirmed by their previous FDA approval for clinical MRI.

For *in vivo* applications, the administration mode must also be considered in regards to the potential toxicity of the nanomaterials. For example, IONPs injected systemically may lead to significant toxicity in a dose and size dependent manner.[185] The impact of the IONPs

developed during this project will be investigated *in vitro* and *in vivo* and detailed in a later chapter.

1.4 THESIS OUTLINE

This thesis reports the synthesis of superparamagnetic IONPs for MRI applications. The objective was to develop and optimise a novel and reproducible synthesis method from which could be obtained IONPs with finely controlled properties and with MRI relaxivity values as good as previously FDA approved IONPs. To fulfil these requirements, the thesis will address each one in the following chapters:

- The different materials and methods used during this project are reported in chapter 2.

- In order to obtain IONPs with desired sizes and shapes for MRI applications, chapter 3 investigates the optimisation of the polyol synthesis method using different experimental conditions. The impact of reaction parameters such as the reaction time or temperature is reported and optimised.

- After optimising the synthesis conditions, the polyol coating of the IONPs is found to be unstable and lead to aggregation of the nanoparticles in aqueous solution. If these IONPs are to be considered for any biomedical application, they must remain stable and disperse homogenously in biological media. To achieve this, their functionalisation and stabilisation with different ligands is investigated in chapter 4.

- Finally, once colloidal stability was achieved with a selected ligand, their biocompatibility with human mesenchymal stem cells and their potential as MRI contrast agents is investigated in chapter 5.

- The main conclusions which can be drawn from this thesis are reported in chapter 6, as well as suggestions for further work.

Chapter 2   MATERIALS AND METHODS

2.1 MATERIALS

2.1.1   *Chemicals for the synthesis of IONPs*

Iron(III) acetylacetonate (Fe(acac)$_3$, 99.9%), triethylene glycol (TREG, 99%), diethylene glycol (DEG, 99%), and tetraethylene glycol (TEG, 99%) were purchased from Sigma-Aldrich, UK. Acetone was purchased from VWR International, UK. All chemicals were used as received without further purification.

2.1.2   *Chemicals for the functionalisation of IONPs*

L-Tartaric acid ($\geq$ 99.5%), 3,4-dihydroxyhydrocinnamic acid (3,4-DHCA, 98%), citric acid monohydrate ($\geq$ 99%), 3-mercaptopropionic acid (3-MPA, $\geq$ 99%), folic acid ($\geq$ 97%), oxalic acid (98%), succinic acid ($\geq$ 99%), PEG 200 (United States Pharmacopeia Reference Standard), PEG 300, PEG 2000, PEG 6000, PEG diacid 600, L-glutamic acid ($\geq$ 99%), Tiopronin (99%), terephtalic acid (98%) were purchased from Sigma-Aldrich, UK. 2-mercaptopropionic acid (2-MPA, 97%) was purchased from Alfa Aesar, Thermo Fisher Ltd GmbH, Germany. Meso-2,3-dimercaptosuccinic acid (DMSA, 98%), L-cysteine (L-Cys, > 99%), and azelaic acid (98%) were purchased from Acros Organics, Thermo Fisher Scientific Ltd, UK. Oxamic acid (98%) was purchased from VWR International Ltd, UK. Slide-a-Lyzer dialysis cassettes with a 10 kDa molecular weight cut off (MWCO) were purchased from Thermo Fisher Scientific Ltd, UK. All chemicals were used as received without further purification.

2.1.3   *Human mesenchymal stem cells (hMSCs)*

Bone marrow derived mesenchymal stem cells (MSCs) were obtained from Professor Mark Lowdell (Department of Haematology, University College London) at the UCL/Royal Free Biobank and from Thermo Fisher Scientific, UK. Progenitor cells or hMSCs were cryopreserved after samples were collected from patients of various clinical trials.

2.1.4   *MSC culture*

Nuclear fast red solution (0.1% in 5% aluminium sulfate), hydrochloric acid (HCl 36.5-38.0%), dimethyl sulfoxide (DMSO, sterile-filtered, ≥ 99.9%), paraformaldehyde (PFA), and Trypan blue solution (0.4%, sterile-filtered) were obtained from Sigma-Aldrich, UK. Trypsin of fungal origin (TrypLE™ Select Enzyme (1X) without phenol red), foetal bovine serum (FBS), minimum essential medium alpha (MEMα) with GlutaMAX^{TM} supplement and without nucleosides, Hank's balanced salt solution (HBSS) without calcium or magnesium were obtained from Life Sciences Technologies Ltd, UK. All reagents were used as purchased without any further modification. The complete media (cMEM) is defined as MEMα complemented with 10% FBS.

2.1.5   *In vitro studies of cell-nanoparticle interactions*

3-(4,5-Dimethylthiazol-2-yl)-2,5-diphenyltetrazolium (MTT, BioReagent, ≥ 97.5%), potassium hexacyanoferrate(II) trihydrate (≥ 99.95%, trace metals basis), agarose (BioReagent, low electroendosmosis) and Triton™ X-100 were obtained from Sigma-Aldrich, UK. CellTiter 96® Aqueous Non-Radioactive Cell Proliferation Assay (MTS) was purchased from Promega Corporation, Madison WI, USA. Annexin V apoptosis detection kits were purchased from BD Biosciences, Oxfordshire, UK. DRAQ7 was obtained from BioStatus Limited, Leicestershire, UK. CM-H$_2$DCFDA was purchased from Molecular Probes, Invitrogen, Belgium. MitoTracker Red CMXRos and Hoechst 33342 were obtained from Thermo Fisher Scientific, Belgium. Acti-stain 488 was purchased from Tebu-Bio, Belgium. Cell scrapers were purchased from VWR, United Kingdom.

2.2 METHODS

2.2.1   *Conventional polyol synthesis using a Schlenk line*

Iron (III) acetylacetonate (from 0.35 g to 0.7 g) was dissolved in 20 - 30 ml of polyol solvent previously degassed by the freeze-thaw method. The reaction mixture was then transferred into a round bottom flask under a nitrogen atmosphere, purged with nitrogen three times before being heated up to 250 – 280 °C and maintained at this temperature for 5 to 90 min, before being cooled back down to room temperature (RT). The black dispersion of nanoparticles obtained was washed with acetone by centrifugation (8500 rpm, 10 min, 3 times) in a Heraeus Biofuge Stratos centrifuge, and then redispersed in dH_2O before further characterisation. An aliquot (approximately 2 ml) was freeze-dried over 48 h (Lyolab 3000, Thermo Scientific Heto) for XRD and SQUID-VSM characterisation.

2.2.2   *Microwave synthesis*

IONPs were synthesised by the polyol method in a CEM SP-Discovery Microwave (CEM, USA). Iron (III) acetylacetonate (from 0.35 g to 1.4 g) was dissolved in 15 ml of polyol solvent, then transferred into a 35 ml vial and sealed with a pressure cap. The solution was heated to 250 – 280 °C (250 W, power max off) and maintained for 5 to 90 min at this temperature. Samples were automatically cooled down back to RT, before being washed by centrifugation with acetone (8500 rpm, 10 min, 3 times) and redispersed in dH_2O for further characterisation. An aliquot (approximately 2 ml) was freeze-dried over 48 h (Lyolab 3000, Thermo Scientific Heto) for XRD and SQUID-VSM characterisation.

2.2.3   *Polyol synthesis in high pressure high temperature conditions*

$Fe(acac)_3$ (0.35 g to 2.1 g) was mixed with the polyol solvent and sonicated for 30 to 60 min in order to homogenise the red dispersion. Shorter sonication times were found insufficient as traces of $Fe(acac)_3$ could still be visualised at the bottom of the tube. The resulting

mixture was then transferred into a 45 ml capacity Teflon liner and this was assembled with the autoclave jacket and placed into an oven (Memmert, model UFP400). The autoclave vessels have a flat polytetrafluoroethylene (PTFE) gasket that is sealed with a screw cap. The screw caps and bodies of the vessel are made of alloy steel which allows experimental conditions of up to 300 °C and maximum working pressure of 1700 psi (115 bar). A pre-set program was run where the oven was heated up to 250 °C then maintained this temperature for 30 min to 24 h before ramping down to RT for 2 h. Samples were washed by centrifugation with acetone (8500 rpm, 10 min, 3 times) and redispersed in dH_2O for further characterisation. An aliquot (approximately 2 ml) was freeze-dried over 48 h (Lyolab 3000, Thermo Scientific Heto) for XRD and SQUID-VSM characterisation.

2.2.4   *Ligand exchange with IONP powder and magnetic separation*

For the ligand exchange process, IONPs in powder form were redispersed in water to 10 mg/ml and sonicated in order to improve their dispersion. The ligands of choice were dissolved in 2 ml DMSO to a final concentration of 30 mg/ml. The resulting mixture was kept under continuous stirring overnight to achieve the total displacement of TREG on the nanoparticle surface. The next day, the IONPs were separated by magnetic separation and repeatedly washed with distilled water until a clear supernatant was obtained.

2.2.5   *Ligand exchange with IONP powder and dialysis*

Iron oxide nanoparticles were prepared as in section 2.2.4. The ligands of choice were dissolved in 2 ml distilled water to a final concentration of 30 mg/ml. The next day, the IONPs were separated by magnetic separation and further purified by dialysis against distilled water with a molecular weight cut-off (MWCO) of 10 kDa.

2.2.6   *Ligand exchange with IONP solution and dialysis*

A colloidal dispersion of IONPs in water (10 mg/ml) was added to the ligands of choice in water. Different ratios of IONPs to ligand (1:1 up to 1:50) were tested. The resulting mixture was stirred for 48 to 72 h at 300 rpm at RT. Then, the IONPs were purified by dialysis in a 5 l beaker against water with a membrane of MWCO 10 kDa. The volume of ultra-purified water used in the process is at least 100 times the volume of IONP solution. The dialysis was performed for 7 d and the water was changed daily, unless specified otherwise.

2.2.7   *Cell culture of human mesenchymal stem cells (hMSCs)*

hMSCs were supplemented with cMEM. An initial stock of 700 000 cells was cultured at 37 °C in a 5% CO_2 atmosphere. When 70 – 75% confluency was achieved, adherent fibroblast-shaped cells were trypsinised, passaged and returned to culture, unless cells were needed for experiments. If cultured, the seeding density chosen was in the range of 1000 to 3000 cells/cm^2.

2.2.8   *Cell thawing after cryopreservation*

Cells stored in liquid nitrogen at -80 °C were returned to cell culture by thawing the cryovial in a water bath at 37 °C until only a small pellet could be observed. The cells were then transferred into a larger vial and then 10 ml of warm medium was added drop wise while the sample was lightly agitated. An additional 10 ml of warm medium was then added, before counting the number of cells by Trypan Blue exclusion using a haemocytometer. Cells were then introduced into a tissue culture flask at a seeding density of 500 cells/cm^2. The medium was then changed every 2 to 3 d, until 70-75% confluency was reached.

2.2.9 *Trypsinisation of cells*

Cell culture medium was aspirated from the tissue culture flask, and the cells were rinsed with HBSS 3 times. Then 10 ml of pre warmed TrypLE™ (trypsin of fungal origin) was added and the flask was returned to the incubator for 7 min. The flask was then gently tapped to ensure the detachment of the cells. cMEM (10 ml) was added to neutralise the action of TrypLE™. The cell suspension was centrifuged at 200 g for 10 min, after which the supernatant was discarded and the number of cells remaining in the pellet was determined by Trypan blue staining and a haemocytometer. The cells could then be cryopreserved in liquid nitrogen with 10% FBS in cMEM, or returned to culture, or used immediately for experiments.

hMSCs may be detached with diluted Trypsin-EDTA (0.05%) for very brief exposure times (2 to 3 min maximum). However, in this method, TrypLE is our reagent of choice as it is gentler and there is little risk of damaging cells. Furthermore, these hMSCs have been expanded by Professor Mark Lowdell and his team for the development of Advanced Therapy Medicinal Products (ATMP) which require animal-free products in cGMP grade cultures.[186]

2.2.10 *Quantification of uptake of IONPs in hMSCs by a colourimetric method*

This protocol was obtained from a method previously published.[187, 188] hMSCs were seeded on a 24 well plate (20 000 cells/well) and returned to culture overnight. Cell loading with IONPs was carried out at concentrations 0, 10, 100 and 150 μg Fe per ml (V = 500 μl), over a period of 24 h. Cells were then rinsed 3 times with HBSS to remove any free iron oxide, cellular debris, and traces of FBS which contains protease inhibitors. A set of standards ranging from 0 to 100 μg Fe^{3+} per ml were also constructed. After rinsing with HBSS, HCl (9.6 μl, 37%) and HNO_3 (3.2 μl, 65%) were added to each well in order to ensure the oxidation of all Fe^{2+} to Fe^{3+}, and the volume was adjusted with 2-[tris(hydroxymethyl)-methylamino]-ethanesulfonic acid (TES) buffer (28.8 μl) pH 9.5-10. Solubilisation was enhanced by placing

the plate on a shaker at room temperature for 2 h. After shaking, distilled water (52 µl) was added to each well. Then, both the samples and standards were mixed with a 5:1 solution (96 µl) of Tiron (16 µl, 0.25 M) and KOH (80 µl, 4 M), followed immediately by the addition of PBS (160 µl, 0.2 M, pH 9.5). After 15 min, A_{480nm} was measured.

2.2.11   *Visualisation of cellular uptake of IONPs by Prussian Blue staining*

hMSCs were seeded on a 96 well plate (1000 cells/ well) and returned to culture overnight. The visualisation of cellular uptake of IONPs by Prussian Blue staining being an image-based assay, we aimed for the cells to remain in a monolayer for efficient staining and visualisation. Cell loading with nanoparticles was carried out at a range of concentrations from 0 to 250 µg Fe per ml (V = 100 µl), over a period of 24 h. Cells were then rinsed 3 times with HBSS to remove any free IONPs, before fixing with 4% PFA for 15 min at room temperature. The fixative was removed, and then the hMSCs were incubated for 10 min with 2% potassium ferrocyanide and 6% HCl in a volume ratio 1:1, until the appearance of blue colour. The cells were then rinsed with distilled water 3 times leaving the water on the cells for 5 min for each wash. Finally, cells were rinsed twice with HBSS to get rid of any excess stain before being observed and captured using an Olympus BX51 light microscope.

2.2.12   *Visualisation of IONP uptake in hMSCs by TEM imaging*

For TEM imaging, cells were harvested by gentle trypsinisation and the cell number was determined with Trypan Blue staining and a haemocytometer. The cells were then seeded on 12 mm cover slips in 24 well plates and allowed to adhere overnight. The next day, they were rinsed with sterile HBSS twice, before incubating them with IONPs at a concentration previously deemed safe (50 µg Fe/ml, V = 500 µl) (*see chapter 5)* and for different periods of time (1 h, 4 h or 24 h). The media was then removed and the cells were rinsed again with cold sterile HBSS before adding a fixative solution of 2% paraformaldehyde (PFA), 1.5% glutaraldehyde in 0.1 M PBS pH 7.3 for at least 24 h. The cells were then washed twice with 0.1 M PBS buffer for 5 min, before being post-fixed in a solution of 1% osmium tetraoxide

and 1.5% potassium ferrocyanine (1 h, 4 °C). Cells were rinsed with 0.1 M PBS, 1% tannic acid in 0.05 M PBS for 5 min, 0.1 M PBS for 5 min and then with dH_2O for 5 min. The cells were then dehydrated with increasing ethanol (25, 50, 70, 90 and 100%) each for 5 min. Cell layers were infiltrated with increasing embedding medium of epoxy resin (25, 50, 66%) in propylene oxide and transferred into polyethylene capsules. Fresh resin (100%) was added and allowed to harden at 60 °C for 24 h. The resin blocks obtained were sectioned and mounted onto copper TEM grids and examined under a JEOL 1010 TEM at 80 kV.

2.2.13   *Colorimetric viability assays (MTT and MTS)*

The MTS assay is based on the reduction of the tetrazolium salt MTS (3-(4,5-dimethylthiazol-2-yl)-5-(3-carboxymethoxyphenyl)-2-(4-sulfophenyl)-2H-tetrazolium) and an electron coupling reagent PES (phenyl ethosulfate) into a soluble formazan product (purple colour). This reaction takes place solely in metabolically active cells by the mitochondrial dehydrogenase enzyme. The formazan product, which is measured by absorbance at 490 nm, is therefore directly proportional to the number of metabolically active cells.

hMSCs were seeded on a 96 well plate (5000 cells/well) and returned to culture overnight. Cell loading with IONPs was carried out at concentrations of Fe from 0 to 1 mg/ml, over a period of 24 h. Sterile-filtered MTS solution (20 µl) was then added to each well. After 4 h of incubation, the absorbance was read at 492 nm using BMG FluoStar Galaxy Optima Microplate Reader (BMG LabTech GmbH).

The MTT colorimetric assay reflects the ability of viable cells to convert the soluble MTT [3-(4,5-dimethylthiazol-2-yl)-2,5-diphenyltetrazolium salt (yellow colour) into an insoluble formazan precipitate (purple colour). These reactions are the result of the succinate dehydrogenase enzyme's activity, which is part of the mitochondrial electron transport system. The precipitate obtained is dissolved in organic solvents and its concentration can

be determined by absorbance at 570 nm. The amount of the formazan dye is therefore directly proportional to the number of metabolically active cells.

hMSCs were seeded on a 96 well plate (5000 cells/well) and returned to culture overnight. Cell loading with IONPs was carried out at concentrations of Fe from 0 to 1 mg/ml, over a period of 24 h. Cells were then rinsed 3 times with HBSS to remove any free IONPs. MTT was dissolved at a concentration of 5 mg/ml in HBSS and sterile-filtered. To each well 190 µl of HBSS and 10 µl of the MTT solution were added. After 4 h, the MTT solution was removed, and then 200 µl of DMSO or acidic isopropanol (0.04 - 0.1 N HCl in absolute isopropanol) was added to each well. After shaking for 10 min, the absorbance was read at 570 nm and the background was read at 620 nm using BMG FluoStar Galaxy Optima Microplate Reader (BMG LabTech GmbH).

2.2.14   *Apoptosis detection by flow cytometry using Annexin V*

Cell viability was initially assessed by flow cytometry (MACSQuant Analyzer, Miltenyi Biotech, Bergisch Gladbach, Germany) with FITC (fluorescein isothiocyanate) - Annexin V and 7-AAD (7-aminoactinomycin D) - Annexin V apoptosis detection kits.[189] Cells cultured and adherent to tissue culture flasks were trypsinised, counted by Trypan Blue staining, and resuspended in 1x binding buffer at 10^6 cells/ml. The 1x buffer is obtained from dilution in water of a 10x concentrate solution. The latter is composed of 0.2 µm sterile filtered 0.1 M HEPES (pH 7.4), 1.4 M NaCl, and 25 mM $CaCl_2$ solution. The cell solution (100 µl, 10^5 cells) is transferred into a flow cytometry tube and 5 µl of Annexin V-FITC and 5 µl of propidium iodide (PI) or 7-AAD are added. The tube is gently mixed and incubated for 15 min at RT in the dark. 1x binding buffer (400 µl) is added to each tube and the cells are maintained on ice and analysed by flow cytometry within 1 h.

Apoptosis is a physiological process, which occurs to maintain tissue homeostasis. One of the early stage signs of apoptosis is the translocation of a phospholipid , phosphatidylserine

(PS), from the inner to outer layer of the membrane, resulting in membrane asymmetry.[190] Annexin V is a protein, which will bind PS when it expressed on the outer cellular membrane. Annexin V is conjugated to fluorophores such as FITC, and thus allows us to determine by flow cytometry if cells are in the early stages of apoptosis. In addition, a viability dye such as PI or 7-AAD is used.[191, 192] These will bind to DNA and emit fluorescence only when the cellular membrane is no longer intact and the cells are therefore no longer considered viable.

2.2.15   *Apoptosis detection by flow cytometry using DRAQ7*

To overcome the large number of false positives obtained with Annexin V viability assay by flow cytometry, an additional method was investigated to determine the viability of cells after incubation with different concentrations of IONPs.

DRAQ7 is a far-red fluorescent dye, which binds to DNA and emits fluorescence only in dead cells when the cell membrane is no longer intact. In comparison to PI, the use of DRAQ7 is advantageous as it does not absorb in the UV range, and is non-toxic to cells so it may be used to study of viability of cells by live imaging or high content screening on a longer timescale. Indeed, UV excitation is not generally available on most common bench top flow cytometers. Furthermore, this avoids any double staining with Hoechst, a nuclear stain routinely used and which is excited in the 350 to 450 nm range.

Cells from a tissue culture flask were trypsinised, counted by Trypan blue staining and haemocytometer, and resuspended in HBSS at 10^6 cells/ml. An aliquot of the cell solution is transferred into a flow cytometry tube and DRAQ7 is added to a final concentration of 3 μM (1 μl per 100 μl media). The tube is gently mixed and incubated for 10 min at RT in the dark. The cells are maintained on ice and analysed by flow cytometry within 1 h.

2.2.16   *High content imaging analysis*

Cell viability, oxidative stress and mitochondrial health

hMSCs were seeded in 96 well plates (1000 cells/well) and were allowed to adhere in a humidified atmosphere. The media was then removed and the cells were incubated with increasing concentrations of IONPs (0, 5, 10, 50, 100, 150, 200 and 250 µg Fe per ml) for 24 h. After cell labelling, cells were washed three times with HBSS to remove any remaining free IONPs, after which the cells were incubated with 10 µM 5-(and-6)-chloromethyl-2',7'-dichlorodihydrofluorescein diacetate, acetyl ester (CM-H$_2$DCFDA) containing media for 30 min at 37 °C. The dye was then removed and cells were washed with HBSS after which they were exposed to 200 nM MitoTracker Red CMXRos cell containing media and incubated for 30 min at RT in the dark. Cells were then washed and incubated with cell media containing 3 µM DRAQ7 for 10 min at RT in the dark. The cells were then fixed with 4% PFA for 15 min. The fixative was washed away, after which the cells were rinsed once with HBSS. The nucleus was then stained with Hoechst 33342 for 10 min at RT in the dark. The cells were then rinsed with HBSS and the plates were analysed with the InCell analyser 2000, where bright field and fluorescence-based images for the following channels were acquired: DAPI/DAPI (Hoechst nuclear counterstain), FITC/FITC (DCFDA ROS probe), DsRed/DsRed (MitoTracker Red CMXRos) and Cy5/Cy5 (DRAQ7) for a minimum of 500 cells per condition. Data analysis was performed on the InCell Developer software (GE Healthcare Life Sciences, Belgium) using in-house developed protocols. Cell numbers were first determined by counting the number of nuclei. Cell nuclei were segmented based on the DAPI/DAPI channel (Hoechst stain). The level of oxidative stress was based on the FITC/FITC channel. Cell cytoplasm were segmented based on the FITC/FITC channel (autofluorescence), using the DAPI/DAPI channel as seed images. Then, the average intensity of the FITC/FITC channel was measured for every individual cell and normalised to the intensity level of untreated control cells (100%). Mitochondrial health was evaluated similarly using the DsRed/DsRed channel, where the intensity of the MitoTracker Red CMXRos probe depends on the mitochondrial

membrane potential and thus is lost in non-functional mitochondria. All red spots localised within a single cytoplasm (based on the FITC/FITC channel) were counted and the average intensity of all mitochondria per cell was then measured. This value was then normalised to the intensity level of untreated control cells (100%). Viability was based on the Cy5/Cy5 channel as DRAQ7 emits at wavelengths above 650 nm. Dead cells were defined as DRAQ7 signal that had an intensity of 3-fold higher than background levels and that co-localised with cell nuclei of the DAPI/DAPI channel. The relative number of dead cells was then determined based on the number of red-stained cell nuclei over the total number of nuclei and normalised to the number of dead cells found for untreated control cells (100%).

Cell morphology

After cell exposure to the IONPs, cells were washed three times with HBSS and fixed for 15 min at RT with 4% PFA. The fixative was removed, cells were washed with HBSS after which they were permeabilised with Triton X-100 (1%) for 10 min at RT. Cells were then blocked with 10% serum-containing HBSS for 30 min at RT followed by the addition of 200 µl (1/40 dilution) Acti-Stain 488. Cells were incubated for 30 min at RT in the dark. The dye was removed, cells were washed with HBSS and the nucleus was stained with Hoechst 33342 for 10 min at RT in the dark. The cells were then rinsed before 200 µl fresh HBSS was added to each well and plates were analysed on the InCell analyser 2000, where phase contrast and fluorescence-based images for the DAPI/DAPI and FITC/FITC channels were collected at minimum of 500 cells/condition. Data analysis was performed on the InCell Developer software (GE Healthcare Life Sciences, Belgium) using in-house developed protocols. First, cell nuclei were segmented based on the blue channel (Hoechst stain). Using the green channel, cells were then segmented, where any holes in the cells were filled up and included any cells on the border of the field of view were excluded from the analysis. The segmentation was based on the blue channel as seed channel for the nucleus. The total area of every individual cell was then determined. For determination of skewness (*i.e.* the shape of the cells, being the ratio of cell width over cell length), the same approach was used.

After segmentation, the "form factor" was calculated which provides the ratio of the cell width over cell length. This value will always be between 0 (straight line) and 1 (perfect circle).

2.3 IONP ANALYTICAL TECHNIQUES

2.3.1   *Magnetic measurements by SQUID-VSM magnetometry*

Different methods can be used to characterise the magnetic properties of a sample such as Mossbauer spectroscopy, Hall effect magnetometry and superconducting quantum interference device (SQUID) magnetometry for example. In order to determine the magnetic properties of IONPs, a Quantum Design Magnetic Property Measurement System (MPMS) SQUID Vibrating sample magnetometer (VSM) was used (LOT Quantum Design, Germany). This is a device which can measure the magnetisation of IONPs with high sensitivity ($\leq 10^{-8}$ emu). As represented in Figure 2-1, it is composed of two Josephson junctions in a loop. Each junction is made of 2 layers of semiconductors, which are separated by a thin insulator through which a tunnel current can flow. The current generated will depend on the magnetic field. The measurement consists in moving the vibrating sample (υ = 14 Hz) through superconducting detection coils at a given temperature
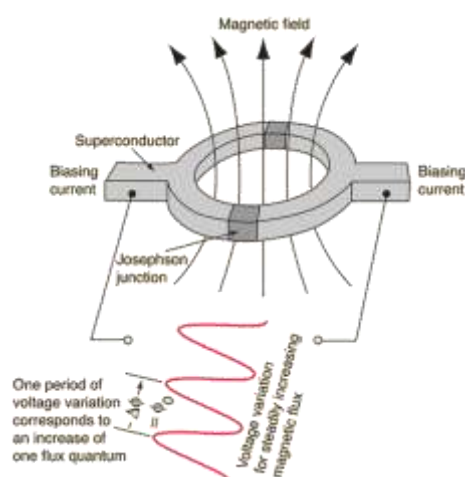
Figure 2-1 Scheme of principle of a SQUID magnetometer. Adapted from http://hyperphysics.phy-astr.gsu.edu/hbase/solids/squid.html

and in a homogenous magnetic field. A change in the magnetic flux will induce a change in the current.

The SQUID is the most sensitive apparatus available for the measurement of induced current due to the magnetic sample and is an extremely sensitive current-to-voltage convertor. The induced voltage measured is proportional to the magnetic moment of the sample.[193]

SQUID-VSM was routinely used to obtain hysteresis curves of the IONPs, by measuring the magnetisation against the applied magnetic field. These measurements are carried out at 300 K or 5 K, and magnetic fields applied between -7 and 7 T. Prior to each measurement, samples were demagnetised to ensure there was no magnetic memory effect and that electron spins were randomly oriented.

By varying the temperature, essential information was obtained such as the saturation magnetisation, coercivity, and remanence. These parameters will allow us to determine if the NPs are superparamagnetic behaviour (as described in section 1.1.2 of chapter 1). This is critical as MNPs with any remanent magnetisation cannot be considered for biological applications as this may lead to inter-particle magnetostatic interactions causing their agglomeration. As explained in section 1.2.3 of chapter 1, higher saturation magnetisation will be ideal for MRI as this will lead to higher relaxivity values.[194, 195]

SQUID samples were mounted using soft gelatin capsules and plastic straws according to the manufacturer's instructions. Approximately 5 mg of the IONP sample as powder was placed at the bottom of the capsule, so as to limit the height of the sample to 1 mm. Cotton wool was then added to the capsule in order to fill the remaining space and ensure the immobilisation of the sample in the capsule. The latter was then placed inside a plastic straw at 66 mm from the base of the sample rod, then immobilised by two additional straw supports on either side to prevent the capsule from moving during the measurement.

2.3.2   *Magnetic measurements by Mössbauer spectroscopy*

This technique is based upon the Mössbauer effect. Briefly, upon the emission or absorption of a gamma ray, nuclei in atoms will undergo energy level transitions. The local magnetic and electronic environment can modify or split these energy levels. During emission or absorption of a ɣ-ray in a free nucleus, the latter will recoil due to conservation of momentum. Rudolf Mössbauer made the discovery that within a solid or matrix, if the ɣ energy is small enough, the recoil of the nucleus is too small to be transmitted as a phonon as this is the case of a free nucleus. Instead the whole system recoils, which means that when the absorbing and emitting nuclei are in the same matrix, the energy of absorbed and emitted ɣ-rays are the same and resonance occurs. Resonance will only occur when the transition energy of the emitting and absorbing nucleus match. The number of recoil-free events is dependent upon the ɣ-ray energy and so the Mössbauer effect is only observed with isotopes with very low lying excited states. The most used isotope for this technique is ^{57}Fe as it has a very low energy ɣ-ray and long-lived excited state.

The Doppler Effect is used to detect the minute energy level changes due to the hyperfine interactions of the nucleus with its environment. The radioactive ɣ-ray source will oscillate with a velocity of a few mm/s and the recorded spectrum will be expressed as a function of the source velocity. When the modulated ɣ-ray energy matches the energy of a nuclear transition in the absorber the ɣ-rays are resonantly absorbed and a peak is observed. There are three hyperfine interactions originating from the nucleus' electron density: the isomer shift, quadrupole splitting and magnetic splitting. These will be explained briefly.

The isomer shift is due to the electron density of the nucleus by the presence of the s-electrons. A difference in the environment of the s-electrons will produce a shift in the resonance energy; as such the whole spectrum will be shifted positively or negatively relative to a known absorber, such as alpha-iron at RT. This shift provides information on valency or the bonding of ligands for example.

For nuclei with an angular momentum quantum number I> ½, as this is the case with the excited state of ^{57}Fe, the charge distribution is non-spherical. The asymmetric electronic charge distribution will define the quadrupole moment Q of the nucleus. The latter will be able to interact with any asymmetric electric field from surrounding electrons. As a consequence of the asymmetric field, the nuclear energy levels will split and this will lead to a doublet instead of a single line. The magnitude of splitting, delta, will be related to the nuclear quadrupole moment Q.

In the presence of a magnetic field, the nucleus spin moment will experience dipolar interaction with the latter; this is also known as Zeeman splitting. The ground state energy splits into 2 levels and the excited state splits up into 4 levels, leading to a sextet of lines. The line positions are related to the splitting of the energy levels, but the intensities are related to the angle between the ɣ-ray and the nuclear spin moment.

^{57}Fe Mössbauer spectra were collected from freeze-dried samples mixed with boron nitride and measured in transmission mode in a commercial spectrometer (SEE Co Inc, USA) working in constant acceleration mode, calibrated relative to metallic α-Fe at room temperature.

2.3.3   *Determination of core size by Transmission Electron Microscopy*

TEM is commonly used in the development of nanomaterials in order to observe their morphology (size and shape). Unlike optical microscopy, which relies on the use of photons, TEM will have a source which emits electrons, an electron gun, which may be a tungsten filament or a lanthanum hexaboride single crystal. The electrons will allow for an enhanced resolution in comparison to optical microscopy. The resolution in optical imaging is defined by the Rayleigh criterion R_c: two point sources are considered resolved when the principal diffraction maximum of one image coincides with the first minimum of the other. If the distance between the points is greater, they are well resolved and if it is smaller, they

are not resolved. When considering light passing through a circular aperture, R_c is defined by the following equation where λ is the wavelength of radiation, n is the refractive index of the imaging medium and sin θ is the sine of the aperture angle:

$$R_C = \frac{0.61\lambda}{n \sin \theta}$$
(Equation 2-1)

$$\lambda = \frac{h}{p}$$
(Equation 2-2)

On the other hand, when using electrons with a smaller wavelength, this resolution can be as low as 0.1 Å, which is ideal for nanomaterials with dimensions between 1 – 100 nm. The De Broglie equation (Equation 2-2) defines the wavelength of an electron as a wave-particle duality where λ is the wavelength, h is Planck's constant and p is the electron momentum.

High voltages used in TEM (up to 450 kV) accelerate electrons towards the speed of light. The electrons will be accelerated from an electron gun and focused using electromagnetic lenses; the image will then be formed upon a digital camera as shown in Figure 2-2. The electrons are accelerated at several hundred kV leading to much smaller wavelengths; however the resolution will be limited by aberrations in electromagnetic lenses (condenser and objective) to about 0.1 nm.

The most common mode of use for a TEM is the bright field imaging mode: only the direct beam contributes to image formation. Thicker regions of the sample or regions with a higher atomic number will appear dark, whilst regions with no sample in the beam path will appear bright, hence the term "bright field".
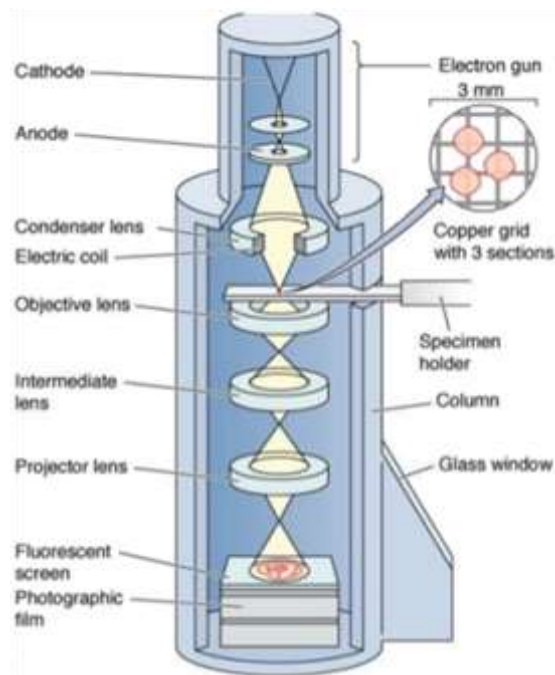
Figure 2-2 Schematic view of a transmission electron microscope (TEM) with its lenses and the pathway of the electrons. Reproduced from A. Mescher, Junqueira's Basic Histology: Text and Atlas, McGraw Hill Professional, 2009, 12th Edition.

Care must be taken when interpreting the images obtained by TEM, as sample preparation-induced artefacts may for example lead to aggregation of NPs on the grid. During sample preparation, attractive inter-particle forces will dominate and lead to aggregation which is enhanced by drying as the NP concentration increases during the drying of the grid. This is known as surface dewetting or the 'coffee-ring' effect.[196] Also, although some TEM staining techniques allow visualisation of the NP coating,[197] the drying process causes it to collapse and it will vary with environmental conditions such as the temperature or solvent, the shell thickness can therefore not be determined accurately by this method.

In our case, a JEOL 1200EX TEM was used at 120 kV for IONP dispersions. In the case of biological samples, a JEOL 1010 TEM was used at 80 kV. After their synthesis, 5 μl of the obtained IONP dispersion was diluted in approximately 1.5 ml of water, so that the diluted solution remained transparent. The TEM samples were prepared by dropping 5 μl of the diluted aqueous solution of the IONPs onto a carbon coated 200 mesh copper grid (EM

Resist Ltd, United Kingdom) which was then air dried overnight. The preparation of biological samples is explained in section 2.2.12.

2.3.4   *Determination of crystallite phase and size by X-ray diffraction (XRD)*

To determine the crystallographic arrangement of atoms present in NPs, X-ray diffraction (XRD) is used. This method can be used to determine the lattice parameter of the nanomaterial synthesised, as well as the crystallite size. As can be seen in Figure 2-3, X-rays are produced in an X-ray tube consisting of 2 metal electrodes in a vacuum chamber. Electrons are produced from a tungsten filament cathode and are accelerated towards the anode, from which the loss of energy of the electrons after impact is emitted as X-rays.[198]

XRD relies on the physical phenomena of X-ray diffraction, which occurs when the X-rays interact with crystallographic lattice planes. Upon diffraction, constructive interference can occur with specific wavelengths and incident angles, which must be met by Bragg's law:

$$n\lambda = 2d_{hkl}\sin\theta$$
(Equation 2-2)

Where n is an integer, λ is the wavelength of the incident X-ray, d is the spacing between the atomic planes and Ɵ is the incident X-ray angle.
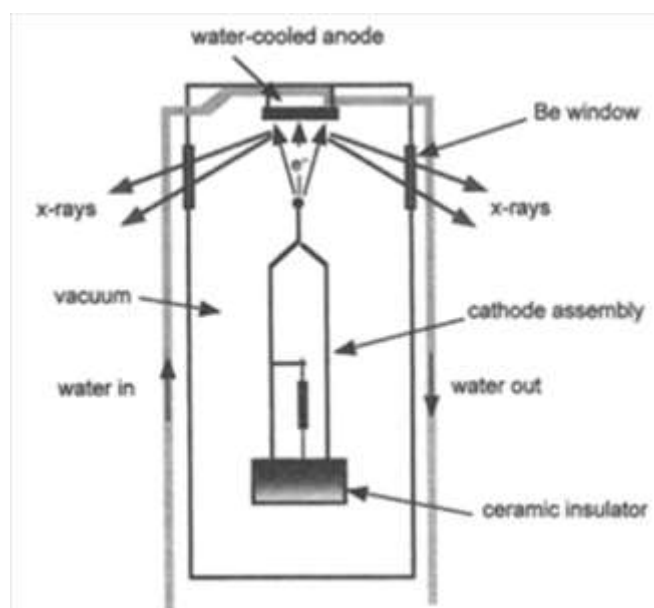
Figure 2-3 Scheme showing the components of a modern X-ray tube. Beryllium is used for the window because it is highly transparent to x-rays. Reproduced from Suryanarayana et al., X-ray diffraction: a practical approach, 2013, Springer Science & Business Media.

Once the diffraction pattern is obtained, the position, width, intensity and shape of the peaks obtained can be compared to reference patterns in known databases. These peak parameters are characteristic of a material in a specific crystallographic arrangement and therefore help identify the crystalline structure of the NPs as well as the crystallite size. The Scherrer equation may be used to determine the approximate size of the crystallites by relating it to the broadening of a peak in a diffraction pattern:

$$\tau = \frac{K\lambda}{\beta \cos \theta}$$
(Equation 2-3)

Where τ is the mean crystallite size, K is a dimensionless shape factor, λ is the wavelength of the incident X-ray, β is the line broadening at half the maximum intensity (FWHM) after subtraction of the background, and θ is the incident angle of the X-ray.

This should not be confused with the NP size, as the crystallite size is defined as the area or volume of the material where x-ray diffraction is coherent. This analysis was carried out with the PANalytical X'Pert Highscore Plus software. It is worth mentioning that only a few peaks distinguish Fe_3O_4 and γ-Fe_2O_3 and their low intensity is blurred by background noise or crystallite size effect (broadening due to instrumental effects and crystal strains).

XRD patterns were obtained with a PanAlytical X-ray diffractometer, using CoKα radiation (λ = 1.789010 Å). The patterns were collected from 2θ degrees = 20° to 100°. Samples were prepared by pressing dried powders on a zero background silicon wafer.

2.3.5 *Determination of surface functionalisation by Attenuated total reflectance – Fourier transform infrared spectroscopy (ATR-FTIR)*

ATR-FTIR is a variant of FTIR spectroscopy, which allows identification of different surface functional groups of NPs. It relies on the absorption of infrared electromagnetic radiation (4000 – 400 cm^{-1}) by different chemical bonds in various functional groups. This occurs when the radiation is at the resonance frequency of these chemical bonds; this corresponds to their transition energy. ATR-FTIR therefore allows us to obtain information on the nature of the chemical groups and the bonds by which they are linked.[199] ATR-FTIR was used in chapter 4 to obtain information regarding changes in the functional groups before and after the ligand exchange reaction of IONPs. FTIR is routinely used in the mid-infrared region (400 to 4000 cm^{-1}) as this provides information on the rotational-vibrational structure of the surface of MNPs. For example, by determining the wavenumber difference between the asymmetric and symmetric stretching modes of the coordinated carboxylate group, information can be obtained as to whether or not the COOH group is linked by chemisorption to the NP.[200, 201] The vibration for the asymmetric stretching of the COOH groups of citric acid will shift when binding to the surface of the NP occurs.[202] Also, depending on whether ligands bind to the surface *via* a mono-dentate or bi-dentate form, a change in the spectrum may be noticeable.[203, 204]
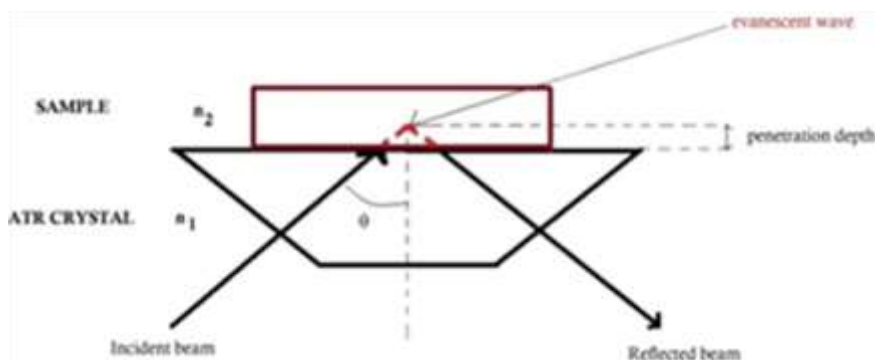
Figure 2-4 Schematic diagram of a horizontal ATR sampling accessory illustrating the important parameters. Reproduced from Atitar et al., The Relevance of ATR-FTIR Spectroscopy in Semiconductor Photocatalysis, Emerging Pollutants in the Environment - Current and Further Implications, 2015, InTech.

The Fe-O band is also useful to evaluate the influence of the surface functionalisation reaction on the oxidation of IONPs. Indeed, the core of magnetite will be surrounded by an oxidized layer due to the fact that surface Fe^{2+} is very sensitive to oxidation.[205] Also, when studying IONPs, the Fe-O peak of magnetite is found around 570 cm^{-1}, while maghemite will have several peaks between 400 to 800 cm^{-1}, the number peaks increasing with the structural ordering of its vacancies.[49, 206]

In ATR-FTIR, the infrared (IR) radiation passes through a crystal on top of which the sample is placed (Figure 2-4).[207] The crystal must be made of an IR transparent material with high refractive index. The IR beam will enter the crystal and be reflected at the crystal-sample interface. Due to its wave properties, the IR will emit an evanescent wave that will interact with the sample and be attenuated in the regions where the sample absorbs the energy. Then IR radiation then exits the crystal and interacts with a detector. A spectrum will be obtained by measuring the interaction of the evanescent wave with the sample. If an absorbing material is placed in contact with crystal, the wave will be absorbed by the sample and its intensity is reduced in regions of the IR spectrum where the sample absorbs, thus, less intensity can be reflected (attenuated total reflection).[208]

In the analysis of NPs, one characteristic phenomenon is the breaking of a large number of bonds of surface atoms, leading to electrons being rearranged on the surface.[209] As a result, the surface bond force constant increases as Fe_3O_4 is reduced to the nanoscale dimension, so the absorption bands of IR spectra shift to higher wavenumbers.

ATR-FTIR analysis was carried out using a Spectrum 100 spectrophotometer from Perkin Elmer. Spectra were acquired from 4000 to 650 cm^{-1} with a resolution of 2 cm^{-1} and averaging over 16 scans. The samples were used in powder form after freeze drying for 48 h minimum and did not need to undergo any further preparation. The powder was ground and placed on the crystal and a screw press was used to compress the sample. Data acquisition was monitored in real time to ensure sufficient signal to noise ratio by adjusting the pressure exerted on the sample.

2.3.6   *Hydrodynamic diameter measurements by Dynamic Light Scattering (DLS)*

DLS allows us to determine the hydrodynamic diameter of the IONPs in solution. The hydrodynamic diameter is defined as the diameter of a hard sphere that diffuses at the same speed as the NP being measured. This parameter will depend on the size, shape and speed of the NP in solution as well as the environment it is in such as the ionic strength of the solution. This measurement allows us to estimate the NP's behaviour in solution and whether or not any aggregation can be expected in different conditions such as varying salt concentration of pH for example. Dynamic Light Scattering (DLS), also known as Photon Correlation Spectroscopy (PCS), is a non-destructive method, which determines the size of particles or molecules.

In a solution, if the particles are small enough (Ø ≤ 250 nm) they undergo a random Brownian motion due to thermal energy. When a monochromatic He-Ne laser beam (λ = 633 nm) interacts with particles in solution, the latter scatter the light in all directions in a uniform manner, this is known as Rayleigh scattering. This will depend on the particle's size,

shape and the interactions with the surrounding solvent molecules in solution. A photomultiplier detector allows one to observe time-dependent fluctuations in the scattered intensity because of the Brownian movement. The intensity of the scattered light fluctuates at a rate that depends on the size of the particles, and is correlated to the diffusion coefficient. Using the following Stokes-Einstein formula, the latter leads us to the radius, hence the size of the NPs:

$$D = \frac{k_B T}{6\pi a \eta}$$
(Equation 2-4)

Where D is the diffusion coefficient, k is the Boltzmann constant, T is the temperature, η is the viscosity of the solvent and *a* is the radius of the particle. The measurement will depend on the particles shape or the temperature. DLS allows us to obtain an average diameter of NPs dispersed in a solvent, but is unable to distinguish NPs with slight variance in their diameter or to resolve polydisperse samples. This is because it measures the intensity of the scattered light which is proportional to the sixth power of the particle diameter in the Rayleigh equation. Therefore, in the case of a polydisperse sample, the scattered light of larger particles will strongly overlay that of smaller particles.

This measurement is carried out with the Zetasizer Nano S instrument distributed by Malvern Instruments Ltd, UK. For hydrodynamic diameter measurements, 20 μl of an aqueous solution of IONPs was pipetted into a disposable polystyrene cuvette. These cuvettes were purchased from Malvern Instrument Ltd, UK. The average diameter and polydispersity index were measured and presented as the average value of three measurements. The mean and standard deviation of size were calculated for each sample.

2.3.7 *Determination of surface charge by zeta potential measurements*

The apparatus used to determine the zeta potential (also ζ-potential or electrokinetic potential) is the same as previously described in section 2.3.6. For ζ-potential measurements, the NPs were diluted and adjusted to the desired pH (from 3 to 10).

Measurements were recorded at 25 °C within a disposable capillary cell (DTS1070) purchased from Malvern Instrument Ltd, UK. The ζ-potential was determined in the solvent of choice and presented as the average value of three measurements. The mean and standard deviation were calculated for each sample.

The ζ-potential is correlated to the surface charge and provides an estimation of the charge interactions that the NP will have with its environment. It can also give qualitative information about surface functional groups. Indeed, the NPs in solution will acquire a surface charge by adsorption of solvent molecules or by ionisation of chemical groups on their surface. Consequently, counter ions gather around the surface of the NP and assemble into a double layer: an inner concentrated layer (or stern layer) and an external more diffuse layer.[210] Within the diffuse layer there is a boundary at which the ions and NPs form a stable entity. The potential at this boundary is the ζ-potential.[211]

It is determined by applying an electric field upon which the NPs will move towards the oppositely charged electrode. Viscous forces will oppose this movement until equilibrium is reached and the NPs reach a final equilibrium velocity. This velocity can then be correlated to the ζ-potential by the Smoluchowski approximation of the Henry equation in aqueous solutions:

$$U_E = \frac{\zeta 2\varepsilon \int(Ka)}{3\eta}$$
(Equation 2-5)

Where U_E is the electrophoretic mobility, ε the dielectric constant, $\boldsymbol{\zeta}$ is the zeta potential, $\int(Ka)$ is Henry's function and η is the viscosity.[212] The Smoluchowski approximation is used when measuring the ζ-potential in aqueous solutions of moderate electrolyte concentration and gives the value of 1.5 to Henry's function. This is applied for systems fitting the Smoluchowski model, and is used for folded capillary cells with aqueous samples as this is the case in our project. Arbitrarily, a ζ-potential value of ± 30 mV indicates a stable

suspension of NPs by charge repulsion. Values smaller than this (-30 mV < ζ < 30 mV) indicate unstable NPs in solution.
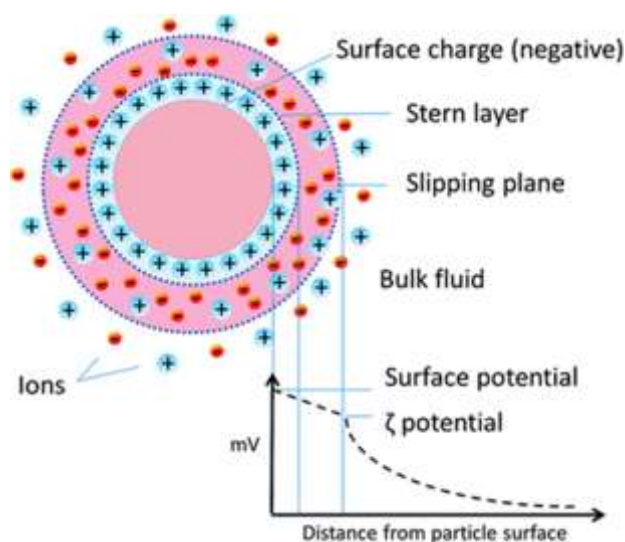
Figure 2-5 Schematic representation of zeta potential: ionic concentration and potential differences as a function of distance from the charged surface of a particle suspended in a medium. Reproduced from A. Liese et al., Chem. Soc. Rev., 2013 with permission from The Royal Society of Chemistry.

2.3.8 *Determination of the iron content of IONPs*

2.3.8.1 Inductively coupled plasma – Atomic Emission spectroscopy

This method (ICP-AES) was used to determine the total iron content of IONPs in solution. This was provided as a service by the National History Museum in London, and by PhD student Sarah Belderbos from the MoSAIC laboratory in KU Leuven, Belgium.

In ICP-AES, the sample is introduced in the spectrophotometer and is atomised before being carried into a plasma with a stream of argon gas. The plasma is used to dissociate the sample whereby the atoms in the sample are excited to a higher energy state. When returning to their ground state, the energy is emitted from the atoms at characteristic

wavelengths that provide qualitative multi-elemental analysis of the sample. It is also possible to determine the concentrations of the elements present by measuring the intensity of the emitted radiation. Strong acids must be used to ensure the entire dissolution of the sample and avoid clogging the nebuliser which is responsible for the initial atomisation of the sample into a mist.

The sample preparation consisted in the aqueous solution of IONPs being mixed with aqua regia (very strong acid obtained from a mixture 1:3 of nitric acid and hydrochloric acid) to ensure their entire dissolution. The solution was then diluted with deionised water until reaching a final acid concentration of 5% and an estimated iron concentration of 2 mg/l. A colorimetric assay (2.3.8.2) was used to estimate the iron concentration in the samples.

2.3.8.2   Colorimetric method

A colorimetric method used to determine the iron content of our samples was based on the intrinsic enzyme mimetic activity of IONPs similar to that found in natural peroxidases which oxidise organic substrates and lead to the formation of a coloured product measured by absorbance at 510 nm.[187, 188]

A calibration curve was initially plotted using serial dilutions of known concentrations of iron. Each dilution (1 ml) was mixed with 1 ml of 4 M HCl and heated to 90 °C for 30 min. Each aliquot (400 µl) was mixed with 900 µl of sodium acetate, 100 µl of hydroxylamine hydrochloride and 600 µl of 1,10-phenanthroline. A red colour developed and the absorbance of the solution was measured at 510 nm and plotted as concentration of iron *vs* absorbance. The determination of the iron content in IONP solutions was conducted using the same protocol, but using 1 ml of dilute IONP solution at the first step, instead of the 1 ml of iron standard dilution.

2.3.9 *Quantification of organic content by Thermogravimetric Analysis (TGA)*

Some experiments were carried out by fellow PhD student Aziliz Hervault at the Japan Advanced Institute of Science and Technology (JAIST), Ishikawa, Japan and Georgios Kasparis at University College London (UCL), London, UK.

In JAIST, thermogravimetric analysis (TGA) was performed using freeze-dried IONP powder samples with a TGA Seiko Exstar6000 TG/DTA6200 instrument. At UCL, a TA Instruments Discovery TGA was used to analyse powders. A nitrogen flow rate of 25 ml/min and a temperature ramp of 10 °C/min from 25 to 600 °C were used in both cases. As the sample is heated, the changes in mass of the sample are monitored. This method allows us to determine the quantity of organic coating or any impurities present on the IONPs. More precisely, TGA allows us to obtain the residual weight accounting for the mass of IONPs. This allows us to correct the magnetisation by taking into account the percentage of organic coating which does not contribute to the magnetic material weight used for the SQUID-VSM measurements for example. Also, the temperature at which organic ligands are burnt off, can give an indication as to whether they are bound to the IONPs or not.

2.4 CHARACTERISATION OF IONPs AS POTENTIAL MRI CONTRAST AGENTS

2.4.1 *MR relaxivity measurements of nanoparticles in solution*

Relaxivity measurements at 1.47 T were performed in collaboration with Professor Sylvie-Begin Colin and Dr Damien Mertz from the Department of Chemistry and Inorganic Materials in the University of Strasburg, France.

All experiments were performed on a Bruker MQ60 NMR Analyzer, BrukerCanada, Milton, Ont. Canada, working at a Larmor frequency of 60 MHz (1.41 T) and at 37 °C. The T_1 and T_2 measurements were performed according to the procedure described in the literature.[213] Briefly, a series of IONP aqueous dispersions with different Fe concentrations (0.25, 0.5,

0.75 and 1 mM) determined by ICP-AES were prepared. A limited volume (300 μl) of each sample was transferred into a glass 5 mm nuclear magnetic resonance (NMR) spectroscopy tube with a level sufficient to fit the size of the coil. Using a temperature-controlled probe cavity with an external water bath, each sample was preheated to 37 °C as the relaxation rates are temperature dependent. Each measurement was repeated three times to measure variations within the readings. T_1 values were obtained using the instrument's inversion-recovery pulse sequence with a recycle delay (repetition time) 2 sec, a delay sampling window 0.05 msec, and a sampling window 0.02 msec. A total of 15 data points were collected for fitting, starting at 10 msec and ending at one sec. T_2 curves were obtained using the instrument's Carr-Purcell-Meiboom-Gill (CPMG) pulse sequence with a recycle delay of one sec and a of 0.5 msec. The first echo was not included for fitting and 250 data points were collected. T_2 curves were fit to a monoexponential decay equation using CFTOOL in Matlab® 7.0. Relaxivities ($mM^{-1}\ s^{-1}$) were calculated by taking the inverse of T_1 and T_2 times (sec) and dividing these values by the iron concentration (mM) of each sample. Measurements were plotted as r_1 and r_2 values according to the linear relationship of longitudinal and transverse relaxation rates versus the magnetic metal concentrations of Fe.

Relaxivity measurements at 7 T were performed by Cody Amir Gharagouzloo, a PhD student under the supervision of Professor Srinivas Sridhar from Northeastern University (Boston, MA, USA). The protocol used was the following:

Six 2-ml vials containing the diluted solutions were arranged in a circular pattern around a blank vial of distilled water for the IONP formulation. Relaxivity r_1 was measured with a variable TR spin-echo sequence and r_2 was measured with a multi-echo spin-echo sequence with TR fixed. ParaVison 5.1 software was used to draw regions of interest (ROIs) and calculate relaxation rate values. Decay curves were fit with a mono-exponential decay equation to calculate T_2, $y = A + Ce^{-TE/T_2}$ and a mono-exponential growth saturation recovery equation to calculate T_1, $y = A + C\left(1 - e^{-TR/T_1}\right)$, where A is the absolute bias

and C is the signal intensity. T_2 of the samples was measured using the Bruker Multi-Slice Multi-Echo (MSME) pulse sequence with the following parameters: Effective TE: 4.25 ms, with 30 echoes ranging 4.25 - 127.5 ms, TR = 2500 ms, 40 x 40 mm^2 x-y field of view (FOV), 30 mm slice thickness, 200 × 200 matrix size providing 200 μm^2 x-y resolution, number of averages = 2, total acquisition time = 11 m 55 s.

T_1 of the samples was measured using a Rapid Acquisition with Refocused Echoes variable TR (RARE VTR) pulse sequence with the following parameters: TE = 4.25 ms, Rare Factor: 1, 8 TRs ranging from 100 – 2500 ms, 40 x 40 mm^2 x-y FOV, 30 mm slice thickness, 200 × 200 matrix size providing 200 μm^2 x-y resolution, number of averages = 1, total acquisition time = 27 m 15 s. For DI-H_2O T_1 & T_2, two separate scans were run with effective TE = 40 ms for T_2 and TRs ranging from 100 - 3500 for T_1.

2.4.2 *In vitro MR image acquisition of hMSCs labelled with IONPs*

These experiments were performed by Willy Gsell, Dr Bella B. Manshian, Dr Stefaan J. Soenen and Professor Uwe Himmelreich from the MoSAIC laboratory in KU Leuven (Leuven, Belgium).

hMSCs were seeded on a 24-well plate (10 000 cells/ well) and returned to culture overnight. Cell loading with IONPs was carried out at a range of concentrations from 0, 1, 2, 5 and 100 μg Fe per ml of cMEM on cells, over a period of 24 h. Cells were then rinsed 3 times with HBSS to remove any free IONPs, before fixing with 4% PFA for 15 min at RT. The fixative was removed, and then the hMSCs were stored at 4 °C until use.

Cells were detached from the multiwall plate using cell scrapers and counted on a haemocytometer. 10 000 cells were retained for each sample, which were aliquoted into a 0.25 ml Eppendorf microfuge tube containing 1.5% agar in PBS. Samples were mounted onto a phantom holder and stored at 4 ^{o}C until ready for MRI scanning. All images were

acquired with a 9.4 T Biospec small animal MR scanner (Bruker Biospin, Ettlingen, Germany, horizontal magnet) equipped with actively shielded gradients of 440 mT m^{-1} and using a transmit/receive 72 mm quadrature resonator (Rapid Biomedical, Rimpar, Germany).

Phantom homogeneity and positioning was assessed using FLASH 3D sequence (TE/TR: 15/200 ms, matrix: 512x512x128, FOV: 60x60x30 mm, resolution: 0,117x0,117x0,234 mm).

For T_1 measurements, data were extracted using a spin echo sequence with inversion preparation (TR: 10 000 ms, TE: 5,67 ms, TI: array of 12 Tis starting from 50 ms with regular increment of 500 ms, FOV: 60 x 60 mm, matrix: 256 x 256, 5 slices of 1 mm thickness and 1 mm gap). Data were fitted to a mono-exponential recovery function and T_1 extracted (processing performed in PV5,1 using image sequence analysis tool).

For T_2 measurements, data were using a multi Spin Echo sequence (TR: 5000 ms, TE: 20 TEs equally spaced by 11,35 ms, FOV: 60 x 60 mm, matrix: 512 x 512, 5 slices of 1 mm thickness and 1 mm gap). Data were fitted to a mono-exponential and T_2 extracted (processing performed in ImageJ using the MRI processor plugin. T_2 maps were generated for pixels for which the R^2 of the fit was higher than 0,9 and capped at 1000 ms)

2.4.3 *In vivo magnetic resonance imaging of IONPs*

These experiments were performed in collaboration with Dr Willy Gsell, Dr Bella B. Manshian, Dr Stefaan J. Soenen and Professor Uwe Himmelreich from the MoSAIC laboratory in KU Leuven, Belgium.

All MR images were acquired with the 9.4 T Biospec small animal MR scanner (Bruker Biospin, Ettlingen, Germany, horizontal magnet) described in section 2.4.2. Prior to scanning, mice were anaesthetised with 2% isoflurane for induction and 1.5% isoflurane for maintenance (carrier gas O_2). Three female Swiss mice received PBS only (control), while 3 others received IONPs through intravenous injection of 200 µl of 300 µg Fe/ml diluted in

PBS. Animals were scanned on the day of the injection, then once a week for the next 2 weeks. The *in vivo* MR imaging protocol used for liver imaging consisted of 2DT_2*-weighted fast low angle shot (FLASH) and a multi-slice-multi-echo (MSME) sequence. The FLASH sequence (TE = 2.3 ms, TR= 203 ms, flip angle = 30 degrees, FOV = 30 x 30 mm, matrix = 256 x 256, 9 contiguous axial slices of 1 mm thickness acquired in an interleaved scheme, averages = 10) was used to determine the decrease in the signal intensity (SI) post injection. T_2 values (maps) were determined from the MSME experiments and were used for a semi-quantitative analysis. Parameters for the MSME sequences were TR of at least 3000 ms, echo spacing of 7 ms, with 234 mm² in plane resolution with six slices of thickness 1 mm each. In order to evaluate particle distribution post intravenous administration in other organs, mice were subjected to whole body scan with a Rapid Acquisition with Relaxation Enhancement (RARE) sequence (TE = 15.88 ms, TR = 6000 ms, spatial resolution of 200 mm², slice thickness = 0.5 mm with 50 slices) was performed. Mice were monitored using a monitoring and gating model (type 1030) from Small Animal Instruments Inc. (SAII, Stony Brook, NY, USA) for controlling physiological parameters. Temperature and respiration were monitored throughout the experiment and maintained at 37 °C and 40 to 100 breaths min^{-1}.

Chapter 3   POLYOL SYNTHESIS OF IRON OXIDE NANOPARTICLES

3.1   AIMS AND OBJECTIVES

A background on the use of IONPs in biomedical applications has been provided, in particular their use as contrast agents in MRI. The chemical and physical properties of these IONPs will depend on the synthesis method chosen. In order to obtain biocompatible NPs, the main objective is to produce monodisperse water dispersible NPs and the polyol synthesis has been chosen to achieve this. This is a simple and effective method to produce IONPs and will not require a post synthesis step of phase transfer from an organic solvent to water, unlike more conventional methods as described in chapter 2. The polyol acts as the solvent, a surfactant, as well as the reducing agent. The polyols are known to reduce the metal salts to metal nuclei which then nucleate to form metal particles.[214]

This chapter will focus on the polyol synthesis of IONPs by different experimental set-ups: under inert atmosphere (N_2) using a Schlenk line, using a microwave reactor, and in high pressure high temperature conditions. The influence of the latter on the NPs obtained will be studied, as well as the impact of the different reaction parameters such as the amount of iron precursor, temperature and reaction time on the formation of the IONPs. The objectives of the research described in this chapter were to optimise the synthesis method so as to obtain IONPs in the range of 5 – 10 nm suitable for biological applications, stable in aqueous solution, as monodisperse as possible, with relevant magnetic properties for potential MRI applications and in a reproducible manner.

3.2 RESULTS AND DISCUSSION

3.2.1 *Conventional polyol synthesis of IONPs using a Schlenk line*

3.2.1.1 Preliminary experiments

These initial experiments were carried out to determine whether or not a reproducible method using the polyol synthesis could be found in current literature. IONPs were initially synthesised using a modified polyol synthesis described by F. Hu *et. al* and by both Cai and Wan.[65, 66, 75, 215] This reaction was carried out with different conditions as reported in literature, listed in Table 3-1, to study the effect of the temperature, reaction steps and times on the IONPs obtained. Degassed diethylene glycol (DEG) (20 ml) was mixed with 2.4 mmol Fe(acac)$_3$ (0.85 g) and stirred for 45 min at 100 °C to ensure the complete dissolution of the iron precursor. The reaction mixture was heated up to 200 °C for 7 h, the colour of the solution changing from dark purple to black, before cooling down back to room temperature (RT). Samples were washed by centrifugation with 100 ml of ethanol/ether (v/v = 1:8) (8500 rpm, 10 min, 3 times) and redispersed in dH$_2$O for further characterisation. An aliquot (approximately 2 ml) was freeze-dried for 48 h (Lyolab 3000, Thermo Scientific Heto) for XRD and SQUID-VSM characterisation.

The reaction was initially carried out in a 2 step process according to the protocol described in literature (samples IONP-A and IONP-B). The purpose of the first step is the dissolution of the iron precursor in solution while the second step is to ensure the nucleation and growth of the particles. This step was carried out initially at 230 °C for 7 h as per reference 53, however the IONPs obtained had a broad size distribution as determined by TEM: d_{TEM} = 11.6 nm ± 2.1 nm (δ = 18%, n = 207) where δ is the dispersity of the mean diameter and n the number of particles counted. The TEM images of the IONPs obtained are shown in Figure 3-1.

Table 3-1 Synthesis of IONPs using a Schlenk line as reported in the literature along with their reaction conditions.

Sample	DEG (ml)	Quantity of Iron precursor Fe(acac)$_3$ (mmol)	Reaction step 1	Reaction step 2	Reference
IONP-A	20	2	1 h at 140 °C	7 h at 230 °C	54
IONP-B	20	2	1 h at 140 °C	4 h at 230 °C	54
IONP-C	20	1	30 min at 240 °C	N/A	53
IONP-D	30	1	30 min 180 °C	2 h 250 °C	53,54
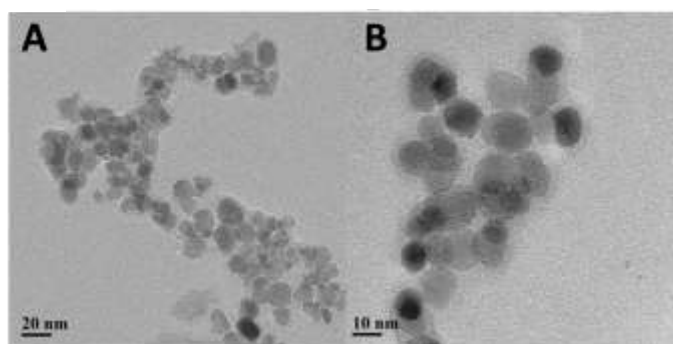
Figure 3-1 TEM images of samples obtained at 230 °C for 7 h. (A) magnification 50 k scale bar 20 nm, (B) magnification 100 k scale bar 10 nm.

In comparison to Hu *et. al* who obtained nanoparticles of 6 nm ± 0.6 nm, IONPs with a larger mean size distribution and which were not monodisperse were obtained. In literature, monodisperse IONPs have been defined as a population of particles with a dispersity of the mean diameter being less than 10%.[66, 216] Throughout our project, this definition was used to characterise the size distribution and dispersity of the IONPs. This parameter is critical as the magnetic properties (in particular their saturation magnetisation) strongly depend on the size distribution of the IONPs, and this in turn will determine their relaxivity values and their potential as MRI contrast agents. As per suggested in the literature, in order to decrease the size distribution of the IONPs, the next strategy investigated was to shorten the second reaction time. For example, Hu *et. al* were able to decrease the size of the IONPs obtained from 6 nm to 3 nm by decreasing the reaction time from 8 h to 2 h.

3.2.1.2   Influence of the reaction time on IONP formation

In an effort to reduce the mean size and size distribution of the IONPs, the duration of the second reaction was decreased to 4 h (IONP-B). The IONPs obtained had a larger mean size distribution as well as an increased standard deviation as determined by TEM in Figure 3-2: d_{TEM} = 13.5 ± 2.7 nm (δ = 19.8%, n = 332). In order to determine if the reaction time, and hence the size distribution and dispersity of the IONPs obtained, had an influence on their magnetic properties, a magnetisation curve was obtained at 300 K for both samples (IONP-A and IONP-B). As is shown in Figure 3-3 below, the SQUID-VSM measurements demonstrated that both samples had similar magnetic properties with saturation magnetisation values of M_s = 63.5 emu/g and M_s = 58.9 emu/g for samples IONP-A and IONP-B respectively. The XRD diffraction patterns for both samples can be found in Figure 3-7. Using the Scherer equation approximation (described in chapter 2), the crystallite size for each sample was respectively determined to be d_{XRD} = 10 nm and d_{XRD} = 11 nm. Both samples had an inverse spinel structure although, as explained in section 2.3.4, distinguishing maghemite and magnetite by XRD is not a trivial issue.
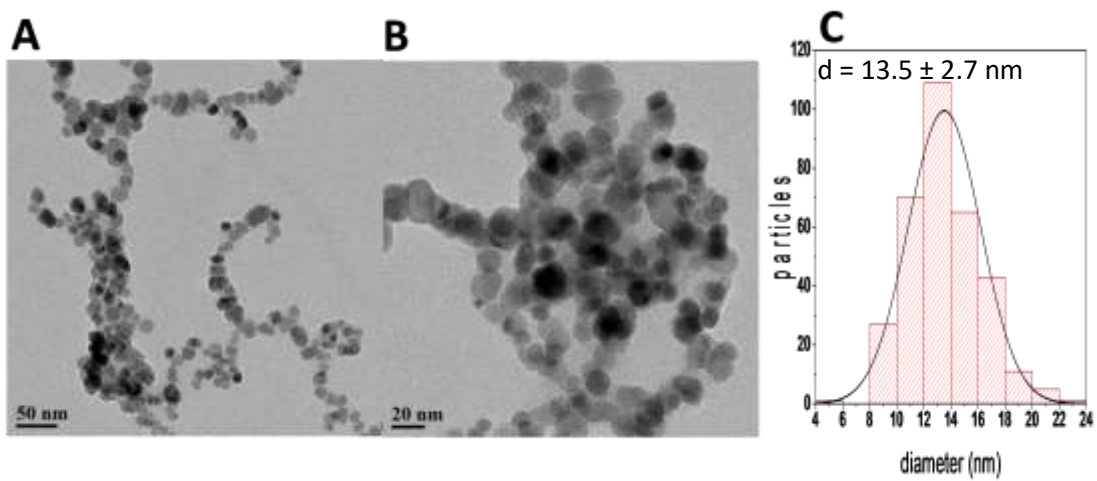
Figure 3-2 TEM images of samples obtained at 230 °C for 4 h. (A) magnification 25 k scale bar 50 nm, (B) magnification 50 k scale bar 20 nm. (C) TEM size distribution was fitted with a log normal function.
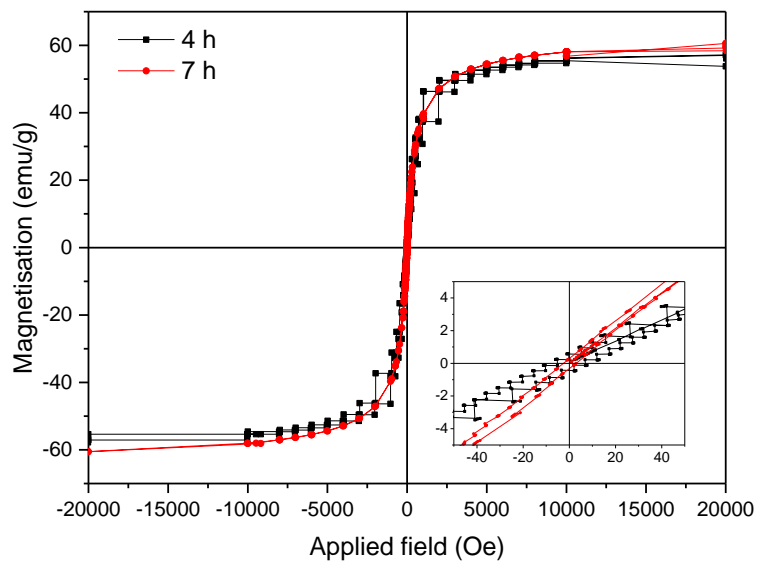
Figure 3-3 Magnetisation curves of IONPs synthesised for 4h (■) or 7 h (●) at 230 °C during the second reaction step.
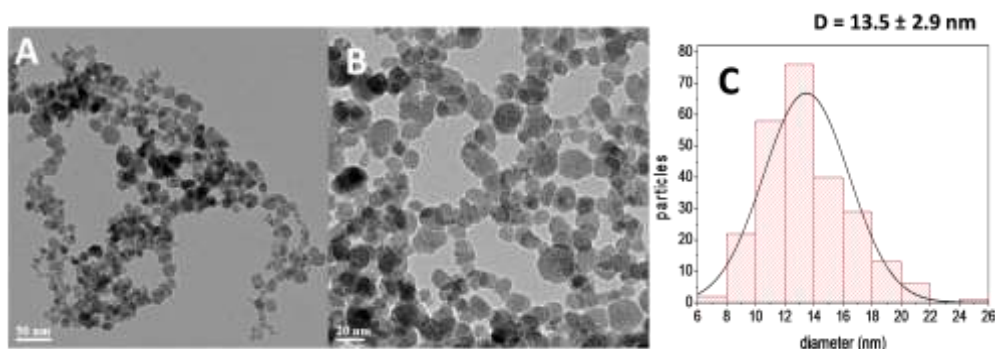
Figure 3-4 TEM images of IONPs obtained with 1 mmol of Fe(acac)₃ heated at 250 °C for 2 h. (A) magnification 25 k scale bar 50 nm, (B) magnification 50 k scale bar 20 nm. TEM size distribution (C) was fitted with a log normal function

3.2.1.3   Influence of the reaction temperature on IONP formation

Another strategy to reduce the size of the IONPs and obtain a better size distribution was explored. It consisted in an increase of both reaction temperatures. The first reaction is carried out at 180 °C in order to ensure the entire dissolution of Fe(acac)$_3$, the latter has been reported to take place at approximately 180 – 190 °C.[77] The second reaction is further reduced to 2 h but the temperature is increased to 250 °C. Indeed, this was chosen to test the formulated hypothesis that the nucleation of the IONPs occurs at high temperatures, close to the boiling point of the solvent (t = 245 °C for DEG). Increasing the temperature aims to increase the generation of new iron species through decomposition of the intermediate complexes formed and the remaining Fe(acac)$_3$ in solution.

However, as can be seen in Figure 3-4, the IONPs obtained were polydisperse with a size distribution measured from TEM as: d_{TEM} = 13. 5 ± 2.9 nm (δ = 21.9%, n = 248). The results obtained were compared with those of several publications reporting the use of the polyol method and these suggested that a one-step reaction at the boiling point of the solvent could improve the size distribution of IONPs. From the initial experiments, it is plausible that the two-step reaction led to the nucleation of NPs at two different temperatures, hence leading to a polydisperse sample.
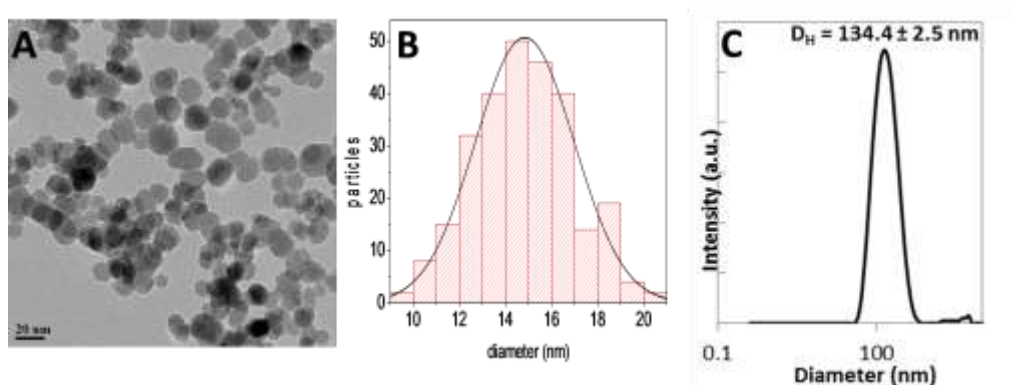
Figure 3-5 (A) TEM image of IONPs synthesised at 240 °C for 30 min, magnification 50 K, scale bar 20 nm (B) TEM size distribution fitted with a log normal function and (C) hydrodynamic diameter in water measured by DLS.

In comparison to the previous samples, these new reaction conditions affected the magnetic properties of the IONPs as can be seen in Figure 3-6. The sample was characterised by an increased saturation magnetisation of M_s = 83.4 emu/g, coercivity H_c ± 30 Oe and remanent magnetisation H_r ± 4 emu/g. The M_s > 78 emu/g indicates the presence of non-oxidised magnetite within the core of the IONPs obtained. However, the sample's dispersity is still above the threshold for monodispersity of 10% defined earlier. Some IONPs being larger than the superparamagnetic critical size, the hysteresis curve is not that of superparamagnetic NPs as it shows coercivity of about 40 emu/g and slight remanence. The magnetic properties of the obtained NPs are crucial for their potential biomedical applications and these will later be assessed as a function of the shape and morphology of the IONPs.
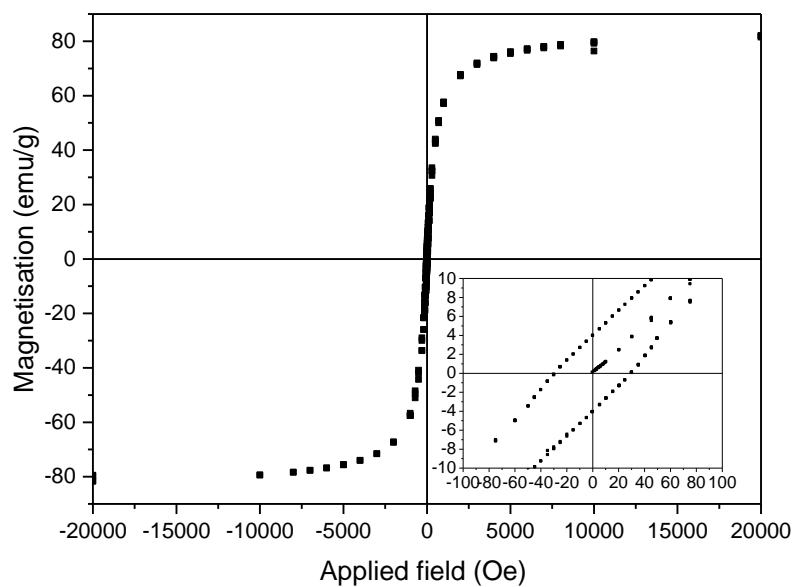
Figure 3-6 Magnetisation curve measured at 300 K of IONPs obtained at 240 °C for 30 min in a single-step reaction (sample IONP-C).
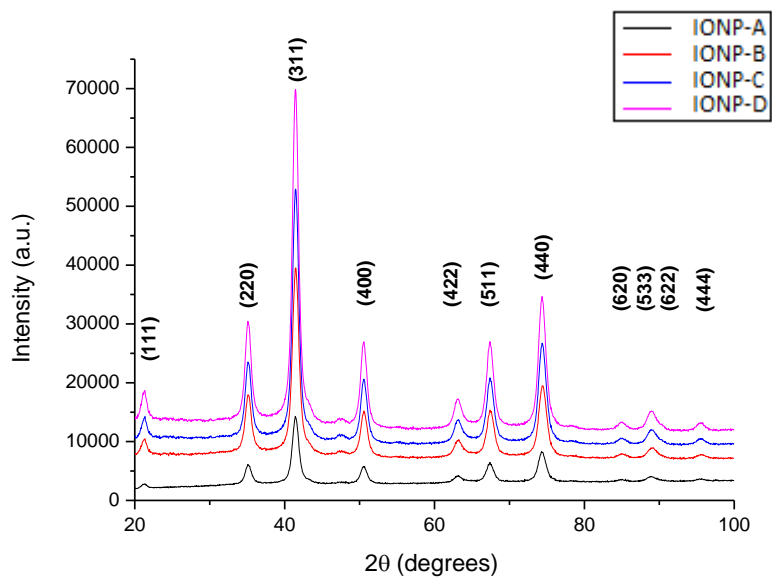
Figure 3-7 XRD pattern of iron oxide nanoparticles synthesised using the Schlenk line. Peaks have been indexed according to the reference pattern for magnetite (pdf ref. 01-088-0315). Diffraction patterns have been offset along the y-axis for better comparison.

Nevertheless, all synthetic reactions allowed us to obtain iron oxide nanoparticles with inverse spinel structure as confirmed by their XRD diffraction patterns in Figure 3-7.

3.2.1.4   In situ PEG functionalisation

In order to functionalise the surface of IONPs and improve their morphology, *in situ* functionalisation with different PEG polymers was attempted as suggested in literature.[74] It has been reported that PEG may be easily adsorbed on the surface of metal oxide colloids, and this phenomenon will hinder the growth of the NPs thus controlling and limiting their size.[217, 218] In these experiments, 2 mmol of $Fe(acac)_3$ with PEG of various molecular weight (200, 2000 and 6000 g/mol) was heated for 1 h at 260 °C. The XRD patterns of the three samples of IONPs synthesised with PEG are shown in Figure 3-9. The crystal structure of the IONPs obtained was unaffected by the addition of PEG as peaks present are in accordance with those of the reference pattern for the inverse spinel structure of magnetite (ref. 01-088-0315). However, the peaks are broader as the molecular weight of the polymer increases, which is certainly due to size effect of the crystals.[219, 220] This was confirmed by the crystallite sizes determined by the Scherer equation for all samples: 4 nm for PEG 200, and 5.8 nm for PEG 2000 and 6000. However there is a decrease in the intensity of the peaks obtained for PEG 200 which might be due to the poor growth of the nuclei when critical concentration of the spontaneous nucleation was reached.[220, 221]

The hydrodynamic diameter of these samples could not be measured as the IONPs precipitated during the measurement. The TEM images of the IONPs obtained with PEG of various molecular weights can be found in Figure 3-8 below. The morphology of the IONPs obtained was not spherical, and was irregular in shape and size.
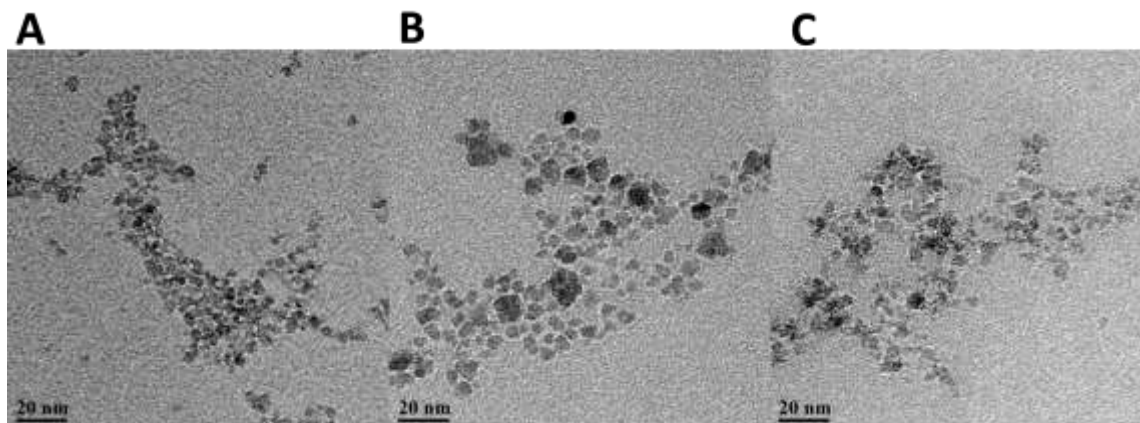
Figure 3-8 TEM images of IONPs synthesised with PEG of different molecular weights (A) 6000, (B) 2000 and (C) 200 g/mol. Magnification 75 k scale bar 20 nm.

Furthermore, the saturation magnetisation decreased significantly with the addition of PEG *in situ*. Although not shown here, the magnetisation curve of the sample obtained with PEG 6000 was characterised by a saturation magnetisation of $M_s = 60$ emu/g, coercive field of approximately 28 Oe and remanence of 0.25 emu/g.
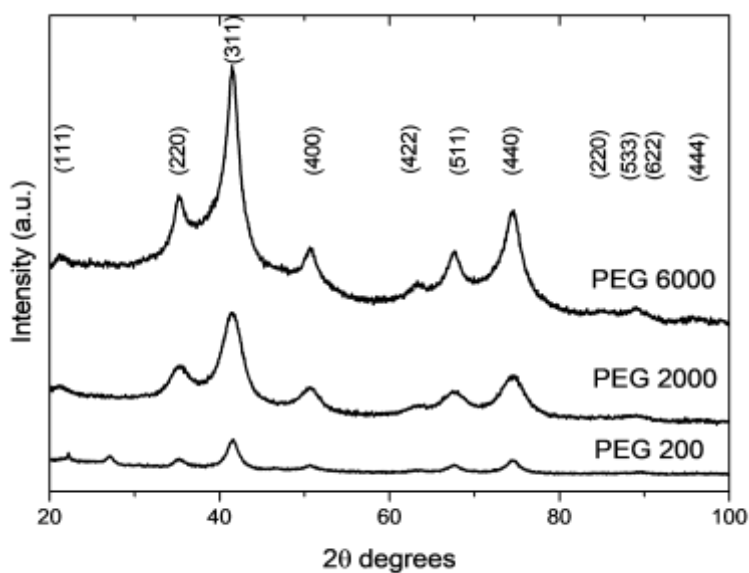
Figure 3-9 XRD patterns of IONPs synthesised using 2 mmol of Fe(acac)$_3$ in the presence of PEG 6000, 2000 and 200. Peaks have been indexed according to the reference pattern for magnetite (ref. 01-088-0315). Diffraction patterns have been offset along the y-axis for better comparison.

To determine the effect of the addition of PEG during the synthesis, all samples were characterised by ATR-FTIR. Figure 3-10 below shows the spectra obtained. The peak around 3413 cm^{-1} is attributed to the stretching vibrations of the O-H groups. The peak around 2885 cm^{-1} is attributed to the alkanes of the polymer; the peak at 1467 cm^{-1} is due to C – H scissoring, the bands around 1106 cm^{-1} are due to skeletal vibrations of $CH_2 – O – CH_2$ bonds, the band at 1343 cm^{-1} is due to C-H bending vibrations; the band at 1242 cm^{-1} can be attributed to C-H twisting vibrations and the peak at 963 cm^{-1} is due to C-O stretching vibrations.[222-224] These peaks are characteristic of the polymer and are present in all samples, however a shift in wavenumber in comparison to the spectrum of free PEG (found in Appendix 1) suggests hydrogen-bonding and the interaction with the surface of the IONPs.[225]
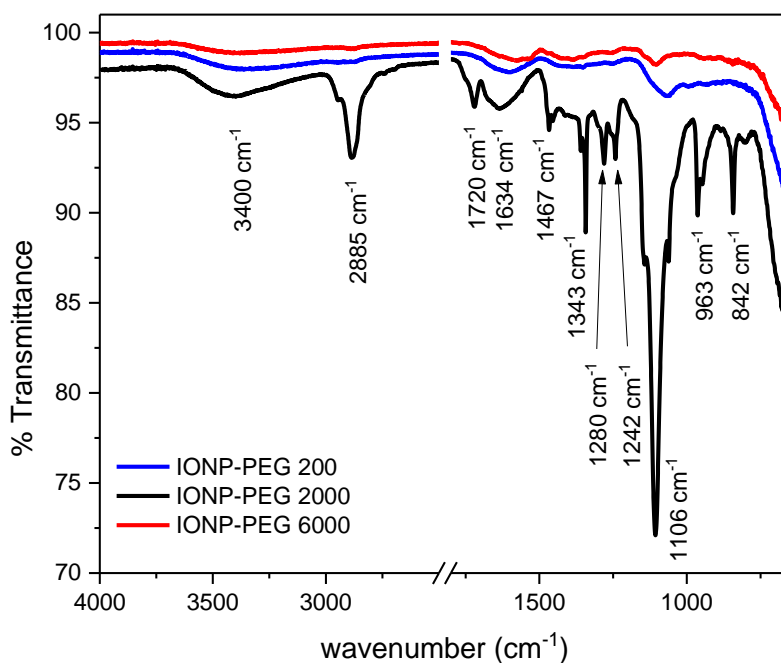
Figure 3-10 ATR-FTIR representative spectra of IONPs obtained after *in situ* functionalisation with PEG 200 (blue), PEG 2000 (black), and PEG 6000 (red). The 1800 - 2500 cm^{-1} range has been excluded as no significant information was found.

The use of PEG did not aid in controlling the shape and size of the IONPs. The samples obtained had lower saturation magnetisation values than those obtained with the polyol solvent. Also, when attempting to determine their hydrodynamic size in aqueous solution, these nanoparticles precipitated out of solution. This could potentially be due to an excess of polymer contributing to the overall nanoparticle mass. These initial attempts with PEG did not allow us to improve the morphology of the IONPs.

3.2.1.5   Conclusion

These initial experiments allowed us to obtain IONPs through a conventional polyol synthesis method using a Schlenk line while following reaction conditions from literature references. However, with these experimental conditions, the size distribution of the IONPs obtained was not monodisperse and strongly dependent on the reaction parameters. The standard deviation of the mean size distribution was improved when carrying out a single step reaction (δ_{TEM} = 14%) as opposed to a two-step heating process (δ_{TEM} = 18 - 20%). The improved size and shape of the IONPs contributed to increasing the saturation magnetisation values of the samples up to M_s = 83 emu/g. However, the IONPs were not superparamagnetic as some larger NPs contributed to the remanence and coercivity of the sample.

To improve the dispersity of the sample, the single step reaction was maintained, but the solvent was changed in order to gain better control over the morphology of the IONPs. For this, *in situ* functionalisation of IONPs with PEG of different molecular weight (6000, 2000 and 200 g/mol) was attempted. FTIR allowed us to prove the presence of PEG in all samples of IONPs obtained with PEG. By XRD, it was determined that the addition of the polymer did not affect the inverse spinel structure of the IONPs. However, their crystallite size was found to be dependent on the Mw of the PEG used, and their shape and size were observed to be irregular by TEM. Their hydrodynamic size could not be determined by DLS as the samples precipitated out of solution. Additional studies could be carried out in the future with PEG

polymer with various functional groups. For example, catechol-derived functional groups have been proven to present a high affinity with metal oxides and have been used successfully to functionalise the surface of IONPs with PEG derivatives.[226-228]

To further improve the synthesis of the polyol coated nanoparticles, alternative heating methods were then investigated. Indeed, the shape of the NPs obtained led to the hypothesis that a conventional heating apparatus using a Schlenk line was not ideal as heating will occur through convection. So for example, a seed of nanoparticle will not be at the same temperature if it closer to the glass (edge of the flask) or if it is in the centre of the flask due to the steep thermal gradients created. Sections 3.2.2 and 3.2.3 will explain how a microwave reactor and high pressure and high temperature conditions can help overcome these limitations.

3.2.2   *Microwave synthesis of polyol coated IONPs*

The polyol reactions carried out using a Schlenk line led to IONPs with a broad size distribution. We hypothesise that the inhomogeneities of the nucleation and the growth process are caused at least partially by the thermal gradients in the reaction vessel. This is due to inefficient transfer of thermal energy from the heat source to the precursors in solution.

Indeed, most synthetic reactions of NPs have been developed with a conventional heating mantle because of the need to have high-temperature conditions which initiate their nucleation. This is then followed by the addition of the precursor, as is the case in hot injection methods for example. However, the reaction vessel acts as an intermediary for the energy transfer from the heating mantle to the solvent and reactant molecules in solution. This, in turn, will lead to steep thermal gradients in solution which imply non uniform reaction conditions making it difficult to obtain uniform and scalable NPs.

Microwave (MW) chemistry is based on the ability of a specific material, in our case the polyol solvent, to absorb MW energy, which is in the low frequency in the range of 300 to 300 000 MHz, and to convert it into heat. In comparison to a classic round bottom flask heated through an aluminium block or an electromantle controlled heating block, MW heating is much more homogenous as the sample itself is heated. This method takes advantage of the polar nature of certain solvents which are selectively heated by their dielectric losses. Unlike convective heating, volumetric heating will lead to the temperature being raised in a uniform manner throughout the whole liquid volume by direct coupling and absorption of the MWs by the reactants in solution. It has been established that this volumetric heating will lead to fewer thermal gradients and thus more uniform reaction temperatures.[229] This should lead to a two-step process: a short burst of nucleation followed by a growth stage, which is the basis for the formation of homogenous NPs.

MW radiation of a sample will lead to the alignment of the dipoles or ions with the electric field. The use of a MW requires less time and energy consumption in comparison to conventional high temperature decomposition methods and may decrease the surface reactivity of the NPs which could be beneficial for biomedical applications.[230] However, since this is an electromagnetic radiation, the reaction vessel is in presence of an oscillating field, so the dipoles or ions will continuously attempt to realign themselves, and this in turn will lead to different amounts of heat being produced through molecular friction and dielectric loss.

The dielectric loss tangent (tan δ) of a solvent reflects its ability to be polarised by the electric field and its ability to convert the MW radiation to heat. Solvents such as ethanol, polyols or dimethyl sulfoxide present a high tan δ and are therefore able to be heated efficiently by this method. For example, ethylene glycol is classified as a high absorbing solvent (tan δ > 1) with a loss tangent value of 1.35.[231] Selective heating which can occur in MW reactions will arise due to the relative difference of dielectric constants between the solvent and reactants in solution. Due to the strong polarity of the polyol solvent, the

microscopic temperature instantly increases when the MW field is applied, so the internal temperature near the NP seed surface is high.

The volume of reaction was limited to 15 ml as the MW vessel mustn't be filled to its maximum capacity for security purposes, in order to not exceed the vessel's pressure limit The concentration of iron precursor Fe(acac)$_3$ was varied from 33 mM to 200 mM, the reaction time was varied between 10 min and 1.5 h with the temperature range being between 240 °C and 280 °C.

3.2.2.1   Effect of the reaction time on IONP formation

To study the influence of the reaction time on the IONPs obtained, the reaction times were varied in the range of 5 min to 90 min. The IONPs were synthesised with DEG at 240 °C and a concentration of Fe(acac)$_3$ of 33 mM and 100 mM. Reaction times can be significantly reduced from hours to minutes using MW reactors as the sample itself will be heated, in comparison to Schlenk line reactions which rely on convective transfer of thermal energy to the reactants in solution.[88]

Table 3-2 reports the size (measured by XRD and TEM) and magnetic properties of the IONPs obtained in a MW reactor with different reaction times. By TEM, a change in the size of the NPs with the reaction time was observed. Up to 30 min there was an increase in the core size of the nanoparticles. When increasing the reaction time above 30 min there was initially a decrease in the size of the IONPs, before another increase in their size. This evolution of the size was correlated with the values of saturation magnetisation measured: 69.5 emu/g for the 30 min reaction, then decreasing to 55.1 emu/g for a 60 min reaction, before increasing to 58.4 emu/g for a 90 min reaction. This trend was also confirmed with the crystallite sizes determined by XRD.

This increase in size of the IONPs with the reaction time up to 30 min before decreasing briefly then increasing again, was a pattern that was also noticed at other concentrations of iron precursor such as 100 mM as is confirmed with the data provided in Table 3-2. There is no linear relationship between the reaction time and the size of the IONPs obtained. Furthermore, the IONPs obtained are not regular with high polydispersity values determined by TEM between 10 and 20% on average. This could potentially be due to a non-defined separation between the nucleation and growth phases of the reaction, thus increasing the polydispersity of the samples. In the case of microwave-assisted reactions, increasing the reaction time does not necessarily lead to an increase in the size of the IONPs and their magnetic properties.[2] This can be due to dissolution of the nanoparticles initially formed in solution under oxidative conditions for longer reaction times, as this has been previously demonstrated with silver nanoparticles.[89]

Table 3-2 Summary size and magnetic characterisation of the IONPs obtained in a microwave reactor with different reaction times and Fe(acac)$_3$ = 33 mM. Core diameter (D$_{TEM}$), standard deviations (σ$_{TEM}$) and dispersity (δ$_{TEM}$) were calculated from TEM images, counting at least 300 particles per sample. Crystallite sizes (D$_{XRD}$) were obtained from the Scherer equation of room temperature XRD patterns and saturation magnetisation (M$_s$) was obtained at 300 K.

	Fe(acac)$_3$ (mM)	reaction time (min)	M$_s$ (emu/g)	D$_{XRD}$ (nm)	D$_{TEM}$ ± σ$_{TEM}$ (nm)	δ$_{TEM}$ (%)
IONP-1	33	5	41	4	2.4 ± 0.5	21
IONP-2	33	20	47.4	4.1	5 ± 2.2	44
IONP-3	33	30	69.5	5.6	5.6 ± 0.8	14
IONP-4	33	60	55.1	5.1	6 ± 0.7	12
IONP-5	33	90	58.4	5.8	6 ± 0.9	15
IONP-6	100	5	45.1	4.1	4.5 ± 0.6	13
IONP-7	100	10	64.6	5.8	6 ± 0.8	13
IONP-8	100	20	59.7	6	6.9 ± 0.9	13
IONP-9	100	60	66.3	4.8	5.9 ± 0.7	12
IONP-10	100	90	60.2	5.4	5.5 ± 0.7	13

3.2.2.2 Effect of the amount of iron precursor Fe(acac)$_3$ on IONP formation

An important factor in the synthesis of nanoparticles is the amount of initial metal precursor, in our case iron (III) acetylacetonate. The concentration of precursor was varied in DEG from 33 to 190 mM while keeping the reaction at 250 °C for 15 min.

Table 3-3 Summary size and magnetic characterisation of the IONPs obtained in a microwave reactor with different concentrations of Fe(acac)$_3$. Core diameter (D$_{TEM}$), standard deviations (σ_{TEM}) and dispersity (δ_{TEM}) were calculated from TEM images, counting at least 300 particles per sample. Crystallite sizes (D$_{XRD}$) were obtained from the Scherer equation of room temperature XRD patterns and saturation magnetisation (M$_s$) was obtained at 300 K.

	Fe(acac)$_3$ (mM)	M$_s$ (emu/g)	D$_{XRD}$ (nm)	D$_{TEM}$ ± σ_{TEM} (nm)	δ_{TEM} (%)
IONP-A	33	42.7	6	5.8 ± 0.8	14
IONP-B	47	71	10.6	13 ± 3	23
IONP-C	132	54.9	5.6	5.7 ± 0.7	12
IONP-D	152	75.7	6	6.8 ± 1	15
IONP-E	190	74.2	15.4	16.9 ± 3.8	22

It is difficult to conclude on the impact the amount of Fe(acac)$_3$ has because the results are inconclusive. There is no definite linear relationship between these two parameters when considering Fe(acac)$_3$ in the range of 47 to 150 mM, as can be seen in Figure 3-11 below.
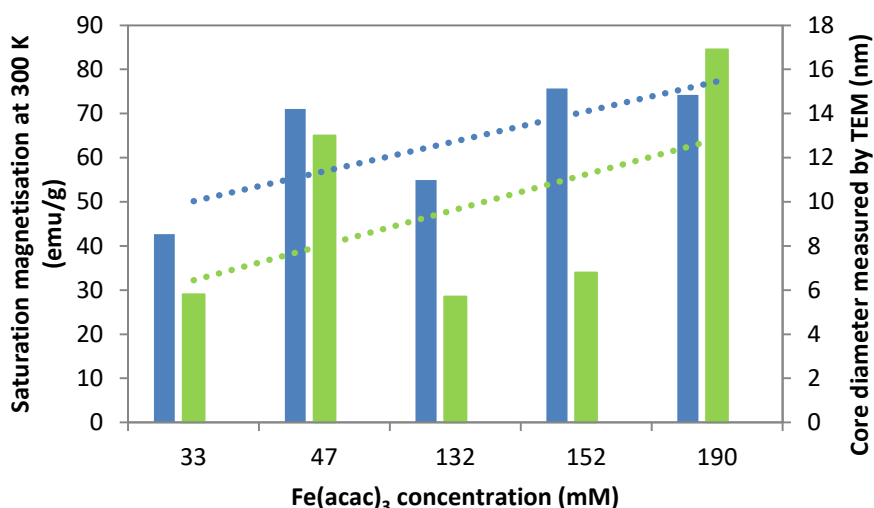
Figure 3-11 Graphical representation of saturation magnetisation (blue) and average core diameter (green) for various concentrations of precursor, as well as their respective forecast linear trend line (dashed line).

However, there is a clear difference between particles obtained with 33 mM and those obtained with 190 mM of Fe(acac)$_3$. The smaller concentration of iron precursor leads to small IONPs with d_{TEM} = 5.8 ± 0.8 nm (δ = 14.1%, n = 372) with M_s (300 K) = 42.7 emu/g, while the larger amount of iron precursor results in IONPs with a size of: d_{TEM} = 16.9 ± 3.8
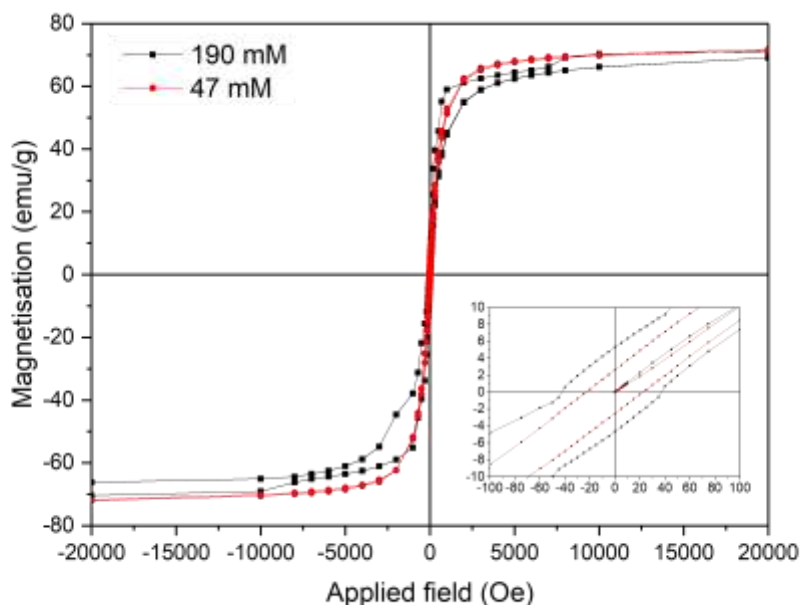
Figure 3-12 Magnetisation curves of IONPs obtained with Fe(acac)$_3$ = 47 mM (●) and 190 mM (■) at 300 K.

nm (δ = 22.7%, n = 218) with M_s (300 K) = 74.2 emu/g.

The most notable difference is the morphology of the IONPs obtained, especially at high concentrations of Fe(acac)$_3$. As it can be seen in Figure 3-13, in comparison to IONPs obtained with 47 mM of precursor, the NPs obtained with 190 mM of Fe(acac)$_3$ are polydisperse and of irregular shape with some being spherical and others being hexagonal or square shaped. The increase in Fe(acac)$_3$ has a detrimental effect on the nanoparticle size distribution and morphology. When measuring the hysteresis curve of all samples at 300 K, these could all be characterised by the presence of a small coercive and remanent field. However, when Fe(acac)$_3$ = 190 mM, some NPs are non-spherical and above the superparamagnetic size threshold and are therefore blocked at 300 K. At this concentration of precursor, with a population of larger and irregular IONPs, H_c and H_r increased to 23 Oe and 2.65 emu/g respectively.
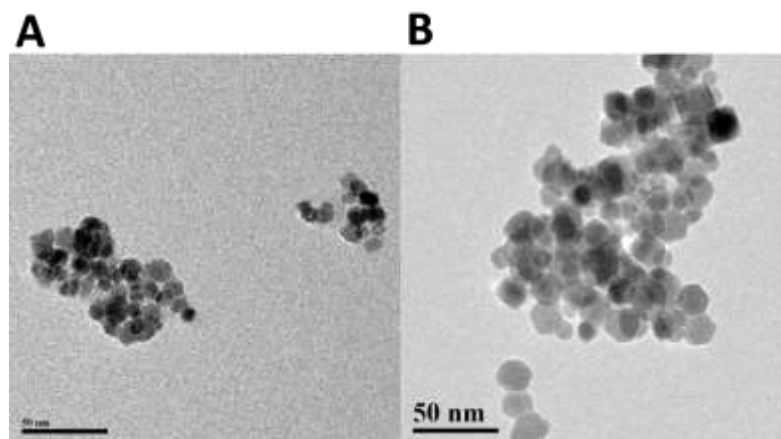
Figure 3-13 TEM images of samples obtained with (A) Fe(acac)$_3$ = 47 mM and (B) Fe(acac)$_3$ = 190 mM magnification 25 k scale bar 50 nm.
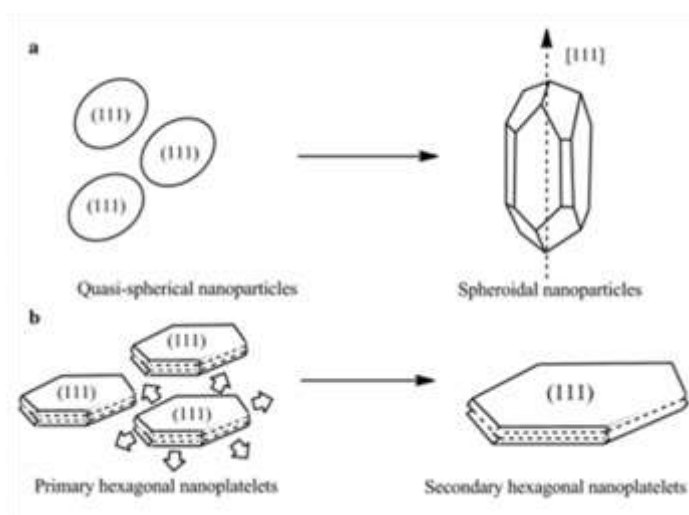
Figure 3-14 Proposed faceting processes leading to (a) spherical nanoparticles or (b) hexagonal nanoparticles. Reproduced from A. Rizzuti et al., Journal of Nanoparticle Research, 2015 with permission from Springer.

It has been hypothesised that the different shapes of IONPs reflects a difference in growth processes (Figure 3-14).[232] In MW synthesis of nanocrystals, several reactions conditions have been identified as disruptive to the isotropic growth of NPs, leading to the formation of nanostructures with anisotropic shapes such as nanorods or ellipsoids for example.[233] In our case, this may depend on the amount of precursor and hence the shape and size of seeds initially formed. To this day, the effect of reaction parameters, such as the amount of precursor, on the morphology of nanocrystals is not yet fully understood.[234] The faceting process allows us to obtain spherical nanoparticles from small spherical seeds in the initial stages of the reaction. With lower amounts of $Fe(acac)_3$ present in solution, the initial spherical seeds will fuse along well-defined crystallographic directions as a way to get rid of any unstable facets. This is a thermodynamically driven process which aims to minimise the overall surface energy. However, anisotropic growth may occur in reactions which are kinetically driven.[235] These can occur far from the thermodynamic equilibrium state, when there is a steep concentration gradient of monomers in solution. With the high concentration of $Fe(acac)_3$ in solution, it is plausible that the non homogenous spatial distribution of monomers in solution will induce instabilities which will promote the growth

of certain crystal facets at high-energy corners and edges of these seeds, thus leading to hexagonal or other anisotropic shaped NPs as seen in Figure 3-14 b. Several causes for this may include the preferential adsorption of capping molecules on certain crystal facets, structural defects, anisotropic interactions of various facets with the surfactant or solvent, or formation of twin planes in the seed particles for example.[236-243]

3.2.2.3   Effect of the reaction temperature on IONP formation

Another critical parameter in the synthesis of IONPs is the reaction temperature. When using DEG (boiling point = 248 °C), the reaction temperature was varied between 240 and 280 °C to determine if this had an impact on the properties of the IONPs synthesised. The concentration of $Fe(acac)_3$ was kept constant at 100 mM with a reaction time of 10 min. In Table 3-4 below are summarised the size and magnetic characterisation of the IONPs obtained.

Table 3-4 Summary size and magnetic characterisation of the IONPs obtained in a microwave reactor with different reaction temperatures. Core diameter (D_{TEM}), standard deviations (σ_{TEM}) and dispersity (δ_{TEM}) were calculated from TEM images, counting at least 300 particles per sample. Crystallite sizes (D_{XRD}) were obtained from the Scherer equation of room temperature XRD patterns and saturation magnetisation (M_s) was obtained at 300 K.

	Reaction temperature (° C)	M_s (emu/g)	D_{XRD} (nm)	D_{TEM} ± σ_{TEM} (nm)	δ_{TEM} (%)
IONP-A	240	64.6	5.8	6 ± 0.8	13
IONP-B	250	54.1	6.4	7.1 ± 1	14
IONP-C	260	55.6	6.4	6.3 ± 0.7	11
IONP-D	280	87.2	10.1	8.5 ± 1.7	20
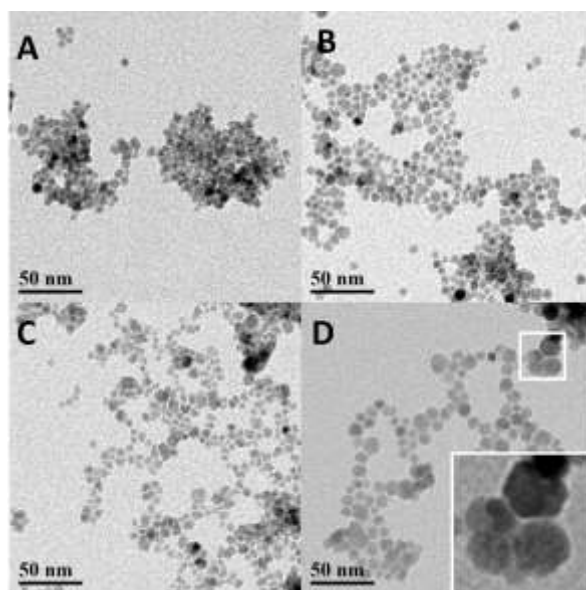
Figure 3-15 TEM images of IONPs obtained with different reaction temperatures (A) 240 °C, (B) 250 °C, (C) 260 °C and (D) 280 °C. Magnification 25 k, scale bar 50 nm.

As can be observed from the TEM images in Figure 3-15, when the temperature is close to the boiling point of the solvent, there is no significant change in the morphology of the IONPs obtained. However, when increasing the reaction temperature to 280 °C some IONPs obtained are hexagonal shaped. Although the exact mechanism of formation has not been studied, we hypothesise that this could be due to specific microwave (MW) effects. For example, this could be caused by superheating of the solvent by MW. It has been suggested that this phenomenon arises from the rapid dissipation of MW power which leads to the absence of bubble nucleation sites in the solvent which are necessary for the boiling of the solvent.[244] MW heating is more rapid and homogenous than convective heating by uniform loss processes at high enough temperatures, there may however be the creation of local "new nucleation points", at temperatures above 280 °C, which could contribute to the formation of hexagonal shaped IONPs. These can be due to local areas of higher temperatures in the solution due to "selective heating" within a non homogenous dispersion. MWs are preferentially absorbed by a material with a higher tan δ value,

however if these are not well dispersed within a reaction solution, this may lead to an increased local temperature.[245] According to Richert, "local heating can occur in cases where absorptivity is a spatially varying quantity".[246] The viscosity in this area will decrease, more collisions will occur and nuclei will aggregate locally. This mechanism has been shown to take place during the synthesis of ZnO nanoparticles using a MW reactor.[29] Although this strategy has not been explored during this project, the phenomenon of selective heating in the context of NP synthesis may be interesting when dealing with solid/liquid interfaces, as the metal oxide NP strongly absorbs MW which leads to local overheating and a change in surface properties such as their functionalisation with ligands for example.[247, 248]

However, when performing the syntheses using a MW reactor, it was challenging to demonstrate the reproducibility of the synthetic conditions. In an attempt to replicate reactions and determine the reproducibility of this method, 2 reactions were performed back to back on the same day in identical conditions. 2 mmol of $Fe(acac)_3$ and 15 ml of DEG were heated up to 280 °C and maintained at that temperature for 10 min. The temperature reached was monitored and the first reaction only reached 205 °C, whereas the second reached 260 °C. This impacted their magnetic properties significantly as the first sample had a saturation magnetisation of M_s = 73.9 emu/g while the second sample had a measured magnetisation M_s = 56.3 emu/g. This may potentially be due to the limited MW power of 300 W that was not always sufficient to heat DEG to its boiling point. However, as suggested in literature, IR detection with which was performed the temperature measurement, is not accurate as it is a read of the vial surface temperature, unlike a fibre optics probe. As the polyol strongly absorbs MW radiation, the IR sensor will tend to underestimate the reaction temperature, measuring the cooler outside temperature of the vial. Materials with large tan δ values have the most apparent discrepancies due to rapid heating of the solution while the vessel itself remains cooler.

3.2.2.4   Effect of the solvent

Another parameter that has been shown to have a significant impact on the synthesis of IONPs is the solvent. To evaluate this, identical reactions were carried out using DEG and triethylene glycol (TREG). However, since their boiling points differ DEG was heated up to 250 °C whereas TREG was heated up to 280 °C. As can be deduced from the results presented in Table 3-5, the solvent had a significant impact on the IONPs obtained. In this method, this is also due to the fact that the polyol will act not only as the solvent, but also as a surfactant and reducing agent. It has been demonstrated that when the solvent is a polyol, nanoparticles may be produced without any additional surfactants to stabilise them thanks to the polyols and their low viscosity, their role as a reducing agent and minimal steric hindrance.[249] These experiments show that as the length of the polyol surfactant increases, larger nanoparticles are obtained. As this has been reported in several studies, it is believed that the viscosity of the polyol solvent will determine the mobility of diffusion of ions or NP seeds, which in turn will have a significant impact on the growth of NPs.[249-251] DEG is less viscous than TREG with a viscosity of 35.7 millipascal second (mPa) s at 25 °C in comparison to 49 mPa s for TREG. The lower viscosity of DEG could aid in the mobility and diffusion of monomers in solution, thus leading to more nucleation, and with less monomers in solution smaller IONPs are obtained. On the contrary, with TREG, which has a higher molecular weight and is more viscous, the diffusion of species on solution is limited. This implies a slower nucleation rate, fewer seeds are formed, more iron-TREG chelates are available for the subsequent growth of IONPs, thus larger NPs are obtained.

Table 3-5 Summary size and magnetic characterisation of the IONPs obtained in a microwave reactor with diethylene glycol (DEG) and triethylene glycol (TREG). Core diameter (D_{TEM}), standard deviations (σ_{TEM}) and dispersity (δ_{TEM}) were calculated from TEM images, counting at least 300 particles per sample. Crystallite sizes (D_{XRD}) were obtained from the Scherer equation of room temperature XRD patterns and saturation magnetisation (M_s) was obtained at 300 K.

	Reaction solvent	$Fe(acac)_3$ (mM)	M_s (emu/g)	D_{XRD} (nm)	$D_{TEM} \pm \sigma_{TEM}$ (nm)	δ_{TEM} (%)
IONP-A	DEG	47	56.2	4.7	3.9 ± 0.6	15
IONP-B	TREG	47	49.4	6.9	7 ± 0.9	13
IONP-C	DEG	132	80	6.2	6.5 ± 0.9	14
IONP-D	TREG	132	94.6	16.5	15.7 ± 3.2	20
IONP-E	DEG	152	77.8	4.9	5.9 ± 0.8	14
IONP-F	TREG	152	86.3	11.9	12.5 ± 2.4	19

3.2.2.5   Conclusion

The effect of different reaction parameters on the synthesis of IONPs by the polyol method in a MW reactor was studied. No direct correlation could be established between the reaction time and the size or properties of the IONPs obtained. Indeed, increasing the reaction time did not necessarily lead to larger IONPs with enhanced magnetic properties. An increase in the concentration of iron precursor $Fe(acac)_3$ did lead to overall larger IONPs and increased saturation magnetisation, but no direct linear correlation could be observed. The hypothesis is that this could be merely due to insufficient mixing of the reactants in solution which are not properly dissolved in the polyol solvent. Furthermore, at high concentrations of $Fe(acac)_3$ such as 190 mM, anisotropic growth could be observed with IONPs being hexagonal shaped.

The reaction temperature had an impact on the IONPs obtained, as the MW can provide sufficient energy to cause superheating of the solvent. If the reaction mixture is not homogenous, materials with higher tan δ values may preferentially absorb the MW energy which can lead to the formation of new local nucleation points at high temperatures where there is an increase in the local temperature. In turn, these may affect the crystalline growth of IONPs and their surface properties, leading to potential hexagonal shaped IONPs. To avoid this effect, careful attention must be provided to ensure the homogeneity of the reaction solution and the temperature must be carefully monitored. Finally, these experiments led to the conclusion that the length of the polyol had an impact on the size of the IONPs obtained. Due to its smaller molecular weight, DEG is less viscous than TREG, which in turn will allow for a more rapid diffusion of species in solution hence for more nucleation events to take place and thus smaller IONPs are obtained.

3.2.3   *High pressure – high temperature synthesis*

In the next phase of this work, the polyol synthesis was adapted to high pressure and high temperature conditions of an oven. Synthesis in these conditions offers the opportunity to examine their effect on the properties of IONPs obtained. Indeed, several publications link the high pressure conditions to NPs with improved crystallinity, as well as the possibility for superheating conditions which can also have an impact on the synthesis of nanomaterials.[204] The aim of the next section was to attempt to contribute to a better comprehension of the polyol synthesis and to improve the properties of the IONPs by carrying out a systematic study of the process. For this, the conditions were finely tuned (reaction time, type of solvent and concentration of iron precursor) and their effects on the final size, morphology and magnetic properties of the obtained NPs were investigated.

3.2.3.1   Effect of polyol solvent on IONP formation

As discussed in section 3.2.2.4, when the polyol synthesis was carried out in a MW reactor, the type of polyol solvent had a significant impact on the size of the NPs, hence on their

magnetic properties. Section 3.2.3.1 aims to determine if this effect was also observed in the case of IONP synthesis in high pressure high temperature conditions.

In a typical reaction, the following reaction conditions were used: 0.7 g Fe(acac)$_3$ were dissolved in 20 ml of polyol solvent (diethylene glycol (DEG), triethylene glycol (TREG) and tetraethylene glycol (TEG)), then heated up to 250 °C and maintained at that temperature for 8 h. The characterisation of the IONPs obtained with different polyols can be found in Table 3-6 below.

The TEM analysis of IONPs synthesised with different polyols, as can be seen in Figure 3-16, revealed that IONPs obtained with DEG and TREG were spherical and below the superparamagnetic critical size with an average diameter of 5.8 ± 0.8 nm (δ = 14.1%) and 9.1 ± 0.9 nm (δ = 9.8%) respectively. On the other hand, when a longer polyol ligand such as tetraethylene glycol (TEG) was used, larger nanoparticles of 13.9 nm ± 3.4 nm (δ = 24.5%) were obtained with an increase in the polydispersity of the sample. There is a correlation between the length of glycol and size of NPs, as the higher the length of the glycol, the larger the size of the synthesised NPs. The magnetic properties of these polyol coated IONPs

Table 3-6 Summary size and magnetic characterisation of the IONPs obtained in high pressure-high temperature conditions with different solvents DEG, TREG and TEG. Core diameter (D_{TEM}), standard deviations (σ_{TEM}) and dispersity (δ_{TEM}) were calculated from TEM images, counting at least 300 particles per sample. Crystallite sizes (D_{XRD}) were obtained from the Scherer equation of room temperature XRD patterns and saturation magnetisation (M_s) was obtained at 300 K.

Reaction solvent	M_s (emu/g)	D_{XRD} (nm)	$D_{TEM} \pm \sigma_{TEM}$ (nm)	δ_{TEM} (%)
DEG	71.5	6.1	5.8 ± 0.8	14
TREG	80.8	8.4	9.1 ± 0.9	10
TEG	79.1	12.8	13.9 ± 3.4	25

were measured at 300 K, the hysteresis curves obtained can be seen in Figure 3-17. IONPs obtained with DEG and TREG exhibited superparamagnetic behaviour with a saturation magnetisation M_s = 71.5 and M_s = 80.8 emu/g respectively and negligible coercivity. On the other hand, when using TEG, IONPs were characterised by M_s = 79.1 emu/g but also a small coercive field H_c = 4.6 Oe and remanence of approximately M_r = 1 emu/g. Since the particle size distribution increased, it is plausible that amongst the TEG coated IONPs, a population of larger IONPs above the superparamagnetic threshold become blocked at 300 K.[27]
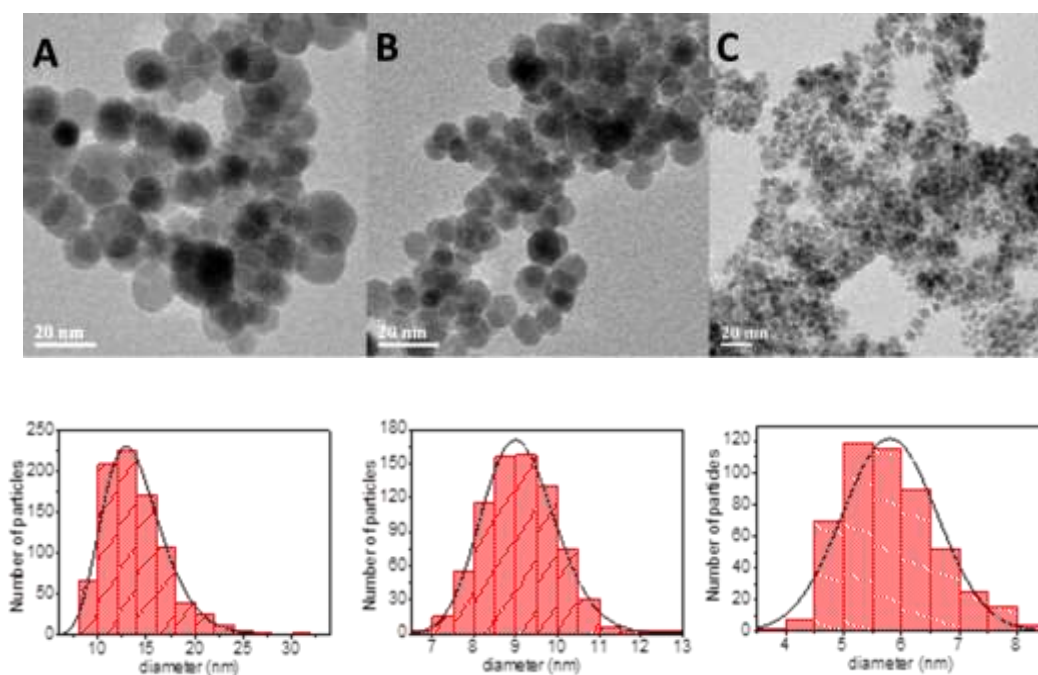
Figure 3-16 TEM images and particle size distributions of iron oxide nanoparticles synthesised using different polyols A) TEG, B) TREG and C) DEG. Magnification 75 k scale bar 20 nm. Size distributions were fitted with a normal function (solid line), d = mean diameter, δd = standard deviation and n = number of particles counted.
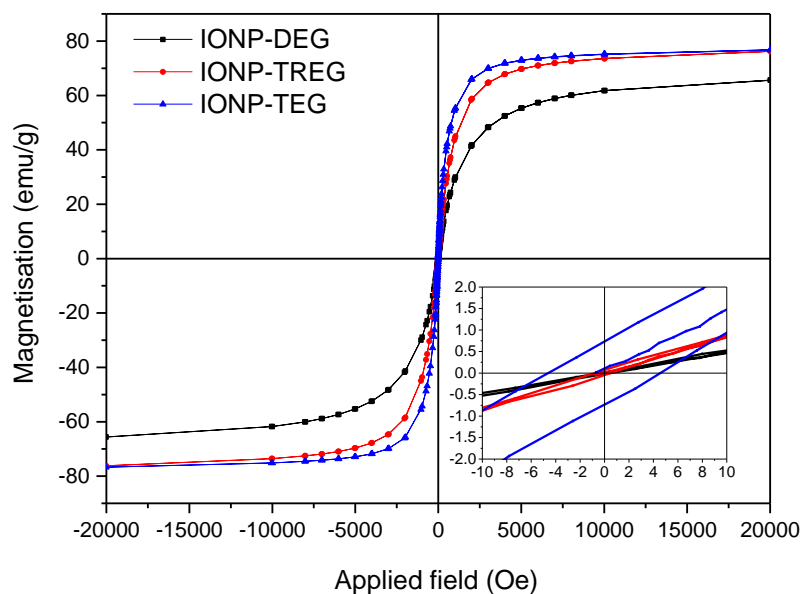
Figure 3-17 Magnetisation curves of IONPs synthesised in high pressure-high temperature conditions with different polyol solvents (■) DEG, (●) TREG and (▲) TEG.

Different sizes of NPs were obtained with different polyol ligands in identical high pressure and high temperature conditions.

The exact nucleation and growth process for this reaction remains poorly understood to this day. As observed by Douglas *et al.,* the mechanism here is not consistent with a classic LaMer mechanism.[249] This study highlights the importance of the solvent on the final NP morphology, especially in the case of an unstirred system. The solvent viscosity will play a critical role in the diffusion of species in solution, thus having an impact on the nucleation and growth of NPs. As this has also been observed with various NP systems such as with titanium dioxide and gold NPs, it is plausible that the higher the length of the carbon chain of the polyol, the more effective they are as capping ligands, hence bigger NPs are obtained as it was shown to be the case with poly(ethylene glycol) of different molecular weight.[249, 252-254]

These experiments confirm that the choice of the solvent is critical in obtaining high quality nanoparticles with a desired size and with a narrow size distribution.[249, 255, 256] From these results, it was determined that IONPs produced in DEG and TREG were suitable for further investigations as they had a narrow size distribution, were superparamagnetic, and had a high saturation magnetisation which are necessary for biomedical applications.[257]

3.2.3.2   Effect of the reaction time on IONP formation

To study the effect of the reaction time on the NPs obtained, in a typical synthesis 1.4 g of Fe(acac)$_3$ was dispersed in 20 ml of TREG. The reaction mixture was transferred to a 45 ml capacity Teflon lined autoclave vessel then heated up to 250 °C and maintained at that temperature for 1 h, 2 h, 4 h, 8 h, 12 h and 24 h. The results obtained are summarised in Table 3-7.

The increase in the reaction time from 1 h to 24 h led to an increase in the size of the NPs
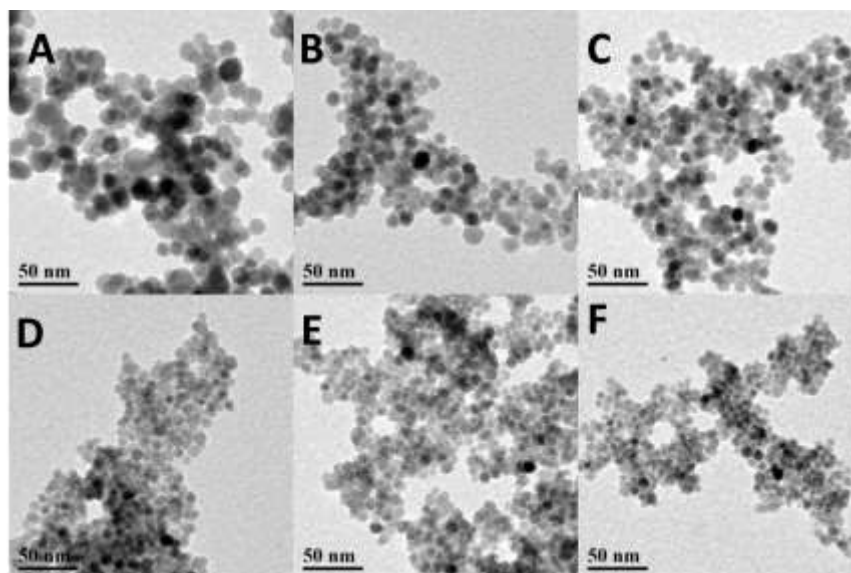
Figure 3-18 TEM images of IONPs synthesised with TREG in high pressure high temperature conditions with different reaction times A) 24 h B) 12 h C) 8 h D) 4 h E) 2 h F) 1 h. Magnification 25 k scale bar 50 nm.

obtained from 7.2 nm ± 0.8 nm (δ = 11%) to 15 nm ± 1.9 nm (δ = 12.5%). This was also coupled with an increase in the saturation magnetisation from 61.2 emu/g to 88 emu/g. Longer reaction times led to particle growth with narrow size distribution, leading us to the hypothesis that the reaction mechanism is coalescence.[258] This allows us to finely control the size of the nanoparticles, which is crucial for their biomedical applications.

This trend in the evolution of the core size determined by TEM, crystallite size determined by XRD and the saturation magnetisation measured at 300 K as a function of the reaction time also occurred with DEG. A graphical representation of the evolution of core diameter measured by TEM and saturation magnetisation as a function of the reaction time in DEG and TREG can be found in Figure 3-19 below. This confirms the overall linear evolution of these parameters with the reaction time in high pressure high temperature conditions.
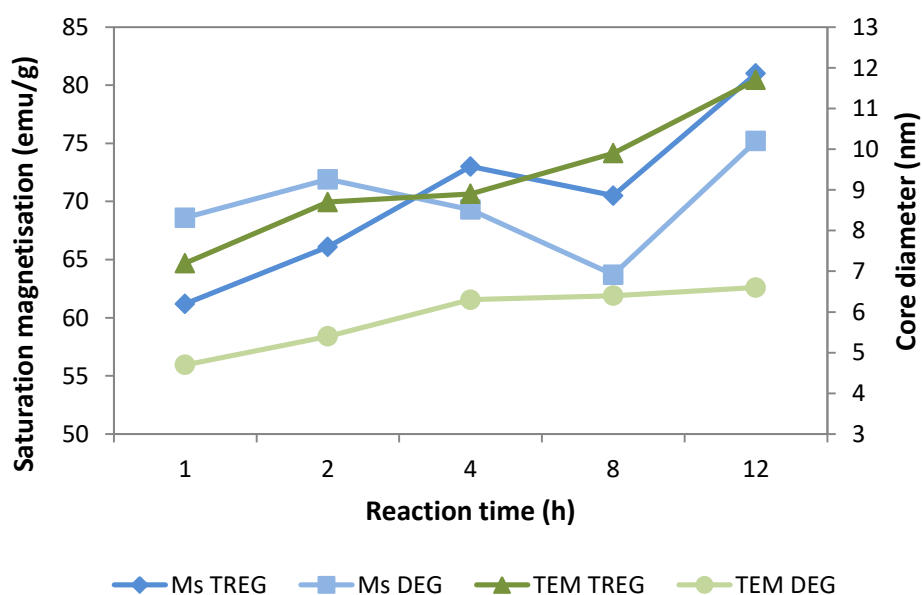
Figure 3-19 Graphical representation of the core diameter measured by TEM and saturation magnetisation measured at 300 K of the IONPs obtained in TREG and DEG in high pressure high temperature conditions with different reaction times.

140

Table 3-7 Summary size and magnetic characterisation of the IONPs obtained in TREG and DEG in high pressure high temperature conditions with different reaction times. Core diameter (D_{TEM}), standard deviations (σ_{TEM}) and dispersity (δ_{TEM}) were calculated from TEM images, counting at least 300 particles per sample. Crystallite sizes (D_{XRD}) were obtained from the Scherer equation of room temperature XRD patterns and saturation magnetisation (M_s) was obtained at 300 K.

Sample	Solvent	Reaction time (h)	M_s(emu/g)	D_{XRD} (nm)	$D_{TEM} \pm \sigma_{TEM}$ (nm)	δ_{TEM} (%)
IONP-A	TREG	1	61.2	6.2	7.2 ± 0.8	11
IONP-B	TREG	2	66.1	7.3	8.7 ± 1	11
IONP-C	TREG	4	73	7.8	8.9 ± 1	11
IONP-D	TREG	8	70.5	9.4	9.9 ± 1.1	11
IONP-E	TREG	12	81	29.2	11.7 ± 1.4	12
IONP-F	TREG	24	88.8	13.5	15.1 ± 1.2	8
IONP-A	DEG	0.5	65.7	4.1	4 ± 0.5	13
IONP-B	DEG	1	68.6	4.6	4.7 ± 0.8	17
IONP-C	DEG	2	71.9	5	5.4 ± 0.6	11
IONP-D	DEG	4	69.3	5.5	6.3 ± 0.7	11
IONP-E	DEG	8	63.7	5.9	6.4 ± 0.7	11
IONP-F	DEG	12	75.2	18.6	6.6 ± 0.7	11

3.2.3.3   Effect of the amount of Fe(acac)$_3$ on IONP formation

The final parameter that was studied was the effect of the amount of precursor Fe(acac)$_3$ on the IONPs synthesised with TREG at 250 °C for 8 h. The amount of precursor was varied from 100 mM up to 500 mM and the results obtained are presented in Table 3-8.

From the IONPs obtained, a direct linear relationship between the concentration of Fe(acac)$_3$ and the crystallite size determined by XRD was observed. On the other hand, the core diameter measured by TEM and the saturation magnetisation measured at 300 K did overall increase with the amount of precursor but not in a proportional manner. Further thermogravimetric analysis was carried out on all samples to confirm the amount of polyol coating and determine its contribution to the overall NP mass. This data can be found in Appendix 2. This allows for a more accurate magnetic characterisation of the IONPs obtained. Along with the saturation magnetisation of these samples, this trend was also observed for the core size of the IONPs measured from TEM images which increased from 10.3 ± 1 nm for Fe(acac)$_3$ = 100 mM to 13.6 ± 2.4 nm for Fe(acac)$_3$ = 500 mM. Overall, these experiments allowed us to observe a direct correlation between the amount of precursor used and the size of the NPs obtained. In turn, this was directly linked to the magnetic properties of the IONPs. However, the concentration of 500 mM was deemed too high as IONPs obtained had an estimated crystallite size of 22 nm and a core diameter measured by TEM of 13.6 ± 2.4 nm. These values are consistent with the small coercive field of approximately 15 Oe which characterises this sample (data not shown here), and which is not desirable when for superparamagnetic IONPs in biomedical applications.

Table 3-8 Summary size and magnetic characterisation of the IONPs obtained in a TREG in high pressure-high temperature conditions with different amounts of precursor Fe(acac)$_3$. Core diameter (D$_{TEM}$), standard deviations (σ$_{TEM}$) and dispersity (δ$_{TEM}$) were calculated from TEM images, counting at least 300 particles per sample. Crystallite sizes (D$_{XRD}$) were obtained from the Scherer equation of room temperature XRD patterns and saturation magnetisation (M$_s$) was obtained at 300 K.

Sample	Fe(acac)$_3$ (mM)	M$_s$ (emu/g)	M$_s$ (TGA corrected)	D$_{XRD}$ (nm)	D$_{TEM}$ ± σ$_{TEM}$ (nm)	δ$_{TEM}$ (%)
IONP-A	100	65.4	73.7	8.6	10.3 ± 1	10
IONP-B	150	72.9	74.1	8.5	9.9 ± 1.2	12
IONP-C	200	64	72.4	9.1	9.5 ± 1	11
IONP-D	250	73.4	80.8	12	10 ± 1.2	12
IONP-E	500	83.3	90.8	22	13.6 ± 2.4	18

3.2.3.4 Reproducibility studies

While it was found that the IONPs obtained were consistent under the same experimental conditions, the reproducibility of the synthetic conditions was investigated in order to evaluate the reliability of this method and its potential for mass-production of IONPs. Most publications reporting the synthesis of nanoparticles for biomedical applications fail to study the reproducibility of the synthetic method which is critical before any commercialisation or clinical trials can be considered. Each reaction, using TREG as the polyol capping agent, was repeated three times and the properties of the IONPs obtained were assessed. A standard condition for the reaction was kept constant: 1.4 g of Fe(acac)$_3$ and 20 ml of TREG were heated up to 250 °C and maintained at that temperature for 8 h before cooling down to room temperature over 2 h. Indeed, previous results presented in Table 3-7 indicate that the IONPs obtained with these conditions lead to the formation of superparamagnetic

IONPs with interesting magnetic properties and with an appropriate size for biomedical applications. For simplicity, the triplicates obtained with these reaction conditions are named IONP-1, IONP-2 and IONP-3. The results are illustrated in Table 3-9.

Table 3-9 Summary size and magnetic characterisation of the triplicates obtained (as described in section 3.2.3.4). Core diameter (D_{TEM}), standard deviations (σ_{TEM}) and dispersity (δ_{TEM}) were calculated from TEM images, counting at least 300 particles per sample. Crystallite sizes (D_{XRD}) were obtained from the Scherer equation of room temperature XRD patterns and saturation magnetisation (M_s) was obtained at 300 K.

Sample	$D_{TEM} \pm \sigma_{TEM}$ (nm)	δ_{TEM} (%)	D_{XRD} (nm)	M_s (emu/g)
IONP-1	9.9 ± 1.1	11	9.4	70.5
IONP-2	10.9 ± 1.1	10	8.9	77.8
IONP-3	10.5 ± 1.1	10	9.3	81.1
Overall average	10.2 ± 1.2	12	9.2 ± 0.3	76.5 ± 5.4

These results indicate a well-controlled synthesis route with a standard deviation of the core size determined by TEM which is very narrow. Similarly, the crystallite size determined by XRD only presented a standard deviation of 0.3 nm. It was therefore possible to obtain IONPs in high temperature high pressure conditions by a reproducible and reliable method when controlling the synthesis conditions.

To demonstrate the advantage of high pressure high temperature conditions, the same reaction was replicated (1.4 g Fe(acac)$_3$ in 20 ml of TREG) using a conventional set-up consisting of a round bottom flask, condenser and magnetic stirring. The IONPs obtained in these conditions differed by their polydispersity and magnetic properties.
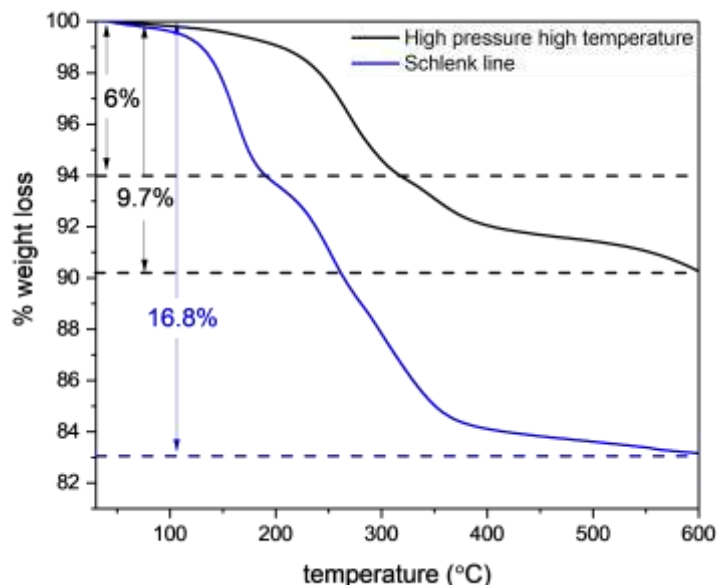
Figure 3-20 Thermogravimetric analysis of TREG coated IONPs obtained in high pressure high temperature conditions (black) and TREG coated IONPs obtained with a Schlenk line (blue).

TGA of these samples differed significantly in terms of the percentage of organic coating present. Both samples had an initial 6% weight loss due to elimination of water and solvent evaporation (T < 200 °C). For IONPs obtained in a round bottom flask, a 16.8% weight loss of organic material was observed in the range of T = 200 °C to T = 400 °C. IONPs obtained in high pressure high temperature conditions were characterised by a 9.7% weight loss in the same temperature range. However, both samples present a single step of mass loss which is characteristic of chemisorption of the surfactant,[259-261] TREG in this case.

As can be seen in Figure 3-21, the hysteresis curves at 300 K of TREG coated IONPs obtained with a Schlenk line showed that they exhibited a superparamagnetic behaviour with M_s = 81.8 emu/g. At 5 K a value of M_s = 90 emu/g was measured indicating that spins are blocked at that temperature. While the magnetic properties are similar to the IONPs obtained in

high pressure and high temperature conditions, the size distribution of the core diameter measured by TEM is significantly larger. As can be seen in Figure 3-22, IONPs obtained had a much broader size distribution: d_{TEM} = 9.9 ± 1.8 nm (δ = 18%), in comparison to IONPs obtained in high pressure high temperature conditions: d_{TEM} = 10.5 ± 1 nm (δ = 10%). High pressure conditions allowed better control of the morphology of the IONPs obtained, hence leading to monodisperse nanoparticles as demonstrated in the summary of the characterisation of these IONPs found in Table 3-10.
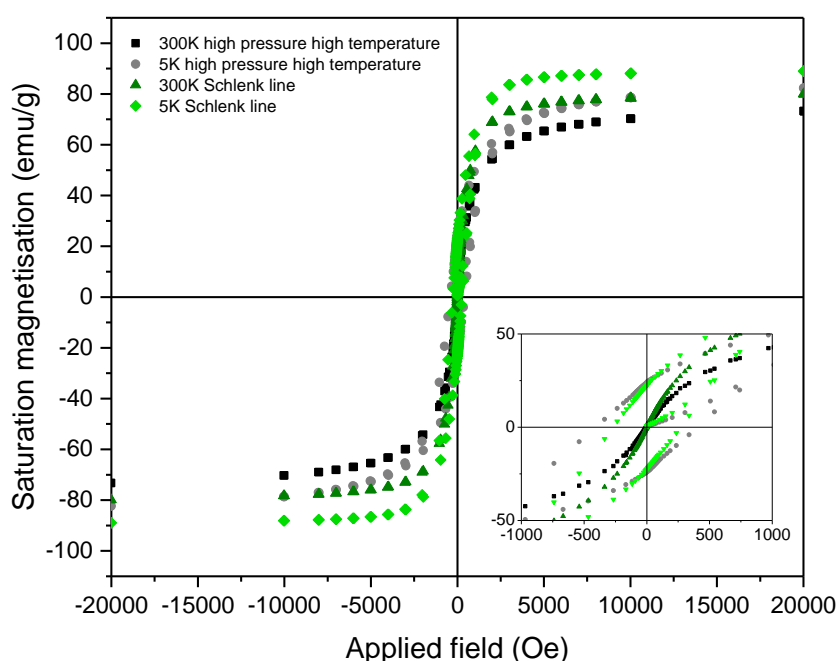
Figure 3-21 Magnetisation curves of TREG coated IONPS obtained with a conventional apparatus consisting of a round bottom flask, magnetic stirring and condenser at 300K (△) and 5K (◊), and of IONPs obtained in high pressure high temperature (HPHT) conditions at 300K (□) and 5K (○).
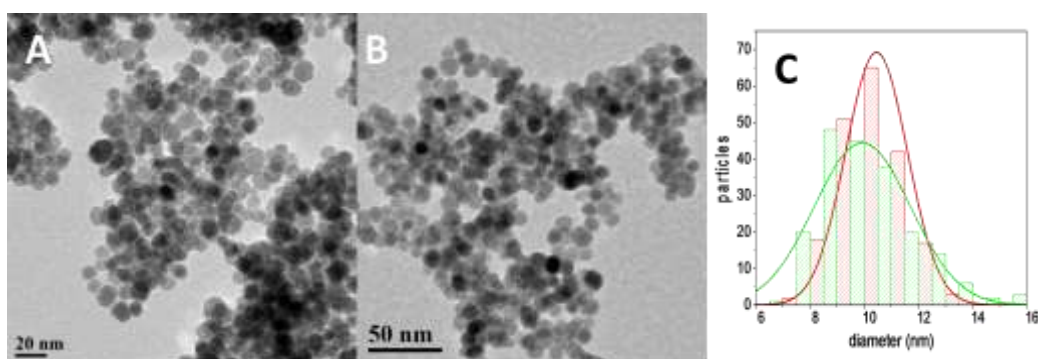
Figure 3-22 TEM image of IONPs obtained with TREG (A) in a conventional apparatus consisting of a round bottom flask, magnetic stirring and condenser, magnification 75 K scale bar 20 nm or (B) in high pressure high temperature conditions, magnification 25 K scale bar 50 nm. (C) Particle size distributions were fitted with a log normal function for IONPs obtained using a Schlenk line (green) and in high pressure high temperature conditions (red).

Table 3-10 Summary size and magnetic characterisation of the IONPs obtained in high pressure high temperature conditions or using a conventional set-up consisting of a round bottom flask, condenser and magnetic stirring. The same reaction conditions were used: 1.4 g Fe(acac)$_3$ in 20 ml of TREG were heated up to 250 °C and maintained at that temperature for 8 h before cooling down to RT over 2 h. Core diameter (D_{TEM}), standard deviations (σ_{TEM}) and dispersity (δ_{TEM}) were calculated from TEM images, counting at least 300 particles per sample. Saturation magnetisation (M_s) was obtained at 300 K.

	$d_{TEM} \pm \sigma_{TEM}$ (δ_{TEM})	TGA weight loss (%)	M_s 300 K (emu/g)
Schlenk line	9.9 ± 1.8 nm (18%)	16.8	81.8
High pressure high temperature conditions	10.5 ± 1.1 nm (10%)	9.7	76.2

3.2.3.5   Magnetic characterisation of polyol coated IONPs

A sample was made in identical conditions as previously (Section 3.2.3.4) and characterised by SQUID-VSM at 300 K and 5 K. Briefly, 1.4 g of Fe(acac)$_3$ and 20 ml of TREG were heated up to 250 °C and maintained at that temperature for 8 h before cooling down to RT over 2 h. Furthermore, Mössbauer spectroscopy was conducted on a sample obtained in identical

conditions by Dr Lara Bogart from University College London, UK in an attempt to identify the phase of iron oxide obtained. SQUID-VSM was used to measure the magnetic properties of the IONPs at 5 K and 300 K and these are reported in Figure 3-23.
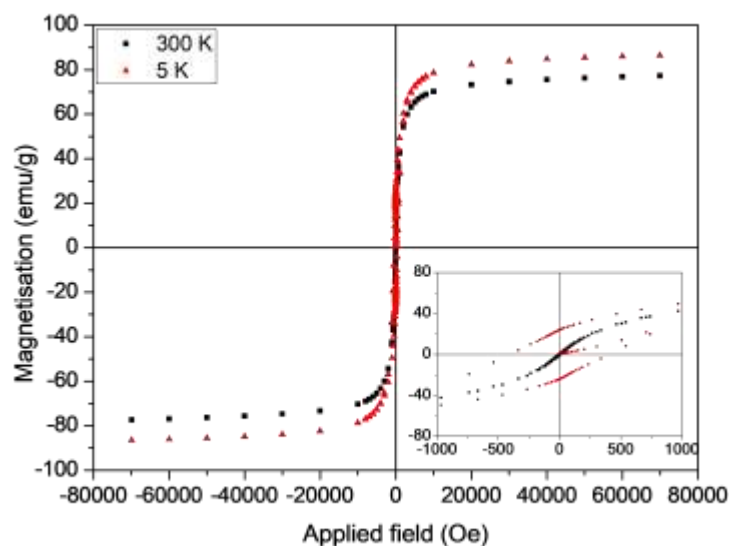
Figure 3-23 Magnetisation curves of IONPs obtained with TREG in high pressure high temperature conditions at 300 K (■) and 5 K (▲), showing the transition from a superparamagnetic state at 300 K to a blocked state at 5 K.

Saturation magnetisation M_s at 300 K was measured at 77.3 emu/g which is close to the bulk value of maghemite (78 emu/g at 300 K) and magnetite (92 emu/g at 300 K),[34, 35] which indicates that the contribution of the polyol ligand to the mass of the nanoparticle structure is negligible. The decrease in the M_s in comparison to the bulk could be due to surface and nanoscale effects. Indeed, the spherical morphology of the IONPs is consistent, so we do not attribute the decrease of M_s to shape effects.[86, 249, 262] This value is slightly smaller than the theoretical magnetisation value for bulk maghemite,[36, 81] and this is due to a finite size effect: canting of surface spins which are unaligned with the spins present in the rest of the magnetic domain.[133] This effect is more pronounced for NPs of smaller size.[263] At 5 K a M_s of

86.5 emu/g was measured indicating that spins are blocked at that temperature hence a higher value than at 300 K.

All curves were corrected by taking into account the organic layer's contribution due to polyol. Indeed, the presence of the polyol on the surface of the NPs was confirmed by TGA measurements (Figure 3-24).

The thermal decomposition of TREG coated IONPs is characterised by a two-stage weight loss profile. The first stage from approximately 40 to 200 °C corresponds to the removal of the physically adsorbed water molecules. The second step from 200 to 570 °C, which
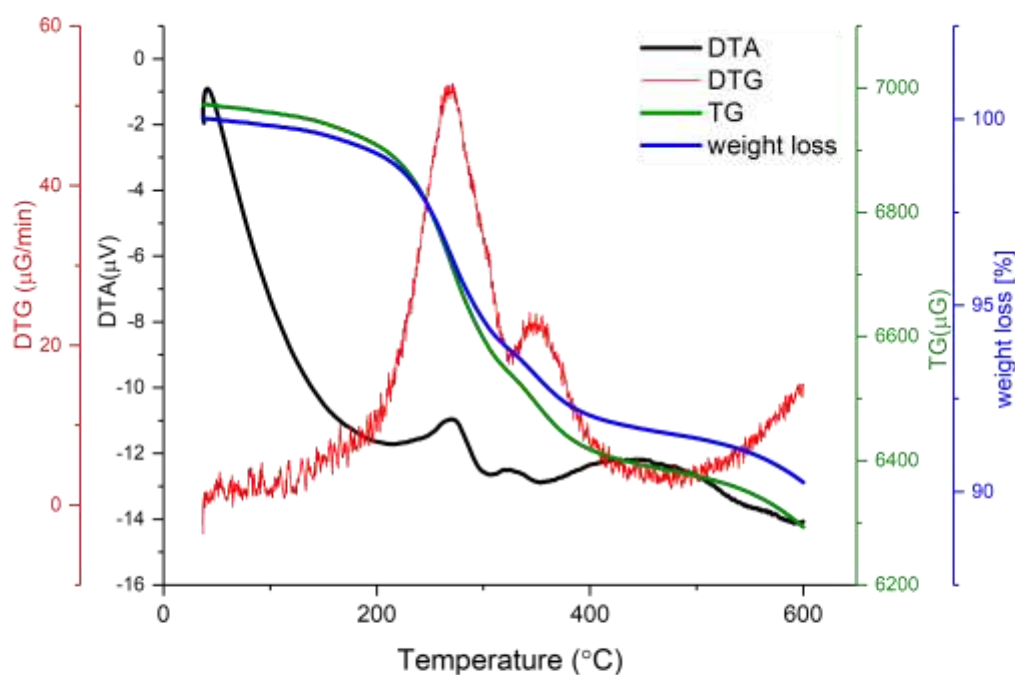
Figure 3-24 TGA curves for TREG coated IONPs obtained by heating 1.4 g Fe(acac)$_3$ at 250 °C before cooling back down to RT for 2 h. Thermogravimetric (TG) curve (green) represents the mass of sample versus temperature. The corresponding weight loss curve (blue) is obtained by dividing the weight of the samples by its initial mass. The differential of the weight loss curve (red) is the first derivative of the weight loss curve. The differential thermal analysis (DTA) of an inert reference Al$_2$O$_3$ is indicated by the black curve and reflects the temperature difference between the sample and reference.

represents the most significant loss, can be attributed to the removal of TREG in the sample (or other polyols such as DEG or TEG) as the boiling point is in that temperature range.[264, 265] This is supported by the peaks of the first derivative curve, also known as inflection points, which indicate the greatest rate of change on the weight loss curve. In this sample, beyond the initial 1.5% weight loss due to elimination of water (T < 200 °C), an 8.5% weight loss of organic material was observed in the range of T = 200 °C to T = 400 °C. A residual mass of approximately 90 wt% of the initial sample remained at the end of the TGA experiment. This allowed to correct the SQUID-VSM measurements by correcting the mass of iron oxide sample with the organic ligand contribution determined by TGA. The corrected hysteresis curves are those presented in Figure 3-23.

XRD does not allow distinction between maghemite (γ-Fe_2O_3) and magnetite (Fe_3O_4) phases (section 2.3.4). Room temperature ^{57}Fe Mossbauer spectra were recorded by Dr Lara Bogart at UCL on samples obtained in the same reaction conditions as in section 3.2.3.4. Briefly, 1.4 g of Fe(acac)$_3$ and 20 ml of TREG were heated up to 250 °C and maintained at that temperature for 8 h before cooling down to RT over 2 h. After cleaning the sample with acetone and centrifugation as described in chapter 2, the sample was freeze-dried and a first Mössbauer spectrum was recorded on the day of the synthesis and over time until 18 d after the synthesis, when the spectrum changed. As seen in Figure 3-25, these spectra exhibited absorption out to ± 8 mm/s, indicative of magnetic hyperfine splitting, due to the dipole interaction between the nuclear spin moment and a magnetic field. However, the spectra were dominated by a very broad central absorption peak, as is typical of disordered and/or fine particle materials.[266] The mean isomer shift of the spectra, relative to alpha-iron, was determined to be in the range delta = 0.38 to 0.42 mm/s. These values lie between those of pure maghemite (delta = 0.32 mm/s) and pure magnetite (delta = 0.53 mm/s), implying that the samples were either non-stoichiometric magnetites, or magnetite/maghemite composites, or some combination of the two.[267] After 18 d, the shape of the spectrum had changed possibly suggesting the formation of clusters, but this

was difficult to confirm as the broadening of the main absorption peak did not allow to determine whether a change in the mean isometric shift had occurred.
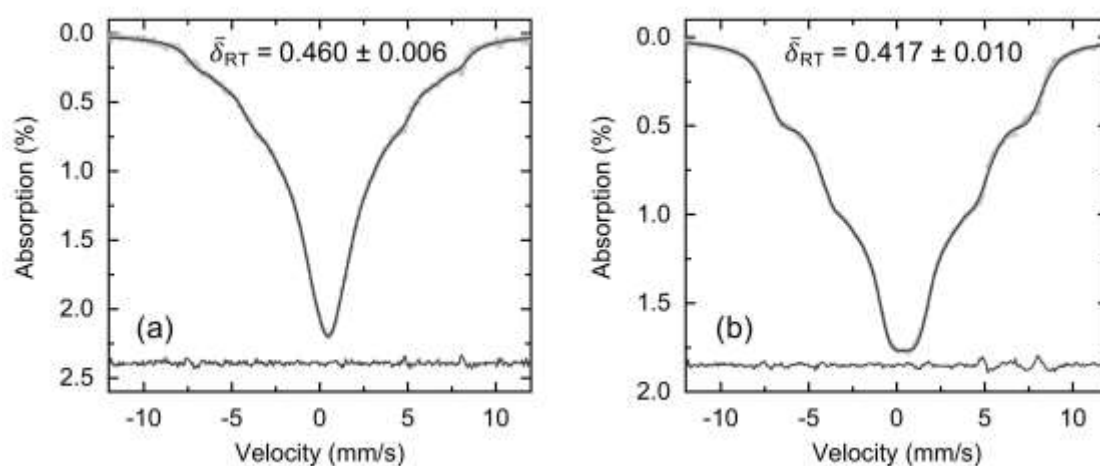
Figure 3-25 Mössbauer spectrum of TREG coated IONPs obtained in high pressure-high temperature conditions recorded (a) on the day of their synthesis (b) 18 d after their synthesis.

Room temperature [57]Fe Mossbauer spectra could also be correlated with the instability demonstrated by DLS of this same sample in Figure 3-26 below. These TREG coated IONPs were well dispersed in water; however the hydrodynamic diameters measured were quite large (> 200 nm) in comparison to the core and crystallite size determined by TEM and XRD respectively. Furthermore, sedimentation was visible in the centrifuge tubes after several days. This observation along with the information obtained by Mössbauer spectroscopy suggested that the polyol coating was unstable, thus leading to the formation of NP clusters or agglomerates in solution. At this stage, it was confirmed visually by precipitation out of solution of these IONPs in water and salt conditions (NaCl 150 mM) in less than 30 min.

$D_H = 149.4 \pm 2.05$ nm
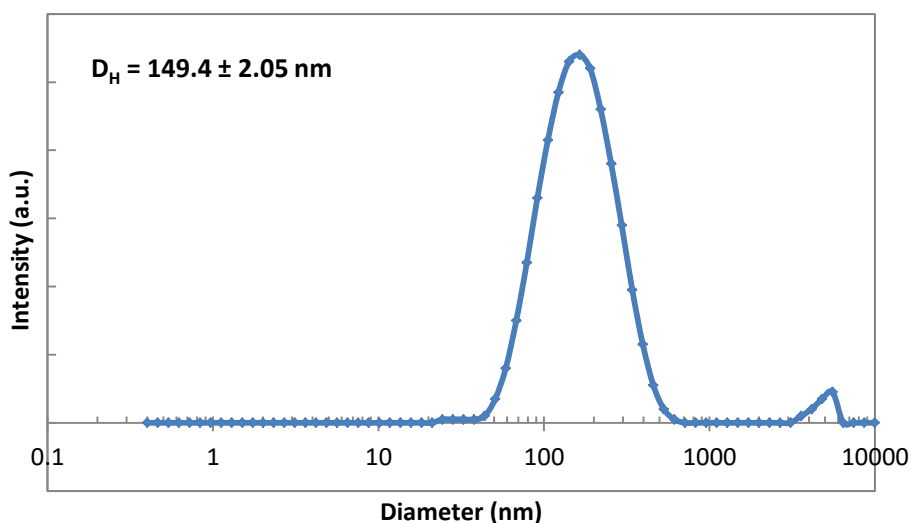
Figure 3-26 Representative DLS measurement in water of TREG coated IONPs synthesised in high pressure high temperature conditions

While the exact binding mechanism of polyols to the surface of IONPs has not been confirmed experimentally, recent literature suggests that the polyol, such as DEG, chelates iron. However, the exact structure of this chelate remains undetermined. Under high pressure high temperature conditions, the stainless steel vessel does not allow for direct observation or analysis of the reaction mixture so no mechanistic insight may be obtained from physical or chemical changes of the solution. The underlying mechanism may involve three consecutive steps as determined by Dey *et al*.: metal complexation reaction between hydrated metal precursor and the polyol which acts as a chelating agent and the solvent, followed by hydrolysis to transition to a metal hydroxide and finally dehydration due to heat treatment forming spinel structured metal ferrites.[268] In recent publications, TREG coated IONPs synthesised by the polyol method in an autoclave or under standard conditions using a Schlenk line were reported to be unstable and aggregate in solution. It is suggested that the polyol coating is labile and is only weakly linked to the IONPs by physisorption, meaning there are no chemical bonds between the polyol coating and the IONP, thus leading to the aggregation of the nanoparticles in solution.[73, 77]

3.2.3.6   In situ functionalisation

Nanoparticles must be stable in aqueous and salt conditions in order to be considered for biomedical applications. After determining that aggregation of TREG coated IONPs takes place, the stability of the polyol coated IONPs obtained in high pressure high temperature conditions must be improved. It has been reported that IONPs may be synthesised in polyols with structural agents such as polyvinylpyrrolidone (PVP) or polyethyleneimine (PEI) to help stabilise the NPs obtained as well as to control their shape and size.[147, 151] *In situ* functionalisation strategies using PEG were therefore investigated. PEG of different molecular weight was added to the polyol synthesis. The reaction conditions were: 20 g of PEG 300, 2000 or 6000 was added to 2 mmol of $Fe(acac)_3$ and heated up to 250 °C for 1 h.

Below are the TEM images obtained with the addition of 20 g of PEG of different molecular weight (Figure 3-27).

From the morphology of the IONPs obtained, only the use of PEG 300 allowed us to obtain spherical IONPs. Using PEG of higher molecular weight (2000 and 6000) led to polydisperse nanoparticles and irregularly shaped IONPs including some cubic and triangular shapes. Uniformity in size and shape was best observed using PEG 300, however the polydispersity still remained elevated as the average core diameter measured by TEM was determined: $d_{TEM} = 11.2 \pm 2.1$ nm ($\delta = 18.9\%$).
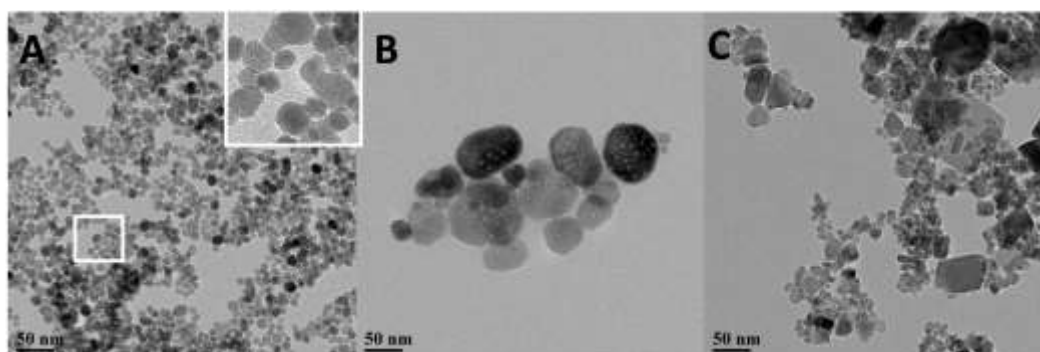
Figure 3-27 TEM images of TREG coated IONPs synthesised in high pressure high temperature conditions with A) PEG 300 B) PEG 2000 and C) PEG 6000. Magnification 25 k scale bar 50 nm.

To determine the effect of the addition of PEG during the synthesis, all three samples were characterised by ATR-FTIR. Figure 3-28 below shows the FTIR spectra IONPs after *in situ* functionalisation with PEG 200 as well as the spectrum of PEG 200. The peak around 3413
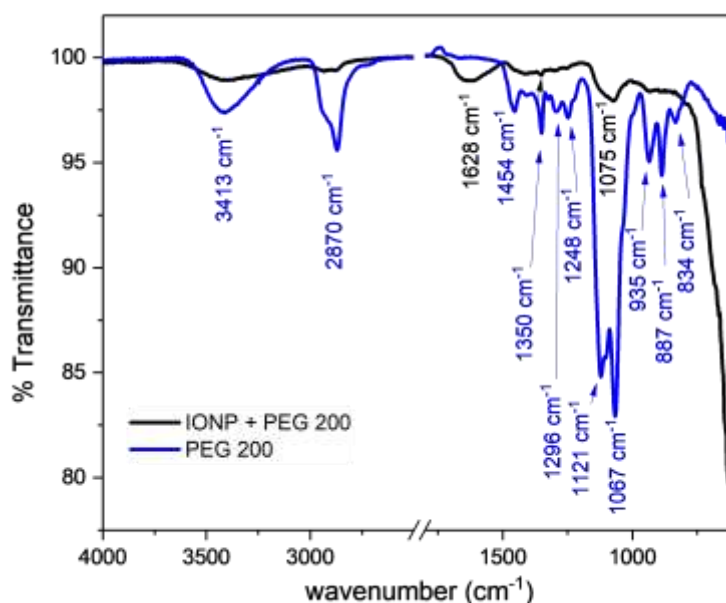
Figure 3-28 ATR-FTIR representative spectra of PEG 200 (blue) and IONPs obtained after *in situ* functionalisation with PEG 200 (black). The 1800 - 2500 cm^{-1} range has been excluded as no significant information was found.

cm^{-1} is attributed to the stretching vibrations of the hydroxyl groups. The peak around 2870 cm^{-1} is attributed to the alkanes of the polymer; the peak at 1454 cm^{-1} is due to C – H scissoring, the bands at 1121 cm^{-1} and 1067 cm^{-1} are due to skeletal vibrations of CH_2 – O – CH_2 bonds, the band at 1350 cm^{-1} is due to C-H bending vibrations; the band at 1248 cm^{-1} can be attributed to C-H twisting vibrations and the peak at 935 cm^{-1} is due to C-O stretching vibrations. New bands are visible in the spectrum of IONPs after the reaction with PEG 200. These include the bands around 3413, 2882, 1352 and 1075 cm^{-1}, however a shift in wavenumber in comparison to the spectrum of PEG suggests hydrogen-bonding and the interaction with the surface of the IONPs.[225]

Figure 3-29 shows the FTIR spectra of PEG 2000 and IONPs after *in situ* functionalisation with PEG 2000. Similarly to PEG 200, characteristic peaks of the polymer can be identified on the spectrum of PEG 2000. The peak around 2886 cm^{-1} is attributed to the symmetric stretching of CH_2 groups in PEG; the peak at 1467 cm^{-1} is due to C – H scissoring, the bands at 962, 1101 cm^{-1} and 1061 cm^{-1} are due to the C-O-C stretching vibrations, the band at 1342 cm^{-1} is due to C-H bending vibrations; and the band at 1241 cm^{-1} can be attributed to C-H twisting vibrations.[222-224] After the reaction with PEG 2000, the broad peak observed around 3385 cm^{-1} due to O-H stretching vibrations confirms the presence of the polymer as it is due to O-H groups present in PEG 2000. Other characteristic peaks are observed in the spectrum of these IONPs. These include the bands around 2933, 1542, and 1412 cm^{-1}, however a shift in wavenumber in comparison to the spectrum of PEG suggests hydrogen-bonding and the interaction with the surface of the IONPs.[225]

For simplification purposes, the FTIR spectrum of IONPs obtained after functionalisation with PEG 6000 has been included in Figure 3-29 as the wavenumber of peaks in FTIR spectra of PEG with various Mw does not change, only the intensity of the peaks can vary with the local organisation of certain structure-sensitive bands.[269-271] As with PEG 200 and PEG 2000, after the reaction with PEG 6000, characteristic peaks of the polymer are observed in the spectrum of these IONPs. These are identical to those identified with PEG 200 and 2000,
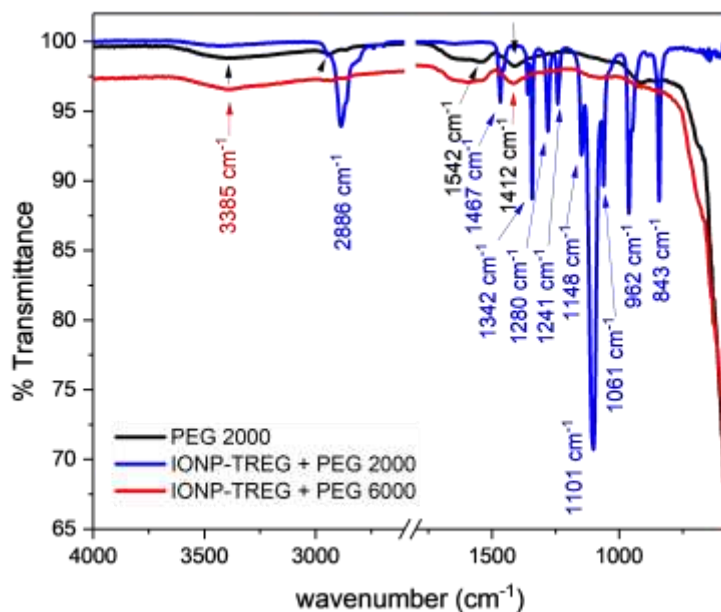
Figure 3-29 ATR-FTIR representative spectra PEG 2000 (blue) and IONPs obtained after *in situ* functionalisation with PEG 2000 (black) or PEG 6000 (red). The 1800 - 2600 cm^{-1} range has been excluded as no significant information was found.

also with a shift in wavenumber in comparison to the spectrum of the polymer, suggesting hydrogen-bonding and the interaction with the surface of the IONPs.[225]

3.3 DISCUSSION AND CONCLUSIONS

Results in this chapter have shown that both the experimental conditions and the reaction parameters have an impact on the IONPs obtained by the polyol method.

In the initial experiments, the reaction was carried out using a Schlenk line according to several literature references. A two-step reaction did not allow for a separation of the growth and nucleation phases, hence very polydisperse samples were obtained (δ_{TEM} = 15 to 20% *ca.*). A one-step reaction allowed for better control of the morphology of polyol coated IONPs, but these were still not monodisperse (δ_{TEM} > 10%). One possible explanation for the

lack of monodispersity is the creation of thermal gradients in solution due to convective transfer of thermal energy from the heating mantle to the reactants in solution.

In order to improve the heating uniformity, the use of a microwave (MW) reactor was investigated. This works by direct coupling and absorption of the MWs by the reactants in solution, also known as volumetric heating, which will lead to the temperature being raised in a uniform manner throughout the whole liquid volume.[272] This increases the speed and efficiency of chemical reactions by dipolar polarisation and ionic conduction.[229]

When determining the effect of the amount of precursor on the IONPs obtained, an overall increase in the size of the NPs was obtained with larger concentrations of $Fe(acac)_3$ used. The experiments on the effect of temperature on the synthesis of IONPs, suggested that MWs can provide sufficient energy to superheat the solvent. Furthermore, solvents or solutes with high $\tan \delta$ values may preferentially absorb MWs in comparison to other reactants with lower $\tan \delta$ values. This can lead to the formation of local new nucleation points and an increase in the local temperature. In terms of nanoparticle synthesis, this can modify the surface morphology or reactivity of the NPs obtained.[230] This should be avoided by ensuring a more homogenous initial reaction mixture. Finally, the effect of the polyol solvent on the IONPs obtained was studied. Results revealed that when using a polyol with a larger molecular weight, larger IONPs were obtained. One possible reason for this is that the difference in viscosity of the solvent will impact the diffusion of species in solution which in turn will have an effect on the nucleation and growth of nanoparticle seeds in solution. For example, with DEG, the smallest polyol studied, the less viscous solution would allow for a more rapid diffusion of species in solution, so more nucleation events would take place, thus leading to the formation of smaller IONPs.

While the microwave reactor is an ideal system through its simplicity and reduced reaction times, results obtained were not reproducible with batch to batch variations being observed. Indeed, it is plausible that the microwave power was not regular and sufficient to

achieve the boiling point of some of the polyol solvents used. In the case of polyol reactions using iron, the reaction temperature is critical and should reach the boiling point of the polyol, in order to allow oxidation to its diacetyl form, leading to the reduction of the metal. In the future, it could be worthwhile carrying out this reaction with a higher MW power (above 300 W), as well as using a more sensitive fibre optics temperature probe to avoid local irregular MW radiation leading to local "new nucleation points".

Mixing problems, supersaturation and the formation of local heating spots can be minimised by starting the synthesis with an already homogenous mixed solution of precursors, allowing for the MW to be a viable method for rapid and efficient reactions. Careful attention is needed when measuring the temperature using an infrared sensor as this gives a reading of the external glass vial temperature. One of the limitations to carry out the synthesis of nanomaterials with the use of a MW remains the limited temperature and pressure range (10 ml, 20 – 25 bar) of most instruments in research laboratories which could limit scaling up and nature of the reactions carried out.

Polyol coated IONPs were successfully obtained in a reproducible and reliable manner in high pressure and high temperature conditions of an oven. The influence of different synthetic parameters such as the polyol solvent used, the reaction time and the amount of iron precursor $Fe(acac)_3$ were studied.

As in the case of the MW reactor, the type of polyol solvent used was critical to the size of the IONPs obtained. The shape of the NPs obtained remained spherical with all three polyols studied, however it was observed that the larger the size of the polyol used the larger the NPs were. From the results obtained, TREG coated IONPs were deemed the most suitable as these were characterised by superparamagnetic behaviour with a core diameter measured by TEM *ca*. 8 to 10 nm. On the other hand, IONPs obtained with DEG were too small and hence had smaller saturation magnetisation values, while using TEG led to larger and polydisperse IONPs (δ_{TEM} = 24.5%) above the superparamagnetic critic domain size which

could explain the remanence and coercive field of these IONPs determined at 300 K by SQUID-VSM.

On the other hand, it was difficult to conclude on the effect of the amount of precursor. As in the case of the MW synthesis, an increase in the size of the NPs obtained was observed when increasing the amount of Fe(acac)$_3$ from 100 mM to 500 mM, but no direct proportional effect between these two parameters could be established.

Also, a direct correlation between the size of IONPs and the reaction time was determined. As it can be seen in Figure 3-30 below, this was also linked to an increase in the crystallite size obtained by XRD and the saturation magnetisation measured at 300 K. An odd value for the crystallite size determined by XRD for the 12 h reaction was obtained. It was not taken into consideration as the M$_s$, core size and crystallite size led to believe that this was an experimental error and did not fit the data trend.
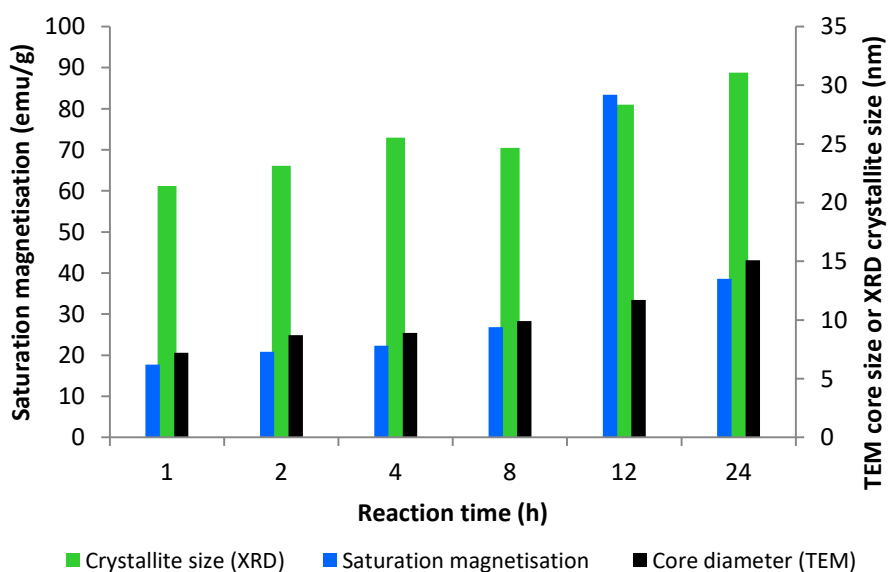
Figure 3-30 Evolution of the average core diameter determined by TEM (black), the crystallite size determined by XRD (green) and the saturation magnetisation measured at 300 K (blue) as a function of the reaction time with TREG in high pressure-high temperature conditions.

In addition, while the synthesis of IONPs with the classic polyol method using the Schlenk line has already been reported in literature,[75] in comparison, the IONPs obtained during our project in high pressure and high temperature conditions can be obtained in a reliable and reproducible manner in order to finely tune their magnetic properties.

IONPs in the range of 5 – 10 nm suitable for biological applications, as monodisperse as possible, with interesting magnetic properties and in a reproducible manner were obtained with TREG in high pressure high temperature conditions. The optimisation of the reaction in these conditions, the ability to finely control the morphology of the NPs obtained and the reproducible results may allow for potential scale up and GMP manufacturing of these types of NPs for biomedical applications. Unfortunately, the TREG coated IONPs obtained in high pressure high temperature conditions were found to be unstable, as their precipitation out of aqueous solution was observed rapidly after their purification and dispersion in dH_2O. These IONPs were further characterised by DLS and Mössbauer spectroscopy. Both these methods confirmed the colloidal aggregation of IONPs. Future studies will include thermogravimetric analysis in order to determine the loss of the polyol coating over different time points. A recent study by Miguel Sancho *et al.* has speculated that the polyol coating is only weakly linked to the IONPs by physisorption and may therefore be insufficient to stabilise IONPs long term in solution. In the next chapter, different surface functionalisation strategies are investigated to overcome this limitation.

Chapter 4 FUNCTIONALISATION OF IRON OXIDE NANOPARTICLES

4.1   BACKGROUND AND OBJECTIVES

The stabilisation of IONPs is essential for their biomedical applications as they possess an isoelectric point close to physiological pH of 7.4 meaning that they will aggregate at this pH.[218] Furthermore, nanoparticle-cell interactions will rely heavily on their ability to be stable in a variety of pH environments such as the endosome or lysosome (pH 4-5)[216] or a tumour (pH 7 approximately).[213] It is therefore essential to ensure their stability across a range of pH conditions.

Polyethylene glycol is commonly used to render IONPs stealth for biomedical applications as it provides steric hindrance and reduces protein adsorption.[94] PEG may also provide free functional groups which can be used for further functionalisation with biomolecules such as peptides or antibodies.[95, 96] Coating the NPs with an inert silica shell is also another way of minimising interactions with biological environments while also adding functional groups on the surface for functionalisation with biomolecules.

It has been shown that carboxylic ligands are able to bind covalently to IONPs and act as surface ligands. This strategy was investigated with the goal of displacing the polyol TREG coating of IONPs synthesised in high pressure high temperature conditions, and replacing it with different ligands in order to confer better stability to these IONPs. These will include carboxylic acid ligands, polymers, silica coating or phosphonic acid ligands.

The functional groups with the most affinity towards the iron oxide NPs include: carboxylic acids, phosphonate or catechol-based ligands.[45-47, 91] Adsorption of carboxylic acids at the surface of metal oxide NPs occurs through coordination of the carboxylate group to the metal atoms at the surface of the NP. The carboxylate will act as a ligand for vacant coordination sites of surface Fe^{3+} ions.[273] Deacon and Philips studied the carboxylate-metal

coordination modes,[274] and these can be categorised as either monodentate or bidentate. In the case of a bidentate coordination, chelating or bridging modes can be observed.

To choose different surface ligands, the fact that these IONPs are developed for potential biomedical applications, such as cell tracking by MRI for example, was taken into consideration. This means several requirements need to be met by the IONPs:

- Water-soluble ligands only were chosen to avoid any phase transfer step
- Ideally, their size was limited so as to not increase significantly the hydrodynamic diameter
- They contained at least two functional groups: one which would interact with IONPs and the other to provide surface functional groups for further potential biofunctionalisation.

Within this chapter, different ligands were tested which all had the above characteristics as potential stabilisers for the TREG coated IONPs, and their impact on the properties of the IONPs was studied. The aims of the work carried out in this chapter were:

 - To determine an efficient method of ligand exchange to replace the TREG coating

 - To obtain a stable suspension of IONPs in aqueous solution in the short term and long term

 - To ensure these stable and functionalised nanoparticles have good relaxivity properties which allow them to be considered as potential MRI contrast agents

 - To determine if, and how the ligand exchange method can influence these relaxivity properties.

4.2   RESULTS AND DISCUSSION

4.2.1   *Ligand exchange with IONP powder and magnetic separation*

In our initial attempts, was used the standard ligand exchange (section 2.2.4) with a variety of ligands: meso-2,3-dimercaptosuccinic acid (DMSA), tartaric acid, trisodium citrate, citric acid, L-cysteine, folic acid, 2-mercaptopropionic acid (2-MPA). These ligands have extensively been reported in literature as surface ligands of IONPs with which they have a strong affinity, and they fulfil our requirements listed above (section 4.1).

4.2.1.1   Meso-2,3-dimercaptosuccinic acid (DMSA)

DMSA has been recently reported as a ligand to successfully displace the polyol surfactant in order to stabilise IONPs.[77] Furthermore, it has been a surface ligand of choice for IONPs as it has strong affinity with these NPs and provides functional groups for further surface functionalisation.[91] ATR-FTIR was used to obtain information regarding changes in the functional groups before and after the ligand exchange process. In this sample, the peak at 1064 cm^{-1} corresponding to the C-O stretching absorption of the primary alcohol group in CH$_2$-OH is present for IONPs before and after ligand exchange with DMSA. This is also the case of the broad band centred at about 3400 cm^{-1} due to the O–H stretching vibrations attributed to water and TREG molecules adsorbed to the IONP surface.[65] The carboxylic group of DMSA is identified through different peaks: at 1394 cm^{-1} due to the C-O stretch, and at 1710 cm^{-1} due to the stretching vibration of the C=O bond. These are present in the sample after ligand exchange but not with polyol coated IONPs. These indicate the presence of COOH groups due to DMSA.

However, there is no confirmation that DMSA had been linked to the surface of IONPs as there is no shift in the peaks of the COOH which would occur after chemisorption to IONPs. The peak due to C=O vibration (asymmetric stretching) of the carboxylic group at 1696 cm^{-1} in the spectrum of the free ligand (blue curve) is still present in the spectrum of the IONPS
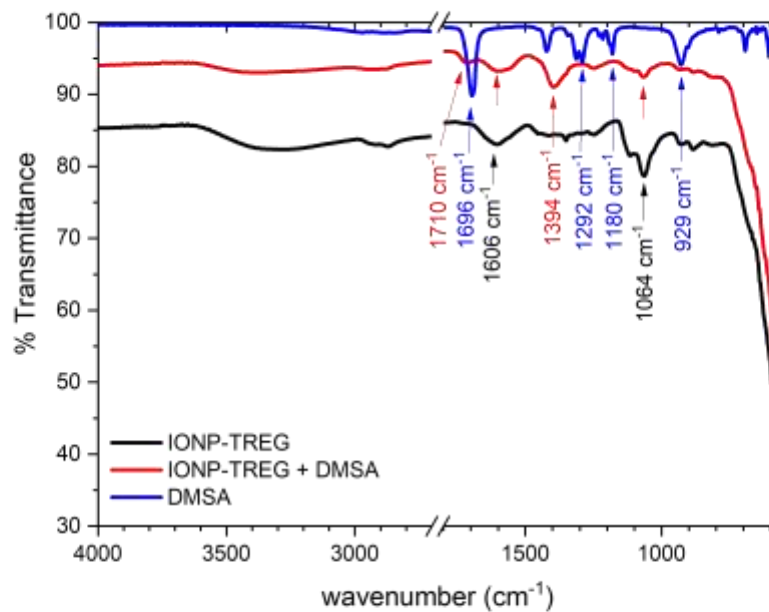
Figure 4-1 ATR-FTIR representative spectra of DMSA (blue), TREG coated IONPs before (black) and after (red) ligand exchange with DMSA. The 1800 - 2700 cm^{-1} range has been excluded as no significant information was found.

after ligand exchange at 1710 cm^{-1}, suggesting the presence of unbound COOH groups in the sample. Furthermore, the sample was not stable and its precipitation was observed rapidly.

4.2.1.2   2-mercaptopropionic acid (2-MPA) and 3-mercaptopropionic acid (3-MPA)

This method of ligand exchange was also investigated with 2-mercaptopropionic acid (2-MPA) and 3-mercaptopropionic acid (3-MPA). There ligands were chosen as it has been confirmed in the literature that a covalent bond can be established between the thiol group and the iron metal of IONPs.[217, 228]

In the spectrum of TREG coated IONPs, the following characteristic peaks can be observed: a broad peak at 3371 cm^{-1} due to O-H stretching vibrations in the alcohol groups that are intra molecularly bonded (polyols), as well as a sharper peak at 1230 cm^{-1} due to C-O stretching vibrations in the same hydroxyl groups. When using 2-MPA as a ligand, distinctive peaks within the spectrum of the functionalised IONPs were noted (blue curve in Figure 4-2):
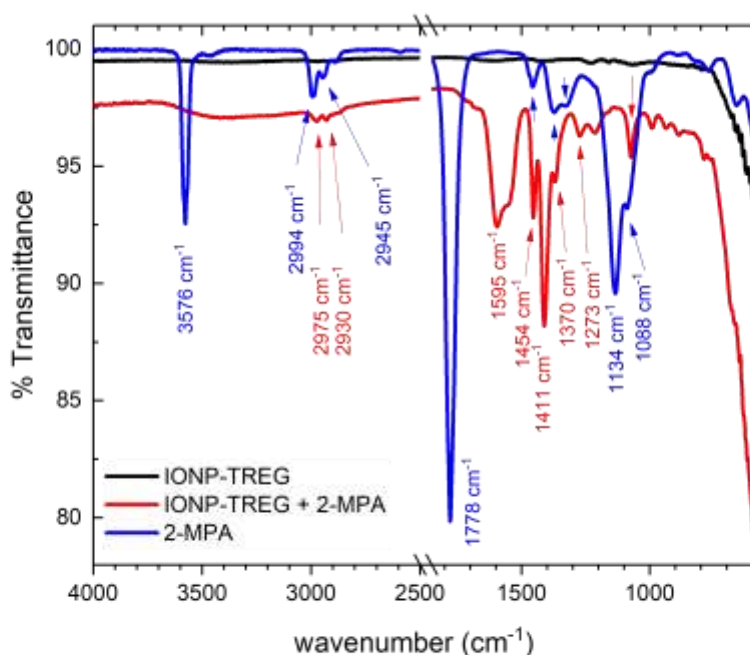
Figure 4-2 ATR-FTIR representative spectra of 2-MPA (blue), TREG coated IONPs before (black) and after (red) ligand exchange with 2-MPA. The 1850 - 2500 cm^{-1} range has been excluded as no significant information was found. The FTIR spectrum of 2-MPA was obtained from the infrared spectrum database of the National Institute of Standards and Technology.[1]

- Sharp peaks at 2930 and 2975 cm^{-1}: C-H stretching vibrations in the –CH$_3$ methyl group
- 1411 cm^{-1}: bending vibrations due to CH$_3$ deformation
- The weak broad band at 2592 cm^{-1} attributed to the vibrations of the S-H group.
- The strong peaks at 1595 cm^{-1} and 1454 cm^{-1} attributed to a shift in the peak of C=O vibration (asymmetric stretching) of the carboxylic group from 1778 cm^{-1} in the spectrum of the free ligand (blue curve). This could potentially indicate the binding of a 2-MPA to the IONPs by chemisorption of the COOH groups. Indeed, carboxylate groups can form complexes with Fe atoms on the surface, rendering partial single bond character to the C=O bond, resulting in a weaker bond, which in turn leads to a shift in the stretching frequency to a lower wavenumber value.[48, 202, 275]

As illustrated by the FTIR spectrum in Figure 4-3, when using 3-MPA, in the TREG coated IONPs spectrum, the same characteristic peaks can be observed: a broad peak at 3371 cm^{-1} due to O-H stretching vibrations in the alcohol groups that are intra molecularly bonded (polyols), as well as a sharper peak at 1242 cm^{-1} due to C-O stretching vibrations in the same hydroxyl groups. When using 3-MPA as a ligand the following distinctive peaks were noted:

- 1698 cm^{-1}: C=O stretching vibrations of COOH groups. This strong peak can be due to a shift in the peak of C=O vibration (asymmetric stretching) of the COOH group from 1782 cm^{-1} in the spectrum of the free ligand (black curve). As with 2-MPA, this could indicate the binding of a 3-MPA to the surface of the IONPs by chemisorption of COOH.
- Two peaks at 1536 cm^{-1} and 1436 cm^{-1} which can be attributed to C=O vibration (asymmetric and stretching respectively) of the COOH group from 3-MPA immobilised on the IONP surface.[276] The wavenumber separation (Δv_0) between the asymmetric and symmetric IR peaks can be used to identify the type of interaction between the carboxylate group and the metal atom.[274] In this case, $\Delta v_0 = 100$ cm^{-1}, which indicates a bidentate mode in which two oxygen atoms of COO$^-$ are coordinated to the iron atom.[277]
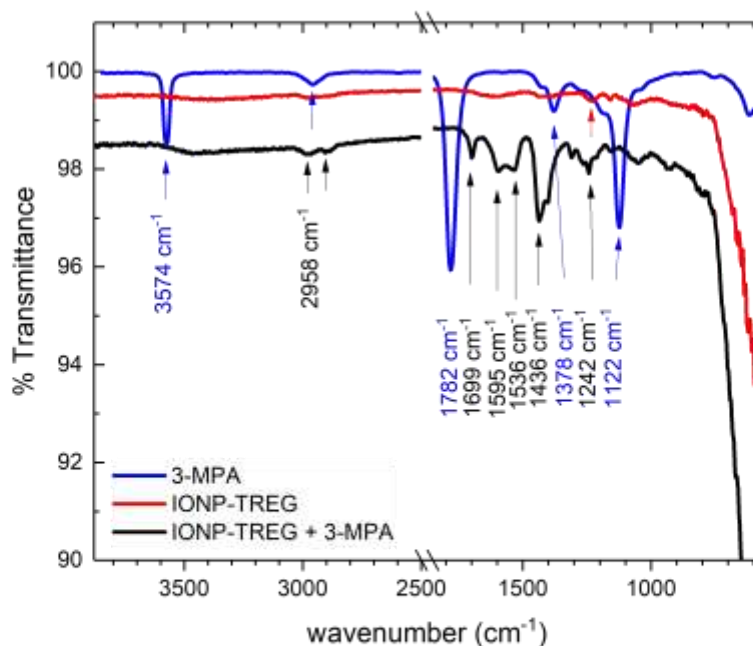
Figure 4-3 ATR-FTIR representative spectra of 3-MPA (blue), TREG coated IONPs before (black) and after (red) ligand exchange with 3-MPA. The 1850 - 2500 cm^{-1} range has been excluded as no significant information was found. The FTIR spectrum of 3-MPA was obtained from the infrared spectrum database of the National Institute of Standards and Technology.[1]

- 1402 cm^{-1}: alkene bending vibrations due to CH_2 deformation.

- 1378 cm^{-1}: C-H bending of the CH_2 group.

- No weak broad band at 2550 - 2600 cm^{-1} attributed to the vibrations of the S-H group is observed.

- Figure 4-3 demonstrates that 3-MPA is present and can be linked to the surface of the IONPs by the carboxylate group and/or the thiol group.

The magnetic properties of the IONPs functionalised with 2-MPA and 3-MPA were measured at 300 K. As observed in Figure 4-4, these samples were characterised by a value of saturation magnetisation of Ms = 73.5 emu/g for the TREG coated IONPs, Ms = 45.3 emu/g for the 2-MPA coated IONPs and Ms = 66.4 emu/g for the 3-MPA coated IONPs. These values of M_s are smaller than those of bulk maghemite and magnetite (respectively 78 emu/g and 92 emu/g at 300 K),[36, 81] For all samples, H_c and M_r were close to zero with values
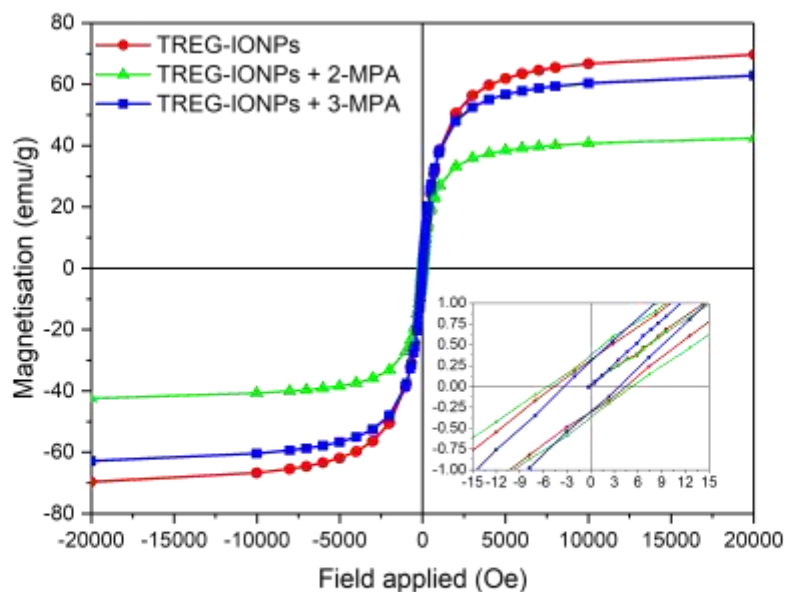
Figure 4-4 Magnetisation curves of TREG coated IONPs before (●) and after the ligand exchange reaction with 2-MPA (▲) and 3-MPA (■) using Method 1. The hysteresis curves were measured at 300 K, and the inset shows a zoom into the low magnetic field region.

of 5 Oe and 0.3 emu/g respectively, which indicates quasi superparamagnetic behaviour. The decrease in magnetisation can be attributed to the removal of surface cations, which takes place during ligand exchange, particle dissolution, oxidation of the particles, higher surface magnetic disorder or an excess of organic ligand which contributes to the larger overall NP mass.[78,278]

This, along with the precipitation of these nanoparticles after several days, suggests that the removal of the excess ligand by magnetic separation is not sufficient and should be improved.

4.2.1.3   Other ligands tested

Citric acid has been used extensively as a surface ligand of IONPs in various biomedical applications. Indeed, the carboxylic groups present are advantageous as they provide electrostatic stability and surface functional groups for further biofunctionalisation. As explained previously, the carboxylate groups can form complexes with Fe atoms on the

Figure 4-5 ATR-FTIR representative spectra of citric acid (blue), TREG coated IONPs before (black) and after (red) ligand exchange with citric acid. The 1800 - 2500 cm^{-1} range has been excluded as no significant information was found.

surface thereby binding to the surface of IONPs by chemisorption. It has also been shown to enhance the uptake of IONPs by MSCs,[7] and this was also confirmed by some preliminary data studying the uptake of IONPs made by a colleague, Dr. Blanco-Andujar, with bone marrow derived hMSCs (data not shown here). This enhanced uptake may be due to an altered endocytotic mechanism because of the high negative surface charge this ligand provides. The high surface charge allows for electrostatic interactions with phospholipids of the cellular membrane, and the increased cell-nanoparticle interactions lead to enhanced cellular uptake.[79, 85]

Citric acid was tested as a ligand, but as it can be seen in Figure 4-5, no difference in the FTIR spectrum was observed between before and after the ligand exchange process. In particular, no shift in the symmetric and antisymmetric stretching frequencies of the COOH group (peaks at 1740 and 1388 cm^{-1} respectively) were observed which would be the case had the ligand been linked to the IONPs.

As shown in Figure 4-6, this was also the same result obtained when L-tartaric acid (TA) was used: no difference in the FTIR spectrum was observed in the samples obtained before and after the ligand exchange reaction. These samples were therefore not additionally characterised. Due to the observed precipitation of samples obtained with DMSA, 2-MPA and 3-MPA as well as the decrease in the saturation magnetisation demonstrated in Figure 4-4, this method was proven to be inefficient in the stabilisation and functionalisation of the polyol coated IONPs. In order to improve the method, it was hypothesised that the excess of organic ligand which could contribute to the decrease in saturation magnetisation with 2-MPA and 3-MPA functionalised IONPs, could be eliminated by an additional purification step: dialysis.

4.2.2 Ligand exchange with IONP powder and dialysis

In an attempt to obtain a stable dispersion of functionalised nanoparticles, the ligand

Figure 4-6 ATR-FTIR representative spectra of tartaric acid (blue), TREG coated IONPs before (black) and after (red) ligand exchange with tartaric acid. The 1800 - 2500 cm^{-1} range has been excluded as no significant information was found.

exchange and magnetic separation were followed by additional purification step of dialysis. A variety of ligands were tested using this second method, including tartaric acid, COOH-PEG-SH, L-cysteine, or folic acid for example. However, the samples obtained were not characterised additionally as the FTIR spectra did not vary before or after the ligand exchange process: no significant peaks belonging to the ligand in question could be observed, the spectra remained identical to those of TREG coated IONPs. In the next section are presented the results obtained with ligands which could potentially allow efficient stabilisation and functionalisation of the polyol coated IONPs.

4.2.2.1   DMSA

In Figure 4-7, the peak at 1063 cm^{-1} corresponding to the C-O stretching absorption of the primary alcohol group of polyols is present for IONPs before and after ligand exchange with DMSA. This is also the case of the broad band centred at about 3300 cm^{-1} due to the O–H stretching vibrations attributed to water and TREG molecules adsorbed to the IONP

Figure 4-7 ATR-FTIR representative spectra of DMSA (blue) and TREG coated IONPs before (black) and after (red) ligand exchange with DMSA. The inset shows a zoom into the range 700 - 575 cm^{-1}.

surface.[65] The COOH group of the ligand DMSA is identified through different peaks: at 1292 cm^{-1} due to the C-O stretch, and at 1696 cm^{-1} due to the stretching vibration of the C=O bond. However, these peaks are not observed after ligand exchange, proving that DMSA has not been linked to the surface of IONPs.

When using DMSA during the ligand exchange, flocculation of the solution was observed and the magnetic properties were significantly altered in comparison to the TREG coated IONPs. The hysteresis curves measured at 300 K are found in Figure 4-8 and allow for comparison of the polyol coated IONPs (blue curve) with those obtained after ligand exchange with DMSA without dialysis (green curve) and with an additional dialysis step (red curve). Quasi superparamagnetic behaviour can be attributed to all samples, as they present coercive field and remanence values close to zero: 5 Oe and 0.3 emu/g for IONP-TREG, and 10 Oe and 0.5 emu/g for IONP-DMSA. TREG coated IONPs presented a saturation magnetisation of 73.5 emu/g. Once the ligand exchange reaction with DMSA took place, this value decreased to 45.1 emu/g for samples purified solely by magnetic separation and 51.3 emu/g for IONPs purified with an additional dialysis step. These values of saturation magnetisation are noticeably different from the bulk value of maghemite or magnetite (78 emu/g and 91 emu/g respectively at 300 K).[36, 81] The decrease in saturation magnetisation could be due to the removal of surface cations which can occur during ligand exchange, particle dissolution, oxidation of the particles, higher surface magnetic disorder or an excess of organic ligand which contributes to the larger overall NP mass.[78,278] However, the increase in M_s obtained after the dialysis step suggests that this method of purification does help eliminate any additional unbound ligands which contribute to the overall NP mass.

Figure 4-8 Magnetisation curves of TREG coated IONPs before (▲) and after the ligand exchange reaction with DMSA. The IONPs with DMSA have been purified by magnetic separation solely (●) or magnetic separation and dialysis against distilled water for 24 h (■). The curves were measured at 300 K, and the inset shows a zoom into the low magnetic field region.

In Figure 4-7, IONPs before and after reaction with DMSA are characterised by Fe-O bands at 579 and 585 cm^{-1}. Since the Fe-O peak of magnetite is found around 570 cm^{-1}, and maghemite will have several peaks between 400 to 800 cm^{-1}, this leads to the conclusion that the decrease in magnetisation cannot be due to the oxidation of the IONPs but rather to higher surface magnetic disorder or an excess of DMSA which contributes to the larger overall NP mass.

4.2.2.2   2-mercaptosuccinic acid (2-MPA)

As seen in Figure 4-9, the FTIR spectrum obtained was identical to the one observed with the first method (Figure 4-2), which seems to indicate the conjugation of 2-MPA to the IONPs through the carboxylate group or the thiol group.
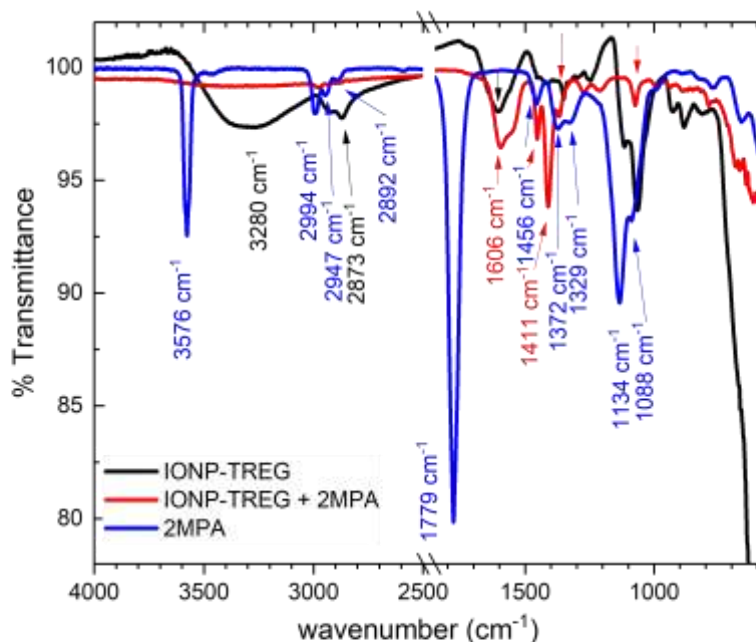
Figure 4-9 ATR-FTIR representative spectra of 2-MPA (blue), TREG coated IONPs before (black) and after (red) ligand exchange with 2-MPA. The 1850 - 2500 cm^{-1} range has been excluded as no significant information was found. The FTIR spectrum of 2-MPA was obtained from the infrared spectrum database of the National Institute of Standards and Technology.[1]

In the TREG coated IONPs spectrum, the characteristic peaks can be observed: a broad peak at 3280 cm^{-1} due to O-H stretching vibrations in the alcohol groups that are intra molecularly bonded (polyols). Characteristic peaks within the spectrum of the functionalised nanoparticles were noted (blue curve in Figure 4-9):

- Sharp peaks at 2936 and 2975 cm^{-1}: C-H stretching vibrations in the –CH$_3$ group
- 1411 cm^{-1}: bending vibrations due to CH$_3$ deformation
- The strong peaks at 1606 cm^{-1} and 1456 cm^{-1} can be attributed to a shift in the peak of C=O vibration (asymmetric and symmetric stretching) of the carboxylic group from 1779 cm^{-1} in the spectrum of the free ligand (blue curve). This could potentially indicate the binding of a 2-MPA to the IONPs by chemisorption of the COOH groups.

On the other hand, as can be seen in Figure 4-11, the magnetic properties of the IONPs obtained were significantly different. The saturation magnetisation measured at 300 K after the ligand exchange reaction with 2-MPA was 23.3 emu/g, which could be caused by oxidation of the IONPs, the removal of cations during the ligand exchange or by an excess of 2-MPA contributing to the overall NP mass. Additional characterisation by TGA shown in Figure 4-10 below provides the percentage of organic ligand present in the sample. This Figure also shows that 2-MPA is eliminated at temperatures ranging between 100 and
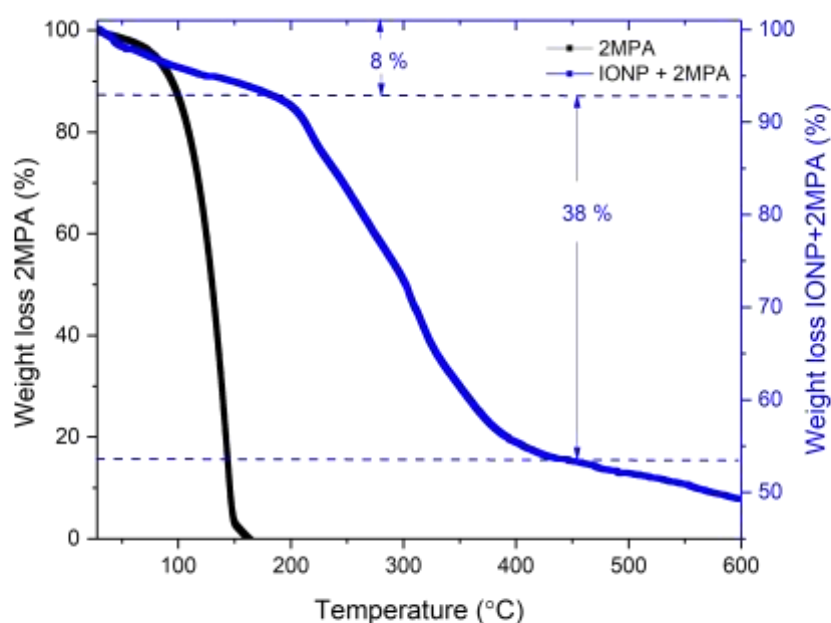
Figure 4-10 Thermogravimetric analysis of 2-MPA (black) and IONPs after ligand exchange with 2-MPA and purification by magnetic separation followed by dialysis (blue).

170 °C which are consistent with its boiling point of 120 °C. The sample had an initial 8% weight loss due to elimination of water, solvent evaporation and 2-MPA (T < 200 °C). This was followed by a 38% weight loss of organic material in the range of T = 200 °C to T = 400 °C which is due to the elimination TREG linked by chemisorption to the IONPs.[259-261] This TGA analysis validates our previous hypothesis that the decrease in the saturation magnetisation of the IONPs after ligand exchange is, at least partially, due to a significant contribution by the organic layer coating the NPs.
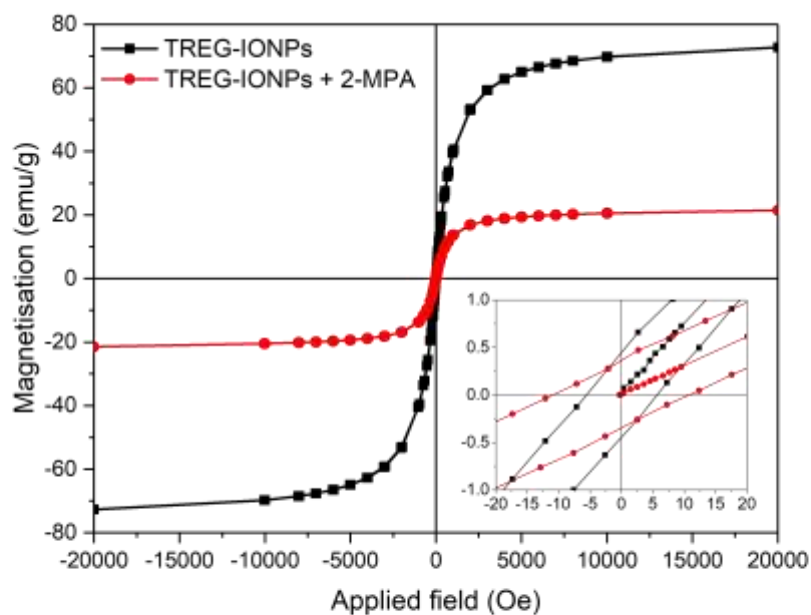
Figure 4-11 Magnetisation curves of TREG coated IONPs before (■) and after (●) the ligand exchange reaction with 2-MPA. The IONPs with 2-MPA have been purified by magnetic separation and dialysis against distilled water for 24 h. The curves were measured at 300 K, and the inset shows a zoom into the low magnetic field region.

4.2.2.3   L-cysteine

L-cysteine was chosen as a ligand for the stabilisation of TREG-coated IONPs as it fulfils all the criteria listed in section 4.1, and is a naturally occurring essential amino acid, which could contribute to better biocompatibility of the obtained IONPs. The FTIR spectra of IONPs after ligand exchange with L-cysteine followed by magnetic separation with or without additional dialysis are found in Figure 4-12. After the additional purification step by dialysis, only the intensity of the peaks has changed in comparison to the sample cleaned by magnetic separation only.

The alkanes of L-Cysteine were identified through the following peaks: stretching vibrations with 2 strong peaks centred at 2980 cm^{-1}, CH$_2$ rocking (bending vibrations) at 724 cm^{-1}, and CH$_2$ deformation (bending vibrations) at 1348 cm^{-1}. The primary amine group of L-Cysteine was identified by: C-N stretching vibrations at 1065 cm^{-1}, primary amine NH$_2$ scissoring
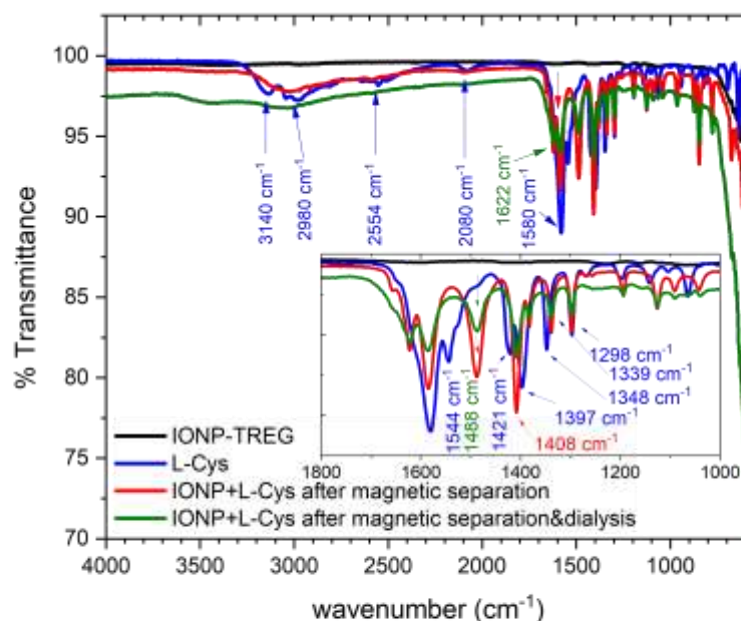
Figure 4-12 ATR-FTIR representative spectra of L-Cysteine (blue) and TREG coated IONPs before (black) and after ligand exchange with L-Cysteine. IONPs were purified by magnetic separation only (red) or by magnetic separation followed by dialysis against distilled water for 24 h (green).The inset shows a zoom into the range 1800 - 1000 cm^{-1}.

(bending vibrations) at 1580 cm^{-1}, and NH and NH$_2$ wagging (shifts on H-bonding) at 847 and 777 cm^{-1}.

The carboxylic acid group of L-cysteine was identified with: broad O-H stretching vibrations at 3140 and 2554 cm^{-1}, C-O stretching vibrations at 1256, 1268 and 1298 cm^{-1}, and C-O-H bending vibrations at 1397 cm^{-1}.

Also, a weak broad band centred at 2554 cm^{-1} and attributed to the vibrations of the S-H group is observed for all samples. Collectively, this data suggests that there is no difference between the spectrum of L-Cysteine and the IONPs after the ligand exchange process, proving that this ligand has not bound to the IONPs through any of its functional groups. More importantly, rapid precipitation of the IONPs in solution a few hours after the dialysis step was observed, demonstrating the lack of stability of these samples.

4.2.2.4   Folic acid

The presence of the ligand, folic acid is confirmed by FTIR through its different functional groups (Figure 4-13). In the TREG coated IONPs spectrum, the following characteristic peaks are observed: a broad peak at 3262 cm^{-1} due to O-H stretching vibrations in the alcohol groups that are intra molecularly bonded (polyols), as well as a sharper peak at 1248 cm^{-1} due to C-O stretching vibrations in the same hydroxyl groups.

In the spectrum of the free ligand, the carboxylic acids were identified by: O-H stretching vibrations at 3106 cm^{-1}, C-O stretching vibrations at 1290 and 1300 cm^{-1}, C-O-H bending vibrations at 1408 cm^{-1}. The primary amine was identified through the C-N stretching vibration at 1000 – 1250 cm^{-1} which overlaps with peaks of aliphatic primary amine groups, N-H stretch of primary amines at 3418 and 3324 cm^{-1}, primary amine scissoring in bending mode at 1605 cm^{-1}, NH_2 and NH wagging (shifts on H-bond) which could be attributed to peaks at 765, 818 or 840 cm^{-1}. The phenol group also presented characteristic peaks at 1193 cm^{-1} with the strong C-O bending mode and at 3542 cm^{-1} due to hydrogen bonded O-H stretch.

The aromatic rings and alkanes are distinguishable through the peaks at 2926 and 2963 cm^{-1} due to CH_3, CH_2 and CH stretching vibrations, at 3106 cm^{-1} due to =C-H and =CH_2 stretching vibrations, peaks at 1414, 1450 and 1484 cm^{-1} due to C-C stretches and asymmetric stretching of C-C=C in aromatic rings, as well as a peak at 765 cm^{-1} which could be due to aromatic C-H "oop" bending.

No difference in the FTIR spectrum was observed between before and after the ligand exchange process. In particular, no shift in the symmetric and asymmetric stretching frequencies of the COOH group (peaks at 1638 and 1519 cm^{-1} respectively) was observed which indicates the absence of coordination of the COOH groups to the surface of the IONPs. Also, the peak at 1695 cm^{-1} can be attributed to the asymmetric stretching of C=O in the carboxyl group, and this is consistent with free carboxylic acids rather than the conjugated version.[279] FTIR confirms that conjugation of folic acid to the nanoparticles did not take place.

The magnetic properties of the sample were measured at 300 K (Figure 4-14). The saturation magnetisation measured at 300 K after the ligand exchange step was 30.7 emu/g. The decrease in saturation magnetisation can be due to the removal of surface cations which takes place during ligand exchange, particle dissolution, oxidation of the particles,
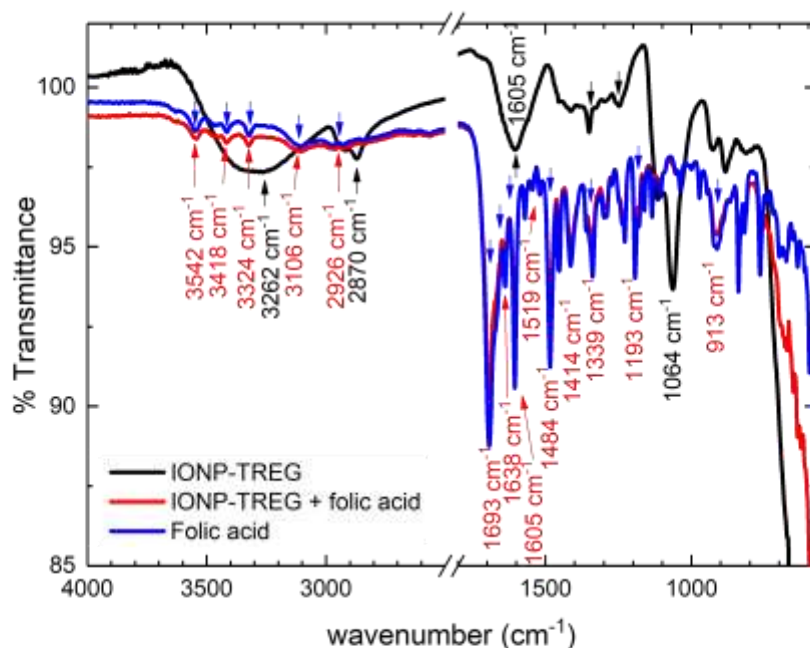
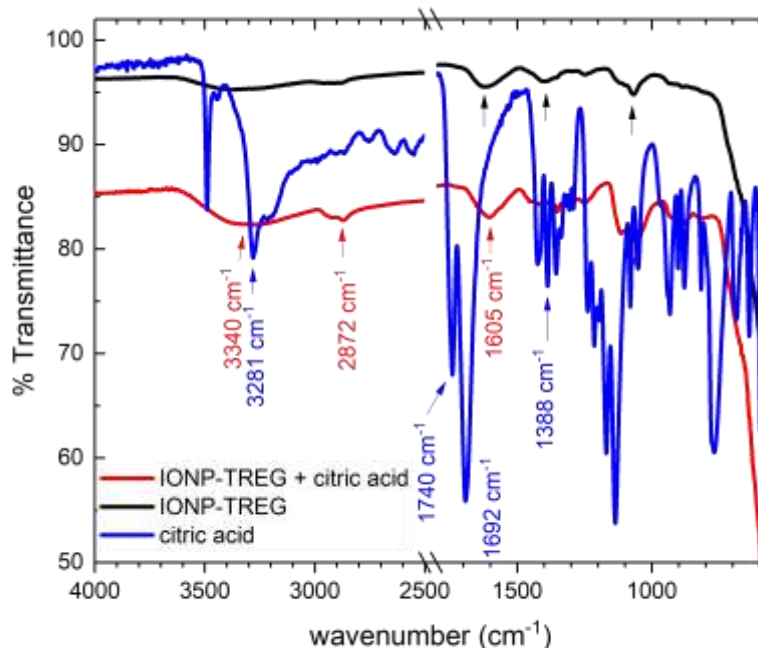 Figure 4-13 ATR-FTIR representative spectra of folic acid (blue), TREG coated IONPs before (black) and after (red) ligand exchange with folic acid. IONPs were purified by magnetic separation followed by dialysis against distilled water for 24 h. The 1800 - 2500 cm^{-1} range has been excluded as no significant information was found.
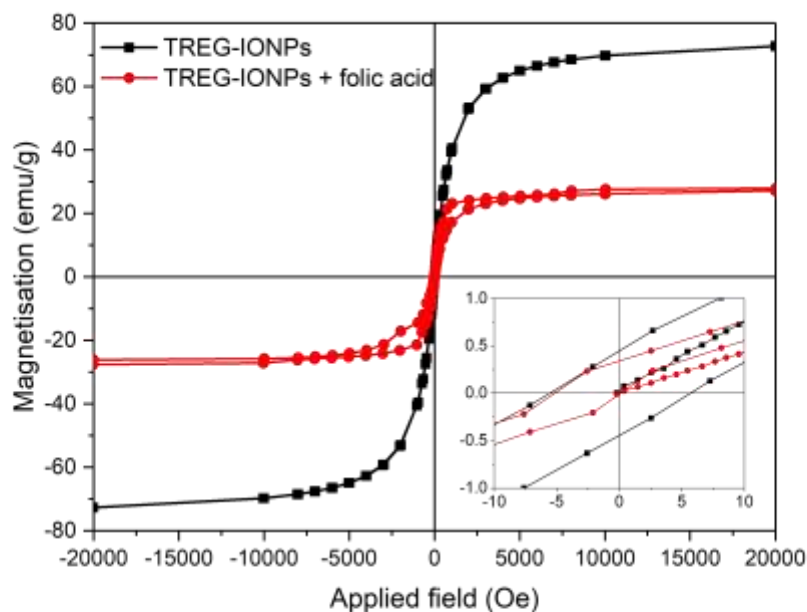
Figure 4-14 Magnetisation curves of TREG coated IONPs before (■) and after (●) the ligand exchange reaction with folic acid. The IONPs with folic acid have been purified by magnetic separation and dialysis against distilled water for 24 h. The curves were measured at 300 K, and the inset shows a zoom into the low magnetic field region.

higher surface magnetic disorder or an excess of organic ligand which contributes to the larger overall NP mass.[78,278] FTIR did not demonstrate any binding to the IONPs, but the decrease in saturation magnetisation suggests that a significant amount of free ligand remained in solution. Indeed, in Figure 4-13, IONPs before and after reaction with folic acid are characterised by Fe-O bands at 579 and 585 cm^{-1}. Since the Fe-O peak of magnetite is found around 570 cm^{-1}, and maghemite will have several peaks between 400 and 800 cm^{-1}, this suggests the decrease in saturation magnetisation is due to higher surface magnetic disorder or an excess of free ligand which contributes to the larger overall NP mass.

4.2.2.5   Oxamic acid

In Figure 4-15, several characteristic peaks of the ligand are identified in the sample after the ligand exchange process including a broad peak from 2500 to 3300 cm^{-1} due to O-H stretching vibrations of the carboxylic group. The latter is also characterised by the C-O-H bending vibration at 1406 cm^{-1} and a strong peak at 1238 cm^{-1} (in the free ligand) or 1300 cm^{-1} (IONP-oxamic acid) due to the C-O stretching vibrations. This overlaps with a broad peak at 3425 cm^{-1} which can be due to the primary amine N-H stretching vibration. The amine also is characterised by the C-N stretching vibration at 1068 cm^{-1} and NH$_2$ scissoring (bending vibrations) at 1598 cm^{-1}. The sharpest peak at 1698 cm^{-1} can be attributed to the asymmetric stretching of C=O in the carboxyl group, and this wavenumber is consistent with free carboxylic acids rather than the conjugated version.[279] This leads to the conclusion that oxamic acid did not bind to the surface of IONPs.
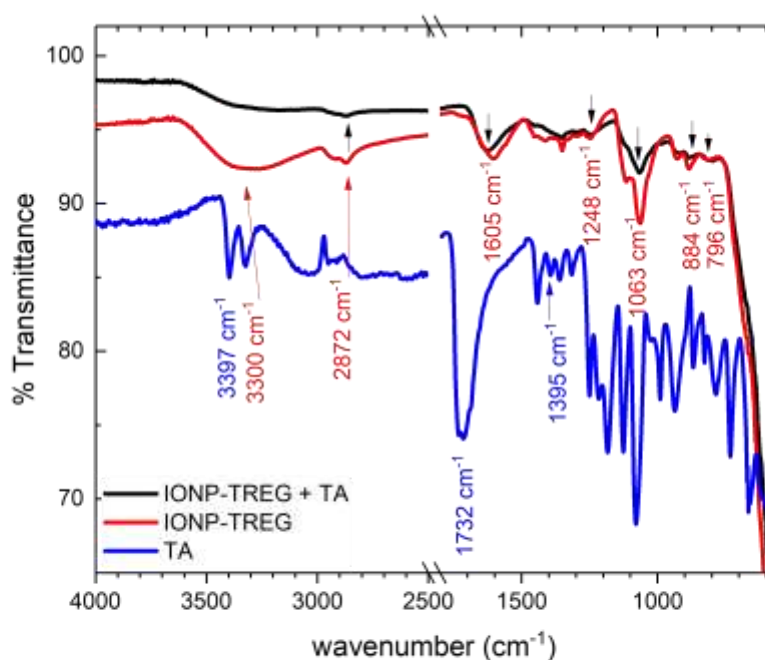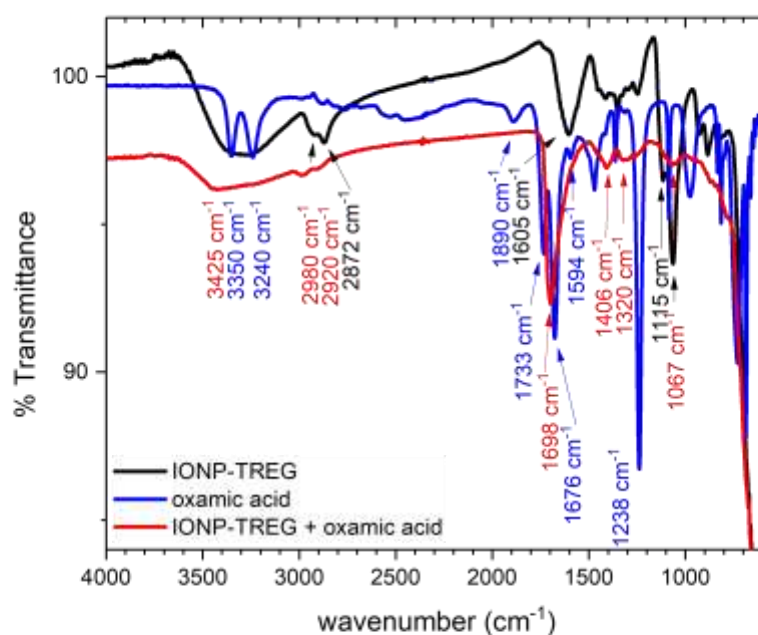

Figure 4-15 ATR-FTIR representative spectra of oxamic acid (blue) TREG coated IONPs before (black) and after (blue) ligand exchange with oxamic acid (red). IONPs were purified by magnetic separation followed by dialysis against distilled water for 24 h.

4.2.2.6 Succinic acid

In the spectrum of IONPs obtained after the ligand exchange (red), the broad band centred around 3375 cm^{-1} may correspond to the stretching vibrations of unbound O-H groups from succinic acid. As it is also present in the spectrum of TREG-IONPs (black), it may also be due to hydrogen bonded water molecules on the IONP surface, valence vibration of the constitutional water,[184, 280] or O-H stretching vibrations in the alcohol groups that are intra molecularly bonded (polyols), and which are also characterised by a sharper peak at 1242 cm^{-1} due to C-O stretching vibrations.

Peaks at 2932 and 2860 cm^{-1} are attributed to the asymmetric and symmetric CH$_2$ stretching respectively.[281] These are found in all three spectra, but this may be due to the succinic acid
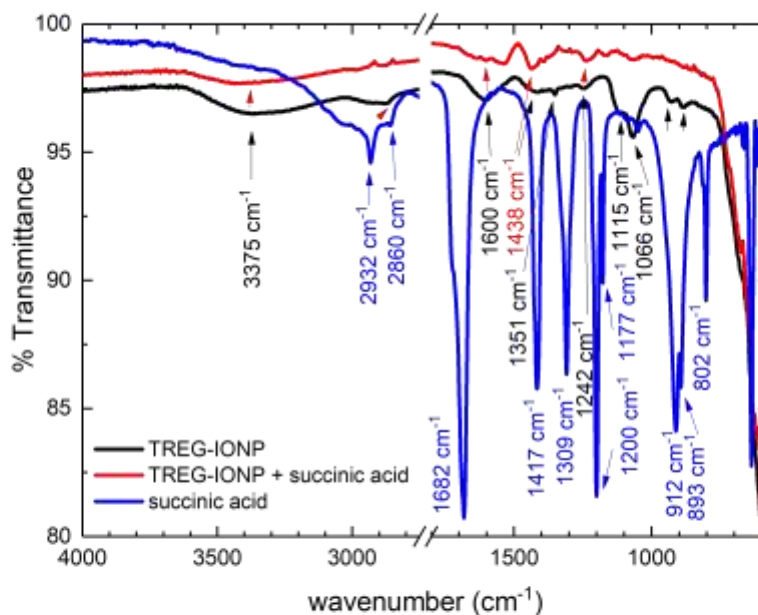
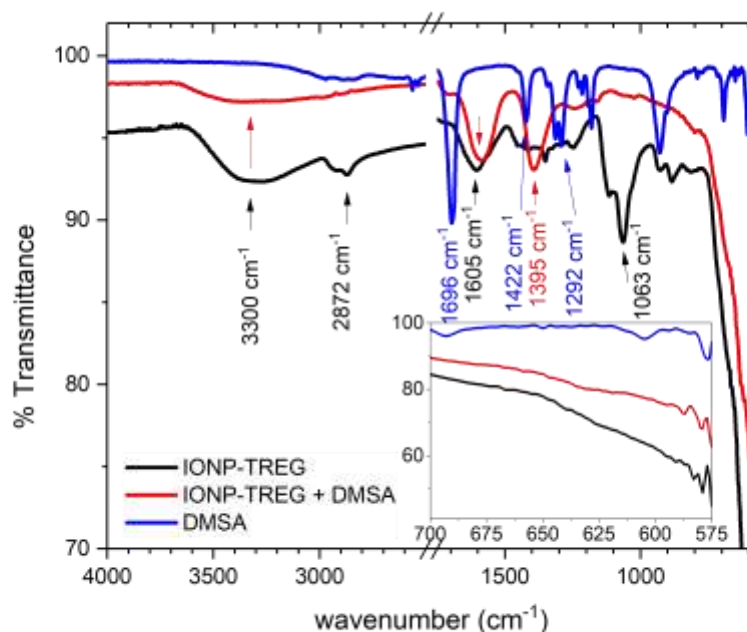**Figure 4-16 ATR-FTIR representative spectra of succinic acid (blue), TREG coated IONPs before (black) and after (red) ligand exchange with succinic acid. IONPs were purified by magnetic separation followed by dialysis against distilled water for 24 h. The 1800 - 2500 cm^{-1} range and relative lower transmittance range have been excluded as no significant information was found.**

or the TREG present in the samples.

Several peaks characterise the free ligand (blue): the carboxylic group is identified through C-O stretching vibrations at 1200 cm^{-1}, C-O-H in-plane bending vibrations at 1417 cm^{-1} and C=O stretching at 1682 cm^{-1}.

The peaks at 1438, 1392 and 1376 cm^{-1} in the spectrum of the IONPs after the ligand exchange also confirm the presence of CH$_2$ groups through their bending vibrations due to deformation. As these are present before and after the ligand exchange, they are certainly due to the CH$_2$ groups present in TREG. The peaks at 1115 cm^{-1} (C-O-C asymmetric stretch) and 1066 cm^{-1} (C-O-C symmetric stretch) appear in the spectra before and after the ligand exchange, indicating TREG is still present after the reaction.

However, the spectra obtained after ligand exchange shows two peaks at 1538 cm^{-1} and 1438 cm^{-1} which can be attributed to C=O vibration (asymmetric and stretching respectively) of the COOH group from succinic acid immobilised on the IONP surface.[276] Indeed, COOH groups can form complexes with Fe atoms on the surface, resulting in a weaker bond, which in turn leads to a shift in the stretching frequency to a lower value.[48, 202, 275] The wavenumber separation (Δv_0) between the asymmetric and symmetric IR peaks can be used to identify the type of interaction between the carboxylate group and the metal atom.[274] In this case, $\Delta v_0 = 100$ cm^{-1}, which indicates a bidentate mode in which two oxygen atoms of COO$^-$ are coordinated to the iron atom.[277]

While FTIR demonstrated the successful functionalisation of IONPs with succinic acid, this reaction did not allow us to obtain stable IONPs as these aggregated and precipitated in solution.

4.2.2.7   Tiopronin

Tiopronin was chosen as it is a pharmaceutical drug known as Thiola® used in the treatment of cystinuria by preventing the formation of kidney stones.[282, 283]

As seen in Figure 4-17, the free ligand is characterised by S-H stretching vibration peaks (2534 cm^{-1}). In the same spectrum, the CH$_3$ function was identified through: stretching vibrations with peaks at 2942, 2980 and 3090 cm^{-1}, as well as CH$_3$ deformation (bending vibrations) at 1378 cm^{-1}. The amine group was identified by: C-N stretching vibrations at 1030 cm^{-1}, secondary amine N-H stretching vibrations at 3310 cm^{-1}, and NH wagging at 861 cm^{-1}. These peaks are absent from the spectrum after ligand exchange with IONPs. In the spectrum of tiopronin, COOH was identified by C-O stretching vibrations at 1199 and 1267 cm^{-1}, C-O-H bending vibrations at 1400 cm^{-1}, C=O stretching at 1617 cm^{-1} and 1744 cm^{-1}. In
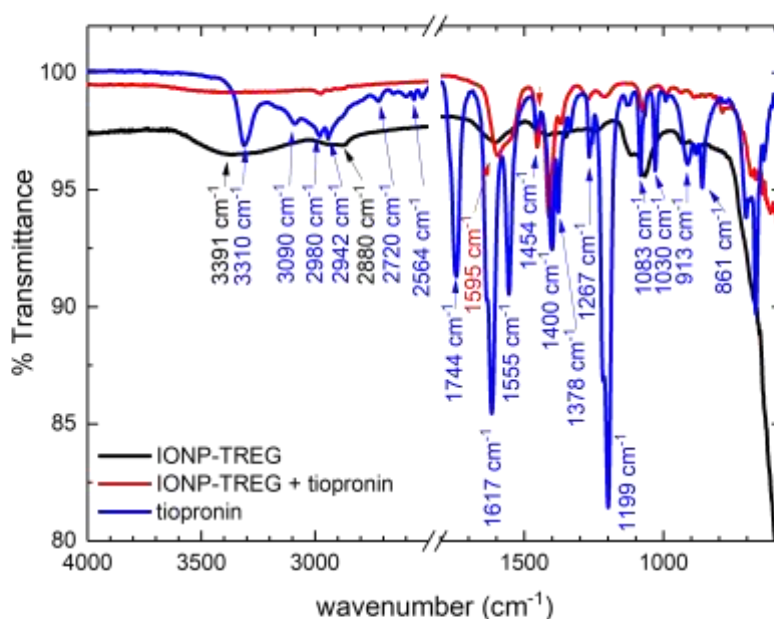
Figure 4-17 ATR-FTIR representative spectra of TREG coated IONPs before (black) and after (red) ligand exchange with tiopronin (blue). IONPs were purified by magnetic separation followed by dialysis against distilled water for 24 h. The 1800 - 2500 cm^{-1} and relative lower transmittance range have been excluded as no significant information was found.
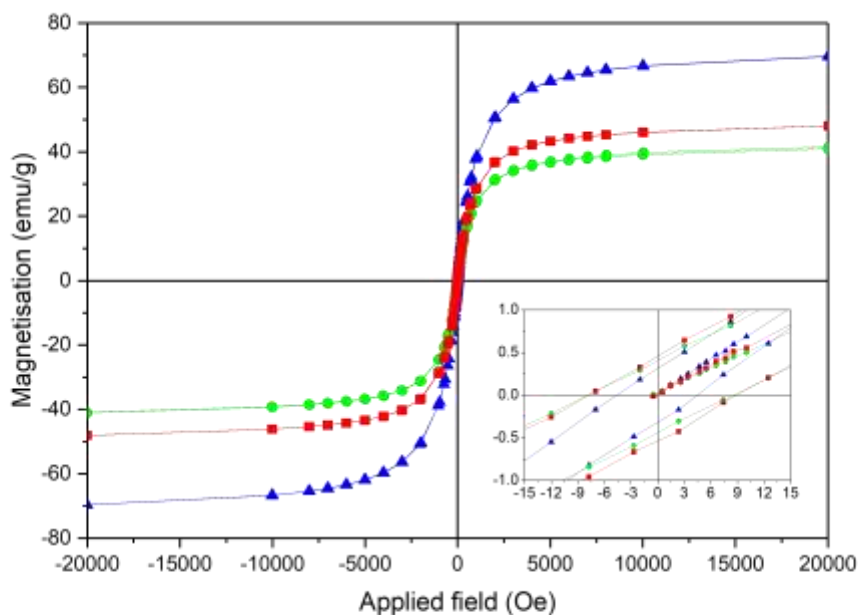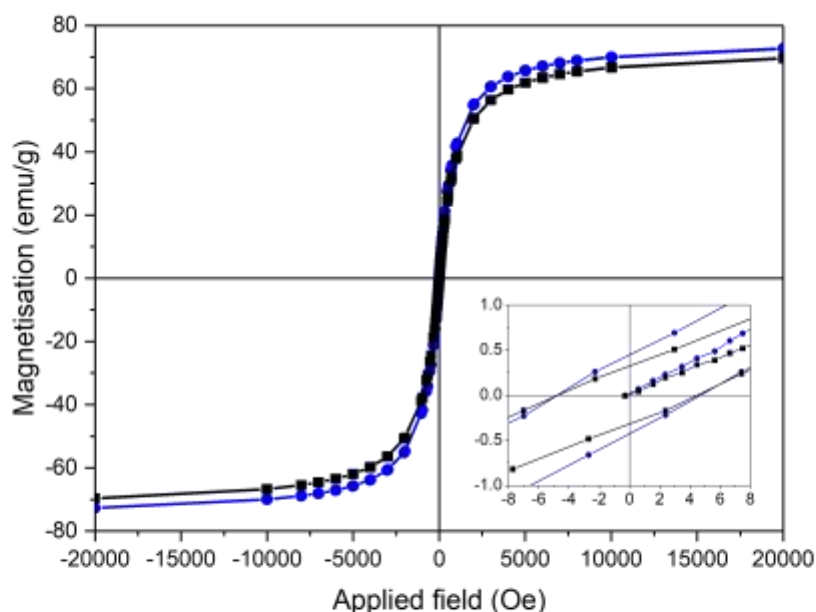
Figure 4-18 Magnetisation curves of TREG coated IONPs before (■) and after (●) the ligand exchange reaction with Tiopronin. The IONPs with Tiopronin have been purified by magnetic separation and dialysis against distilled water for 24 h. The curves were measured at 300 K, and the inset shows a zoom into the low magnetic field region.

the spectrum of IONPs obtained after the ligand exchange, the broad band centred around 3300 – 3400 cm^{-1} may correspond to the stretching vibrations of unbound O-H groups. As it is also present in the spectrum of TREG coated IONPs, it is most certainly due to hydrogen bonded water molecules on the IONP surface, more precisely the valence vibration of the constitutional water therefore it cannot be used for definitive characterisation.[184, 280] The peaks at 1595 cm^{-1} and 1454 cm^{-1} can be attributed to a shift in the peak of C=O vibration (asymmetric stretching) of the carboxylic group from 1744 cm^{-1} in the spectrum of the free ligand (blue curve). This could potentially indicate the binding of tiopronin to the IONPs by chemisorption of the COOH groups.

185

On the other hand, as can be seen in Figure 4-18, the magnetic properties of the IONPs were similar before and after the ligand exchange reaction. The saturation magnetisation measured at 300 K after the ligand exchange reaction with tiopronin was 73.3 emu/g, in comparison to 76 emu/g for TREG coated IONPs. The slight decrease in saturation magnetisation may be caused by oxidation of the IONPs, the removal of cations during the ligand exchange or by an excess of ligand contributing to the overall NP mass.

However, their precipitation in solution was observed, and it was hypothesised that the strong ionic interchange between the TREG molecules and Tiopronin may have resulted in an strong aggregation of the IONPs.

4.2.2.8   PEG diacid 600

The broad band centred around 3422 cm^{-1} may be due to O-H stretching vibrations of unbound O-H functions of the carboxylic group from PEG diacid. Since it is present in the

Figure 4-19 ATR-FTIR representative spectra of TREG coated IONPs before (black) and after (red) ligand exchange with PEG diacid 600 (blue). IONPs were purified by magnetic separation followed by dialysis against distilled water for 24 h. The 1800 - 2500 cm^{-1} range and the relative lower transmittance range have been excluded as no significant information was found.

spectrum of TREG coated IONPs, it is more likely due to hydrogen bonded water molecules on the IONP surface, more precisely it corresponds to the valence vibration of the constitutional water therefore it cannot be used for definitive characterisation of the ligand exchange reaction.[184, 280] This may also be due to O-H stretching vibrations in the alcohol groups that are intra molecularly bonded (polyols), which are also characterised by a sharper peak at 1248 cm^{-1} due to C-O stretching vibrations.

The peaks at 1412 and 1376 cm^{-1} in the spectrum of the IONPs after the ligand exchange also confirm the presence of CH$_2$ groups through their bending vibrations due to deformation. The peak around 2878 cm^{-1} is attributed to the alkyl chain of PEG diacid 600. The bands at 1350 and 1105 cm^{-1} are due to C-H bending and C-O stretching vibrations respectively; and the band at 1245 cm^{-1} is due to C-H twisting vibrations.[222-224]

The characteristic C=O band at 1742 cm^{-1} for the free COOH groups in PEG diacid 600 shifts to a lower wavenumber of 1622 cm^{-1} after the ligand exchange reaction. This indicates the binding of PEG diacid to surface of the IONPs by chemisorption of carboxylate ions. Carboxylate groups of PEG diacid form complexes with Fe atoms on the surface of the IONPs representing partial single bond character to the C = O bond. However, flocculation of the IONPs in solution after a couple of hours was observed. This is most likely due to an insufficient dialysis time of 24 h, after which an excess of polymer remains in solution and causes the precipitation of the IONPs.

From all these previous ligand exchange experiments, few were successful with PEG diacid 600, tiopronin, succinic acid and 2MPA. From their visual observation, nanoparticles were difficult to redisperse after the reaction. For example, an excess of 2MPA was shown to remain in solution by TGA and this led to a decrease in the magnetic properties of the IONPs. Before the ligand exchange reaction, IONPs which had been freeze dried were redispersed in water. However, as confirmed by several publications, freeze drying may have an effect on the colloidal dispersion of NPs and cause their aggregation.[284-286] In the

next method, NPs were therefore maintained in solution after their synthesis and added to dissolved ligands also in solution, before purification by dialysis.

4.2.3 *Ligand exchange with IONP solution and dialysis*

This method was investigated with a variety of ligands including glutamic acid, tiopronin, azelaic acid, terephtalic acid, oxalic acid, succinic acid, PEG diacid and folic acid. The ligands were always added in a ratio 2:1 to the IONP mass in solution, stirred for 48 h before undergoing dialysis with a 10 000 MWCO membrane against distilled water. This ratio of ligand to IONP is generally considered in the literature as a reference in order to ensure sufficient coverage of IONPs by the ligand.[287, 288] However, the DLS data summarised below demonstrates that aggregation took place in aqueous solution with these ligands. Therefore, these samples were not characterised additionally by FTIR. In this chapter, we will focus on the samples which did not aggregate in solution immediately after the ligand exchange reaction.

Ligand	Hydrodynamic diameter measured in water (nm)
L-glutamic acid	381.3 ± 7.2
PEG diacid	507.6 ± 26.9
oxalic acid	589.6 ± 28.3
Folic acid	1310 ± 225.7
Succinic acid	2662 ± 591
tiopronin	3183 ± 199.5
terephtalic acid	16670 ± 4391.3
azelaic acid	17580 ± 5261.6

Most of the ligands which led to the aggregation of the IONPs, were ideally small in size and did possess a carboxylic function through which they should be able to bind to the IONPs by chemisorption; but these ligands were composed of a hydrophobic part made of alkanes or benzene rings which could possibly lead to their incompatibility with IONPs in water. In order to overcome this, similarly small ligands which were more hydrophilic were evaluated: citric acid, tartaric acid and 3,4-dihydroxyhydrocinnamic acid (DHCA).
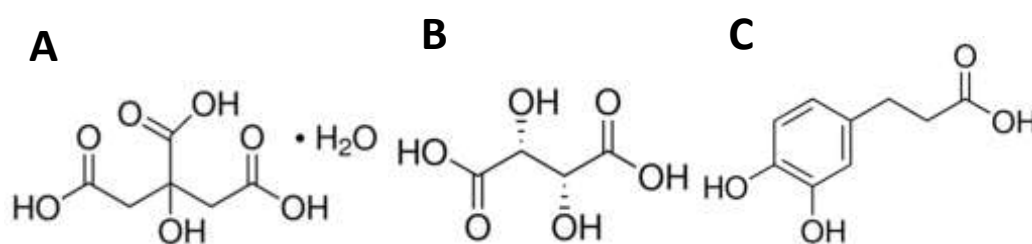
Figure 4-20 Schematic molecular structures of A) citric acid monohydrate, B) L-tartaric acid and C) 3,4-dihydroxyhydrocinnamic acid.

4.2.3.1   Citric acid

60 mg of citric acid was added to 120 mg of TREG-coated IONPs in solution. The ligand is put in excess (6.17 million ligands per NP equivalent to 30.6×10^3 ligands/nm^2) in order to ensure sufficient surface coverage of the IONPs by citric acid. The detailed calculations of the IONP to ligand ratio can be found in Appendix 3. The mixture was stirred for 48 h at RT at 300 rpm before being purified by dialysis over 7 d. The hydrodynamic diameter was then determined by DLS in aqueous solution and saline solution (PBS) immediately after dialysis and 1 week later.
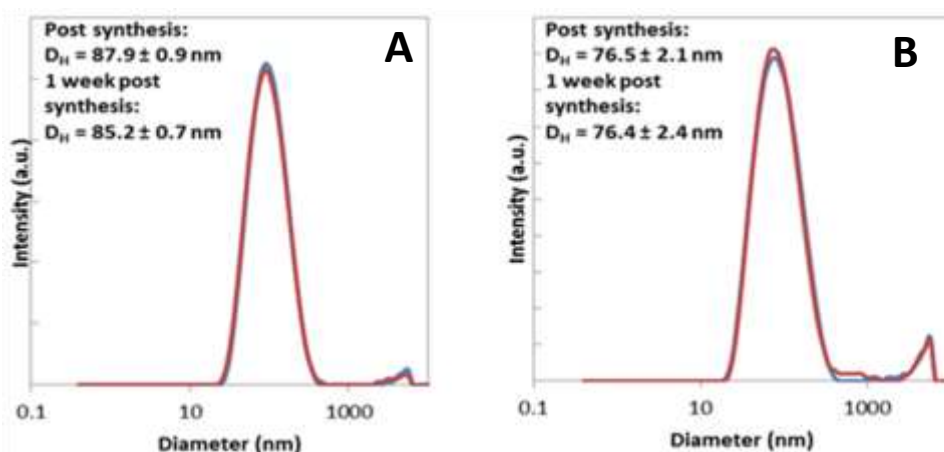
Figure 4-21 Hydrodynamic diameters of IONP-citric acid in (A) water and in (B) PBS immediately after the dialysis purification step and 1 week later.

Immediately after the ligand exchange reaction, the hydrodynamic diameter measured was: D_H = 87.9 ± 0.9 nm in water and D_H = 76.5 ± 2.1 nm in PBS (Figure 4-21). These hydrodynamic diameters were deemed suitable in terms of biocompatibility, size and short term stability, so to the sample was further characterised by SQUID-VSM. The magnetic properties of these IONPs were measured at 300 K and 5 K (Figure 4-22), and this data showed that the IONPs exhibited a superparamagnetic behaviour with a saturation magnetisation M_s = 75.8 emu/g at 300 K which is close to the bulk value of maghemite or magnetite (78 emu/g and 91 emu/g respectively at 300 K)[34, 35] which indicates that the contribution of the ligand to the mass of the nanoparticle is negligible and that the ligand exchange reaction did not significantly alter the IONPs. At 5 K a value of M_s = 83.2 emu/g was measured indicating that spins are blocked at that temperature. Furthermore, at 5 K a relatively high coercive field of H_c ± 444 Oe and remanence of H_r ± 17.6 emu/g were measured.
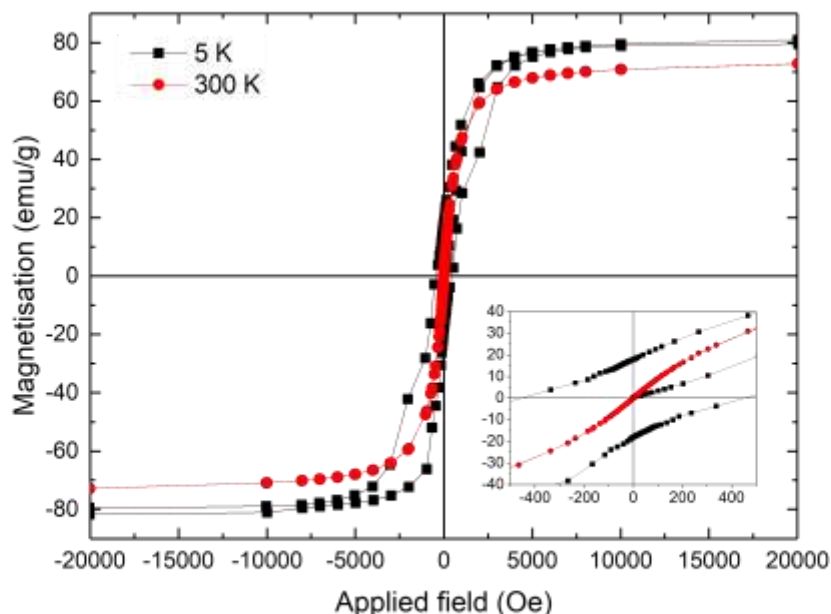
Figure 4-22 Magnetisation curves measured at 300 K (●) and at 5 K (■) after the ligand exchange reaction with citric acid. The inset shows a zoom into the low magnetic field region.

Finally, the ligand exchange reaction was characterised by FTIR to evaluate changes in the functional groups of the IONPs before and after the ligand exchange process. The ATR-FTIR spectra are reported in Figure 4-23.

The broad band centred around 3500 cm^{-1} may correspond to several functional groups: unbound OH groups from citric acid, hydrogen bonded water molecules on the IONP surface (the valence vibration of the constitutional water), or O-H stretching vibrations in the alcohol groups that are intra molecularly bonded (polyols). Therefore this band cannot be used for definitive characterisation of one specific functional group.[184, 280] A sharper peak at 1242 cm^{-1} is due to C-O stretching vibrations in the hydroxyl groups. In the spectrum of IONPs obtained after ligand exchange with citric acid, the carboxylic group is identified through different peaks: O-H bending vibrations at 1066 cm^{-1}, C-O symmetric stretching vibrations at 1250 cm^{-1}, C-O-H symmetric bending vibrations at 1395 cm^{-1}.[289] The smaller peak at 2880 cm^{-1} is attributed to the CH_2 deformation. Most significantly, the 1755 cm^{-1} peak of citric acid usually attributed to the C = O vibration from the carboxylic group
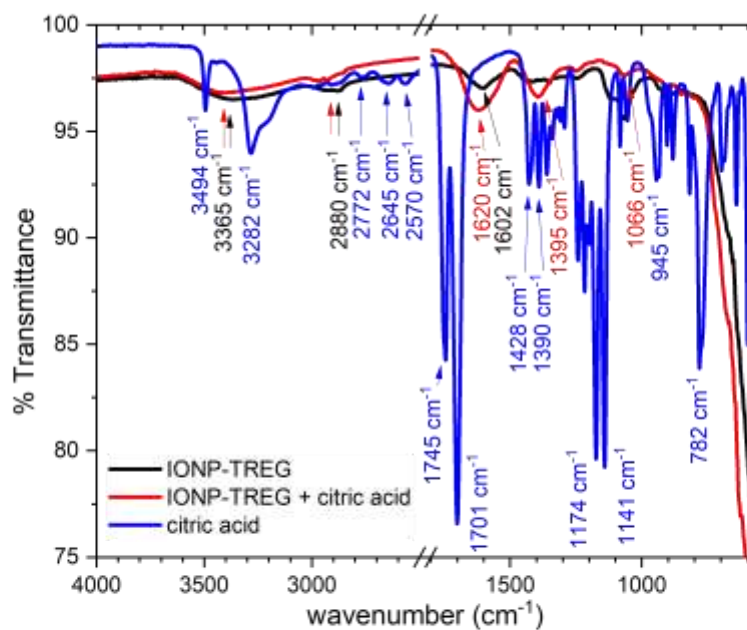
Figure 4-23 ATR-FTIR representative spectra of IONPs before (black) and after (red) ligand exchange with citric acid (blue). IONPs were purified by dialysis against distilled water for 48 h. The 1800 - 2500 cm^{-1} range and the relative lower transmittance range have been excluded as no significant information was found.

shifts to 1620 cm^{-1} for IONP-citric acid. This indicates binding of the ligand to the surface of the IONPs by chemisorption of carboxylate ions. Carboxylate groups of citric acid form complexes with Fe atoms on the surface of the IONPs leading to partial single bond character of the C = O bond which is shifted towards lower wavenumber values.

Additional characterisation by TGA shown in Figure 4-24 provides the percentage of organic ligand present in the sample. This Figure also shows that citric acid is eliminated at temperatures ranging between 200 and 250 °C, because although its boiling point is 310 °C it will decompose before boiling at atmospheric pressure.[290] The sample had an initial 8.5% weight loss due to elimination of water, solvent evaporation and citric acid (T < 500 °C). The offset of temperatures between citric acid and the IONPs indicates the adsorption of citric acid to the surface of the NPs. An additional 1.5% weight loss of organic material is observed in the range of T = 500 °C to T = 600 °C which is due to the phase transformation of Fe_3O_4 to Fe_2O_3.[291] This TGA analysis is in accordance with the ATR-FTIR data confirming the adsorption of citric acid to IONPs. However, as can be seen in Figure 4-26 below, the zeta potential of the citric acid coated IONPs could not be measured as aggregation took place in saline conditions and under the application of an electric field. Although not shown here, this precipitation took place over a range of pH from pH 3 to 10. This suggests that further optimisation of the ligand exchange reaction should be studied including the pH and the
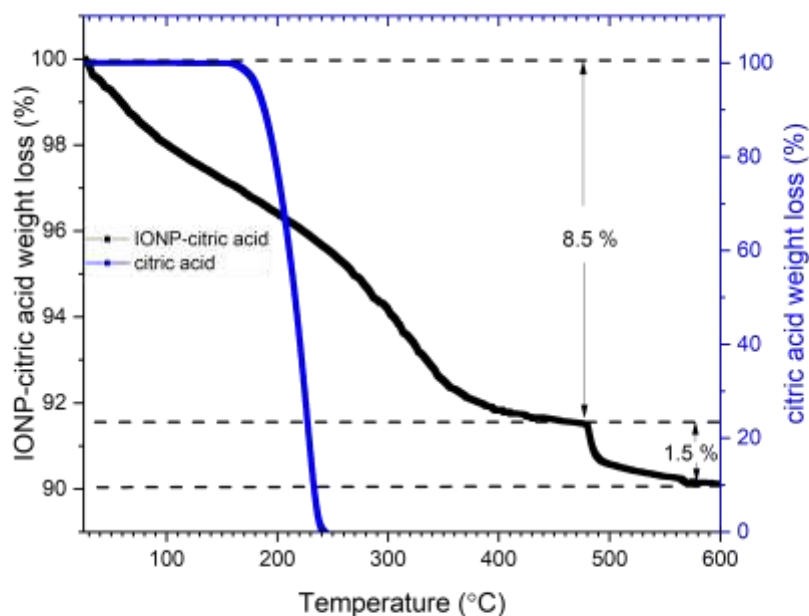
Figure 4-24 Thermogravimetric analysis of citric acid (blue) and IONPs after ligand exchange with citric acid and purification by magnetic separation followed by dialysis (black).

ratio between the ligand and NP for example.

Figure 4-25 (left) Precipitation of citrate coated IONPs in the zeta potential measurement cuvette and (right) precipitation of IONPs in water and NaCl 0.1M.

4.2.3.2   Tartaric acid (TA)
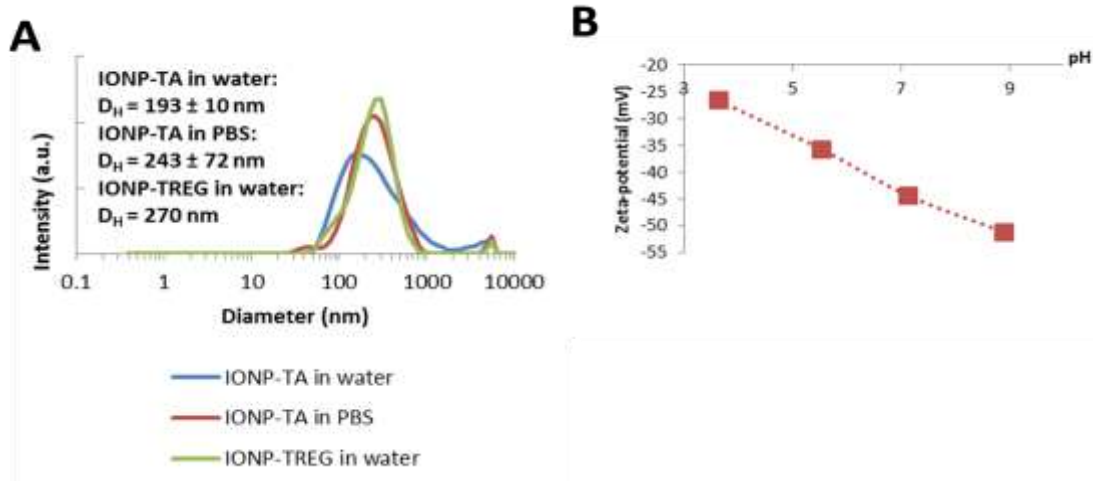
Figure 4-26 (A) Hydrodynamic diameters measured by DLS of IONPs before ligand exchange (IONP-TREG) in water and of IONPs after ligand exchange and dialysis with tartaric acid (IONP-TA) in water and PBS (B) Zeta potential measurements of IONP-TA from pH = 3 to pH = 9 in NaCl 0.1 M
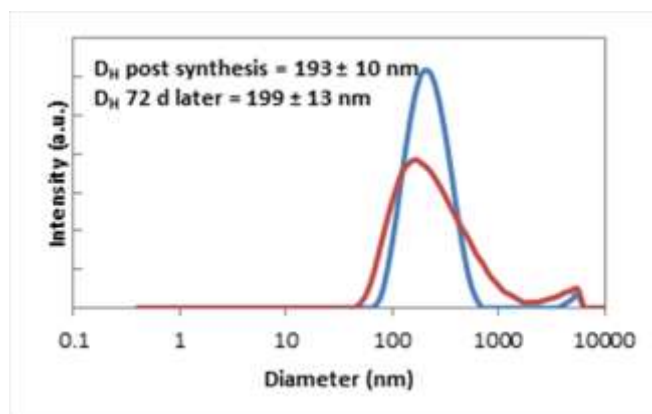
Figure 4-27 Hydrodynamic diameter of IONP-TA measured by DLS in water immediately post synthesis (red) and 72 d later (blue)

The second ligand studied using this method was L-tartaric acid. Initially, 50 mg of tartaric acid was added to the equivalent of 25 mg of IONPs in solution and stirred for 48 h at RT at 300 rpm. Then, the sample was cleaned by dialysis against distilled water for 72 h, the water once was changed once. The ligand is put in excess (7.9 million ligands per NP equivalent to 39.3×10^3 ligands/nm^2) in order to ensure sufficient surface coverage of the IONPs by TA. The detailed calculations of the IONP to ligand ratio can be found in Appendix 3. As illustrated in Figure 4-25, the obtained IONPs have a hydrodynamic diameter $D_H = 192.7 \pm 9.6$ nm ($\delta = 5\%$) in water and 243 ± 72 nm ($\delta = 29\%$) in PBS. The zeta potential seemed to confirm the exchange of the ligand was successful with a strong negative value measured from pH 3 to pH 9 in NaCl 100 mM. This reflects the negative surface charge of the IONPs in solution, probably due to the carboxylic groups of the ligand. Also, the zeta potential being in the range -25 to -50 mV indicates electrostatic stability of the IONPs. However, the stability of these IONPs was found to be limited in time. As seen in Figure 4-27 below, the hydrodynamic diameter was measured 72 d later by DLS, and very slight aggregation had occurred with an increased diameter of $D_H = 199 \pm 13$ nm ($\delta = 6.5\%$). Also, slight precipitation of these IONPs in solution was visually observed.

Furthermore, the magnetic properties of the sample were determined by SQUID-VSM (Figure 4-29). The IONPs obtained displayed a superparamagnetic behaviour with a saturation magnetisation M_s = 48.1 emu/g at 300 K. Before the exchange with TA, the TREG coated IONPs exhibited a higher magnetisation of M_s = 79.6 emu/g. The decrease in saturation magnetisation could be due to the removal of surface cations which can occur during ligand exchange, particle dissolution, oxidation of the particles, higher surface magnetic disorder or an excess of organic ligand which contributes to the larger overall NP mass.[78,278]
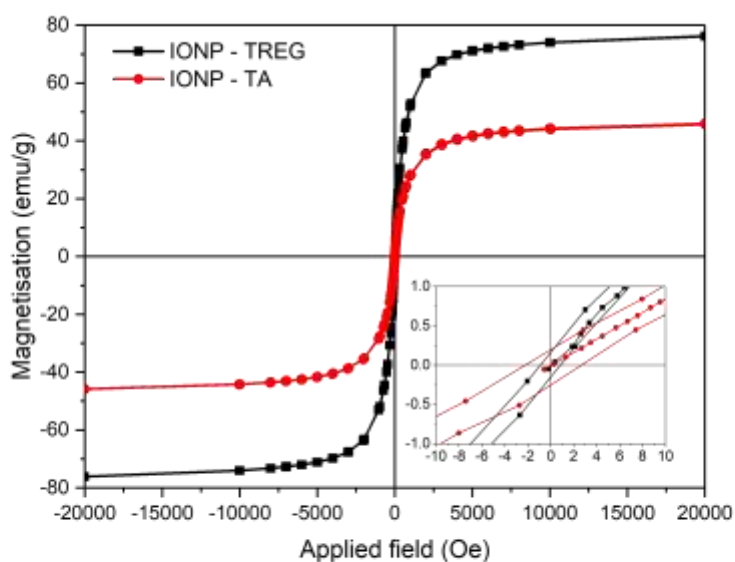
Figure 4-28 Magnetisation curves measured at 300 K before (▪) after (●) the ligand exchange reaction with tartaric acid. The inset shows a zoom into the low magnetic field region.
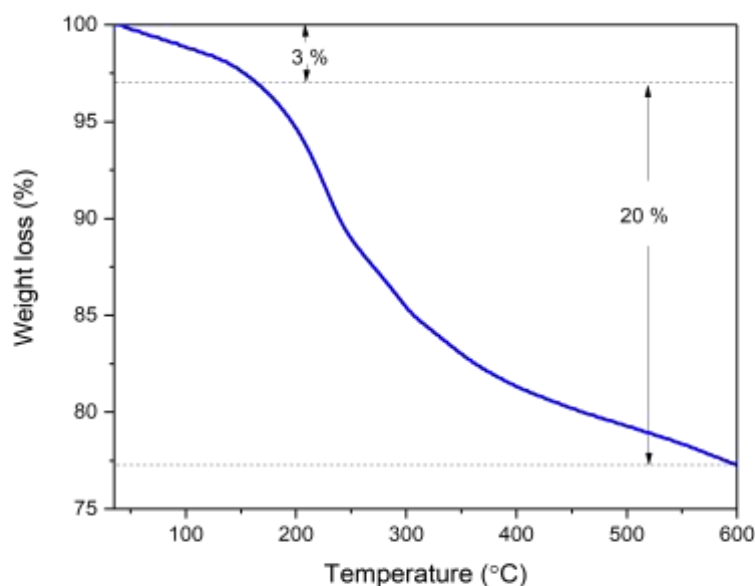
Figure 4-29 Thermogravimetric analysis of IONPs after ligand exchange with tartaric acid and purification by dialysis (blue).

Additional characterisation by TGA shown in Figure 4-28 provides the percentage of organic ligand present in the sample. The sample had an initial 3% weight loss due to elimination of adsorbed water and solvent evaporation (T < 180 °C). This was followed by a 20% weight loss of organic material in the range of T = 180 °C to T = 600 °C which is due to the elimination TREG linked by chemisorption to the IONPs and the decomposition of the supporting tartaric acid.[259-261, 292] This TGA analysis validates our previous hypothesis that the decrease in the saturation magnetisation of the IONPs after ligand exchange is, at least partially, due to a significant contribution by the organic layer coating the NPs.

Finally, to confirm whether tartaric acid was successfully linked to the surface of the IONPs, their FTIR spectrum was obtained (Figure 4-30). In the spectrum of IONPs before and after ligand exchange, the broad band centred around 3300 cm^{-1} is due to hydrogen bonded O-H stretching vibration from surface hydroxyl groups on IONPs and adsorbed TREG and water, therefore it cannot be attributed specifically to the hydroxyl groups of tartaric acid.[293] Tartaric acid functionalised NPs exhibited specific peaks including a sharp peak at 1732 cm^{-1}

due to C=O stretching vibrations in protonated carboxyl groups.[294] At 1635 cm^{-1} and 1378 cm^{-1} were identified sharp peaks corresponding to the asymmetric and symmetric stretching of carbon–oxygen bonds of carboxylate groups, respectively.[276, 295] These are shifted towards lower wavenumber as it is bound to the surface of the NPs.[202, 275] The band observed at 1089 cm^{-1} is due to the C-O stretch in hydroxyl groups. The wavenumber separation (Δv_0) between the asymmetric and symmetric IR peaks can be used to identify the type of interaction between the carboxylate group and the metal atom.[274] In this case, Δv_0 = 257 cm^{-1}, which indicates an unidentate mode in which a monotartrate species is bound to the IONP surface via the deprotonated carboxylate group.[277, 292, 296, 297] ATR-FTIR has therefore confirmed the effective binding of tartaric acid to the surface of the IONPs through the monodentate interaction of the carboxylate group with iron.

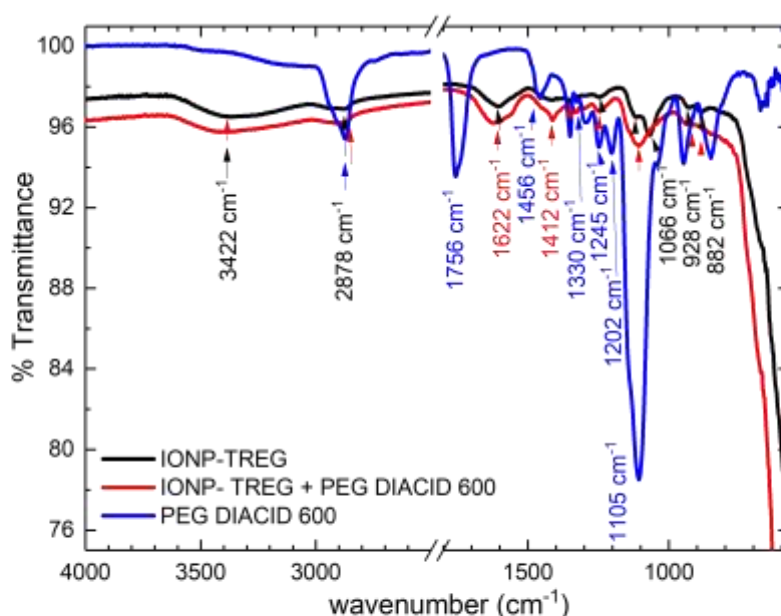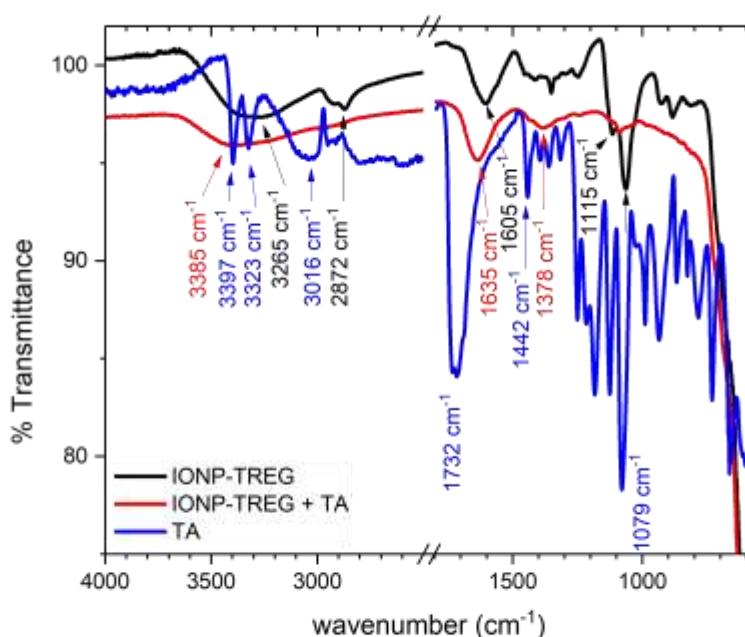**Figure 4-30 ATR-FTIR representative spectra of IONPs before (black) and after (red) ligand exchange with tartaric acid (blue). IONPs were purified by dialysis against distilled water for 5 d. The 1800 - 2500 cm^{-1} range and the relative lower transmittance range have been excluded as no significant information was found.**

In order to optimise the hydrodynamic diameter of IONPs obtained after ligand exchange with tartaric acid, the influence of different parameters during the ligand exchange process was studied, such as the ratio IONPs: ligand or the dialysis time for example.

4.2.3.2.1 Effect of dialysis time on functionalisation of IONPs

The reaction was scaled up while maintaining a constant ratio of IONPs to TA, using 200 mg of TREG-coated IONPs in solution with 500 mg of TA. The solution was stirred at RT for 48 h before being dialysed against distilled water for 5 d. The scale up was successful and, as seen in Figure 4-31, the extended dialysis time produced IONPs with a smaller hydrodynamic diameter of D_H = 168.4 ± 5.7 nm (δ = 3.4%).
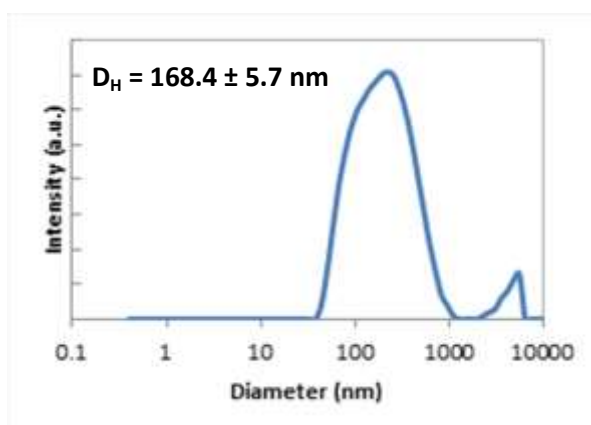
Figure 4-31 Hydrodynamic diameter of IONP-TA measured by DLS in water. A ratio IONP to ligand of 1:2,5 was used and the solution was dialysed against distilled water for 5 d.

This improvement in the size distribution IONPs was confirmed with the magnetic properties of the IONPs obtained (Figure 4-33). The IONPs obtained were characterised by quasi superparamagnetic behaviour at 300 K with a saturation magnetisation M_s = 76.5 emu/g. This value is close to that of bulk maghemite and magnetite (respectively 78 emu/g and 92 emu/g at 300 K),[34-36, 81] and in particular maghemite. The small difference between the bulk value of γ-Fe$_2$O$_3$ and of the IONP-TA sample indicates that the contribution of the

ligand is negligible on the overall nanoparticle mass and that the longer dialysis time of 5 d was beneficial in eliminating any remaining excess ligand in solution.

In Figure 4-32, IONPs before and after reaction with tartaric acid are characterised by FTIR in the range of 400 to 800 cm^{-1} in order to obtain information regarding the crystal structure of the IONPs obtained. In both samples of IONPs are absent Fe-O bands around 570 - 580 cm^{-1}, which supports the lack of magnetite phase in these NPs.[88] IONPs after ligand exchange with tartaric acid are characterised by peaks at 537, 620 and 734 cm^{-1} attributed to maghemite as this iron oxide phase will have several peaks between 400 and 800 cm^{-1}.
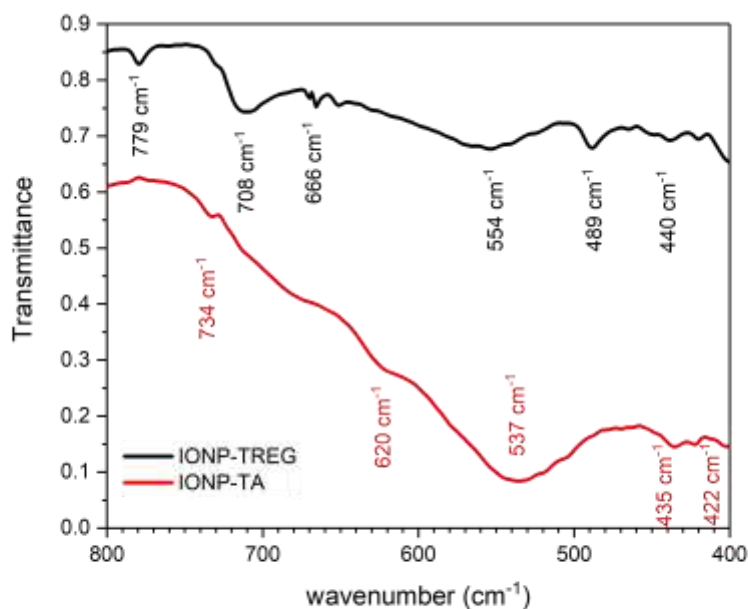
Figure 4-32 ATR-FTIR representative spectra of IONPs before (black) and after (red) ligand exchange with tartaric acid. IONPs were purified by dialysis against distilled water for 5 d. The 800 - 4000 cm^{-1} range has been excluded as it is not relevant to the Fe-O bands of iron oxides.

4.2.3.2.1 Effect of ratio IONP: ligand on functionalisation of IONPs

Finally, another parameter which was studied was the ratio IONP to ligand. 10 mg of TREG-coated IONPs was mixed with either 10 mg (ratio 1:1), 100 mg (ratio 1:10) or 500 mg (ratio 1:50) of tartaric acid to see whether this had an influence on the IONPs. As can be seen in

Appendix 3, this corresponds to a large excess of ligand to IONP from approximately 4 up to 200 million ligands per IONP, equivalent to 19.9 up to 994.5 x 10^3 ligands/nm^2. The dialysis time was kept relatively long at 7 d, as this seems necessary to ensure sufficient purification of free ligands remaining in solution. The summary of the hydrodynamic diameters measured by DLS for each sample is presented below (Figure 4-34). Overall, the data presented in sections 4.2.3.2.1 and 4.2.3.2.1 ascertains that suitable IONPs for biomedical applications could be obtained after ligand exchange with tartaric acid in a ratio 1:1 or 1:2 and with a dialysis time of 5 to 7 d. Indeed, as demonstrated by Figure 4-34, shorter dialysis times or an increased ratio of ligand to IONP led to larger hydrodynamic diameters and lower saturation magnetisation.
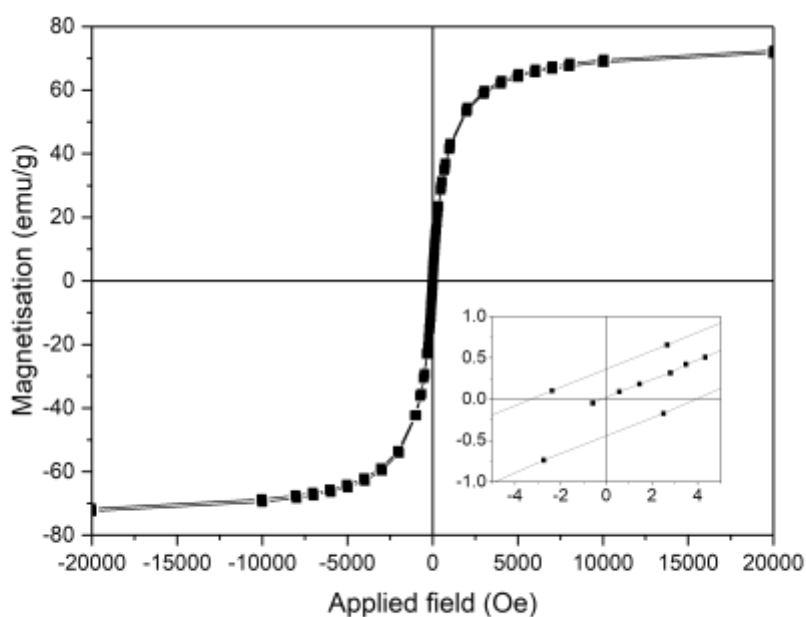
Figure 4-33 Magnetisation curve measured at 300 K after the ligand exchange reaction with tartaric acid and dialysis for 5 d. The inset shows a zoom into the low magnetic field region.
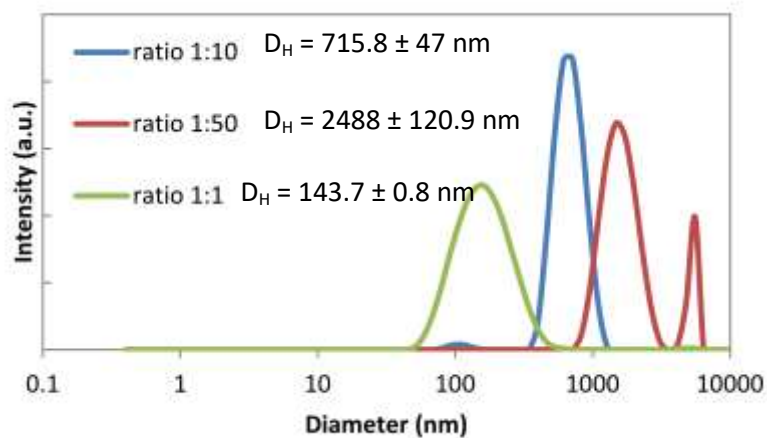
Figure 4-34 Hydrodynamic diameters of IONPs measured by DLS in aqueous solution, obtained after ligand exchange with different ratios of tartaric acid.

4.2.3.2.2   Relaxivity of nanoparticles in solution at 1.47 T

Finally, to determine whether these IONPs could potentially be used for stem cell labelling and imaging by MRI, their relaxivity was measured at 1.47 T. The r_1 and r_2 values were
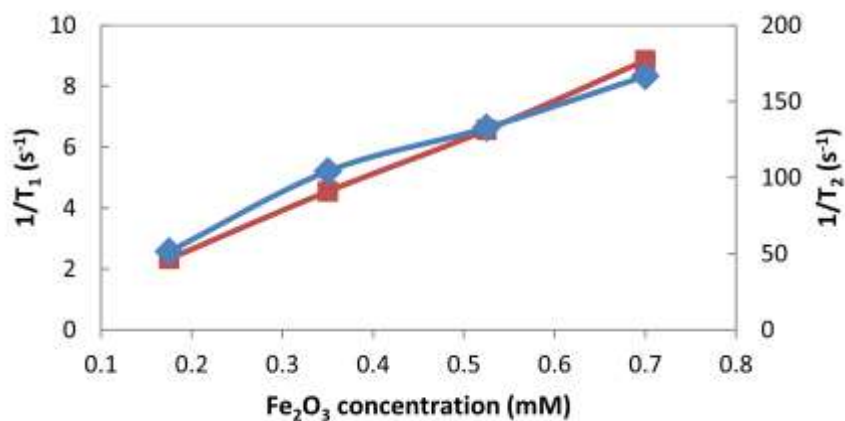
Figure 4-35 Relaxation rates $1/T_1$ (■) and $1/T_2$ (♦) over Fe_2O_3 concentration of the IONP-TA nanoparticles. The slope indicates the specific relaxivity (r_1 or r_2).

measured according to the linear relationship of longitudinal and transverse relaxation rates *versus* the magnetic metal concentrations of Fe (Figure 4-35). The obtained values were: $r_1 = 8.63$ mM^{-1} s^{-1} and $r_2 = 149.68$ mM^{-1} s^{-1}. The relatively high r_2/r_1 ratio of 17.3 suggests these nanoparticles are suitable as T_2 weighted contrast agents. Indeed, to be considered as effective T_2 MRI contrast agents, these must possess a high r_2 and high r_2/r_1 ratio.[298] As demonstrated in Table 4-1, in water and at 37 °C, these tartaric acid functionalized IONPs possess a higher r_2/r_1 ratio than FDA-approved contrast agents Resovist® and Endorem®.[299]

4.2.3.3   3,4-dihydroxyhydrocinnamic acid

Finally, the third ligand using this ligand exchange method was 3,4-dihydroxyhydrocinnamic acid (DHCA). After attempting ligand exchange with dopamine, it not ideal as a surface ligand for these IONPs as it led to their precipitation (data not reported here); however a new hypothesis was developed to determine whether a ligand with similar structure, such as DHCA, would be more efficient as it does also possess a catechol group, and in particular the two hydroxyl groups, which could be linked to IONPs in a similar manner to dopamine.[16, 158, 300] Indeed, dopamine derived ligands present a high affinity for metal oxide surfaces through their catechol groups. This arises from the ability of two adjacent hydroxyl groups of the enediol group to chelate surface metal ions.[227, 301] However, dopamine is no longer a ligand of choice when it comes to the functionalisation of IONPs as it was previously reported to react with Fe^{3+} according to a radical mechanism to produce leucodopaminochrome.[302] Furthermore, in the presence of IONPs the decomposition of dopamine was also observed[303] and this led to a significant decrease in the core size of MNPs after ligand exchange from 7.6 nm to 6.6 nm.[304]
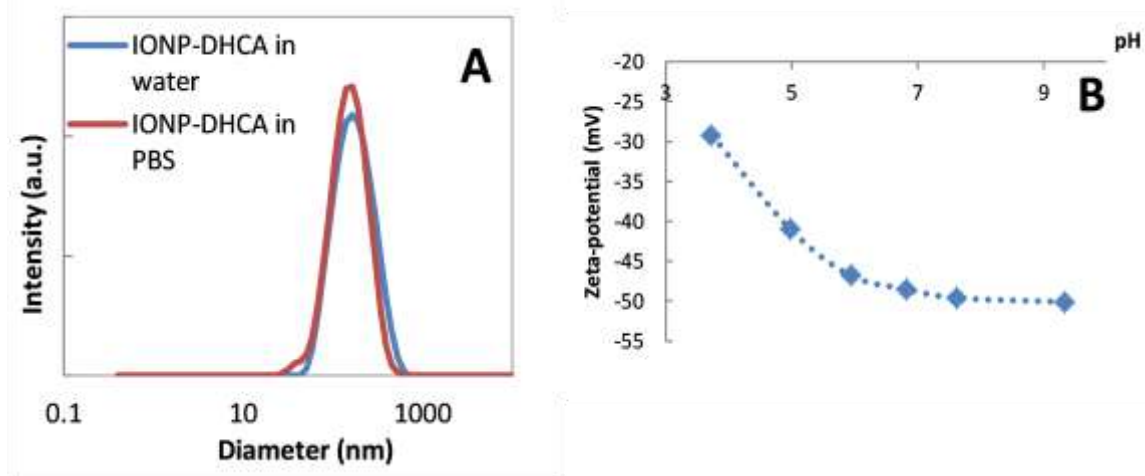
Figure 4-36 (A) Hydrodynamic diameters measured by DLS of IONPs after ligand exchange and dialysis with 3,4-dihydroxyhydrocinnamic acid (IONP-DHCA) in water and PBS (B) Zeta potential measurements of IONP-DHCA from pH = 3 to pH = 9 in NaCl 0.1 M

Initially, 50 mg of DHCA was added to the equivalent of 25 mg of IONPs in solution and stirred for 48 h at RT at 300 rpm. Then, the sample was cleaned by dialysis against distilled water for 7 d. After the ligand exchange step, the hydrodynamic size of the IONPs measured was D_H = 154 ± 4.5 nm (δ = 2.8%) in water. In PBS, the hydrodynamic diameter of IONP-DHCA decreased to D_H = 140 nm ± 4.5 nm (δ = 2.8%), and no aggregation was observed. The zeta potential seemed to confirm the exchange of the ligand was successful with a strong negative value measured from pH 3 to pH 9 in NaCl 100 mM. This reflects the negative surface charge of the IONPs in solution probably due to the carboxylic groups on the ligand. Also, the zeta potential being in the range -25 to -50 mV indicates electrostatic stability of the IONPs in solution. This is contrary to TREG coated IONPs which were unstable and aggregated on the electrodes of the cuvette.
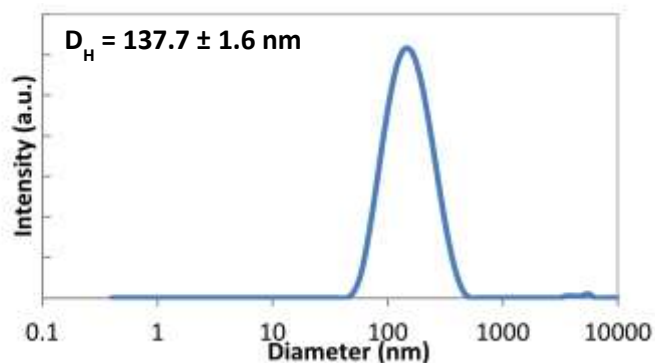
Figure 4-37 Hydrodynamic diameter of IONP-DHCA measured by DLS in water 72 d post synthesis

In a similar manner to IONP-TA, the hydrodynamic diameter was measured 72 d later to see whether any aggregation could be determined. The hydrodynamic diameter had not significantly changed and slightly decreased to D_H = 137.7 ± 1.6 nm (δ = 1.1%), thus indicating that the IONPs were stable in aqueous solution in the long term (Figure 4-37). The ligand exchange of IONP-TREG with DHCA was further confirmed by ATR-FTIR measurements. The FTIR spectra obtained are found in Figure 4-38. For polyol coated NPs, the broad band centred around 3365 cm^{-1} is due to hydrogen bonded O-H stretching vibration from surface hydroxyl groups on nanoparticles and adsorbed TREG and water.[293] Bands at 1115 and 1066 cm^{-1} are characteristic of C–O stretching in TREG molecules. In the case of DHCA functionalised IONPs, the broad band at approximately 1403 cm^{-1} and peaks at 1247 cm^{-1} are attributed to catechol groups binding covalently to various metal oxides as catechol anions.[305] They can be attributed to the benzene ring vibration and a C–O stretch, respectively. The band at 1403 cm^{-1} can also be assigned to symmetric vibrations of carboxylate groups. This suggests the ligand bound to the IONPs through the catechol groups, whereas the carboxylic groups remain free on the surface of the IONPs.

FTIR in the range of 400 to 800 cm^{-1} provides information regarding the crystal structure of the IONPs obtained.[306, 307] In both samples of IONPs Fe-O bands around 570 - 580 cm^{-1} can

be found, which supports the presence of magnetite phase in these NPs.[88] Furthermore, IONPs after ligand exchange with DHCA are characterised by peaks at 554, 620 and 680 cm^{-1} attributed to maghemite as this iron oxide phase will have several peaks between 400 and 800 cm^{-1}. This can be attributed to different events which take place during ligand exchange including the removal of surface cations, particle dissolution, or oxidation of the particles. [78,278] Similarly to tartaric acid, the ligand exchange reaction was optimised through the study of the influence of different parameters on the IONPs obtained.
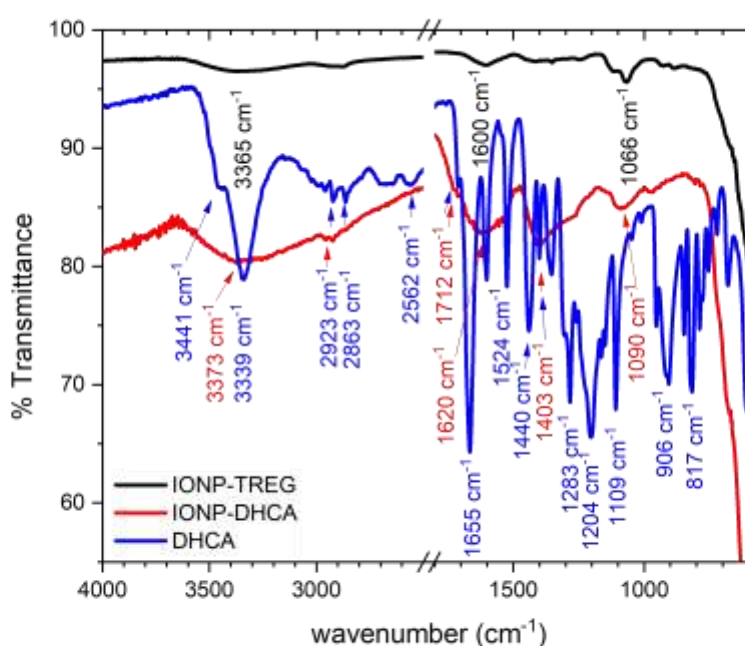
Figure 4-38 ATR-FTIR representative spectra of IONPs before (black) and after (red) ligand exchange with DHCA (blue). IONPs were purified by dialysis against distilled water. The 1800 - 2500 cm^{-1} range and the relative lower transmittance range have been excluded as no significant information was found.

4.2.3.3.1 Effect of dialysis time on functionalisation of IONPs

Keeping the same experimental conditions as mentioned previously, TREG coated IONPs were put in presence of the ligand, before purification by dialysis for 4 d, 6 d or 10 d.

In Figure 4-39 below are presented the DLS measurements of the hydrodynamic diameters of the obtained IONPs after 4 d, 6 d or 10 d dialysis in water.

After 4 d of dialysis, the IONPs obtained had a hydrodynamic diameter of D_H = 214 ± 3.6 nm. The hydrodynamic diameter decreases to D_H = 195.6 ± 1.5 nm after 6 d and D_H = 178.7 ± 0.8 nm after 10 d. This suggests that the extended dialysis time up to 10 d allowed the elimination of excess ligand still present in solution and thus decrease the hydrodynamic diameter of the IONPs in solution.

However, as mentioned in chapter 1, IONPs considered for potential biomedical applications should have limited hydrodynamic diameters (D_H < 100 nm) in solution to maximise their biocompatibility and dispersion in biological conditions. In order to further decrease the hydrodynamic diameter of the IONPs obtained, both the ligand exchange reaction time and dialysis time were increased. In this next set of experiments, the ligand exchange reaction time was extended to 6 d. Furthermore, the effect of various dialysis times (5 d, 10 d and 15 d) on the IONPs obtained was studied. As seen in Figure 4-40, after 5 d of dialysis the IONPs had a hydrodynamic diameter in water of D_H = 203.2 ± 2.2 nm, which then decreased to D_H = 198.1 ± 1.5 nm after 10 d and D_H = 145.5 ± 1.3 nm after 15 d. This seems to indicate that the
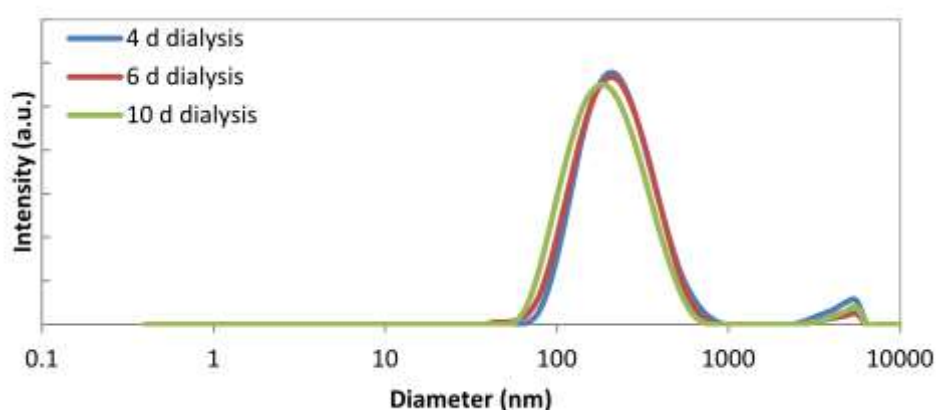
Figure 4-39 Hydrodynamic diameters of IONPs measured by DLS in aqueous solution, obtained after ligand exchange with DHCA for 48 h and dialysis against distilled water for 4 d, 6 d, and 10 d.

excess ligand is progressively removed as the dialysis time is extended.
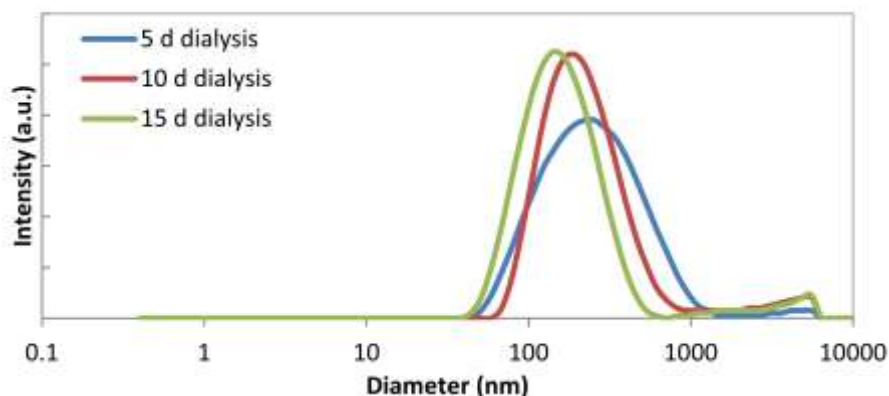
Figure 4-40 Hydrodynamic diameters of IONPs measured by DLS in aqueous solution, obtained after ligand exchange with DHCA for 6 d and dialysis against distilled water for 5 d, 10 d, and 15 d.

The magnetic properties of IONPs obtained after 5 d and 15 d of dialysis were then compared as shown in Figure 4-41. As observed in Figure 4-41, IONPs were characterised by a superparamagnetic behaviour at 300 K with a saturation magnetisation M_s = 73.6 emu/g after 5 d of dialysis and M_s = 73.1 emu/g after 15 d dialysis. This value is close to that of bulk
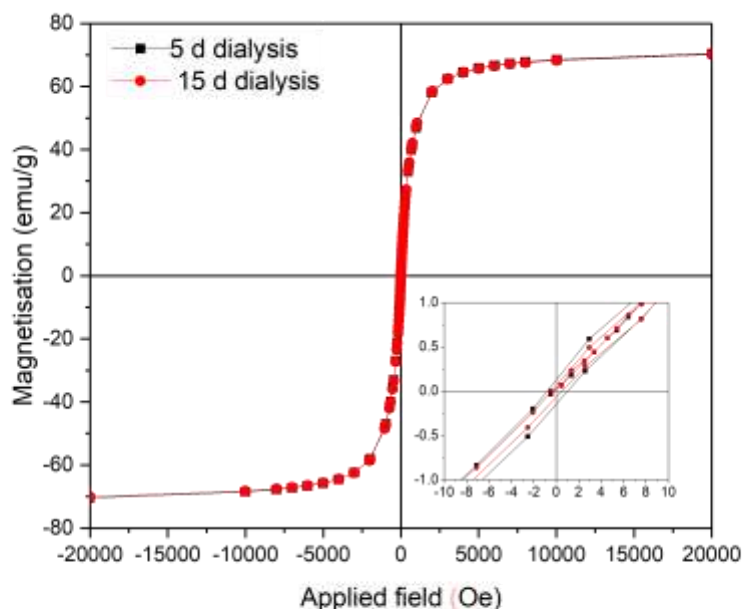
Figure 4-41 Magnetisation curve measured at 300 K after the ligand exchange reaction with DHCA and dialysis for 5 d (black) or 15 d (red). The inset shows a zoom into the low magnetic field region.

maghemite and magnetite (respectively 78 emu/g and 92 emu/g at 300 K).[34-36, 81] This is consistent with the FTIR data of Figure 4-38 which suggests that oxidation of IONPs may take place during the ligand exchange reaction, thus leading to a decrease in the saturation magnetisation in comparison to TREG coated IONPs (M_s = 80 emu/g, data not shown here). Additional characterisation by TGA shown in Figure 4-42 below provides the percentage of organic ligand present in the sample. This figure also shows that DHCA is mostly eliminated at temperatures ranging between 200 and 300 °C. The sample had an initial 5% weight loss due to elimination of water and solvent evaporation (T < 200 °C). This was followed by a 19% weight loss of organic material in the range of T = 200 °C to T = 600 °C which is due to the elimination TREG linked by chemisorption to the IONPs and DHCA.[259-261] TGA reveals that DHCA is bound to the IONP as the free ligand volatilises at lower temperatures than in presence of IONPs after ligand exchange. This TGA analysis also suggests that the decrease in the saturation magnetisation of the IONPs after ligand exchange is, at least partially, due to a significant contribution by the organic layer coating the NPs.
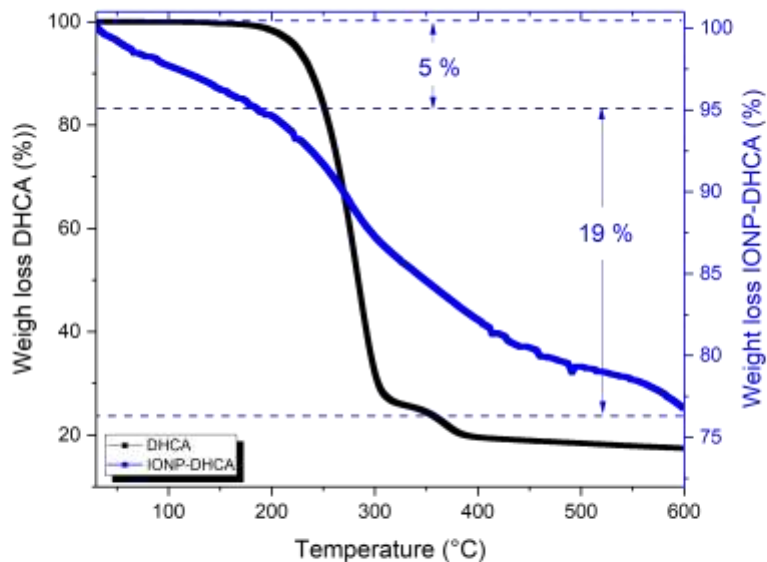
Figure 4-42 Thermogravimetric analysis of DHCA (black) and IONPs after ligand exchange with DHCA and purification by dialysis (blue).

4.2.3.3.2 Effect of ratio IONP:ligand on the functionalisation of IONPs

Finally, another parameter which was studied was the ratio IONP to ligand. DHCA (300 mg) was added to either 300 mg of IONPs (ratio 1:1) or 150 mg of IONPs (ratio 2:1) to determine if this had an impact on the IONPs obtained after ligand exchange, which took place for 48 h. The dialysis time was kept relatively long at 10 d, as section 4.2.3.3.1 indicates that this seems to improve the quality of the IONPs obtained.

In a ratio 1:1, the IONPs obtained had a D_H = 213.8 ± 5.3 nm (δ = 2.5%), whereas in a ratio 2:1 this decreased to D_H = 178.7 ± 0.8 nm (δ = 0.45%). While the change in hydrodynamic diameter was not considerable, this did affect the relaxivity properties of the IONPs.

4.2.3.3.3 Relaxivity of IONP-DHCA in solution

Once the stability of the IONPs obtained after ligand exchange with 3,4-dihydroxyhydrocinnamic acid was confirmed in water and PBS by DLS, their potential as MRI contrast agents was determined by measurement of their relaxivity. Their relaxivity properties were measured at 1.47 T within the facility of our collaborators Professor Begin-Colin and Dr Mertz from the University of Strasbourg, and at 7 T by our collaborators Professor Srinivas and Dr Gharagouzloo from Northeastern University.

Nanoparticles obtained in section 4.2.3.3.2 were initially tested. The r_1 and r_2 values were measured according to the linear relationship of longitudinal and transverse relaxation rates *versus* the magnetic metal concentrations of Fe. The obtained values at 1.47 T were: r_1 = 7.95 mM^{-1} s^{-1} and r_2 = 185.58 mM^{-1} s^{-1}. The relatively high r_2/r_1 ratio of 23.3 confirms that these IONPs are suitable as T_2 weighted contrast agents. As reported in Table 4-1, at the same frequency, in comparison to FDA-approved nanoparticles for MRI Resovist® and Endorem®, the NPs obtained had an improved r_2/r_1 ratio by a factor of more than 3.[299]

Table 4-1 Relaxivities for IONPs functionalised with 3,4-dihydroxyhydrocinnamic acid (DHCA) or tartaric acid (TA), and FDA approved contrast agents Endorem®and Resovist®measured at 1.47 T, at 37 °C in water.

	r_2 (mM^{-1} s^{-1})	r_1 (mM^{-1} s^{-1})	r_2/r_1
IONP-DHCA	185.58	7.95	23.3
IONP-TA	149.68	8.63	17.3
Endorem®	41	4.7	8.72
Resovist®	61	8.7	7

To determine the relaxivity value of the IONP-DHCA solution at 7 T, longitudinal (T_1) and transverse proton relaxation times (T_2) were measured as a function of iron concentration, at 37 °C. The different concentrations of IONPs for relaxivity characterisation were obtained by dilution with deionised water.
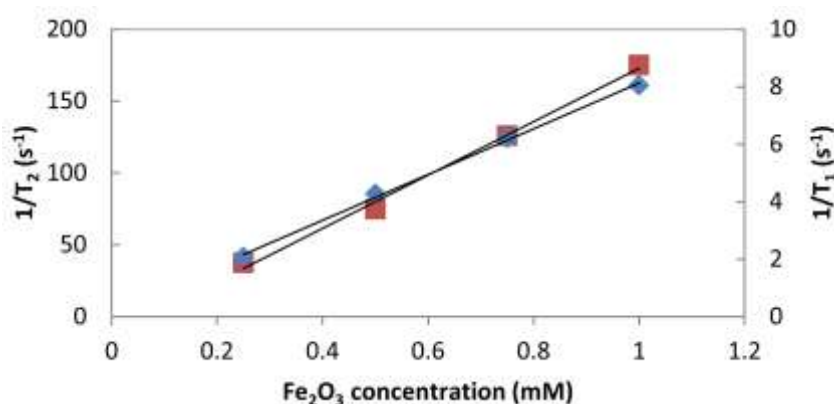
Figure 4-43 Relaxation rates 1/T$_1$ (■) and 1/T$_2$ (♦) over Fe$_2$O$_3$ concentration of the IONP-DHCA nanoparticles. The slope indicates the specific relaxivity (r$_1$ or r$_2$).

The IONPs exhibit r_1 and r_2 values of 0.78 and 142.2 mM^{-1} s^{-1} respectively. The r_2/r_1 value of 182.3 confirms that the IONP-DHCA has a significant advantage as a negative MRI contrast agent. Indeed, IONP-DHCA possess improved relaxivity properties in comparison to the relaxivity properties of FDA approved IONPs at 7 T: Ferumoxides® (r_1 = 1.8 mM^{-1} s^{-1}, r_2 = 132

Table 4-2 Relaxivity properties at 1.4 T of IONP-DHCA obtained with different ligand to IONP ratio after 48 h of ligand exchange and 10 d dialysis

Ratio ligand to IONP	1 : 1	2 : 1
r_1 (mM^{-1} s^{-1})	7.63	6.23
r_2 (mM^{-1} s^{-1})	50.77	72.46
ratio r_2/r_1	6.66	11.63

mM^{-1} s^{-1}, r_2/r_1 = 73.3) and Ferucarbotran® (r_1 = 1.6 mM^{-1} s^{-1}, r_2 = 205mM^{-1} s^{-1}, r_2/r_1 = 128.1).[308]

Finally, the effects of experimental parameters of the ligand exchange reaction were studied. These include the dialysis time or the mass ratio between DHCA and IONPs. For example, when the ratio of ligand to IONP was increased from 1:1 to 2:1, this did not have a significant impact on the hydrodynamic diameter of the IONPs obtained (section 4.2.3.3.2), but this did lead to an increase in relaxivity values as can be seen in the following Table 4-2.

Also, for the sample obtained with a ratio 2:1 in Table 4-2, after only 4 d of dialysis the relaxivity properties of these IONPs in solution were: r_1 = 2.08 mM^{-1} s^{-1}, r_2 = 8.3 mM^{-1} s^{-1} and r_2/r_1 = 3.98. This leads to the conclusion that increasing the dialysis time allowed us to eliminate any excess surface ligand which may hinder the interaction of the nanoparticles with surrounding water molecules as this has been observed with PEGylated Gd_2O_3 nanoparticles.[309]

4.3 CONCLUSIONS

The aim of this chapter was to establish a ligand exchange method to remove the TREG coating of IONPs and find a suitable ligand to confer stability and biocompatibility to the IONPs. Several methods were tested, and one was found to be successful with a ligand exchange method using IONPs in solution which were added to a ligand, stirred for 48 h and purified by dialysis against distilled water. While a number of ligands led to the immediate precipitation of the IONPs as determined by DLS, three other ligands provided stable dispersions of NPs and these were further characterised: citric acid, L-tartaric acid and 3,4-dihydroxyhydrocinnamic acid (DHCA). Table 4-3 provides a summary of the characterisation of the IONPs obtained after these 3 ligand exchange reactions.

ATR-FTIR demonstrated that citric acid could bind to the IONPs through its carboxylic functions. Immediately after the ligand exchange reaction, their hydrodynamic diameter in water was: D_H = 87.9 ± 0.9 nm and in PBS: D_H = 76.5 ± 2.1 nm. These citric acid coated IONPs exhibited superparamagnetic behaviour with M_s = 75.8 emu/g at 300 K. However, the IONPs were found to aggregate in saline conditions and under the application of an electric field. Further optimisation of the ligand exchange reaction conditions should be carried out including the pH and the ratio between the ligand and NP.

With L-tartaric acid, the bond of the ligand to the surface of the IONP was confirmed by ATR-FTIR through its carboxylic group. The IONPs obtained were characterised by superparamagnetic behaviour with M_s = 76.5 emu/g at 300 K. Their hydrodynamic diameter was measured: D_H = 192.7 ± 9.6 nm (δ = 5%) in water and 243 ± 72 nm (δ = 29%) in PBS, however slight aggregation was observed after several weeks. The effect of experimental parameters on IONPs obtained such as the mass ratio of the ligand to IONP, and the dialysis time were studied. Increasing the ratio of L-tartaric acid to IONP led to IONPs with an increased hydrodynamic diameter. However, a longer dialysis time of up to 7 d decreased the diameter to D_H = 168.4 ± 5.7 nm (δ = 3.4%). Finally, their relaxivity values were

measured at 1.4 T: r_1 = 8.63 mM^{-1} s^{-1} and r_2 = 149.68 mM^{-1} s^{-1}. The relatively high r_2/r_1 ratio of 17.3 confirms their potential as MRI T_2 weighted contrast agents. However, as their aggregation could not be resolved, these IONPs are not suitable for potential biomedical applications and will not be further studied *in vitro*. Finally with DHCA, ATR-FTIR showed that this ligand had reacted to the surface of the IONP through its catechol group. Their hydrodynamic diameter was D_H = 154 ± 4.5 nm (δ = 2.9%) in water and 140 nm ± 4.5 nm (δ = 3.2%) in PBS, and no aggregation was observed. The effect of experimental parameters on IONPs obtained such as the mass ratio of the ligand to IONP, and the dialysis time was studied. Increasing the ratio of ligand to IONP did not have a significant effect on the diameter of the IONPs obtained. On the other hand, a longer dialysis time of up to 15 d led to a decrease in their hydrodynamic diameter from D_H = 203.2 ± 2.2 nm (δ = 1.1%) after 5 d to D_H = 145.5 ± 1.3 nm (δ = 0.9%) after 15 d. The IONPs obtained displayed superparamagnetic behaviour with M_s = 73.6 emu/g after 5 d of dialysis and M_s = 73.1 emu/g after 15 d dialysis. Their potential as MRI contrast agents was confirmed at 1.4 T and 7 T. The relaxivity of the IONPs was at 1.47 T: r_1 = 7.95 mM^{-1} s^{-1} and r_2 = 185.58 mM^{-1} s^{-1}, and at 7 T: r_1 = 0.78 mM^{-1} s^{-1} and r_2 = 142.2 mM^{-1} s^{-1}. The r_2/r_1 value of 23.3 at 1.4 T and 182.3 at 7 T confirms these nanoparticles are suitable as T_2 weighted contrast agents and can be tested *in vitro* and *in vivo* to determine their biocompatibility as potential MRI contrast agents.

Table 4-3 Summary characterisation of the IONPs obtained after ligand exchange with different citric acid, L-tartaric acid and 3,4-dihydroxyhydrocinnamic acid (DHCA). The nature of their bond to IONPs was obtained from ATR-FTIR data. Hydrodynamic diameters (D_H) were measured in water and PBS immediately after synthesis. Saturation magnetisation (M_s) was obtained at 300 K. The total organic coating was determined by thermogravimetric analysis between 28 °C and 600 °C. The relaxivity values were measured in water at 37 °C and at 1.47 T.

Ligand	Citric acid	L-tartaric acid	DHCA
ATR-FTIR	Bind to Fe *via* COOH groups	Bind to Fe *via* COOH groups	Bind to Fe *via* catechol groups
D_H (nm)	87.9 ± 0.9 nm in water 76.5 ± 2.1 nm in PBS	192.7 ± 9.6 nm in water 243 ± 72 nm in PBS	154 ± 4.5 nm in water 140 nm ± 4.5 nm in PBS
M_s (300 K)	75.8	76.5	73.6 emu/g after 5 d dialysis 73.1 emu/g after 15 d dialysis
Total organic coating (%)	10	23	24
Relaxivity (1.47 T)	N/A	$r_1 = 8.63$ mM^{-1} s^{-1} $r_2 = 149.68$ mM^{-1} s^{-1} $r_2/r_1 = 17.3$	$r_1 = 7.95$ mM^{-1} s^{-1} $r_2 = 185.58$ mM^{-1} s^{-1} $r_2/r_1 = 23.3$
Stable and biocompatible IONPs obtained?	no	no	yes

Chapter 5 INTERACTION OF FUNCTIONALISED NPS WITH hMSCS

5.1 INTRODUCTION AND OBJECTIVES

In the previous chapters, the synthesis of IONPs within high pressure and high temperature conditions was achieved, followed by the optimisation of their stability through surface functionalisation with 3,4-dihydroxyhydrocinnamic acid (DHCA) were studied. Furthermore, their ability as negative contrast agents for MRI in solution was demonstrated at 1.47 T and 7 T. The relaxivity of the IONPs were at 1.47 T: r_1 = 7.95 mM^{-1} s^{-1} and r_2 = 185.58 mM^{-1} s^{-1}, and at 7 T: r_1 = 0.78 mM^{-1} s^{-1} and r_2 = 142.2 mM^{-1} s^{-1}. The r_2/r_1 value of 23.3 at 1.47 T and 182.3 at 7 T confirms these IONPs are suitable as T_2 weighted contrast agents and they have the potential to be used for cell labelling and cell tracking applications for stem cell therapy for example. Indeed, there is an urgent need for stem cell tracking in cellular therapy and regenerative medicine, superparamagnetic IONPs could be used as contrast agents in MRI to allow visualisation of the implanted cells ensuring they reach the desired sites *in vivo*.

In this chapter, the work presented aims to assess the suitability of these IONP-DHCA for biological applications, in particular for the labelling and tracking of bone marrow-derived primary human mesenchymal stem cells (hMSCs) by MRI.

In order to ensure their potential as contrast agents for cell labelling, their uptake in cells must first be assessed. This was carried out by TEM and iron-specific Prussian Blue staining. In order to quantify their cellular uptake, the amount of iron was determined using a colourimetric method. Finally, several methods were necessary to assess the effect of cell-nanoparticle interactions. Indeed, it was determined that information obtained from conventional methods such as flow cytometry or colourimetric viability assays (for example MTT assay) are not always suitable for IONPs and have certain limitations that must be addressed. However, a multi parametric method such as high-content analysis was suitable to evaluate the effect these IONPs had on cell morphology, cell viability, mitochondrial

health and the production of reactive oxygen species. High-content analysis describes a set of analytical methods using automated high-resolution microscopy, multi-parameter image processing, and molecular tools of cell biology tools to extract quantitative data from large cell populations. Finally, the potential of IONP-DHCA as a negative contrast agent was investigated *in vitro* with hMSCs and preliminary data was obtained *in vivo* using a Swiss female mice model.

5.2   RESULTS

In recent years, research on the development of SC therapy has intensified. The potential to use SCs in tissue engineering and regenerative medicine is promising, as their use has already been implemented in a few human clinical trials.[310-313] However, a number of questions remain regarding the function of the transplanted SCs as well as their localisation and movement. To answer these, certain characteristics of IONPs can be used with a potential of gaining a better understanding of the role of SCs and validating clinical transplantations.[5, 6, 314-316] Indeed, IONPs may be used to monitor the fate of SCs in a non-invasive manner using MRI. As mentioned in chapter 1, to date, IONPs, which were FDA-approved as MRI contrast agents for the liver, have been taken off the market. As reported in the previous chapters, IONPs were successfully synthesised through a high pressure high temperature method using the polyol route, before functionalising the surface with DHCA.[262] For the work described in this chapter, the IONPs obtained were spherical and with an average diameter of d_{TEM} = 16.8 ± 1.9 nm (δ = 11.1%, n = 324) as determined by TEM (Figure 5-1). The hydrodynamic diameter of these IONPs was measured in aqueous solution by DLS and was determined to be d_H = 88.2 ± 2.4 nm (δ = 2.7%). The zeta potential determined from at least three measurements in water was: ζ = - 23.5 ± 1.8 mV, at pH = 6.8 and electrical conductance = 0.173 µS. XRD was used to confirm that these IONPs were indeed iron oxide and have an inverse spinel structure, either magnetite Fe_3O_4 or maghemite γ-Fe_2O_3, although these phases cannot be distinguished by XRD due to their similar diffraction pattern and peak broadening effects. The IONPs may contain either or
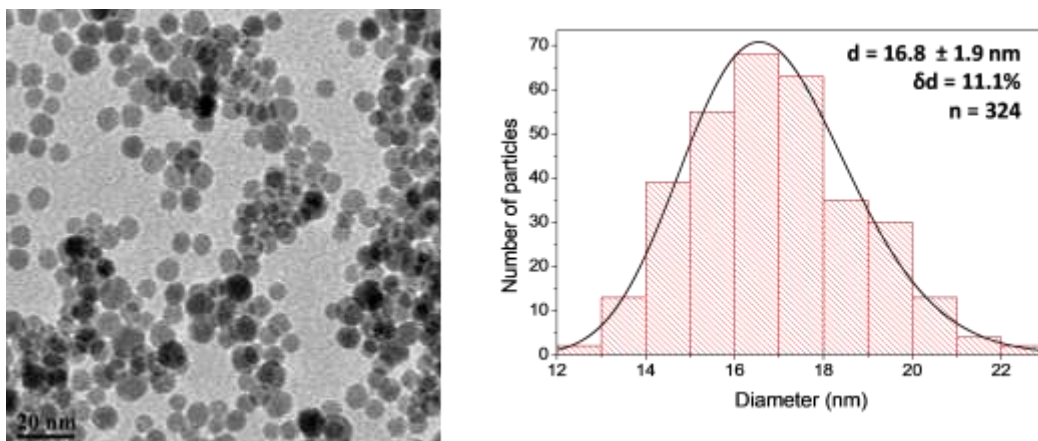
Figure 5-1 TEM images and particle size distributions of iron oxide nanoparticles synthesised. Magnification 25 k scale bar 20 nm. Size distributions were fitted with a log normal function (solid line), d= mean diameter, δd = standard deviation and n = number of particles counted.

both of these iron oxide phases. The crystallite diameter of d_{XRD} = 7.8 nm determined approximately by the Scherer equation was coherent with that of the core size measured by TEM. The IONPs displayed a superparamagnetic behaviour at RT as determined by SQUID-VSM between -7 and 7 T at 300 K, with M_s = 90 emu/g. This value is consistent with superparamagnetic IONPs of similar size and obtained by the polyol method.[86, 249, 262] This value is slightly smaller than the theoretical magnetisation value for bulk magnetite (92–100 emu/g),[36, 81] and this is due to a finite size effect: canting of surface spins which are unaligned with the spins present in the rest of the magnetic domain.[133] This effect is more pronounced for nanoparticles of smaller size.[263]

5.2.1 *Prussian Blue staining of hMSCs with IONP-DHCA*

hMSCs were incubated with IONP-DHCA for 24 h at various concentrations ranging from 0 to 150 µg Fe per ml, then the cells were fixed and stained with Prussian blue, and the extent of IONP uptake was confirmed by optical microscopy.

The iron-specific Prussian Blue staining (Figure 5-2) allowed visual confirmation of the association of IONP-DHCA and hMSCs. The labelling efficiency seemed to increase in a dose dependent manner with the incubation concentration. However, these results lead to the hypothesis that the uptake is not necessarily higher at 50 µg Fe per ml, but instead that aggregates of IONPs were formed, which may have attached to the bottom of the well or to the extracellular surface. In the future, this may be optimised by modifying the IONP surface ligand or the incubation conditions. Overall, it is essential to note that hMSCs incubated with IONP-DHCA remained adherent and maintained their usual fibroblast-like shape similarly to the control.

5.2.2 *Cell uptake visualised by TEM*

Cell uptake and intracellular IONP distribution in MSCs were visually confirmed by TEM. Images were obtained at different incubation times of 1 h, 4 h and 24 h and at a concentration of 50 µg Fe per ml, as this concentration is deemed non-toxic and safe where the IONPs did not have any effect on cell morphology, viability, mitochondrial health and did not lead to the production of any reactive oxygen species (section 5.2.6).
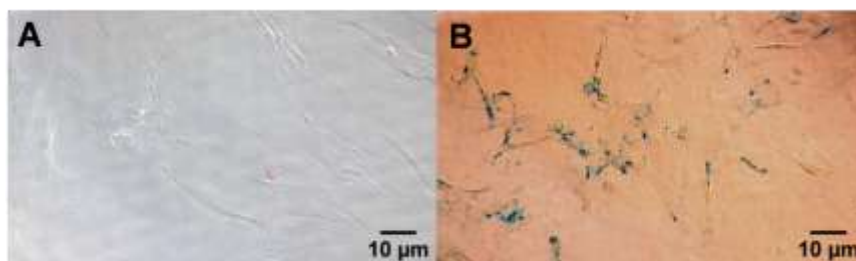
Figure 5-2 Prussian Blue staining images of cells labelled for 24 h with A) 0 and B) 50µg Fe per ml of IONP-DHCA. Scale bar 10 µm.
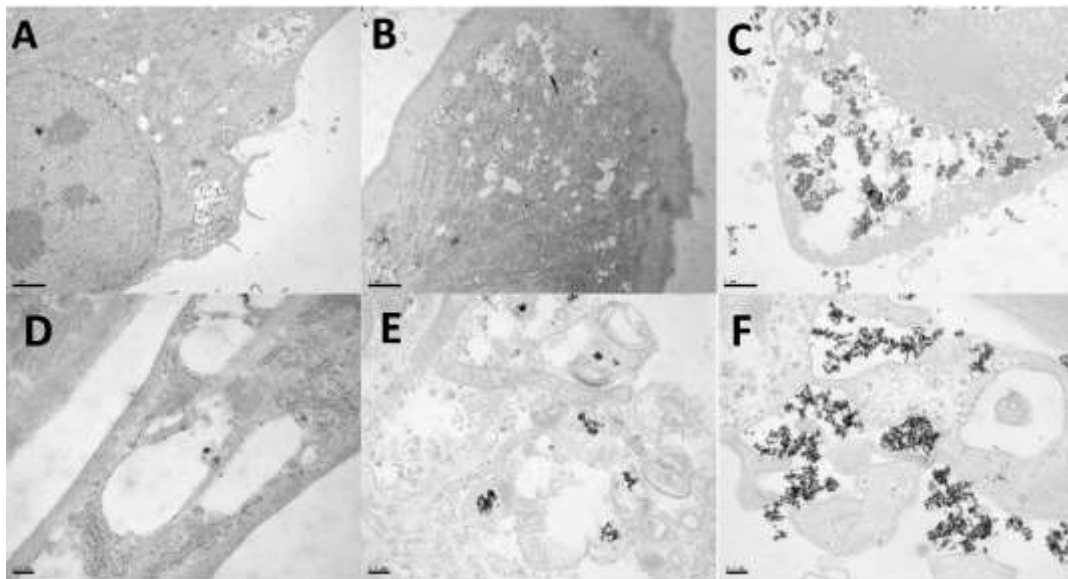
Figure 5-3 TEM images of hMSCs incubated with IONPs at 50 µg Fe/ml for 1 h (A, D), 4 h (B, E) and 24 h (C,F). A-C images scale bar = 2 µm and D-F scale bar = 0.2 µm.

From these images can be confirmed the successful uptake of IONPs by hMSCs; however this process is relatively slow as few IONPs are observed after incubation times of 1 h and 4 h. It is only after 24 h that significant amounts of IONPs can be visualised within the cells and at their surface as seen in Figure 5-3. As it has been reported extensively in literature,[317-320] these IONPs also seem to undergo endocytosis and are therefore located in endosomes. The IONPs which are internalised within the cell vacuoles could mainly be found as aggregates. Furthermore, IONPs were not observed near the nucleus, as it seems these aggregates would be physically unable to breach the nuclear membrane pores with sizes in the range of 10 – 20 nm. Membrane deformation was also observed, confirming the internalisation of IONPs by endocytosis.

5.2.3 *Quantification of cell uptake by a colorimetric method*

To quantify the amount of IONPs taken up by hMSCs, a colorimetric method based on the chelation of Fe^{3+} by Tiron was used. The quantity of IONPs taken up by cells is an important factor to consider as this will determine how efficient the nanoparticles are as MRI contrast

agents, as well as the impact they will have on the cell viability and proliferation. Below, Table 5-1 sums up the amount of iron taken up by hMSCs and the uptake efficiency after 24 h of incubation. The uptake percentage was determined as the ratio between the final amount of iron measured with 20 000 cells/well, and the initial incubation amount of iron.

These results confirm that, for all concentrations studied, the uptake of these IONPs by hMSCs is significant; this can be supported by the TEM images obtained *in vitro* (Figure 5-3). The significant uptake in IONPs of hMSCs may be correlated to their strong negative surface charge and is dose dependent. These results tend to confirm that some of the IONPs accounted for may not be internalised, but remain on the surface of the cells. It is a well-established fact that the uptake of IONPs depends on the size of the cells, more precisely their surface area.[321]

The surface ligand may contribute to this phenomenon, and may cause IONPs to stick to the bottom of the wells and the surface membrane of cells thus overestimating the amount of iron taken up by cells. For high incubation concentrations, it was noticed that as the nanoparticles are in excess in the culture medium, aggregates can be observed (Figure 5-3 F). A more accurate method of quantifying the cellular uptake is by measurement of relaxivities in each well, but this required a large number of cells (500 000 cells/well). It is quite difficult to obtain high enough number of hMSCs for this analysis, due to their limited proliferation capacity which is dependent on the age of the donor from which they are sourced and the culture conditions (media composition, temperature, CO_2 and humidity) which are used for their expansion. The uptake efficiency is within the range of values reported in the literature with, for example, an efficiency of 26% for 5 nm NPs.[322] However, this parameter is strongly dependent on the NP size, shape and type as well as the cell line considered, with values as high as 80 to 90% measured with gold NPs in presence of liver cells.[323]

Table 5-1 Quantification of cellular uptake of IONPs by hMSCs determined by the colorimetric method

Incubation concentration (µg Fe/ml)	Iron uptake per cell determined by colourimetric method (pg) / Uptake percentage (%)
10	72 / 29
100	819 / 33
150	1108 / 30

Single-cell magnetophoresis is a method, which would allow us to obtain accurate and single cell information about the amount of iron taken up by cells. When cells are moving towards a magnet, any IONPs bound to their surface and which have not been internalised will be visualised as small chains of aggregates transported by the cell. This technique also previously revealed that colorimetric assays can lead to overestimation of the quantity of iron taken up by a factor of three in the case of agglomerated IONPs.[324] Also, flow cytometry is another method used to determine if the nanoparticles are internalised within the cells or not. Nanoparticles must be labelled with a fluorescent dye such as FITC. Trypan blue is a stain routinely used to determine cell viability because it is excluded by viable cells. This characteristic, in addition to the fact that it can quench the fluorescence of FITC,[325, 326] has been used to differentiate between nanoparticles extracellularly associated and those internalised by viable cells.[327] Indeed, their uptake in cells is assessed by flow cytometry with Trypan Blue staining before the measurement. This stain will quench the fluorescence of nanoparticles bound to the cellular surface, whereas the fluorescence of internalised nanoparticles will not be affected.[328]

5.2.4   *Colorimetric viability assays (MTT and MTS)*
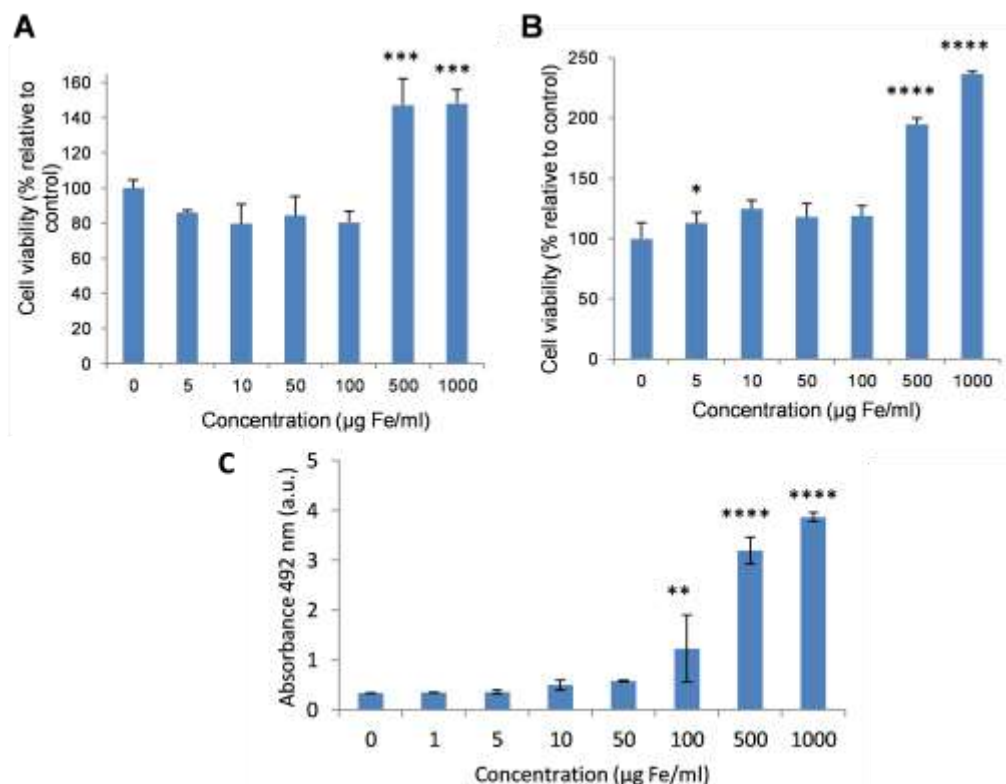
Figure 5-4 *In vitro* **cell viability studies on human mesenchymal stem cells after 24 h incubation with IONP-DHCA** at **concentrations ranging from 0 to 1000 µg Fe per ml. A) MTT assay and B) MTS assay. C) Absorbance of IONP-DHCA only at different Fe concentrations, measured at 492 nm in the same conditions as MTT and MTS assays performed on hMSCs. Each graph shows the mean ± SD (standard deviation) of three independent experiments. The degree of significance is indicated when appropriate *P < 0.05, **P < 0.01, ***P < 0.001 and ****P < 0.0001 (*one-way ANOVA*, Dunnett post-hoc test).**

TEM and Prussian Blue staining have demonstrated that the synthesised IONPs were successfully taken up by endocytosis in hMSCs after 24 h. However, in order to be considered for stem cell labelling applications, it must be ensured that these IONPs are biocompatible and not toxic to hMSCs when exposed to increasing concentrations of IONPs. For this, conventional colourimetric assays, MTT and MTS assays, were carried out, which determine the cytotoxic effects of IONPs on cell metabolic activity or cell viability.

These cytotoxicity assays rely on the same principle and only differ by the nature of the product obtained: the MTS assay does not require solubilisation of the formazan compound formed. Initial assays were conducted with hMSCs incubated during 24 h with IONP-DHCA concentrations ranging from 0 – 1 mg Fe/ml. The results obtained are presented in Figure 5-4.

At lower concentrations of Fe, up to 100 µg Fe/ml, no significant toxic effects were observed by either assay: a cell viability of about 80% was measured at 100 µg Fe/ml. However, it can be observed that the cell viability increases significantly for elevated concentrations of IONPs (500 and 1000 µg Fe/ml). Figure 5-4 C demonstrates that this method is not suitable to assess the cytotoxic effects of IONPs at high concentrations (above 100 µg Fe/ml) as the values measured (Abs > 1) are no longer within the linear absorbance range. As a consequence, the percentage of viable cells is abnormally high for these concentrations. This increase in cell viability measured with both assays is therefore due to interference of the IONPs present in solution with the MTT and MTS dye (Figure 5-4). This finding is in line with literature data, where interference of IONPs with the MTT assay has been reported,[329, 330] and demonstrates that colorimetric assays are not technically suitable for high concentrations of IONPs. In most of today's published research, these assays remain routinely used to confirm the biocompatibility of nanoparticles synthesised with various cell lines.[331, 332] While the interference of IONPs may be subtracted from the absorbance values measured, it is not possible to conclude with certainty the effect of the internalised nanoparticles *in vitro*. Furthermore, these assays only give us information on the bulk of the cell populations present, without being able to directly observe and determine the impact of the nanoparticles on the cells.

5.2.5   *In vitro analysis of cell viability by flow cytometry*

To assess the effect of IONP-DHCA, and the mode of death they may induce on hMSCs, flow cytometry was tested as it is suitable to determine which cells are viable, apoptotic or
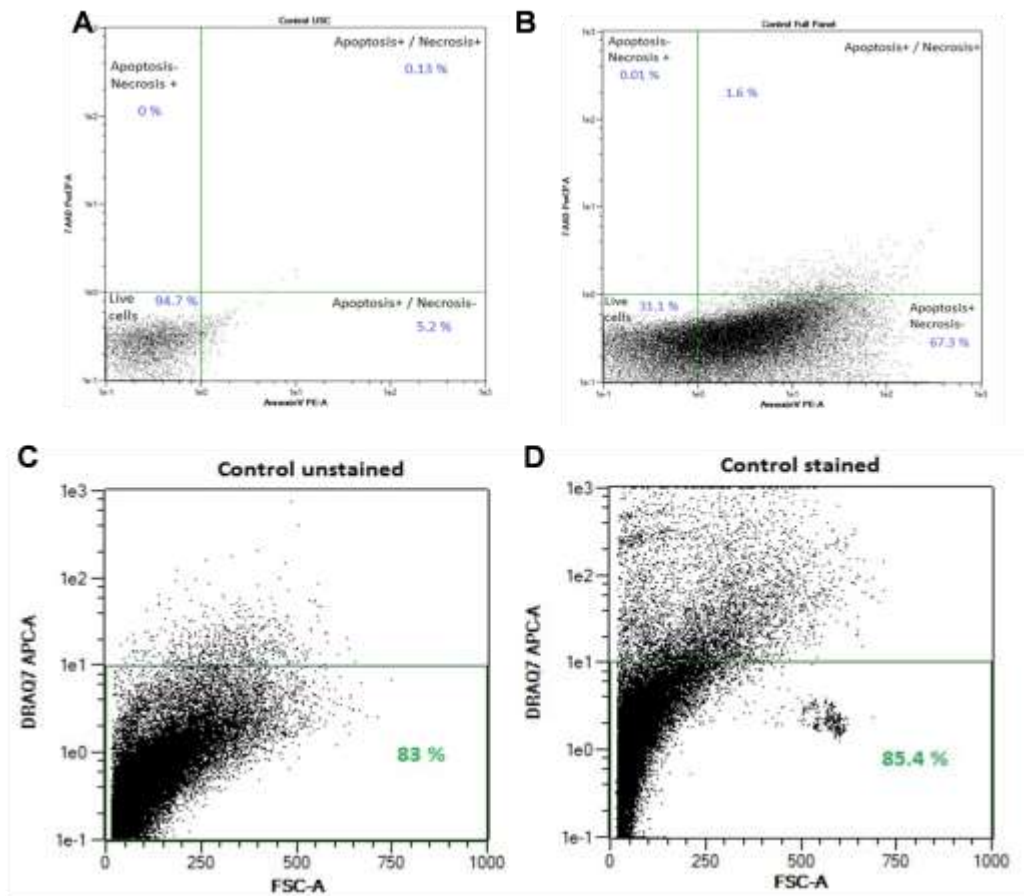
Figure 5-5 Representative flow cytometry dot-plots obtained of a control sample consisting of only hMSCs. A) Before and B) after staining cells with Annexin V- phycoerythrin (x-axis) and 7-Aminactinomycin D (y-axis); C) Before and D) after staining cells with DRAQ7 (y-axis)

necrotic. Annexin V-phycoerythrin (PE) and 7-aminactinomycin D (7-AAD) double staining was used to detect cell membrane changes as this is routinely used to investigate the effect of nanoparticles on various cell populations.

Annexin V binds to phosphatidylserine (PS), which is normally located in the inner cell membrane in healthy cell populations. However, when a cell undergoes apoptosis, phosphatidylserine is flipped and can be found on the external cellular membrane, and can thus bind Annexin V.

7-AAD will bind to DNA, and thus is a marker of necrotic cell death. Unlike propidium iodide (PI), another DNA marker which is more frequently used than 7-AAD in flow cytometry, the fluorescence emitted by 7-AAD has been shown to be more stable and it does not leach from cells.[333] Indeed, late apoptosis is also characterised by the formation of pores appear on the membrane making it permeable to PI, which gives the cells double staining (Annexin-PI). In case of necrosis, the cell membrane also becomes permeable leading to PI staining. While externalisation of PS during necrosis does not always occur, when it does, the porous membrane can lead to the possible internalisation of Annexin V. In this case, it is not possible to differentiate the process of apoptosis from necrosis.[334, 335]

However, as we can see from the results in Figure 5-5, there are still some difficulties using this method. As it can be seen with the unstained cell population (A), 95% of the cell population is deemed viable (apoptosis negative, necrosis negative), which is expected of a control sample consisting of cells having undergone cell culture, and which is consistent with the Trypan Blue staining conducted (not shown here). When treating cells with Annexin V and 7-AAD, within the same population, only 31% of the cells are viable (apoptosis -, necrosis -), 2% are dead (apoptosis +, necrosis +) and 67% are undergoing apoptosis (apoptosis +, necrosis -). From these experiments, it was hypothesised that the abnormally high percentage of cells which are Annexin V positive are false positives. This is probably due to the detachment of the hMSCs from tissue culture flasks by trypsinisation which may lead to temporary membrane damage, thus leading to an Annexin V positive signal.[336, 337] Indeed, the binding of Annexin V to PS can be affected in adherent cells, which are detached from tissue culture flasks by an enzymatic or mechanical method. The latter may disrupt the cellular membrane and lead to false positives as during cell detachment (with Trypsin or other methods), PS residues in the membrane may translocate and give false positive results. The method of detachment of cells is cell-line dependent and its effect on the integrity of the cellular membrane cannot be predicted. It is therefore crucial to evaluate the cell detachment method and analytical method to ensure the results obtained are conclusive.[338] While some studies still use Annexin V staining for flow cytometry, MSCs are

often limited to low concentrations of IONPs (< 100 µg/ml). Recent publications investigating the impact of IONPs on MSCs have determined the viability of cell populations exposed to NPs through more simple yet reliable optically-based methods such as Trypan Blue staining,[339] or the neutral comet assay which is based on single cell micro-electrophoresis of DNA content.[340, 341]
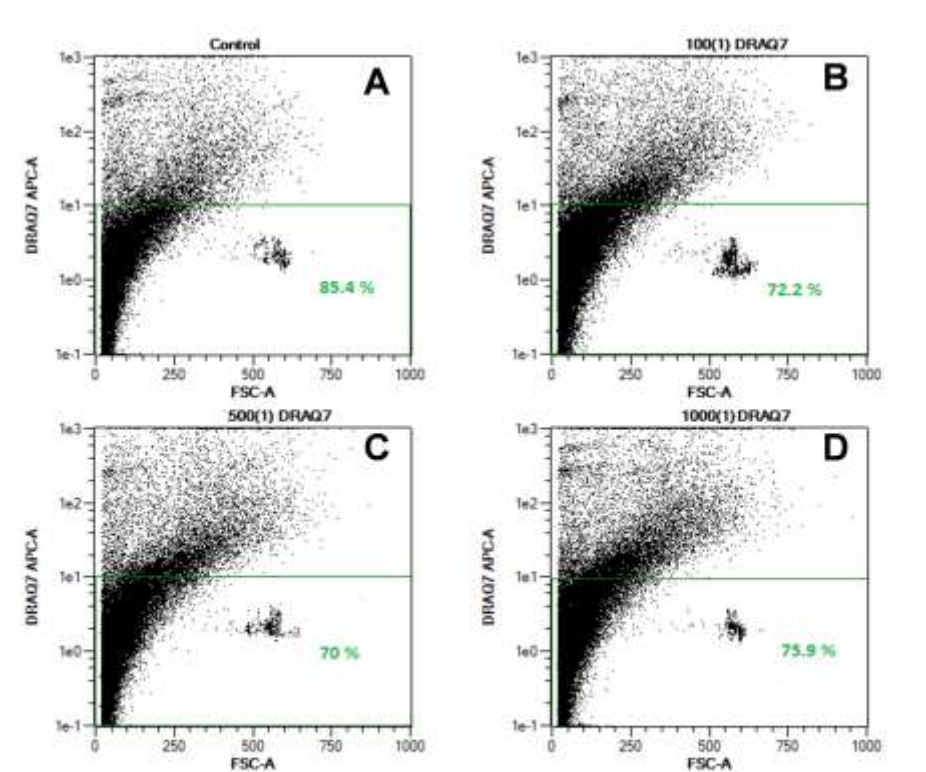
Incubation concentration (ug Fe/ml)	% viable cells
Control	83.4 ± 3.6
100	74 ± 2.6
500	73 ± 4.9
1000	68.7 ± 6.3

Figure 5-6 Representative flow cytometry dot-plots obtained for hMSCs after staining with DRAQ7 and incubation during 24 h with A) no IONP-DHCA, B)100 µg Fe/ml of IONP-DHCA, C) 500 µg Fe/ml of IONP-DHCA and D) 1000 µg Fe/ml of IONP-DHCA. E) Quantification of percentage of viable cells determined by DRAQ7 flow cytometry with each conditions being done in triplicates.

The flow cytometry analysis was repeated with another stain: DRAQ7, which emits in the far-red region and stains dead cells by binding to the DNA of cells with compromised plasma membranes.

This stain did not lead to an abnormally high percentage of dead cells: approximately 85% of non labelled cells were deemed viable which is coherent with Trypan Blue staining and 83% of viable cells in the unstained control. The results obtained with IONP-DHCA are illustrated in Figure 5-6.

After 24 h of incubation with 100 µg Fe/ml of IONP-DHCA, the percentage of viable is 74%, and the corresponding value for 1000 µg Fe/ml is 68.7% (Figure 5-6), indicating that the cell death induced in hMSCs by IONP-DHCA is dose-dependent. These results demonstrate that this method is suitable, and DRAQ7 is an adequate stain to determine the percentage of viable cells after exposure to IONPs.

5.2.6 *High content analysis of cell – nanoparticle interactions*

The MTT assay or other colorimetric assays mentioned previously can be classified as bulk-cell assays because the measurement corresponds to a response from a large cell population.[49] The behaviour of individual cells is not considered as the measurement is the overall absorbance collected from a cell lysate. One major disadvantage of these methods is that it is difficult to distinguish whether the results observed are homogenously obtained from all cells or whether they are due to a large response from a small subpopulation of cells. These colorimetric methods are in fact averaged for the entire cell population analysed and may therefore be misleading. Furthermore, these assays do not provide any information about the mechanism for cell death, such as the enzymatic pathway involved or the gradual changes in cell morphology and activity, as only the end result *ie*. percentage of viable cells, is obtained. As observed in section 5.2.4, it has been demonstrated that interactions of dyes with IONPs are possible and this leads to false positive results.[342]

Furthermore, these colorimetric assays solely report information on a single parameter and on a macroscopic level.

The concentration of IONPs and their incubation time with cells are parameters known to impact their interactions with cells and the cytotoxicity induced. In most literature, it is suggested that a wide range of IONP concentrations are tested with exposure times of at least 4 h. Short incubation times will only provide information on immediate cytotoxic effects due to exposure to the IONPs but long-term effects may remain unknown.

Therefore, to circumvent these issues, for this work high-content imaging analysis was used as it provides multiparametric, image based information on a large number of cells.[343] The large population of cells imaged in an automated manner renders this method quantitative with high statistical power. High content imaging furthermore enables one to measure many parameters at the same time, is able to provide visual confirmation of the results obtained and gives an idea on the variability of any parameter evaluated within the sample tested rather than providing a single unit.[344] This technique allows us to generate large datasets studying various cytotoxicity parameters while experimental conditions are kept consistent for all cellular – IONP interactions. A robust and reliable comparison of potential toxic responses across different conditions can be obtained by this methodology. Furthermore, in comparison to conventional in vitro proliferation assays, visualising and quantifying the nuclear stain intensity and morphology by high content imaging provides essential information regarding the potential toxic mechanisms of nanomaterials which may affect the cell cycle and cell survival.[345]

In high content imaging, several parameters are studied simultaneously and we can directly observe the effect on the IONPs on the cells. In this case was studied the cell viability, oxidative stress, mitochondrial health and the change in the morphology of the cells.

The high-content (HC) imaging based methodology used here has been demonstrated in various publications to be an effective means for determining interactions between cells and NPs.[346, 347] This technique allows the generation of large datasets comprising of thousands of cells per sample per replicate. Coupled with a sophisticated automated image analysis software, multiple parameters can be studied in a population of cells or at a single cell level.

High content imaging was used in order to determine cell viability and changes to cellular morphology. 1000 hMSCs per well in a 96-well plate were incubated with IONP-DHCA for 24 h at concentrations ranging from 0 to 250 µg Fe/ml and stained the nucleus with Hoechst, while actin was stained with Acti-Stain 488 (*see section* 2.2.16) (Figure 5-7).
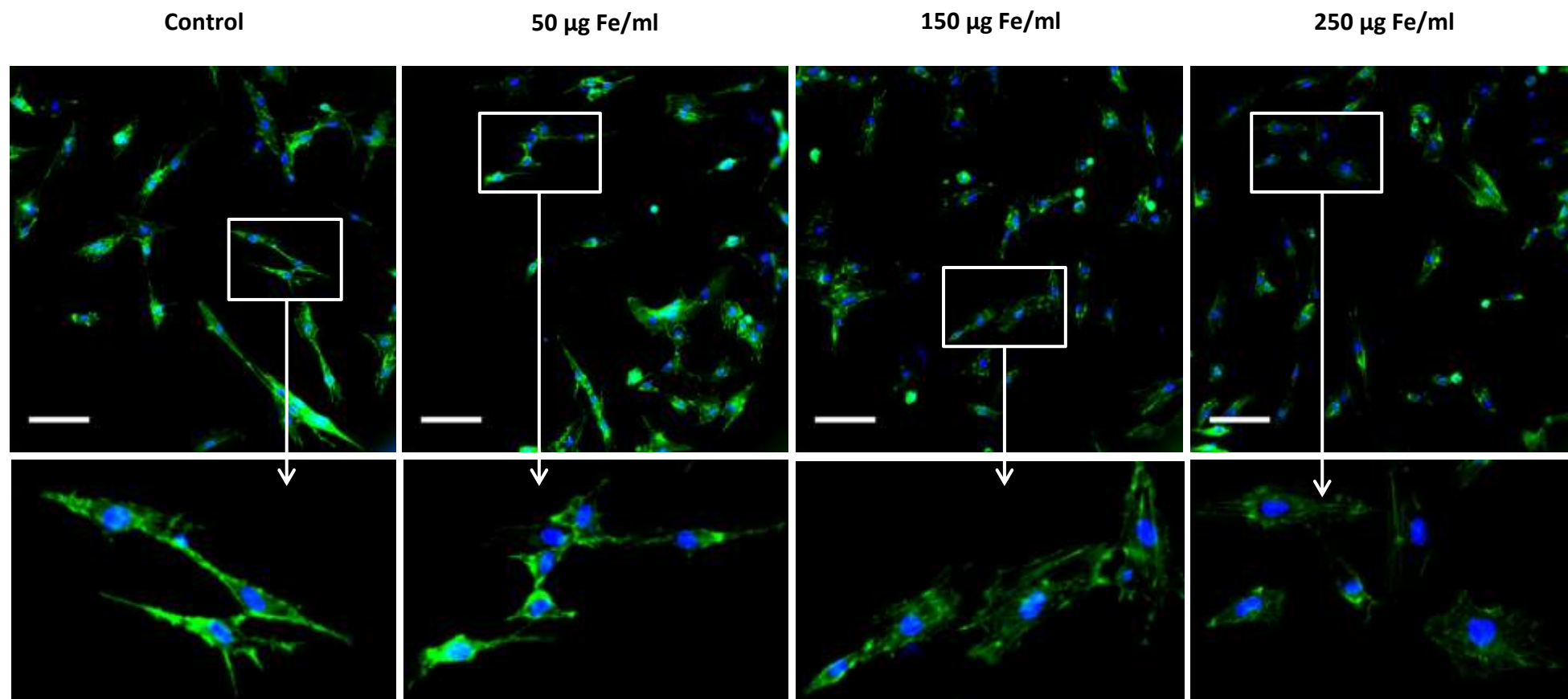
Figure 5-7 Representative images of high-content imaging setup of hMSCs stained for nucleus (blue) and actin (green), scale bar 100 µm.

It has previously been demonstrated that nanoparticles may result in actin cytoskeleton deformation, leading to disruption in actin-mediated cell signalling, and which may in turn disrupt the cell proliferation ability.[348] The exact mechanism of actin cytoskeleton deformation has yet to be established. This phenomenon may be accompanied by a normal actin protein expression level which suggests an indirect effect of NPs on the cytoskeleton through physical deformation by clusters of NP degradation products near the nucleus,[349] and modification of Ca^{2+} cell signalling pathways through degradation of metal-based NPs.[350]
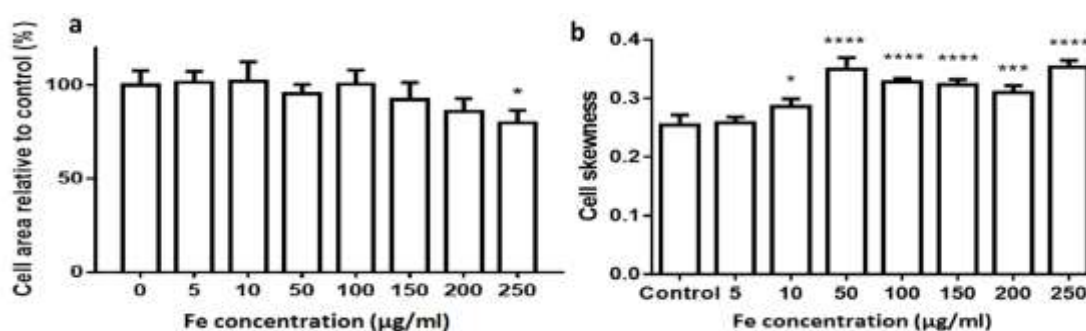
Figure 5-8 From the images captured by high content analysis, the spreading of the cell was calculated (a), as well as the cell skewness (width of the cell over the length of the cell) as seen in (b). Data are represented relative to untreated control cells as mean ± SD for minimum 500 cells per condition, 3 replicates per condition. The degree of significance is indicated when appropriate *P < 0.05, **P < 0.01, ***P < 0.001 and ****P<0.0001 (one-way ANOVA, Dunnett post-hoc test).

As seen in Figure 5-8, high-content imaging analysis determined that the cell area was not affected following exposure to low concentrations of IONPs and that it is only above 100 µg Fe/ml that the cell area starts to decrease. However, the IONPs seemed to have a more significant impact on the cell aspect ratio with the cell skewness increasing above 50 µg Fe/ml. The latter indicates that the cell length decreases as the cells changes from its usual fibroblast-type shape to a slightly more spherical shape. In order to investigate whether this had an impact on the cellular activity, we then used high-content imaging to determine the effect of the IONPs on cell viability, mitochondrial activity and reactive oxygen species formation.

| Control | 50 µg Fe/ml | 150 µg Fe/ml | 250 µg Fe/ml |
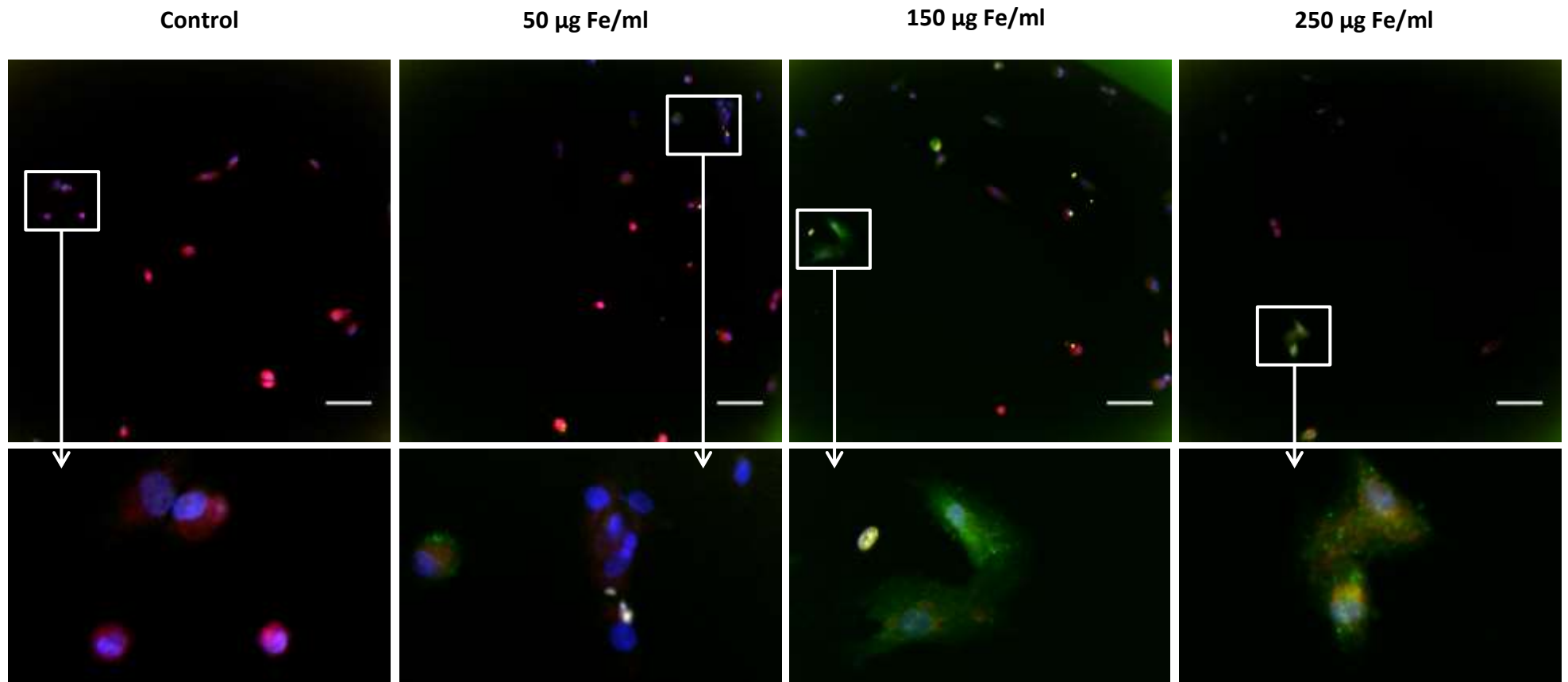
Figure 5-9 Representative images of high-content imaging setup of hMSCs stained for nucleus (blue), cell viability (yellow), oxidative stress (green) and mitochondrial health (red), scale bar 100 µm.

A

B
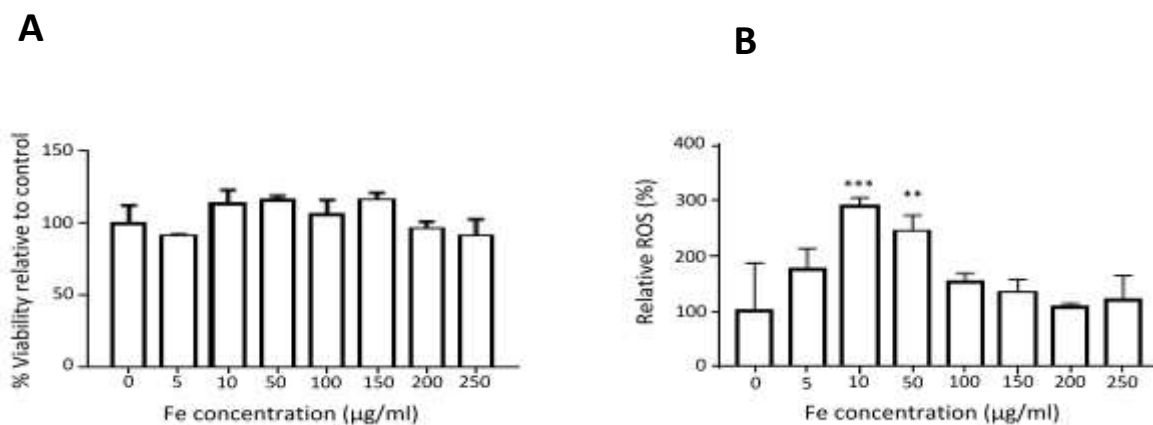
Figure 5-10 Oxidative stress and cell viability of hMSCs labelled with IONPs at various concentrations and determined by high-content imaging reveals significant induction of reactive oxygen species (ROS; green colour) at 10 and 50 µg Fe/ml. Additionally, these particles display reduction in A) mitochondrial viability (red colour) for a high concentration of 250 µg Fe/ml. B) Relative production of ROS determined by high-content imaging. Data are represented relative to untreated control cells as mean ± SD for minimum 500 cells per condition, scale bar 100 µm. The degree of significance is indicated when appropriate *P < 0.05, **P < 0.01 and ***P < 0.001 (one-way ANOVA, Dunnett post-hoc test).

The IONPs did not have a significant effect on the viability of the cells (DRAQ7 in yellow) or on the mitochondrial area (Figure 5-10 and Table 5-2). However, an increase in ROS production was noticeable at 10 and 50 µg Fe per ml, but this did not have a direct impact on the mitochondrial health and was not induced at other concentrations (Table 5-2). Elevated ROS production often does not cause any significant toxicity, as all cells possess intrinsic antioxidant properties that protect them against oxidative stress.[351] Oxidative stress induced by IONPs is due to the intrinsic properties of the NPs such as particle surface, size, composition, and presence of metals. Further studies on the physicochemical properties of IONP-DHCA at 10 and 50 µg Fe per ml will need to be carried out to investigate the possible phenomena which may occur at these concentrations and which are responsible for the slightly elevated levels of ROS.

Table 5-2 From the images captured by high content analysis, mitochondrial area and mitochondrial activity were calculated. Data are represented relative to untreated control cells as mean ± SD for minimum 500 cells per condition. The degree of significance is indicated when appropriate *P < 0.05, **P < 0.01 and ***P < 0.001 (one-way ANOVA, Dunnett post-hoc test).

Fe concentration (μg/ml)	Relative mitochondrial area (%)	Relative mitochondrial activity (%)
0	100 ± 7.6	100 ± 19
5	89 ± 19.9	88.9 ± 8
10	91 ± 18.9	84.6 ± 1.6
50	75.7 ± 14.9	91.3 ± 8.2
100	85.8 ± 20.9	83.6 ± 5.4
150	88.1 ± 5.9	83.2 ± 6.4
200	86.6 ± 4.9	80.4 ± 3.7
250	75 ± 18.7	77.1 ± 2 *

5.2.7 *In vitro MR image acquisition*

In order to determine the suitability of IONP-DHCA as MRI contrast agents, it is essential to determine their physicochemical properties *in vitro* when they interact with the cells. This will allow us to determine whether any change in relaxation effects occurs once they have been internalised by hMSCs. The raw data illustrating the evolution of mean values of T_1, T_2 and T_2^* from *in vitro* MR acquisition can be found in Appendix 4.

Figure 5-11 clearly demonstrates an overall dose dependent decrease of the mean values of T_1, T_2 and T_2^* as a function of the concentration of Fe. This effect has been observed with several types of nanoparticles and has been attributed to their endosomal internalization in cells which causes a clustering and hence an increase in relaxivity.[352-354] Most relevant is the fact that Figure 5-11 demonstrates that the IONP-DHCA may be used in MRI to provide contrast enhancement.
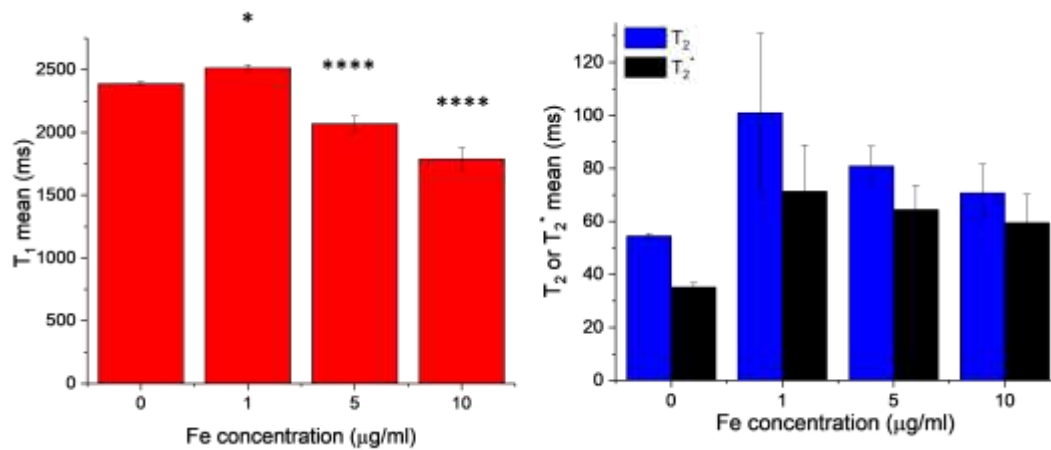
Fe concentration (µg/ml)	T_1 mean	T_2 mean
0	2388 ± 19	54.5 ± 0.9
1	2515 ± 27	101.0 ± 29.9
2	2565 ± 61	127.2 ± 69.0
5	2071 ± 60	80.9 ± 7.5
10	1788 ± 92	70.8 ± 10.8

Figure 5-11 Evolution of mean values of T_1, T_2 and T_2^* determined from *in vitro* MR acquisition with the Fe concentration. The degree of significance is indicated when appropriate *P < 0.05, **P < 0.01 and ***P < 0.001 (one-way ANOVA, Dunnett post-hoc test).

5.2.1 *In vivo MR imaging of IONP-DHCA*

Iron oxide nanoparticles as T_2 contrast agents have been extensively used in liver MRI. Before the animal study, the cytotoxicity of IONP-DHCA was first determined using hMSCs as a model. The high-content imaging method was shown to be a suitable technique and proved that IONP-DHCA have no appreciable cytotoxicity for 24 h even at concentrations up to 250 µg Fe per ml, suggesting the high biocompatibility of these nanoparticles. Furthermore, in our previous work,[262] their potential as potential MRI contrast agents was confirmed with their high relaxivity values measured at 1.4 T in solution(results in chapter 4). Results regarding the safety and properties of NPs may differ between *in vitro* and *in vivo* experiments. To verify their ability as contrast agents *in vivo*, T_2-weigthed MRI of liver was conducted using 6 female Swiss mice as a model. The images of the MRI scans included in Figure 5-12 are all from the same slice number, the main organs have been labelled in the control for identification purposes.
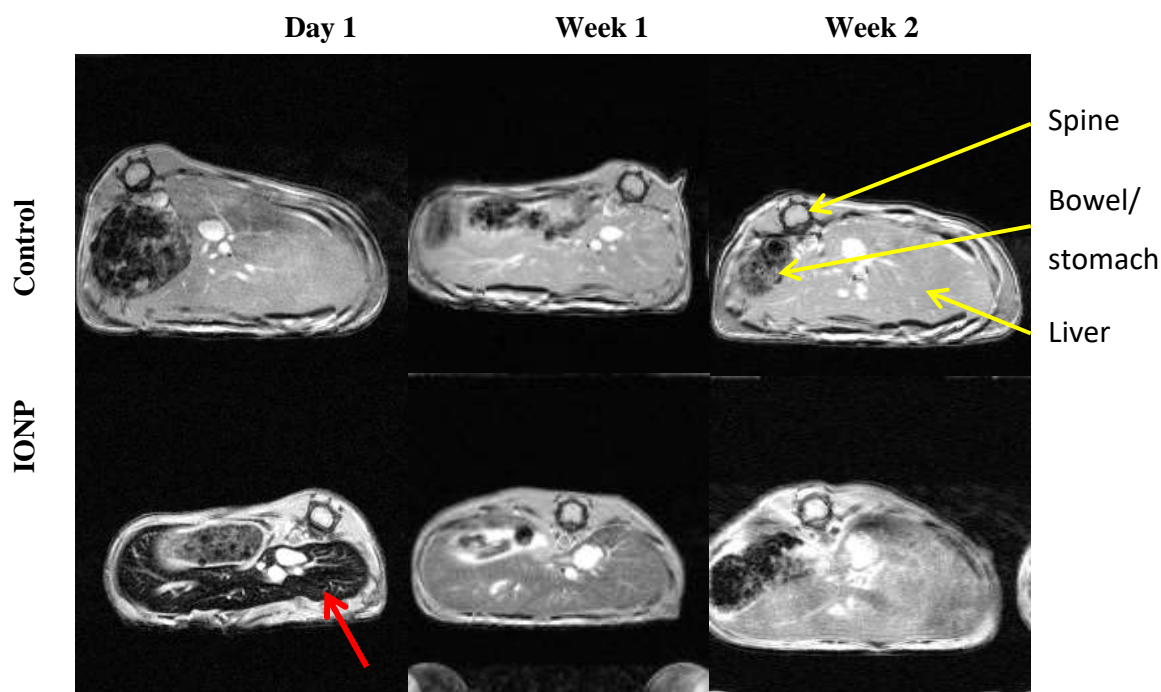
Figure 5-12 *In vivo* T$_2$* weighted MR imaging showed axial views of mice liver area up to 2 weeks after injection, with an area of hypointensity due to the IONP indicated by the arrow. Selected MRI images are representative of three mice that received IONP-DHCA nanoparticles or just PBS (control).

After intravenous injection of IONP-DHCA at a dose of 300 µg Fe per ml, was immediately observed significant signal attenuation in the liver region for IONP-DHCA (Figure 5-12). This concentration was deemed safe as no cytotoxic effects of IONP-DHCA were visible up to 250 µg Fe/ml. More importantly, the administered dose *in vivo* (42.3 µmol Fe/kg) is within the mid-range of clinical dose of IONPs typically used: between 15 µmol – 75 µmol Fe/kg.[79, 355]

To quantify the contrast, the liver was identified as the region of interest and the normalized T_2 weighted signal intensity was calculated for each animal over a period of 2 weeks. These results are found in Figure 5-13. As can be expected, the accumulation of IONP-DHCA in the liver was observed, thus leading to a hypointense signal. This was quantified with the measured T_2 signal in the liver, with a significant decrease in its value immediately post injection and 1 week later. On the other hand, the control remained relatively constant over the 2 week period. The MRI signal in the region recovered gradually 2 weeks after the injection of the IONP- DHCA nanoparticles, thus indicting that the IONP-DHCA are efficiently cleared from the liver, which is an important condition for the safe use of these NPs in clinical settings as prolonged retention of IONPs in the liver that are slowly converted to ferroproteins are a serious safety concern.[356]
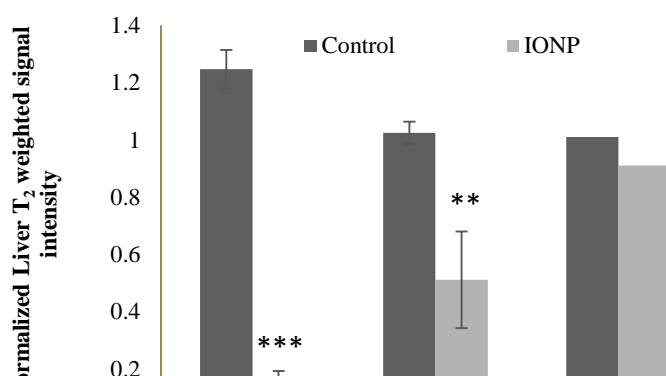
Figure 5-13 Quantification of the signal intensity of the specific region of interest defined as the liver, as evaluated from the MR images in mice administered PBS (control) and mice administered 300 µg Fe per ml of IONP-DHCA. The signal was normalised against muscle tissue around the vertebra column. The analysis was conducted in replicates of three mice per condition over 2 wk. The degree of significance is measured using GraphPad Prism software and is indicated when appropriate *P < 0.05, **P < 0.01 and ***P < 0.001 (*one-way ANOVA*, Dunnett *post-hoc* test).

5.3   CONCLUSIONS

The aim of the work presented in this chapter was to determine the suitability of IONP-DHCA synthesised as potential MRI contrast agents. A comprehensive overview of methods assessing the biocompatibility of IONP-DHCA with hMSCs was presented. As supported by the data obtained in sections 5.2.4 and 5.2.5 there remains a lack of standardisation in the methods used to determine the impact of IONPs on cells, and these techniques assessing the effect of IONPs on cells must be considered carefully in order to obtain accurate data. As highlighted by Paul Weiss *et al.* in ACS Nano editorial in November 2016,[184] the lack of standardisation when it comes to the study of NPs remains an obstacle to their potential biomedical applications.

The uptake of IONP-DHCA by hMSCs was confirmed within 24 h by TEM and iron-specific Prussian blue staining. This is essential to ensure that the amount of IONPs internalised is sufficient contrast by MRI. IONP-DHCA were shown to be taken up in large amounts by hMSCs by a colourimetric method, although the data measured may include aggregates of IONP-DHCA internalised by hMSCs or bound to their surface. This is also supported by the Prussian Blue staining images obtained. Indeed, different parameters will influence the uptake of the IONPs within cultured cells. For example, it was demonstrated that the uptake process varied with the incubation temperature with cell internalisation being disrupted at 4°C, whereas cell-associated IONPs can be seen when at 37 °C.[157, 357] Experimental conditions must therefore be tightly controlled and reproducible for results to be considered and significant.

Also, an important aspect considered is their toxic effects on the cells. Standard colourimetric MTT and MTS assays were initially used but these are not suitable for all IONP concentrations as we observed interference from the IONPs and the data obtained was no longer in the linear absorbance range for the highest concentrations of IONPs (500 and 1000 µg Fe/ml). To overcome this, multiparametric high-content imaging was used to determine

the impact of the IONPs on several factors such as cell viability, mitochondrial activity and cell morphology. No considerable toxic effects were noticed, although a slight elongation of the cells could be observed. Furthermore, at 10 and 50 µg Fe/ml, an increase in ROS production was observed but could not be correlated to impaired mitochondria and was limited to these two IONP concentrations.

Finally, IONP-DHCA was tested *in vivo* in Swiss female mice and confirmed as potential negative contrast agents, as they could be observed in the liver region for up to 2 weeks post injection. This is a longer clearance rate than FDA approved Resovist which has been shown to have a fast liver accumulation and a half-life of 13 min.[358] Additional studies on Ferumoxides or Endorem, both in human and animal models, consistently demonstrate a clearance rate at the time scale of minutes or hours, this of course being dependent on the dose, model or NP considered.[79] Also, IONP-DHCA are safely eliminated by renal clearance and provide sufficient T_2 contrast which can be further optimised by their cell uptake, the latter being dose, incubation concentration or size dependent for example. The administered dose *in vivo* (42.3 µmol Fe/kg) is within the range of clinical dose of IONPs typically used: between 15 µmol – 75 µmol Fe/kg.[79, 355] This highlights the potential clinical relevance of these IONPs as MRI contrast agents. However, additional experiments at higher doses would provide more information regarding the tolerance and biocompatibility of IONPs at these doses. In turn, this could provide additional guidelines for biodistribution studies and also give insight into the possible mechanism of toxicity. Collectively, the work carried out provides new insights into determining biological nanostructures as biocompatible and efficient MRI contrast agents to label and track stem cells *in vivo.*

Chapter 6   DISCUSSION, CONCLUSIONS, AND FUTURE DIRECTIONS

The aim of this thesis was to synthesise superparamagnetic iron oxide nanoparticles as potential MRI contrast agents. This chapter provides an overall discussion of the main findings presented of this thesis and directions for future research.

CONCUSION AND DISCUSSION

In recent years, stem cells (SC) in tissue engineering and regenerative medicine have shown to be promising therapeutic tools as their use has already been implemented in human clinical trials. However, questions remain regarding the function and fate of transplanted SCs. To answer these, certain characteristics of IONPs can be used with a potential of gaining a better understanding of the role of SCs and validating clinical transplantations.[5, 6, 314-316] The work in this thesis has been designed and executed to obtain IONPs which may be potentially used to monitor the fate of SCs in a non-invasive manner using MRI. IONPs offer the possibility of multimodality, surface biofunctionalisation, and better MRI sensitivity than conventional molecular-based contrast agents as long as their magnetic properties are adequate and that they are administered in a sufficient but safe dose.

There exists a wide range of synthesis methods of IONPs, amongst which the polyol synthesis which has the advantage of being a simple low temperature one pot method which leads to the formation of water-dispersible nanoparticles. While the polyol synthesis of IONPs can be found in literature, to our knowledge, no studies comparing different experimental conditions and investigating the reproducibility and reliability of this method have been reported. The work in chapter 1 investigated different experimental conditions: (1) a conventional Schlenk line apparatus with inert atmosphere, (2) a microwave reactor and (3) high pressure high temperature conditions in an oven. The data presented in chapter 1 demonstrates that a one-step reaction was optimal to obtain IONPs using a Schlenk line, however IONPs were not monodisperse: d_{TEM} = 14.8 ± 2.1 nm (δ = 14.4%, n =

272). In order to improve the size distribution of the IONPs, reactions were investigated using a microwave reactor as this has been shown to reduce reaction times, improve size distribution of NPs through volumetric heating and modify the surface reactivity of NPs. The data obtained suggests that this method was not reproducible and that longer reaction times could lead to the re-dissolution of the formed NP seeds in solution. Finally, to overcome these limitations a high pressure high temperature protocol was implemented in an oven. This process yielded IONPs with a narrow particle size distribution in a simple, reproducible and cost effective manner without the need for an inert atmosphere. For example, IONPs with a diameter of *ca.* 8 nm could be obtained in a reproducible manner and with good crystallinity as evidenced by XRD and high magnetic properties with M_s = 84.5 emu/g. Nevertheless, IONPs obtained were found to be unstable and precipitated in solution.

In order to overcome the lack of stability, various ligand exchange protocols were tested in chapter 4. It was determined that storage conditions of IONPs and purification methods are critical in maintaining stable suspensions of IONPs and avoiding their aggregation. This is essential to prolong the shelf life of IONPs developed as potential biomedical products. The use of IONPs in solution and their purification by dialysis were necessary to avoid their immediate aggregation. This method was successful with citric acid, L-tartaric acid and 3,4-dihydrohydrocinnamic acid (DHCA). Although binding of the ligands citric acid and L-tartaric acid to the surface of IONPs was demonstrated by FTIR, the IONPs were found to be not stable in the long term. DHCA proved to be an efficient ligand which provided stability for up to 72d through anchoring of its catechol groups to the surface of the IONPs. Further optimisation of the ligand exchange could be carried out using a conductivity meter. A wider range of ligands could be tested, including those derived from PEG in order to improve the long term stability of the IONPs while maintaining their biocompatibility. Recent literature has highlighted the lack of characterisation techniques to probe the surface chemistry of NPs. More extensive studies and regulation will be needed for researchers in this field to define IONPs synthesised for biomedical applications in terms of the nature and amount of

ligands present. To address this problem, in 2014, Davis and colleagues used radiolabeled oleic acid to assess the ligand exchange of IONPs by PEG with various terminal groups.[59] This study confirmed hierarchal binding of functional groups but showed that even with high affinity ligands, such as catechol derived groups, oleic acid still remained on the surface of the NPs after ligand exchange.

Following their functionalisation with DHCA which provided stability and biocompatibility, the potential of the IONP-DHCA as MRI T_2 weighted contrast agents was confirmed in solution at 1.4 T and 7 T, with an improved r_2/r_1 ratio by a factor of more than 3 in comparison to FDA-approved IONPs for MRI, Resovist® and Endorem®. At 1.47 T, $r_2/r_1 = 23.3$ for IONP-DHCA in comparison to a value of 8.7 for Endorem and 7 for Resovist measured in the same conditions.

The biocompatibility of IONP-DHCA was studied *in vitro* with hMSCs. Their cellular uptake was confirmed by TEM and iron specific Prussian blue staining. The uptake was quantified using a colourimetric method. The data obtained suggested that IONP-DHCA may have bound to the extracellular membrane and/or the well in the cell culture flask. Further studies using single cell magnetophoresis would allow quantitative and qualitative confirmation of this hypothesis. As demonstrated by Fayol *et al.* this technique also previously revealed that colourimetric assays can lead to overestimation of the quantity of iron taken up by a factor of three in the case of agglomerated IONPs.[324] As noted in several recent studies, the use of conventional colourimetric MTT and MTS assays to determine cell viability after exposure to IONP-DHCA was inadequate as interference from the IONPs was observed and values outside of the linear absorbance range were obtained with 500 and 1000 µg Fe/ml of IONP-DHCA. Flow cytometry proved ineffective with Annexin V as this dye led to a large number of false positives following temporary membrane damage caused by trypsinisation. This was overcome with the use of DRAQ7, a far infrared dye, which showed that after 24 h of incubation with 1000 µg Fe/ml of IONP-DHCA, the percentage of viable was 68.7%. Multiparametric high content imaging was shown to be an adequate method to

obtain information on cell-nanoparticle interactions at a microscopic level. This method has been used recently to investigate the potential cytotoxic effects of IONPs in only a couple of studies. No considerable toxic effects were noticed, although a slight elongating of the cells could be observed. Furthermore, at 10 and 50 µg Fe/ml, an increase in ROS production was observed but could not be correlated to impaired mitochondria and was limited to these two concentrations. Finally, IONP-DHCA were tested *in vivo* in Swiss female mice and were confirmed as potential negative contrast agents for MRI, as they could be observed in the liver region for up to 2 weeks post injection. Collectively, our study provides new insights into determining biological nanostructures as biocompatible and efficient MRI contrast agents to label and track stem cells *in vivo.* Whole body imaging has been carried out, and the contrast was only observed in the liver. These IONPs can therefore be used to pre-label hMSCs in order to visualise this cell population by MRI *in vivo*. hMSCs pre-labelled with IONPs could also be used to detect inflammatory processes as reported in the literature.[8, 339, 359]

FUTURE WORK

In the future, these particles could be potentially used for additional functional studies on the SCs transplanted. The aim of these IONPs would be to actively target stem cells at various differentiation stages using well designed antibody fragments to recognise specific surface markers present at these differentiation phases. The initial stages of this research proposal would include the identification of the cluster of differentiation molecules present at the stages of differentiation of hMSCs. Immunocytochemistry would be the most suitable technique to identify the expression of a panel of surface markers. Cluster of differentiation (CD) antigens are surface molecules characterised by the monoclonal antibodies to which they bind. The International Society of Cellular Therapy (ISCT) has recommended three minimal criteria for defining multipotent mesenchymal stromal cells including the expression of CD105, CD90 and CD73 as well as the absence of specific haematological markers.[360] In the case of bone marrow derived hMSCs, we have

determined that CD90 is expressed by more than 95% of the cell population and have therefore chosen to focus on this potential surface marker.

The use of antibodies to actively target IONPs has been essentially used for the active targeting of theranostic nanoparticles towards cancer cells.[114, 227, 361-363] More recently, the strategy to target CD molecules has been investigated in the case of cancer stem cells which may be characterised by the overexpression of certain CD antigens such as CD44 or CD133 for example.[364-366] These cancer stem cells constitute only a small (<5%) fraction of the cells found in tumours, however they possess a high proliferation ability and are resistant to chemotherapy and radiotherapy.

This innovative strategy requires the biofunctionalisation of these IONPs towards CD antigens expressed by the hMSCs targeted. Since we are dealing with biomolecules in the micrometre range, careful attention must be to avoid an increase in the hydrodynamic diameter after the conjugation step as this may lead to some instability and incompatibility with *in vivo* applications. In the case of an antibody, using a Fab fragment may be a strategy to consider as it has recently been shown to lead an enhanced internalisation in comparison with identical nanoparticles functionalised with an entire monoclonal antibody.[367] It is hypothesised that this phenomenon could be due to the reduction in size of the conjugate, which leads to better stability in physiological conditions.

Different strategies can be used to functionalise nanoparticles depending on the surface functional groups involved. This is an essential part to consider as this may influence the efficiency of the nanoparticles in certain biomedical applications.[368] For example, when linking a drug to a nanoparticle, it is worthwhile noting that an amide bond may not be cleaved inside the cell whereas an ester or hydrazine bond may be cleaved according to the pH conditions.[56, 368, 369]

The most routinely used strategy is the carbodiimide method, which allows linking of a carboxylic function to an amine group through the formation of an amide bond. There is no linker involved and so the increase in the hydrodynamic diameter is limited. While this method is straightforward and easy to implement, it is not always suitable for biomedical application of NPs due to the hydrolysis of the reagents in water, and it may also lead to cross-linking of NPs in a non-specific manner. When comparing the carbodiimide reaction *versus* the "click" alkyne-azide chemistry, recent studies have proven that the latter strategy can lead to a 2 to 5 fold increase in the grafting yield of a polymer on the surface of an IONP.[370, 371] Most importantly, this was shown consistently to be specific to the chemical reaction itself independent of the choice of ligand, and in turn this will lead to an increase in binding of IONPs to targeted cells by the ability to graft more targeting peptides on the surface of the NPs. Several excellent reviews report and compare the functionalisation of IONPs with antibodies or antibody-derived fragments,[370, 372-374] and as such will not be treated here. However, in order to choose an appropriate functionalisation methodology, the latter will need to ensure that the properties of both the magnetic IONP and the antibody and maintained. This will mean characterisation of the antibody-nanoparticle (Ab-NP) construct will include for example: determining the hydrodynamic diameter of the Ab-NP, ensuring the biological activity of the antibody is preserved by ELISA assays, and confirming the uptake of the Ab-NP by cells through Prussian Blue staining.

The use of antibody functionalised SPIONs to visualise SCs is a novel concept. It was recently shown *in vivo* that antibody-linked SPIONs can be used to recruit additional stem cells to a spinal cord injury lesion site by magnetic targeting using a clinical grade MRI scanner.[177] In this 2014 study by Cheng *et al.*, IONPs were developed to target exogenous bone marrow-derived SCs (expressing CD45) or endogenous CD34-positive cells to injured cardiomyocytes expressing myosin light chain (MLC). NPs were conjugated with two types of antibodies (one against antigens on therapeutic cells and the other directed at injured cells) in order to link the therapeutic cells to the injured cells and therefore improve the therapeutic efficiency of SCs in the treatment of myocardial infarction. This may also be accompanied by additional

therapeutic and/or diagnostic applications that IONPs offer such as magnetic targeting, MRI or drug delivery just to a name a few.

In the future, our objective is to develop nanoparticle-antibody conjugates that will interact with hMSCs *in* vitro within tissue-engineered scaffolds in order to develop our understanding of the interaction of hMSCs with the scaffolds and other cell populations present, as well as to gain insight into the differentiation of hMSCs and the changes in surface markers it induces. Furthermore, this work may be more interesting when adding further functionalities to the IONPs. Indeed, new nanoparticulate imaging probes, activatable or "smart" probes, which may be switched from the "off" to "on" state upon interaction with a target enzyme, are particularly attractive due to their improved sensitivity and specificity[375]. This principle can also be considered for other biological models where the expression of specific proteins or molecules is triggered in specific conditions. The use of "smart" NPs may reveal important information regarding stem cells used for regenerative medicine purposes. For example, SC apoptosis in a matrix-associated SC implant was detected in a non-invasive manner by MRI using a caspase-3-sensitive nanoaggregation MRI probe (C-SNAM).[376] This could be a potentially useful tool for *in vivo* monitoring of the viability of transplanted SCs and facilitating the development of successful cartilage regeneration techniques or various SC therapies. This platform could represent an innovative tool in the diagnosis of SC failure at an early stage, thus minimizing any health consequences on patients. This approach has also been investigated with IONPs developed to undergo intracellular covalent aggregation in apoptotic cells and tumors which in turn would allow for enhanced T_2 MRI.[377] These IONPs were functionalised with a small peptide [(Ac-Asp-Glu-Val-Asp-Cys(StBu)-Lys-cyanobenzothiazole (CBT)], which could undergo Casp3/7-controlled condensation. Briefly, these IONPs were designed so that after internalisation by Casp3/7-activated cells, the disulfide bonds from cysteine were reduced by intracellular glutathione (GSH), and the peptides were cleaved by the enzymes thus exposing reactive 1,2-aminothiol groups.[377] Then, the condensation reaction between the

free 1,2-aminothiol groups and the cyano groups of the CBT motifs led to cross-linked Fe_3O_4 NPs aggregates, which resulted in enhanced T_2 MR signal.[377]

It is proposed that the IONP-DHCA developed during this thesis could be used as a platform in the future to gain a better understanding of SC therapies. This strategy could be achieved through their active targeting towards CD molecules expressed by hMSCs in specific differentiation stages and/or their targeting towards biological molecules expressed only in certain cellular states such as apoptosis and/or their use in magnetic targeting of hMSCs towards specific sites in tissue-engineered models.

REFERENCES

1.   S. W. Sharpe, T. J. Johnson, R. L. Sams, P. M. Chu, G. C. Rhoderick and P. A. Johnson, *Applied spectroscopy*, 2004, **58**(12), 1452-1461.

2.   C. Blanco-Andujar, D. Ortega, P. Southern, Q. A. Pankhurst and N. T. K. Thanh, *Nanoscale*, 2015, **7**(5), 1768-1775.

3.   K. Niemirowicz, K. Markiewicz, A. Wilczewska and H. Car, *Adv Med Sci*, 2012, **57**(2), 196-207.

4.   J. W. M. Bulte and D. L. Kraitchman, *NMR Biomed.*, 2004, **17**(7), 484-499.

5.   R. Hachani, M. Lowdell, M. Birchall and N. T. K. Thanh, *Nanoscale*, 2013, **5**(23), 11362-11373.

6.   S. M. C. Berman, P. Walczak and J. W. M. Bulte, *Wiley Interdiscip. Rev.-Nanomed. Nanobiotechnol.*, 2011, **3**(4), 343-355.

7.   K. Andreas, R. Georgieva, M. Ladwig, S. Mueller, M. Notter, M. Sittinger and J. Ringe, *Biomaterials*, 2012, **33**(18), 4515-4525.

8.   M. Mahmoudi, H. Hosseinkhani, M. Hosseinkhani, S. Boutry, A. Simchi, W. S. Journeay, K. Subramani and S. Laurent, *Chem. Rev.*, 2011, **111**(2), 253-280.

9.   H. Markides, R. Morris, S. Roberts and J. El Haj, *J. Tissue Eng. Regen. Med.*, 2012, **6** 53-53.

10.   S. Laurent, D. Forge, M. Port, A. Roch, C. Robic, L. V. Elst and R. N. Muller, *Chem. Rev.*, 2008, **108**(6), 2064-2110.

11.   A. C. Anselmo and S. Mitragotri, *Bioengineering & Translational Medicine*, 2016, **1**(1), 10-29.

12.   J. T. Ferrucci and D. D. Stark, *American Journal of Roentgenology*, 1990, **155**(5), 943-950.

13.   C. Poeckler–Schoeniger, J. Koepke, F. Gueckel, J. Sturm and M. Georgi, *Magnetic Resonance Imaging*, 1999, **17**(3), 383-392.

14.   P. Reimer and T. Balzer, *Eur. Radiol.*, 2003, **13**(6), 1266-1276.

15.   Y.-X. Wang, S. Hussain and G. Krestin, *Eur. Radiol.*, 2001, **11**(11), 2319-2331.

16.   L. Babes, B. Denizot, amp, x, G. Tanguy, J. J. Le Jeune and P. Jallet, *Journal of Colloid and Interface Science*, 1999, **212**(2), 474-482.

17.   R. Massart, *Ieee Transactions on Magnetics*, 1981, **17**(2), 1247-1248.

18.   A. H. Lu, E. L. Salabas and F. Schuth, *Angew. Chem.-Int. Edit.*, 2007, **46**(8), 1222-1244.

19.   Z. Liu, X. Zhan, M. Yang, Q. Yang, X. Xu, F. Lan, Y. Wu and Z. Gu, *Nanoscale*, 2016, **8**(14), 7544-7555.

20.   C. Yang, J. Wu and Y. Hou, *Chemical Communications*, 2011, **47**(18), 5130-5141.

21.   A. Weiss, *Berichte der Bunsengesellschaft für physikalische Chemie*, 1976, **80**(2), 175-175.

22.   S. K. O'Reilly W and Banerjee, *Mineralogical Magazine* 1967, **36**(277), 29-37.

23.   G. Menegazzo, S. Carbonin and A. Della Giusta, *Mineralogical Magazine*, 1997, **61**(3), 411-421.

24.   M. M. Modo and J. W. Bulte, *Journal of Nuclear Medicine*, 2007, **48**(12), 2087.

25.   M. P. Morales, C. de Julián, J. M. González and C. J. Serna, *Journal of Materials Research*, 1994, **9**(1), 135-141.

26.   W. Wu, Q. He and C. Jiang, *Nanoscale Research Letters*, 2008, **3**(11), 397.

27.   K. M. Krishnan, *IEEE transactions on magnetics*, 2010, **46**(7), 2523-2558.

28.   J. Baumgartner, L. Bertinetti, M. Widdrat, A. M. Hirt and D. Faivre, *PLoS One*, 2013, **8**(3), e57070.

29.   S.-M. Yu, A. Laromaine and A. Roig, *Journal of nanoparticle research*, 2014, **16**(7), 2484.

30.   A. L. Cortajarena, D. Ortega, S. M. Ocampo, A. Gonzalez-García, P. Couleaud, R. Miranda, C. Belda-Iniesta and A. Ayuso-Sacido, *Nanobiomedicine*, 2014, **1** 2.

31.   N. T. Thanh, *Magnetic nanoparticles: from fabrication to clinical applications*, CRC press, 2012.

32.   Q. A. Pankhurst, J. Connolly, S. K. Jones and J. Dobson, *J. Phys. D-Appl. Phys.*, 2003, **36**(13), R167-R181.

33.   J. Lazarovits, Y. Y. Chen, E. A. Sykes and W. C. W. Chan, *Chemical Communications*, 2015, **51**(14), 2756-2767.

34.   S. Laurent, S. Dutz, U. O. Häfeli and M. Mahmoudi, *Advances in Colloid and Interface Science*, 2011, **166**(1–2), 8-23.

35.   K. Hayashi, K. Ono, H. Suzuki, M. Sawada, M. Moriya, W. Sakamoto and T. Yogo, *ACS Applied Materials & Interfaces*, 2010, **2**(7), 1903-1911.

36.   B. D. Cullity and C. D. Graham, *Introduction to magnetic materials*, John Wiley & Sons, 2011.

37.   R. Massart, *Magnetics, IEEE Transactions on*, 1981, **17**(2), 1247-1248.

38.   A. K. Gupta and M. Gupta, *Biomaterials*, 2005, **26**(18), 3995-4021.

39.   C. Tassa, S. Y. Shaw and R. Weissleder, *Accounts of Chemical Research*, 2011, **44**(10), 842-852.

40.   S. L. Easo and P. V. Mohanan, *Carbohydr. Polym.*, 2013, **92**(1), 726-732.

41.   Z.-T. Tsai, J.-F. Wang, H.-Y. Kuo, C.-R. Shen, J.-J. Wang and T.-C. Yen, *Journal of Magnetism and Magnetic Materials*, 2010, **322**(2), 208-213.

42.   Y. H. Hwang and D. Y. Lee, *Quantitative Imaging in Medicine and Surgery*, 2012, **2**(2), 118-123.

43.   J. M. Lee, B. S. Kim, H. Lee and G. I. Im, *Mol. Ther.*, 2012, **20**(7), 1434-1442.

44.   R. S. Molday and D. Mackenzie, *Journal of immunological methods*, 1982, **52**(3), 353-367.

45.   M. Das, D. Mishra, P. Dhak, S. Gupta, T. K. Maiti, A. Basak and P. Pramanik, *Small*, 2009, **5**(24), 2883-2893.

46.   Y. Lalatonne, C. Paris, J. M. Serfaty, P. Weinmann, M. Lecouvey and L. Motte, *Chemical Communications*, 2008, **22** 2553-2555.

47.   Y. Lalatonne, M. Monteil, H. Jouni, J. M. Serfaty, O. Sainte-Catherine, N. Lievre, S. Kusmia, P. Weinmann, M. Lecouvey and L. Motte, *Journal of osteoporosis*, 2010, **2010** 747852-747852.

48.   Y. Sahoo, H. Pizem, T. Fried, D. Golodnitsky, L. Burstein, C. N. Sukenik and G. Markovich, *Langmuir*, 2001, **17**(25), 7907-7911.

49.   T. Daou, J. Greneche, G. Pourroy, S. Buathong, A. Derory, C. Ulhaq-Bouillet, B. Donnio, D. Guillon and S. Begin-Colin, *Chemistry of Materials*, 2008, **20**(18), 5869-5875.

50.   J. P. Jolivet, P. Belleville, E. Tronc and J. Livage, *Clay Clay Min.*, 1992, **40**(5), 531-539.

51.   E. Tronc, P. Belleville, J. P. Jolivet and J. Livage, *Langmuir*, 1992, **8**(1), 313-319.

52.   C. Blanco Andujar, PhD thesis, Sodium carbonate mediated synthesis of iron oxide nanoparticles to improve magnetic hyperthermia efficiency and induce apoptosis, UCL (University College London), 2014.

53.   S. Sun, H. Zeng, D. B. Robinson, S. Raoux, P. M. Rice, S. X. Wang and G. Li, *Journal of the American Chemical Society*, 2004, **126**(1), 273-279.

54.   J. Park, K. J. An, Y. S. Hwang, J. G. Park, H. J. Noh, J. Y. Kim, J. H. Park, N. M. Hwang and T. Hyeon, *Nature Materials*, 2004, **3**(12), 891-895.

55.   J. Park, E. Lee, N. M. Hwang, M. S. Kang, S. C. Kim, Y. Hwang, J. G. Park, H. J. Noh, J. Y. Kini, J. H. Park and T. Hyeon, *Angew. Chem.-Int. Edit.*, 2005, **44**(19), 2872-2877.

56.   R. A. Sperling and W. Parak, *Philosophical Transactions of the Royal Society of London A: Mathematical, Physical and Engineering Sciences*, 2010, **368**(1915), 1333-1383.

57. A. Lassenberger, O. Bixner, T. Gruenewald, H. Lichtenegger, R. Zirbs and E. Reimhult, *Langmuir*, 2016, **32**(17), 4259-4269.

58. T. Lam, P. K. Avti, P. Pouliot, F. Maafi, J.-C. Tardif, É. Rhéaume, F. Lesage and A. Kakkar, *Nanomaterials*, 2016, **6**(6), 100.

59. K. Davis, B. Qi, M. Witmer, C. L. Kitchens, B. A. Powell and O. T. Mefford, *Langmuir*, 2014, **30**(36), 10918-10925.

60. K. Davis, B. Cole, M. Ghelardini, B. A. Powell and O. T. Mefford, *Langmuir*, 2016, **32**(51), 13716-13727.

61. S. Ge, X. Shi, K. Sun, C. Li, J. R. Baker, M. M. Banaszak Holl and B. G. Orr, *The journal of physical chemistry. C, Nanomaterials and interfaces*, 2009, **113**(31), 13593-13599.

62. M. Khalil, J. Yu, N. Liu and R. L. Lee, *Journal of Nanoparticle Research*, 2014, **16**(4), 2362.

63. A. Ali, M. Z. Hira Zafar, I. ul Haq, A. R. Phull, J. S. Ali and A. Hussain, *Nanotechnology, science and applications*, 2016, **9** 49.

64. M. Berg, H. Ejnell, A. Kovács, N. Nayakawde, P. B. Patil, M. Joshi, L. Aziz, G. Rådberg, S. Hajizadeh, M. Olausson and S. Sumitran-Holgersson, *Tissue Engineering - Part A*, 2014, **20**(1-2), 389-397.

65. W. Cai and J. Wan, *Journal of Colloid and Interface Science*, 2007, **305**(2), 366-370.

66. F. Hu, K. W. MacRenaris, E. A. Waters, T. Liang, E. A. Schultz-Sikma, A. L. Eckermann and T. J. Meade, *Journal of Physical Chemistry C*, 2009, **113**(49), 20855-20860.

67. D. Arndt, V. Zielasek, W. Dreher and M. Baumer, *Journal of Colloid and Interface Science*, 2014, **417** 188-198.

68. S. B. Seif-Naraghi, J. M. Singelyn, M. A. Salvatore, K. G. Osborn, J. J. Wang, U. Sampat, O. L. Kwan, G. M. Strachan, J. Wong, P. J. Schup-Magoffin, R. L. Braden, K. Bartels, J. A. DeQuach, M. Preul, A. M. Kinsey, A. N. DeMaria, N. Dib and K. L. Christman, *Science Translational Medicine*, 2013, **5**(173), 173ra125.

69.   N. Miguel-Sancho, O. Bomati-Miguel, A. G. Roca, G. Martinez, M. Arruebo and J. Santamaria, *Industrial & Engineering Chemistry Research*, 2012, **51**(25), 8348-8357.

70.   F. Jasim and K. Hamid, *Thermochimica Acta*, 1983, **70**(1-3), 105-111.

71.   L. Reijnen, B. Meester, A. Goossens and J. Schoonman, *Journal of the Electrochemical Society*, 2000, **147**(5), 1803-1806.

72.   P. Jiang, X. Yang, Y. Xin, Y. Qi, X. Ma, Q. Li and Z. Zhang, *Journal of Materials Science*, 2013, **48**(6), 2365-2369.

73.   I.-M. Grabs, C. Bradtmöller, D. Menzel and G. Garnweitner, *Crystal Growth & Design*, 2012, **12**(3), 1469-1475.

74.   R. H. Goncalves, C. A. Cardoso and E. R. Leite, *Journal of Materials Chemistry*, 2010, **20**(6), 1167-1172.

75.   J. Wan, W. Cai, X. Meng and E. Liu, *Chemical Communications*, 2007(47), 5004-5006.

76.   C. M. Cheng, F. J. Xu and H. C. Gu, *New J. Chem.*, 2011, **35**(5), 1072-1079.

77.   N. Miguel-Sancho, O. Bomati-Miguel, G. Colom, J. P. Salvador, M. P. Marco and J. Santamaria, *Chemistry of Materials*, 2011, **23**(11), 2795-2802.

78.   F. Alexis, E. Pridgen, L. K. Molnar and O. C. Farokhzad, *Molecular pharmaceutics*, 2008, **5**(4), 505-515.

79.   H. Arami, A. Khandhar, D. Liggitt and K. M. Krishnan, *Chemical Society reviews*, 2015, **44**(23), 8576-8607.

80.   C. Lemarchand, R. Gref, C. Passirani, E. Garcion, B. Petri, R. Muller, D. Costantini and P. Couvreur, *Biomaterials*, 2006, **27**(1), 108-118.

81.   Z.-G. Yue, W. Wei, P.-P. Lv, H. Yue, L.-Y. Wang, Z.-G. Su and G.-H. Ma, *Biomacromolecules*, 2011, **12**(7), 2440-2446.

82.   C. He, Y. Hu, L. Yin, C. Tang and C. Yin, *Biomaterials*, 2010, **31**(13), 3657-3666.

83.   S. E. Gratton, M. E. Napier, P. A. Ropp, S. Tian and J. M. DeSimone, *Pharmaceutical research*, 2008, **25**(12), 2845-2852.

84.   I. I. Slowing, J. L. Vivero-Escoto, C.-W. Wu and V. S.-Y. Lin, *Advanced drug delivery reviews*, 2008, **60**(11), 1278-1288.

85.   E. Fröhlich, *International Journal of Nanomedicine*, 2012, **7** 5577-5591.

86.   A. Verma and F. Stellacci, *Small*, 2010, **6**(1), 12-21.

87.   A. G. Torres and M. J. Gait, *Trends in Biotechnology*, 2012, **30**(4), 185-190.

88.   R. M. Cornell and U. Schwertmann, *The Iron Oxides: Structure, Properties, Reactions, Occurrences and Uses*, Wiley, 2003.

89.   E. Tombacz, A. Majzik, Z. Horvat and E. Illes, *Romanian Reports in physics*, 2006, **58**(3), 281.

90.   J. W. M. Bulte, T. Douglas, B. Witwer, S. C. Zhang, E. Strable, B. K. Lewis, H. Zywicke, B. Miller, P. van Gelderen, B. M. Moskowitz, I. D. Duncan and J. A. Frank, *Nat. Biotechnol.*, 2001, **19**(12), 1141-1147.

91.   A. Ruiz, P. Morais, R. Bentes de Azevedo, Z. M. Lacava, A. Villanueva and M. del Puerto Morales, *Journal of Nanoparticle Research*, 2014, **16**(11), 1-20.

92.   A. Lopez-Cruz, C. Barrera, V. L. Calero-DdelC and C. Rinaldi, *Journal of Materials Chemistry*, 2009, **19**(37), 6870-6876.

93.   A. Ruiz, Y. Hernandez, C. Cabal, E. González, S. Veintemillas-Verdaguer, E. Martinez and M. Morales, *Nanoscale*, 2013, **5**(23), 11400-11408.

94.   S. Salmaso and P. Caliceti, *Journal of Drug Delivery*, 2013, **2013** 19.

95.   A. Quarta, D. Bernareggi, F. Benigni, E. Luison, G. Nano, S. Nitti, M. C. Cesta, L. Di Ciccio, S. Canevari, T. Pellegrino and M. Figini, *Nanoscale*, 2015, **7**(6), 2336-2351.

96.   C. Sun, K. Du, C. Fang, N. Bhattarai, O. Veiseh, F. Kievit, Z. Stephen, D. Lee, R. G. Ellenbogen, B. Ratner and M. Zhang, *ACS Nano*, 2010, **4**(4), 2402-2410.

97.   C. Larsen, *Advanced Drug Delivery Reviews*, 1989, **3**(1), 103-154.

98.   R. Mehvar, *Journal of Controlled Release*, 2000, **69**(1), 1-25.

99.   L. Li, W. Jiang, K. Luo, H. Song, F. Lan, Y. Wu and Z. Gu, *Theranostics*, 2013, **3**(8), 595-615.

100.   M. R. Bashir, L. Bhatti, D. Marin and R. C. Nelson, *Journal of Magnetic Resonance Imaging*, 2015, **41**(4), 884-898.

101.   K. Kim, A. Doi, B. Wen, K. Ng, R. Zhao, P. Cahan, J. Kim, M. J. Aryee, H. Ji, L. I. R. Ehrlich, A. Yabuuchi, A. Takeuchi, K. C. Cunniff, H. Hongguang, S. McKinney-Freeman, O. Naveiras, T. J. Yoon, R. A. Irizarry, N. Jung, J. Seita, J. Hanna, P. Murakami, R. Jaenisch, R. Weissleder, S. H. Orkin, I. L. Weissman, A. P. Feinberg and G. Q. Daley, *Nature*, 2010, **467**(7313), 285-290.

102.   F. Bloch, *Physical review*, 1946, **70**(7-8), 460.

103.   E. M. Purcell, H. Torrey and R. V. Pound, *Physical review*, 1946, **69**(1-2), 37.

104.   P. C. Lauterbur, *Nature*, 1973, **242**(5394), 190-191.

105.   W. S. Hinshaw, P. A. Bottomley and G. N. Holland, *Nature*, 1977, **270**(5639), 722-723.

106.   R. Damadian, M. Goldsmith and L. Minkoff, *Physiological chemistry and physics*, 1977, **9**(1), 97-100, 108.

107.   G. M. Lanza, P. M. Winter, S. D. Caruthers, A. M. Morawski, A. H. Schmieder, K. C. Crowder and S. A. Wickline, *Journal of Nuclear Cardiology*, 2004, **11**(6), 733-743.

108.   C. Khemtong, C. W. Kessinger and J. Gao, *Chemical Communications*, 2009(24), 3497-3510.

109.   P. Caravan, J. J. Ellison, T. J. McMurry and R. B. Lauffer, *Chem. Rev.*, 1999, **99**(9), 2293-2352.

110.   J. P. Goullé, A. Cattanéo, E. Saussereau, L. Mahieu, M. Guerbet and C. Lacroix, *Annales Pharmaceutiques Françaises*, 2009, **67**(5), 335-339.

111. Z. J. K. Y. F. D. Richmond H, *Archives of Dermatology*, 2007, **143**(8), 1025-1030.

112. K. W. Y. Chan and W. T. Wong, *Coord. Chem. Rev.*, 2007, **251**(17-20), 2428-2451.

113. K. Nwe, M. Bernardo, C. A. S. Regino, M. Williams and M. W. Brechbiel, *Bioorganic & Medicinal Chemistry*, 2010, **18**(16), 5925-5931.

114. N. Bertrand, J. Wu, X. Xu, N. Kamaly and O. C. Farokhzad, *Advanced drug delivery reviews*, 2014, **66** 2-25.

115. S. Acharya and S. K. Sahoo, *Advanced Drug Delivery Reviews*, 2011, **63**(3), 170-183.

116. H. Maeda, H. Nakamura and J. Fang, *Advanced Drug Delivery Reviews*, 2013, **65**(1), 71-79.

117. P. Sharma, S. Brown, G. Walter, S. Santra and B. Moudgil, *Advances in Colloid and Interface Science*, 2006, **123–126**(0), 471-485.

118. M. A. Hahn, A. K. Singh, P. Sharma, S. C. Brown and B. M. Moudgil, *Anal. Bioanal. Chem.*, 2011, **399**(1), 3-27.

119. A. Ba-Ssalamah, M. Uffmann, S. Saini, N. Bastati, C. Herold and W. Schima, *Eur. Radiol.*, 2009, **19**(2), 342-357.

120. R. Weissleder, D. D. Stark, B. L. Engelstad, B. R. Bacon, C. C. Compton, D. L. White, P. Jacobs and J. Lewis, *American Journal of Roentgenology*, 1989, **152**(1), 167-173.

121. Y.-X. J. Wang, *Quantitative Imaging in Medicine and Surgery*, 2011, **1**(1), 35-40.

122. S. Chen, D. Alcantara and L. Josephson, *Journal of Nanoscience and Nanotechnology*, 2011, **11**(4), 3058-3064.

123. M. S. Thu, L. H. Bryant, T. Coppola, E. K. Jordan, M. D. Budde, B. K. Lewis, A. Chaudhry, J. Ren, N. R. S. Varma, A. S. Arbab and J. A. Frank, *Nat Med*, 2012, **18**(3), 463-467.

124. Y. W. Jun, J. W. Seo and J. Cheon, *Accounts of Chemical Research*, 2008, **41**(2), 179-189.

125. Y.-w. Jun, Y.-M. Huh, J.-s. Choi, J.-H. Lee, H.-T. Song, KimKim, S. Yoon, K.-S. Kim, J.-S. Shin, J.-S. Suh and J. Cheon, *Journal of the American Chemical Society*, 2005, **127**(16), 5732-5733.

126. A. G. Roca, S. Veintemillas-Verdaguer, M. Port, C. Robic, C. J. Serna and M. P. Morales, *The Journal of Physical Chemistry B*, 2009, **113**(19), 7033-7039.

127. J. Huang, X. Zhong, L. Wang, L. Yang and H. Mao, *Theranostics*, 2012, **2**(1), 86-102.

128. C. G. Hacliipanayis, M. J. Bonder, S. Balakrishanan, X. Wang, H. Mao and G. C. Hadjipanayis, *Small*, 2008, **4**(11), 1925-1929.

129. M.-L. De Temmerman, S. J. Soenen, N. Symens, B. Lucas, R. E. Vandenbroucke, C. Libert, J. Demeester, S. C. De Smedt, U. Himmelreich and J. Rejman, *Nanomedicine*, 2013, **9**(9), 1363-1376.

130. C. Xu, D. Miranda-Nieves, J. A. Ankrum, M. E. Matthiesen, J. A. Phillips, I. Roes, G. R. Wojtkiewicz, V. Juneja, J. R. Kultima, W. Zhao, P. K. Vemula, C. P. Lin, M. Nahrendorf and J. M. Karp, *Nano Letters*, 2012, **12**(8), 4131-4139.

131. C. Chambon, O. Clement, A. Le Blanche, E. Schouman-Claeys and G. Frija, *Magnetic resonance imaging*, 1993, **11**(4), 509-519.

132. S. Mornet, S. Vasseur, F. Grasset and E. Duguet, *Journal of Materials Chemistry*, 2004, **14**(14), 2161-2175.

133. Z. Shen, A. Wu and X. Chen, *Mol. Pharm.*, 2017, **14**(5), 1352-1364.

134. R. H. Kodama, *Journal of Magnetism and Magnetic Materials*, 1999, **200**(1–3), 359-372.

135. A. Roch, R. N. Muller and P. Gillis, *The Journal of chemical physics*, 1999, **110**(11), 5403-5411.

136. J. Fang, P. Chandrasekharan, X.-L. Liu, Y. Yang, Y.-B. Lv, C.-T. Yang and J. Ding, *Biomaterials*, 2014, **35**(5), 1636-1642.

137. M. Lewin, N. Carlesso, C. H. Tung, X. W. Tang, D. Cory, D. T. Scadden and R. Weissleder, *Nat. Biotechnol.*, 2000, **18**(4), 410-414.

138. K. Nohroudi, S. Arnhold, T. Berhorn, K. Addicks, M. Hoehn and U. Himmelreich, *Cell Transplantation*, 2010, **19**(4), 431-441.

139. E. Terreno, S. Geninatti Crich, S. Belfiore, L. Biancone, C. Cabella, G. Esposito, A. D. Manazza and S. Aime, *Magnetic Resonance in Medicine*, 2006, **55**(3), 491-497.

140. G. J. Strijkers, S. Hak, M. B. Kok, C. S. Springer and K. Nicolay, *Magnetic Resonance in Medicine*, 2009, **61**(5), 1049-1058.

141. M. D. Robson, P. D. Gatehouse, M. Bydder and G. M. Bydder, *Journal of computer assisted tomography*, 2003, **27**(6), 825-846.

142. R. Schäfer, R. Bantleon, R. Kehlbach, G. Siegel, J. Wiskirchen, H. Wolburg, T. Kluba, F. Eibofner, H. Northoff and C. D. Claussen, *BMC cell biology*, 2010, **11**(1), 22.

143. A. B. Mathiasen, L. Hansen, T. Friis, C. Thomsen, K. Bhakoo and J. Kastrup, *Stem cells international*, 2013.

144. Z. L. Shi, K. G. Neoh, E. T. Kang, B. Shuter and S. C. Wang, *Contrast Media Mol. Imaging*, 2010, **5**(2), 105-111.

145. C.-Y. Yang, M.-F. Tai, S.-T. Chen, Y.-T. Wang, Y.-F. Chen, J.-K. Hsiao, J.-L. Wang and H.-M. Liu, *Journal of Applied Physics*, 2009, **105**(7), 07B314.

146. A. Stroh, C. Faber, T. Neuberger, P. Lorenz, K. Sieland, P. M. Jakob, A. Webb, H. Pilgrimm, R. Schober and E. E. Pohl, *Neuroimage*, 2005, **24**(3), 635-645.

147. A. A. Faraj, N. Luciani, J. Kolosnjaj - Tabi, E. Mattar, O. Clement, C. Wilhelm and F. Gazeau, *Contrast Media Mol. Imaging*, 2013, **8**(2), 193-203.

148. P. Smirnov, M. Poirier - Quinot, C. Wilhelm, E. Lavergne, J. C. Ginefri, B. Combadière, O. Clément, L. Darrasse and F. Gazeau, *Magnetic resonance in medicine*, 2008, **60**(6), 1292-1297.

149. N. Lee and T. Hyeon, *Chemical Society Reviews*, 2012, **41**(7), 2575-2589.

150. E. Pawelczyk, A. S. Arbab, A. Chaudhry, A. Balakumaran, P. G. Robey and J. A. Frank, *STEM CELLS*, 2008, **26**(5), 1366-1375.

151. J. Terrovitis, M. Stuber, A. Youssef, S. Preece, M. Leppo, E. Kizana, M. Schär, G. Gerstenblith, R. G. Weiss and E. Marbán, *Circulation*, 2008, **117**(12), 1555-1562.

152. A. K. A. Silva, C. Wilhelm, J. Kolosnjaj-Tabi, N. Luciani and F. Gazeau, *Pharmaceutical research*, 2012, **29**(5), 1392-1403.

153. S. H. Bakhru, E. Altiok, C. Highley, D. Delubac, J. Suhan, T. K. Hitchens, C. Ho and S. Zappe, *International journal of nanomedicine*, 2012, **7** 4613.

154. C. Yu, J. Zhao, Y. Guo, C. Lu, X. Ma and Z. Gu, *Journal of Biomedical Materials Research Part A*, 2008, **87**(2), 364-372.

155. C. J. Xu, D. Miranda-Nieves, J. A. Ankrum, M. E. Matthiesen, J. A. Phillips, I. Roes, G. R. Wojtkiewicz, V. Juneja, J. R. Kultima, W. A. Zhao, P. K. Vemula, C. P. Lin, M. Nahrendorf and J. M. Karp, *Nano Letters*, 2012, **12**(8), 4131-4139.

156. J. Riegler, A. Liew, S. O. Hynes, D. Ortega, T. O'Brien, R. M. Day, T. Richards, F. Sharif, Q. A. Pankhurst and M. F. Lythgoe, *Biomaterials*, 2013, **34**(8), 1987-1994.

157. N. Landázuri, S. Tong, J. Suo, G. Joseph, D. Weiss, D. J. Sutcliffe, D. P. Giddens, G. Bao and W. R. Taylor, *Small*, 2013, **9**(23), 4017-4026.

158. D. Tukmachev, O. Lunov, V. Zablotskii, A. Dejneka, M. Babic, E. Sykova and S. Kubinova, *Nanoscale*, 2015, **7**(9), 3954-3958.

159. L. Y. T. Chou, K. Ming and W. C. W. Chan, *Chemical Society Reviews*, 2011, **40**(1), 233-245.

160. N. Oh and J.-H. Park, *International Journal of Nanomedicine*, 2014, **9**(Suppl 1), 51-63.

161. S. Zhang, H. Gao and G. Bao, *ACS Nano*, 2015, **9**(9), 8655-8671.

162. Ž. Krpetić, S. Saleemi, I. A. Prior, V. Sée, R. Qureshi and M. Brust, *ACS Nano*, 2011, **5**(6), 5195-5201.

163. A. S. Arbab, G. T. Yocum, L. B. Wilson, A. Parwana, E. K. Jordan, H. Kalish and J. A. Frank, *Molecular Imaging*, 2004, **3**(1), 24-32.

164. J. A. Frank, B. R. Miller, A. S. Arbab, H. A. Zywicke, E. K. Jordan, B. K. Lewis, L. H. Bryant and J. W. M. Bulte, *Radiology*, 2003, **228**(2), 480-487.

165. M. Babic, D. Horak, M. Trchova, P. Jendelova, K. Glogarova, P. Lesny, V. Herynek, M. Hajek and E. Sykova, *Bioconjugate Chemistry*, 2008, **19**(3), 740-750.

166. E. Farrell, P. Wielopolski, P. Pavljasevic, N. Kops, H. Weinans, M. R. Bernsen and G. van Osch, *Osteoarthritis Cartilage*, 2009, **17**(7), 961-967.

167. A. S. Arbab, G. T. Yocum, A. M. Rad, A. Y. Khakoo, V. Fellowes, E. J. Read and J. A. Frank, *NMR Biomed.*, 2005, **18**(8), 553-559.

168. P. Wunderbaldinger, L. Josephson and R. Weissleder, *Bioconjugate Chemistry*, 2002, **13**(2), 264-268.

169. B. L. Strand, L. Ryan, P. I. Veld, B. Kulseng, A. M. Rokstad, G. Skjak-Braek and T. Espevik, *Cell Transplantation*, 2001, **10**(3), 263-275.

170. A. Khurana, F. Chapelin, G. Beck, O. D. Lenkov, J. Donig, H. Nejadnik, S. Messing, N. Derugin, R. C.-F. Chan, A. Gaur, B. Sennino, D. M. McDonald, P. J. Kempen, G. A. Tikhomirov, J. Rao and H. E. Daldrup-Link, *Radiology*, 2013, **269**(1), 186-197.

171. H. E. Daldrup-Link, In Vivo Iron Labeling of Stem Cells and Tracking these Labeled Stem Cells after their Transplantation, Patent, 2014.

172. N. Singh, G. J. S. Jenkins, R. Asadi and S. H. Doak, *Nano Reviews*, 2010, **1**(1), 5358.

173. A. Louie, *Chem. Rev.*, 2010, **110**(5), 3146-3195.

174. Y. Wei, M. Zhao, F. Yang, Y. Mao, H. Xie and Q. Zhou, *Scientific Reports*, 2016, **6**.

175. H. F. Krug, *Angewandte Chemie International Edition*, 2014, **53**(46), 12304-12319.

176. K. Okita, T. Ichisaka and S. Yamanaka, *Nature*, 2007, **448**(7151), 313-317.

177. K. Cheng, D. Shen, M. T. Hensley, R. Middleton, B. Sun, W. Liu, G. De Couto and E. Marbán, *Nature Communications*, 2014, **5** 4880.

178.   P. Rivera-Gil, D. Jimenez De Aberasturi, V. Wulf, B. Pelaz, P. Del Pino, Y. Zhao, J. M. De La Fuente, I. Ruiz De Larramendi, T. Rojo, X.-J. Liang and W. J. Parak, *Accounts of Chemical Research*, 2013, **46**(3), 743-749.

179.   S. J. Soenen, B. B. Manshian, A. M. Abdelmonem, J.-M. Montenegro, S. Tan, L. Balcaen, F. Vanhaecke, A. R. Brisson, W. J. Parak, S. C. De Smedt and K. Braeckmans, *Particle & Particle Systems Characterization*, 2014, **31**(7), 794-800.

180.   S. Jeon, J. Lee, J. Andrade and P. De Gennes, *Journal of Colloid and Interface Science*, 1991, **142**(1), 149-158.

181.   T. Cosgrove, *Colloid science: principles, methods and applications*, John Wiley & Sons, 2010.

182.   F. Roohi, J. Lohrke, A. Ide, G. Schutz and K. Dassler, *International Journal of Nanomedicine*, 2012, **7** 4447-4458.

183.   A. Ruiz, Y. Hernandez, C. Cabal, E. Gonzalez, S. Veintemillas-Verdaguer, E. Martinez and M. P. Morales, *Nanoscale*, 2013, **5**(23), 11400-11408.

184.   P. Mulvaney, W. J. Parak, F. Caruso and P. S. Weiss, *ACS Nano*, 2016.

185.   T. K. Jain, M. K. Reddy, M. A. Morales, D. L. Leslie-Pelecky and V. Labhasetwar, *Mol. Pharm.*, 2008, **5**(2), 316-327.

186.   J. M. Gimble, B. A. Bunnell, E. S. Chiu and F. Guilak, *Stem Cells*, 2011, **29**(5), 749-754.

187.   S. J. H. Soenen, J. Baert and M. De Cuyper, *ChemBioChem*, 2007, **8**(17), 2067-2077.

188.   J. H. Yoe and A. L. Jones, *Industrial & Engineering Chemistry Analytical Edition*, 1944, **16**(2), 111-115.

189.   A. R. Burke, R. N. Singh, D. L. Carroll, F. M. Torti and S. V. Torti, *Journal of molecular biomarkers & diagnosis Suppl 8*.

190.   S. Mornet, Synthèse et modification chimique de la surface de nanoparticules de maghémite à des fins d'applications biomédicales, Université Sciences et Technologies-Bordeaux I, 2002.

191. M. Cornelissen, J. Philippé, S. De Sitter and L. De Ridder, *Apoptosis*, 2002, **7**(1), 41-47.

192. I. Vermes, C. Haanen, H. Steffens-Nakken and C. Reutellingsperger, *Journal of immunological methods*, 1995, **184**(1), 39-51.

193. H. L. McConnell, D. L. Schwartz, B. E. Richardson, R. L. Woltjer, L. L. Muldoon and E. A. Neuwelt, *Nanomedicine: Nanotechnology, Biology and Medicine*, 2016, **12**(6), 1535-1542.

194. V. Zavisova, M. Koneracka, J. Kovac, M. Kubovcikova, I. Antal, P. Kopcansky, M. Bednarikova and M. Muckova, *Journal of Magnetism and Magnetic Materials*, 2015, **380**(0), 85-89.

195. K. G. Rose, K. Sesterhenn and F. Wustrow, *The Lancet*, 1979, **313**(8113), 433.

196. B. Michen, C. Geers, D. Vanhecke, C. Endes, B. Rothen-Rutishauser, S. Balog and A. Petri-Fink, *Scientific Reports*, 2015, **5** 9793.

197. T. Gelbrich, M. Feyen and A. M. Schmidt, *Macromolecules*, 2006, **39**(9), 3469-3472.

198. C. Suryanarayana and M. G. Norton, *X-ray diffraction: a practical approach*, Springer Science & Business Media, 2013.

199. S. Wilhelm, A. J. Tavares, Q. Dai, S. Ohta, J. Audet, H. F. Dvorak and W. C. Chan, *Nature Reviews Materials*, 2016, **1** 16014.

200. G. Deacon, F. Huber and R. Phillips, *Inorganica chimica acta*, 1985, **104**(1), 41-45.

201. X. Wu, D. Wang and S. Yang, *Journal of colloid and interface science*, 2000, **222**(1), 37-40.

202. M. Răcuciu, D. E. Creangă and A. Airinei, *Eur. Phys. J. E*, 2006, **21**(2), 117-121.

203. D. H. Williams and I. Fleming, *Spectroscopic Methods in Organic Chemistry*, McGraw-Hill, 1995.

204. L. A. Wormell Green and N. T. K. Thanh, *RSC Advances*, 2014, **4**(3), 1168-1173.

205. S. Pal, Y. K. Tak and J. M. Song, *Appl Environ Microbiol*, 2007, **73**.

206. P. V. AshaRani, M. G. Low Kah, M. P. Hande and S. Valiyaveettil, *ACS Nano*, 2009, **3**(2), 279-290.

207. C. M. Simonescu, *Application of FTIR spectroscopy in environmental studies*, INTECH Open Access Publisher, 2012.

208. Z. M. Khoshhesab, *Reflectance IR spectroscopy*, InTech, 2012.

209. S. K. Libutti, G. F. Paciotti, A. A. Byrnes, H. R. Alexander, W. E. Gannon, M. Walker, G. D. Seidel, N. Yuldasheva and L. Tamarkin, *Clinical Cancer Research*, 2010, **16**(24), 6139-6149.

210. A. Liese and L. Hilterhaus, *Chemical Society Reviews*, 2013, **42**(15), 6236-6249.

211. R. J. Hunter, *Zeta potential in colloid science: principles and applications*, Academic press, 2013.

212. J. H. Masliyah and S. Bhattacharjee, *Electrokinetic and colloid transport phenomena*, John Wiley & Sons, 2006.

213. C. Henoumont, S. Laurent and L. Vander Elst, *Contrast Media Mol. Imaging*, 2009, **4**(6), 312-321.

214. H. Dong, Y. C. Chen and C. Feldmann, *Green Chemistry*, 2015, **17**(8), 4107-4132.

215. F. Hu, Q. Jia, Y. Li and M. Gao, *Nanotechnology*, 2011, **22**(24), 245604.

216. C. Xu and S. Sun, *Polymer International*, 2007, **56**(7), 821-826.

217. C. Vidyasagar and Y. A. Naik, *Arabian Journal of Chemistry*, 2016, **9**(4), 507-510.

218. T. Thirugnanam, *Journal of nanomaterials*, 2013, **2013** 43.

219. P. Tripathi, A. Ahmed, T. Ali, M. Obaidurrahman, R. Chitra, S. Bhattacharya and N. Sahoo, 2016 AIP Conference Proceedings,(1731),050067.

220. J. Jayashainy, *Der Pharma Chemica*, 2015, **7**(1), 212-223.

221.   P. Zhang, W. Zeng and L. Chen, *Journal of Materials Science: Materials in Electronics*, 2016, **27**(2), 1201-1208.

222.   G. D. Venkatasubbu, S. Ramasamy, V. Ramakrishnan and J. Kumar, *Advanced Powder Technology*, 2013, **24**(6), 947-954.

223.   S. Naghibi, H. R. M. Hosseini, M. A. F. Sani, M. A. Shokrgozar and M. Mehrjoo, *Ceramics International*, 2014, **40**(4), 5481-5488.

224.   N. D. Abazović, M. I. Čomor, M. D. Dramićanin, D. J. Jovanović, S. P. Ahrenkiel and J. M. Nedeljković, *The Journal of Physical Chemistry B*, 2006, **110**(50), 25366-25370.

225.   A. León, P. Reuquen, C. Garín, R. Segura, P. Vargas, P. Zapata and P. A. Orihuela, *Applied Sciences*, 2017, **7**(1), 49.

226.   W. Wang, X. Ji, H. B. Na, M. Safi, A. Smith, G. Palui, J. M. Perez and H. Mattoussi, *Langmuir*, 2014, **30**(21), 6197-6208.

227.   C. Xu, K. Xu, H. Gu, R. Zheng, H. Liu, X. Zhang, Z. Guo and B. Xu, *Journal of the American Chemical Society*, 2004, **126**(32), 9938-9939.

228.   H. Wei, N. Insin, J. Lee, H.-S. Han, J. M. Cordero, W. Liu and M. G. Bawendi, *Nano letters*, 2011, **12**(1), 22-25.

229.   J. A. Gerbec, D. Magana, A. Washington and G. F. Strouse, *Journal of the American Chemical Society*, 2005, **127**(45), 15791-15800.

230.   O. Pascu, E. Carenza, M. Gich, S. Estradé, F. Peiró, G. Herranz and A. Roig, *The Journal of Physical Chemistry C*, 2012, **116**(28), 15108-15116.

231.   J. Robinson, S. Kingman, D. Irvine, P. Licence, A. Smith, G. Dimitrakis, D. Obermayer and C. O. Kappe, *Physical Chemistry Chemical Physics*, 2010, **12**(18), 4750-4758.

232.   A. Rizzuti, M. Dassisti, P. Mastrorilli, M. C. Sportelli, N. Cioffi, R. A. Picca, E. Agostinelli, G. Varvaro and R. Caliandro, *Journal of Nanoparticle Research*, 2015, **17**(10), 408.

233.   M. Baghbanzadeh, L. Carbone, P. D. Cozzoli and C. O. Kappe, *Angewandte Chemie International Edition*, 2011, **50**(48), 11312-11359.

234. P. R. Sajanlal, T. S. Sreeprasad, A. K. Samal and T. Pradeep, *Nano Reviews*, 2011, **2**(1), 5883.

235. G. Berhault, M. Bausach, L. Bisson, L. Becerra, C. Thomazeau and D. Uzio, *The Journal of Physical Chemistry C*, 2007, **111**(16), 5915-5925.

236. C. Lofton and W. Sigmund, *Advanced Functional Materials*, 2005, **15**(7), 1197-1208.

237. M. Grzelczak, A. Sánchez-Iglesias, H. Heidari, S. Bals, I. Pastoriza-Santos, J. Pérez-Juste and L. M. Liz-Marzán, *ACS Omega*, 2016, **1**(2), 177-181.

238. S. E. Lohse, N. Burrows, L. Scarabelli, L. Liz-Marzán and C. Murphy, *Anisotropic Noble Metal Nanocrystal Growth: The Role of Halides*, 2014.

239. L. Polavarapu, S. Mourdikoudis, I. Pastoriza-Santos and J. Perez-Juste, *CrystEngComm*, 2015, **17**(20), 3727-3762.

240. C. J. Murphy, T. K. Sau, A. Gole and C. J. Orendorff, *Mrs Bulletin*, 2005, **30**(5), 349-355.

241. Z. Fan, X. Huang, Y. Han, M. Bosman, Q. Wang, Y. Zhu, Q. Liu, B. Li, Z. Zeng and J. Wu, *Nature communications*, 2015, **6** 6571.

242. C. Liang, S. Huang, W. Zhao, W. Liu, J. Chen, H. Liu and Y. Tong, *New J. Chem.*, 2015, **39**(4), 2651-2656.

243. M. Chi, C. Wang, Y. Lei, G. Wang, D. Li, K. L. More, A. Lupini, L. F. Allard, N. M. Markovic and V. R. Stamenkovic, 2015, **6** 8925.

244. D. Michael P áMingos, *Journal of the Chemical Society, Chemical Communications*, 1992(9), 674-677.

245. M. R. Rosana, J. Hunt, A. Ferrari, T. A. Southworth, Y. Tao, A. E. Stiegman and G. B. Dudley, *The Journal of organic chemistry*, 2014, **79**(16), 7437-7450.

246. A. Khalife, U. Pathak and R. Richert, *The European Physical Journal B-Condensed Matter and Complex Systems*, 2011, **83**(4), 429-435.

247. W. C. Conner and G. A. Tompsett, *The Journal of Physical Chemistry B*, 2008, **112**(7), 2110-2118.

248. X. Hu, J. C. Yu, J. Gong, Q. Li and G. Li, *Advanced Materials*, 2007, **19**(17), 2324-2329.

249. F. J. Douglas, D. A. MacLaren and M. Murrie, *Rsc Advances*, 2012, **2**(21), 8027-8035.

250. E. S. Cho, F. Qiu and J. J. Urban, *Small*, 2017, **13**(3), 1602572.

251. J. Wang, M. Yao, G. Xu, P. Cui and J. Zhao, *Materials Chemistry and Physics*, 2009, **113**(1), 6-9.

252. G. Fontana, M. Licciardi, S. Mansueto, D. Schillaci and G. Giammona, *Biomaterials*, 2001, **22**(21), 2857-2865.

253. P. G. Koutsoukos, *Trends in Colloid and Interface Science XV*, Springer Berlin Heidelberg, 2003.

254. Y. Liu, M. K. Shipton, J. Ryan, E. D. Kaufman, S. Franzen and D. L. Feldheim, *Analytical chemistry*, 2007, **79**(6), 2221-2229.

255. Y. Zhu, T. Mei, Y. Wang and Y. Qian, *Journal of Materials Chemistry*, 2011, **21**(31), 11457-11463.

256. X. Liang, X. Wang, J. Zhuang, Y. Chen, D. Wang and Y. Li, *Advanced Functional Materials*, 2006, **16**(14), 1805-1813.

257. N. T. K. Thanh, V. F. Puntes, L. D. Tung and D. G. Fernig, *Journal of Physics: Conference Series*, 2005, **17**(1), 70-76.

258. N. T. K. Thanh, N. Maclean and S. Mahiddine, *Chem. Rev.*, 2014, **114**(15), 7610-7630.

259. R. Zboril, A. Bakandritsos, M. Mashlan, V. Tzitzios, P. Dallas, C. Trapalis and D. Petridis, *Nanotechnology*, 2008, **19**(9), 095602.

260. W. R. Viali, G. B. Alcantara, P. P. C. Sartoratto, M. A. G. Soler, E. Mosiniewicz-Szablewska, B. Andrzejewski and P. C. Morais, *The Journal of Physical Chemistry C*, 2010, **114**(1), 179-188.

261. K. Parekh, R. V. Upadhyay, L. Belova and K. Rao, *Nanotechnology*, 2006, **17**(24), 5970.

262. R. Hachani, M. Lowdell, M. Birchall, A. Hervault, D. Mertz, S. Begin-Colin and N. T. K. Thanh, *Nanoscale*, 2016, **8**(6), 3278-3287.

263. D. L. Kraitchman and J. W. M. Bulte, *Basic research in cardiology*, 2008, **103**(2), 105-113.

264. S. Kazan, E. E. Tanrıverdi, R. Topkaya, Ş. Demirci, Ö. Akman, A. Baykal and B. Aktaş, *Arabian Journal of Chemistry*.

265. T. G. Altincekic, İ. Boz, A. Baykal, S. Kazan, R. Topkaya and M. S. Toprak, *Journal of Alloys and Compounds*, 2010, **493**(1–2), 493-498.

266. H. Y. Hah, S. Gray, C. E. Johnson, J. A. Johnson, V. Kolesnichenko, P. Kucheryavy and G. Goloverda, *Journal of Physics: Conference Series*, 2014, **548**(1).

267. G. M. Da Costa, C. Blanco-Andujar, E. De Grave and Q. A. Pankhurst, *Journal of Physical Chemistry B*, 2014, **118**(40), 11738-11746.

268. T. Dey, *Journal of nanoscience and nanotechnology*, 2006, **6**(8), 2479-2483.

269. J. Kucerova, Z. Svobodova, P. Knotek, J. Palarcik, M. Vlcek, M. Kincl, D. Horak, J. Autebert, J.-L. Viovy and Z. Bilkova, *Materials Science and Engineering: C*, 2014, **40** 308-315.

270. G. M. Semenovich, Y. S. Lipatov and L. V. Dubrovina, *Polymer Science U.S.S.R.*, 1986, **28**(2), 460-469.

271. E. Pramono, S. Utomo, V. Wulandari and F. Clegg, 2016 Journal of Physics: Conference Series,(776),012053.

272. I. Bilecka and M. Niederberger, *Nanoscale*, 2010, **2**(8), 1358-1374.

273. K. D. Dobson and A. J. McQuillan, *Spectrochimica Acta Part A: Molecular and Biomolecular Spectroscopy*, 1999, **55**(7), 1395-1405.

274. G. Deacon and R. Phillips, *Coord. Chem. Rev.*, 1980, **33**(3), 227-250.

275. S. Nigam, K. C. Barick and D. Bahadur, *Journal of Magnetism and Magnetic Materials*, 2011, **323**(2), 237-243.

276. F. Montagne, O. Mondain-Monval, C. Pichot, H. Mozzanega and A. Elaïssari, *Journal of magnetism and magnetic materials*, 2002, **250** 302-312.

277. L. N. Okassa, H. Marchais, L. Douziech-Eyrolles, K. Hervé, S. Cohen-Jonathan, E. Munnier, M. Soucé, C. Linassier, P. Dubois and I. Chourpa, *European Journal of Pharmaceutics and Biopharmaceutics*, 2007, **67**(1), 31-38.

278. R. L. Rebodos and P. J. Vikesland, *Langmuir*, 2010, **26**(22), 16745-16753.

279. S. Magnitsky, J. Zhang, D. Idiyatullin, G. Mohan, M. Garwood, N. E. Lane and S. Majumdar, *Magnetic Resonance in Medicine*, 2017, DOI: 10.1002/mrm.26585 n/a-n/a.

280. H. Zhou, J. Tang, J. Li, W. Li, Y. Liu and C. Chen, *Nanoscale*, 2017, DOI: 10.1039/C7NR00089H.

281. J. L Rogers, T. Tarrant and J. S Kim, *Current rheumatology reviews*, 2014, **10**(1), 3-10.

282. M. D. Badry, M. A. Wahba, R. Khaled, M. M. Ali and A. A. Farghali, *Inorganic and Nano-Metal Chemistry*, 2017, **47**(3), 405-411.

283. J. Cai, Y. Q. Miao, B. Z. Yu, P. Ma, L. Li and H. M. Fan, *Langmuir*, 2017, DOI: 10.1021/acs.langmuir.6b03360.

284. J. Bosch, K. Heister, T. Hofmann and R. U. Meckenstock, *Applied and environmental microbiology*, 2010, **76**(1), 184-189.

285. A. M. Grumezescu and E. Andronescu, *Nanostructures for Drug Delivery*, Elsevier Science & Technology Books, 2017.

286. W. Abdelwahed, G. Degobert, S. Stainmesse and H. Fessi, *Advanced Drug Delivery Reviews*, 2006, **58**(15), 1688-1713.

287. H. Takeuchi, B. Omogo and C. D. Heyes, *Nano letters*, 2013, **13**(10), 4746-4752.

288. L. E. Marbella and J. E. Millstone, *Chemistry of Materials*, 2015, **27**(8), 2721-2739.

289. O. Minaeva, E. Brodovskaya, M. Pyataev, M. Gerasimov, M. Zharkov, I. Yurlov, O. Kulikov, A. Kotlyarov, L. Balykova and A. Kokorev, 2017 Journal of Physics: Conference Series,(784),012038.

290. A. Goodarzi, Y. Sahoo, M. Swihart and P. Prasad, *MRS Online Proceedings Library Archive*, 2003, **789**.

291. S. Nigam, K. Barick and D. Bahadur, *Journal of Magnetism and Magnetic Materials*, 2011, **323**(2), 237-243.

292. L. Hadian-Dehkordi and H. Hosseini-Monfared, *Green Chemistry*, 2016, **18**(2), 497-507.

293. G. Busca, V. Lorenzelli, G. Ramis and R. J. Willey, *Langmuir*, 1993, **9**(6), 1492-1499.

294. K. Moovendaran, V. Jayaramakrishnan and S. Natarajan, *Photonics and Optoelectronics*, 2014.

295. E. R. Lippincott, *Journal of the American Chemical Society*, 1963, **85**(21), 3532-3532.

296. M. Nara, H. Torii and M. Tasumi, *The Journal of Physical Chemistry*, 1996, **100**(51), 19812-19817.

297. G. S. Groenewold, W. A. de Jong, J. Oomens and M. J. Van Stipdonk, *Journal of the American Society for Mass Spectrometry*, 2010, **21**(5), 719-727.

298. T.-H. Shin, Y. Choi, S. Kim and J. Cheon, *Chemical Society Reviews*, 2015, **44**(14), 4501-4516.

299. M. Rohrer, H. Bauer, J. Mintorovitch, M. Requardt and H. J. Weinmann, *Investigative Radiology*, 2005, **40**(11), 715-724.

300. F. Schulze, A. Dienelt, S. Geissler, P. Zaslansky, J. Schoon, K. Henzler, P. Guttmann, A. Gramoun, L. A. Crowe, L. Maurizi, J.-P. Vallée, H. Hofmann, G. N. Duda and A. Ode, *Small*, 2014, **10**(21), 4340-4351.

301. E. Amstad, T. Gillich, I. Bilecka, M. Textor and E. Reimhult, *Nano Letters*, 2009, **9**(12), 4042-4048.

302. U. El-Ayaan, E. Herlinger, R. F. Jameson and W. Linert, *Journal of the Chemical Society, Dalton Transactions*, 1997(16), 2813-2818.

303. M. D. Shultz, J. U. Reveles, S. N. Khanna and E. E. Carpenter, *Journal of the American Chemical Society*, 2007, **129**(9), 2482-2487.

304. E. D. Smolensky, H.-Y. E. Park, T. S. Berquó and V. C. Pierre, *Contrast Media Mol. Imaging*, 2011, **6**(4), 189-199.

305. W. Huang, P. Jiang, C. Wei, D. Zhuang and J. Shi, *Journal of Materials Research*, 2008, **23**(07), 1946-1952.

306. M. Mahdavi, M. B. Ahmad, M. J. Haron, Y. Gharayebi, K. Shameli and B. Nadi, *Journal of Inorganic and Organometallic Polymers and Materials*, 2013, **23**(3), 599-607.

307. L. Levy, Y. Sahoo, K.-S. Kim, E. J. Bergey and P. N. Prasad, *Chemistry of Materials*, 2002, **14**(9), 3715-3721.

308. C. Corot, M. Port, I. Guilbert, P. Robert, I. Raynal, C. Robic, J.-S. Raynaud, P. Prigent, A. Dencausse and J.-M. Idee, *Molecular and cellular MR imaging*, 2007 59-83.

309. M. Ahren, L. Selegard, A. Klasson, F. Soderlind, N. Abrikossova, C. Skoglund, T. Bengtsson, M. Engstrom, P. O. Kall and K. Uvdal, *Langmuir*, 2010, **26**(8), 5753-5762.

310. M. J. Elliott, P. De Coppi, S. Speggiorin, D. Roebuck, C. R. Butler, E. Samuel, C. Crowley, C. McLaren, A. Fierens, D. Vondrys, L. Cochrane, C. Jephson, S. Janes, N. J. Beaumont, T. Cogan, A. Bader, A. M. Seifalian, J. J. Hsuan, M. W. Lowdell and M. A. Birchall, *The Lancet*, 2012, **380**(9846), 994-1000.

311. P. Macchiarini, P. Jungebluth, T. Go, M. A. Asnaghi, L. E. Rees, T. A. Cogan, A. Dodson, J. Martorell, S. Bellini, P. P. Parnigotto, S. C. Dickinson, A. P. Hollander, S. Mantero, M. T. Conconi and M. A. Birchall, *The Lancet*, 2008, **372**(9655), 2023-2030.

312. J. Laurance, *British boy receives trachea transplant built with his own stem cells*, 2010.

313. N. Hamilton, M. Kanani, D. Roebuck, R. Hewitt, R. Cetto, E. Culme-Seymour, E. Toll, A. Bates, A. Comerford and C. McLaren, *American Journal of Transplantation*, 2015, **20** 1-8.

314.   M. Edmundson, N. T. Thanh and B. Song, *Theranostics*, 2013.

315.   P. Arora, A. Sindhu, N. Dilbaghi, A. Chaudhury, G. Rajakumar and A. A. Rahuman, *J. Cell. Mol. Med.*, 2012, **16**(9), 1991-2000.

316.   M. Belicchi, R. Cancedda, A. Cedola, F. Fiori, M. Gavina, A. Giuliani, V. S. Komlev, S. Lagomarsino, M. Mastrogiacomo, C. Renghini, F. Rustichelli, E. Sykovà and Y. Torrente, *Materials Science and Engineering: B*, 2009, **165**(3), 139-147.

317.   A. S. Arbab, L. B. Wilson, P. Ashari, E. K. Jordan, B. K. Lewis and J. A. Frank, *NMR Biomed.*, 2005, **18**(6), 383-389.

318.   H.-m. Ding and Y.-q. Ma, *Biomaterials*, 2012, **33**(23), 5798-5802.

319.   V. Mailander and K. Landfester, *Biomacromolecules*, 2009, **10**(9), 2379-2400.

320.   L. Treuel, X. Jiang and G. U. Nienhaus, *Journal of The Royal Society Interface*, 2013, **10**(82).

321.   C. Wilhelm and F. Gazeau, *Biomaterials*, 2008, **29**(22), 3161-3174.

322.   J. Sherwood, K. Lovas, M. Rich, Q. Yin, K. Lackey, M. S. Bolding and Y. Bao, *Nanoscale*, 2016, **8**(40), 17506-17515.

323.   L. Shang, K. Nienhaus and G. U. Nienhaus, *Journal of nanobiotechnology*, 2014, **12**(1), 5.

324.   D. Fayol, N. Luciani, L. Lartigue, F. Gazeau and C. Wilhelm, *Advanced healthcare materials*, 2013, **2**(2), 313-325.

325.   S. Sahlin, J. Hed and I. Runfquist, *Journal of immunological methods*, 1983, **60**(1-2), 115-124.

326.   C. P. Wan, C. S. Park and B. H. Lau, *Journal of immunological methods*, 1993, **162**(1), 1-7.

327.   Z. Ma and L.-Y. Lim, *Pharmaceutical Research*, 2003, **20**(11), 1812-1819.

328. J. Hed, G. Hallden, S. Johansson and P. Larsson, *Journal of immunological methods*, 1987, **101**(1), 119-125.

329. J. K. Hsiao, M. F. Tai, H. H. Chu, S. T. Chen, H. Li, D. M. Lai, S. T. Hsieh, J. L. Wang and H. M. Liu, *Magnetic Resonance in Medicine*, 2007, **58**(4), 717-724.

330. C. Costa, F. Brandão, M. J. Bessa, S. Costa, V. Valdiglesias, G. Kiliç, N. Fernández-Bertólez, P. Quaresma, E. Pereira, E. Pásaro, B. Laffon and J. P. Teixeira, *Journal of Applied Toxicology*, 2016, **36**(3), 361-372.

331. M. Mahmoudi, A. Simchi, A. S. Milani and P. Stroeve, *Journal of Colloid and Interface Science*, 2009, **336**(2), 510-518.

332. M. Gonzales, L. M. Mitsumori, J. V. Kushleika, M. E. Rosenfeld and K. M. Krishnan, *Contrast Media Mol. Imaging*, 2010, **5**(5), 286-293.

333. N. Falzone, C. Huyser and D. Franken, *Andrologia*, 2010, **42**(1), 20-26.

334. T. T. Sibov, L. A. M. Miyaki, J. B. Mamani, L. C. Marti, L. R. Sardinha, L. F. Pavon, D. M. d. Oliveira, W. H. Cardenas and L. F. Gamarra, *Einstein (São Paulo)*, 2012, **10** 180-188.

335. D. S. Albrecht, C. Granziera, J. M. Hooker and M. L. Loggia, *ACS Chemical Neuroscience*, 2016, **7**(4), 470-483.

336. M. A. King, M. A. Radicchi - Mastroianni and J. V. Wells, *Cytometry*, 2000, **40**(1), 10-18.

337. A. Bundscherer, M. Malsy, R. Lange, P. Hofmann, T. Metterlein, B. M. Graf and M. Gruber, *Anticancer research*, 2013, **33**(8), 3201-3204.

338. S. Barlow, G. Brooke, K. Chatterjee, G. Price, R. Pelekanos, T. Rossetti, M. Doody, D. Venter, S. Pain, K. Gilshenan and K. Atkinson, *Stem Cells and Development*, 2008, **17**(6), 1095-1107.

339. Y. Amsalem, Y. Mardor, M. S. Feinberg, N. Landa, L. Miller, D. Daniels, A. Ocherashvilli, R. Holbova, O. Yosef, I. M. Barbash and J. Leor, *Circulation*, 2007, **116**(11), I38-I45.

340. E. Boutet-Robinet, D. Trouche and Y. Canitrot, *The Journal of Cell Biology*, 2012.

341. A. Omidkhoda, H. Mozdarani, A. Movasaghpoor and A. A. P. Fatholah, *Toxicology in Vitro*, 2007, **21**(6), 1191-1196.

342. K. J. Ong, T. J. MacCormack, R. J. Clark, J. D. Ede, V. A. Ortega, L. C. Felix, M. K. M. Dang, G. Ma, H. Fenniri, J. G. C. Veinot and G. G. Goss, *PLoS ONE*, 2014, **9**(3), e90650.

343. B. B. Manshian, D. F. Moyano, N. Corthout, S. Munck, U. Himmelreich, V. M. Rotello and S. J. Soenen, *Biomaterials*, 2014, **35**(37), 9941-9950.

344. M. Persson, A. F. Løye, M. Jacquet, N. S. Mow, A. V. Thougaard, T. Mow and J. J. Hornberg, *Basic & clinical pharmacology & toxicology*, 2014, **115**(1), 18-23.

345. G. K. Y. Chan, T. L. Kleinheinz, D. Peterson and J. G. Moffat, *PLOS ONE*, 2013, **8**(5), e63583.

346. S. Winzen, S. Schoettler, G. Baier, C. Rosenauer, V. Mailaender, K. Landfester and K. Mohr, *Nanoscale*, 2015, **7**(7), 2992-3001.

347. G. Brooke, H. Tong, J. P. Levesque and K. Atkinson, *Stem Cells Dev*, 2008, **17**(5), 929-940.

348. P. Macchiarini, P. Jungebluth, T. Go, M. A. Asnaghi, L. E. Rees, T. A. Cogan, A. Dodson, J. Martorell, S. Bellini, P. P. Parnigotto, S. C. Dickinson, A. P. Hollander, S. Mantero, M. T. Conconi and M. A. Birchall, *The Lancet*, **372**(9655), 2023-2030.

349. S. J. Soenen, B. Manshian, J. M. Montenegro, F. Amin, B. r. Meermann, T. Thiron, M. Cornelissen, F. Vanhaecke, S. Doak and W. J. Parak, *ACS nano*, 2012, **6**(7), 5767-5783.

350. Y.-L. Wu, N. Putcha, K. W. Ng, D. T. Leong, C. T. Lim, S. C. J. Loo and X. Chen, *Accounts of chemical research*, 2012, **46**(3), 782-791.

351. B. Diaz, C. Sánchez - Espinel, M. Arruebo, J. Faro, E. de Miguel, S. Magadán, C. Yagüe, R. Fernández - Pacheco, M. R. Ibarra and J. Santamaria, *Small*, 2008, **4**(11), 2025-2034.

352. J.-C. Brisset, V. Desestret, S. Marcellino, E. Devillard, F. Chauveau, F. Lagarde, S. Nataf, N. Nighoghossian, Y. Berthezene and M. Wiart, *Eur. Radiol.*, 2010, **20**(2), 275-285.

353.   O. M. Girard, R. Ramirez, S. McCarty and R. F. Mattrey, *Contrast Media Mol. Imaging*, 2012, **7**(4), 411-417.

354.   M. B. Kok, S. Hak, W. J. M. Mulder, D. W. J. van der Schaft, G. J. Strijkers and K. Nicolay, *Magnetic Resonance in Medicine*, 2009, **61**(5), 1022-1032.

355.   M. Taupitz, S. Wagner, J. Schnorr, I. Kravec, H. Pilgrimm, H. Bergmann-Fritsch and B. Hamm, *Investigative radiology*, 2004, **39**(7), 394-405.

356.   Y. Wei, R. Liao, H. Liu, H. Li, H. Xu and Q. Zhou, *Journal of biomedical nanotechnology*, 2015, **11**(5), 854-864.

357.   L. Zhu and V. P. Torchilin, *Integrative biology : quantitative biosciences from nano to macro*, 2013, **5**(1), 10.1039/c1032ib20135f.

358.   T. Knopp, S. Conolly, T. Buzug, M. Graeser, A. von Gladiss and M. Weber, *Physics in Medicine and Biology*, 2017, **62**(9), E4.

359.   S. J. Soenen and M. De Cuyper, *Contrast Media Mol. Imaging*, 2009, **4**(5), 207-219.

360.   M. Dominici, K. Le Blanc, I. Mueller, I. Slaper-Cortenbach, F. Marini, D. Krause, R. Deans, A. Keating, D. Prockop and E. Horwitz, *Cytotherapy*, 2006, **8**(4), 315-317.

361.   G. Su, X. Zhou, H. Zhou, Y. Li, X. Zhang, Y. Liu, D. Cao and B. Yan, *ACS Applied Materials & Interfaces*, 2016, **8**(44), 30037-30047.

362.   R. Y. Lin, K. Dayananda, T. J. Chen, C. Y. Chen, G. C. Liu, K. L. Lin and Y. M. Wang, *Contrast Media Mol. Imaging*, 2012, **7**(1), 7-18.

363.   K. L. Vigor, P. G. Kyrtatos, S. Minogue, K. T. Al-Jamal, H. Kogelberg, B. Tolner, K. Kostarelos, R. H. Begent, Q. A. Pankhurst, M. F. Lythgoe and K. A. Chester, *Biomaterials*, 2010, **31**(6), 1307-1315.

364.   R. Thapa and G. D. Wilson, *Stem Cells International*, 2016, **2016** 15.

365.   W. Qin, G. Huang, Z. Chen and Y. Zhang, *Frontiers in Pharmacology*, 2017, **8**(1).

366.   I.-S. Hong, G.-B. Jang, H.-Y. Lee and J.-S. Nam, *International journal of nanomedicine*, 2015, **10**(Spec Iss), 251.

367. L. Fiandra, S. Mazzucchelli, C. De Palma, M. Colombo, R. Allevi, S. Sommaruga, E. Clementi, M. Bellini, D. Prosperi and F. Corsi, *ACS Nano*, 2013, **7**(7), 6092-6102.

368. O. Bixner, A. Lassenberger, D. Baurecht and E. Reimhult, *Langmuir*, 2015, **31**(33), 9198-9204.

369. A. M. Smith, L. E. Marbella, K. A. Johnston, M. J. Hartmann, S. E. Crawford, L. M. Kozycz, D. S. Seferos and J. E. Millstone, *Analytical Chemistry*, 2015, **87**(5), 2771-2778.

370. D. L. J. Thorek, D. R. Elias and A. Tsourkas, *Molecular Imaging*, 2009, **8**(4), 221-229.

371. J. Bolley, E. Guenin, N. Lievre, M. Lecouvey, M. Soussan, Y. Lalatonne and L. Motte, *Langmuir*, 2013, **29**(47), 14639-14647.

372. T. Carter, P. Mulholland and K. Chester, *Immunotherapy*, 2016, **8**(8), 941-958.

373. M. Arruebo, M. Valladares and Á. González-Fernández, *Journal of Nanomaterials*, 2009, **2009** 24.

374. D. A. Richards, A. Maruani and V. Chudasama, *Chemical Science*, 2017, **8**(1), 63-77.

375. R. Yan and D. Ye, *Science Bulletin*, 2016, **61**(21), 1672-1679.

376. H. Nejadnik, D. Ye, O. D. Lenkov, J. S. Donig, J. E. Martin, R. Castillo, N. Derugin, B. Sennino, J. Rao and H. Daldrup-Link, *ACS Nano*, 2015, **9**(2), 1150-1160.

377. Y. Yuan, Z. Ding, J. Qian, J. Zhang, J. Xu, X. Dong, T. Han, S. Ge, Y. Luo, Y. Wang, K. Zhong and G. Liang, *Nano Letters*, 2016, **16**(4), 2686-2691.
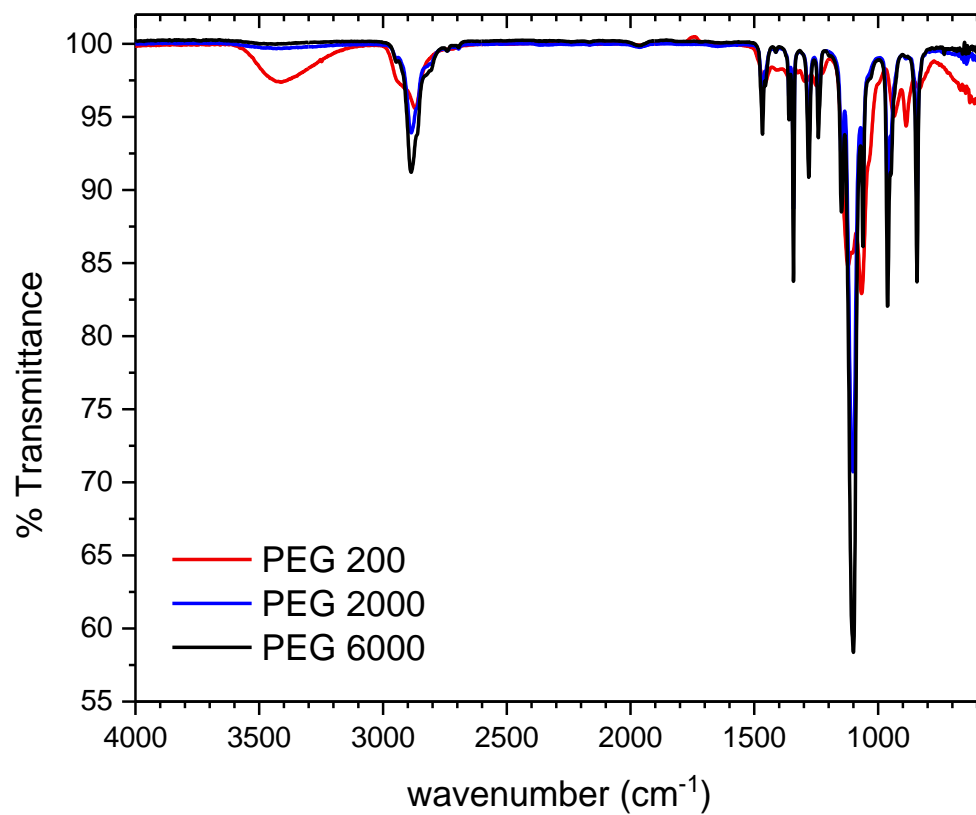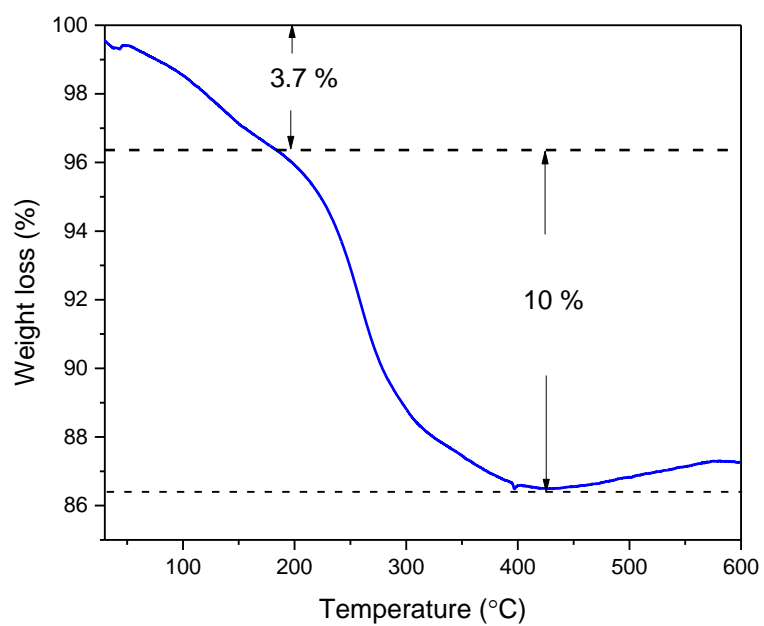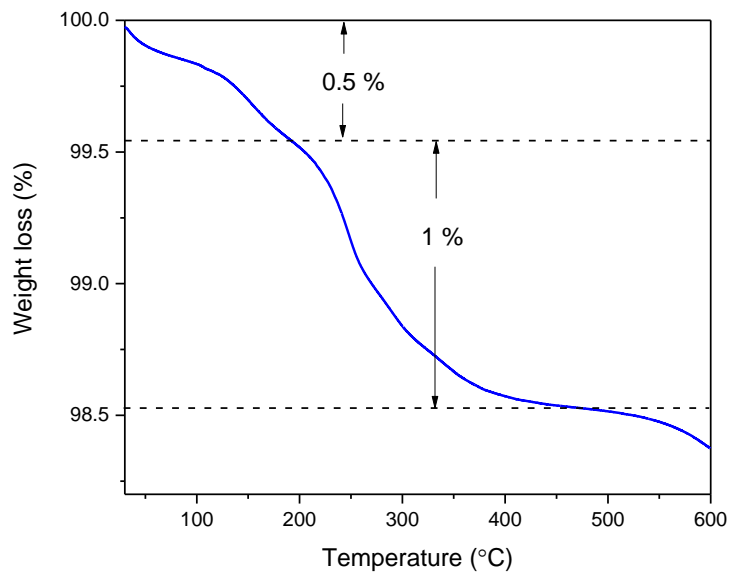
**Figure 14 ATR-FTIR representative spectra of PEG 200 (red), PEG 2000 (blue), and PEG 6000 (black).**
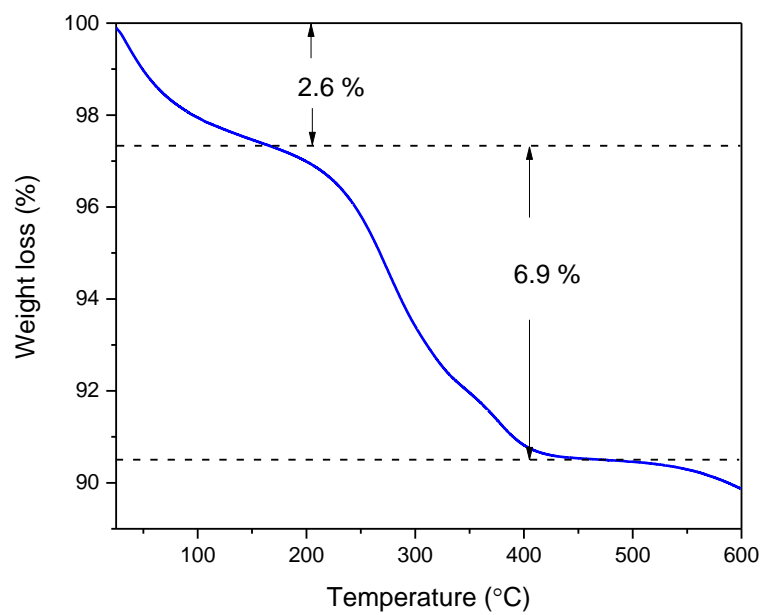
APPENDIX 2

Figure 15 Thermogravimetric analysis of TREG coated IONPs obtained in high pressure high temperature conditions with 100 mM of precursor Fe(acac)$_3$
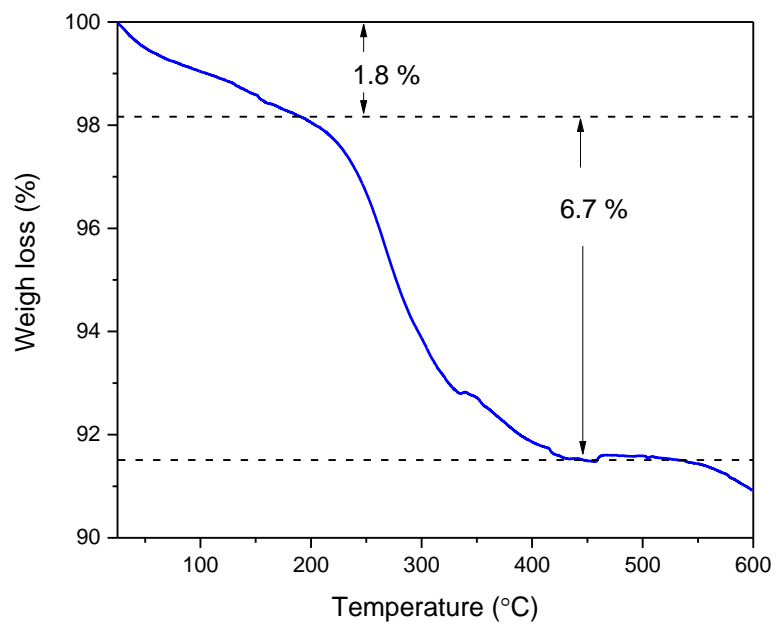
Figure 16 Thermogravimetric analysis of TREG coated IONPs obtained in high pressure high temperature conditions with 150 mM of precursor Fe(acac)$_3$
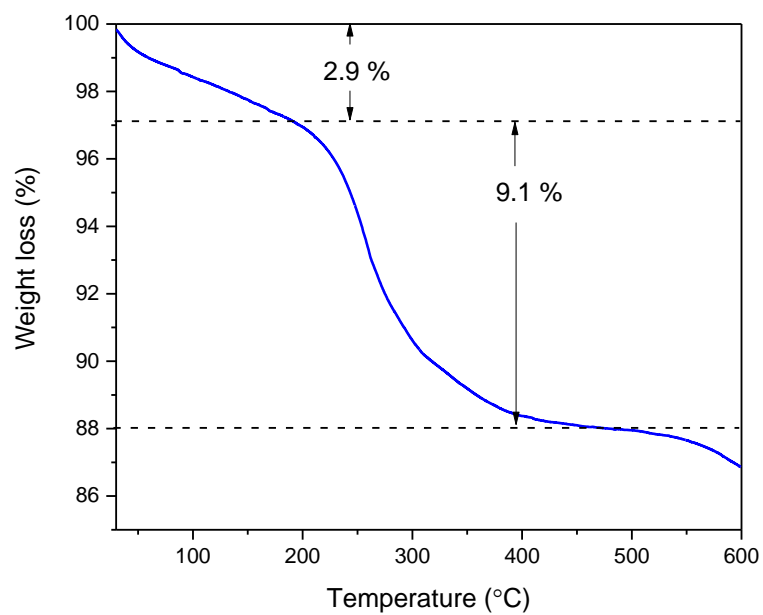
Figure 17 Thermogravimetric analysis of TREG coated IONPs obtained in high pressure high temperature conditions with 200 mM of precursor Fe(acac)$_3$

Figure 18 Thermogravimetric analysis of TREG coated IONPs obtained in high pressure high temperature conditions with 250 mM of precursor Fe(acac)$_3$

Figure 19 Thermogravimetric analysis of TREG coated IONPs obtained in high pressure high temperature conditions with 500 mM of precursor Fe(acac)$_3$

APPENDIX 3

1. Surface coverage of 120 mg citric acid with 60 mg IONPs

Average diameter of IONP determined by TEM in chapter 3: d = 8 nm so radius r = 4nm

Considering $V = 4/3\ \pi\ r^3 = 268.1\ nm^3$

The nanoparticle surface is then determined as $S = 4\ \pi\ r^2 = 201.1\ nm^2$

Considering the density of maghemite γFe_2O_3 is $\rho(Fe_2O_3) = 4.9\ g/cm^3$ then the theoretical mass of one nanoparticle can be calculated as: $m_{NP} = \rho(Fe_2O_3)\ x\ V = 98.54\ x\ 10^{-17}\ g$

So in 60 mg of nanoparticle powder, the theoretical amount of nanoparticles is:

$n = m_{sample}\ /\ m_{NP} = 60\ x\ 10^{-3}\ g\ /\ 98.54\ x\ 10^{-17}\ g = 60.9\ x\ 10^{12}$ particles. This divided by Avogadro's number = molarity of nanoparticles in the sample and as such: $n = 60.9\ x\ 10^{12}$ particles $/\ 6.02\ x\ 10^{23} = 10^{-10}$ mol

Considering $M_{CA} = 192.124\ g/mol$, then in 120 mg there are $n = 6.25\ x\ 10^{-4}$ mol of ligand. In terms of number of molecules this is equivalent to: $N = n\ x\ N_A = 6.25\ x\ 10^{-4}\ x\ 6.02\ x\ 10^{23} = 3.76\ x\ 10^{20}$ molecules, thus corresponding to a ratio of IONP to CA: $3.76\ x\ 10^{20}$ molecules $/\ 60.9\ x\ 10^{12}$ particles = 6.17 million ligands per NP.

2. Surface coverage of 100 mg 3,4-dihydroxyhydrocinnamic acid with 50 mg IONPs

Average diameter of IONP determined by TEM in chapter 3: d = 8 nm so radius r = 4nm

Considering $V = 4/3\ \pi\ r^3 = 268.1\ nm^3$

The nanoparticle surface is then determined as $S = 4\ \pi\ r^2 = 201.1\ nm^2$

Considering the density of maghemite γFe_2O_3 is $\rho(Fe_2O_3) = 4.9$ g/cm^3 then the theoretical mass of one nanoparticle can be calculated as: $m_{NP} = \rho(Fe_2O_3) \times V = 98.54 \times 10^{-17}$ g

So in 50 mg of nanoparticle powder, the theoretical amount of nanoparticles is:

$n = m_{sample} / m_{NP} = 50 \times 10^{-3}$ g / 98.54×10^{-17} g $= 50.74 \times 10^{12}$ particles. This divided by Avogadro's number = molarity of nanoparticles in the sample and as such: $n = 50.74 \times 10^{12}$ particles / $6.02 \times 10^{23} = 8.43 \times 10^{-11}$ mol

Considering $M_{DHCA} = 182.17$ g/mol, then in 100 mg there are $n = 5.49 \times 10^{-4}$ mol of ligand. In terms of number of molecules this is equivalent to: $N = n \times N_A = 5.49 \times 10^{-4} \times 6.02 \times 10^{23} = 3.3 \times 10^{20}$ molecules, thus corresponding to a ratio of IONP to DHCA: 3.3×10^{20} molecules / 50.74×10^{12} particles = 6.5 million ligands per NP.

3. Surface coverage of 50 mg tartaric acid with 25 mg IONPs

Average diameter of IONP determined by TEM in chapter 3: d = 8 nm so radius r = 4nm

Considering $V = 4/3 \pi r^3 = 268.1$ nm^3

The nanoparticle surface is then determined as $S = 4 \pi r^2 = 201.1$ nm^2

Considering the density of maghemite γFe_2O_3 is $\rho(Fe_2O_3) = 4.9$ g/cm^3 then the theoretical mass of one nanoparticle can be calculated as: $m_{NP} = \rho(Fe_2O_3) \times V = 98.54 \times 10^{-17}$ g

So in 25 mg of nanoparticle powder, the theoretical amount of nanoparticles is:

$n = m_{sample} / m_{NP} = 25 \times 10^{-3}$ g / 98.54×10^{-17} g $= 25.37 \times 10^{12}$ particles. This divided by Avogadro's number = molarity of nanoparticles in the sample and as such: $n = 25.37 \times 10^{12}$ particles / $6.02 \times 10^{23} = 4.21 \times 10^{-11}$ mol

Considering M_{TA} = 150.087 g/mol, then in 50 mg there are n = 3.33 x 10^{-4} mol of ligand. In terms of number of molecules this is equivalent to: N = n x N_A = 3.33 x 10^{-4} x 6.02 x 10^{23} = 2 x 10^{20} molecules, thus corresponding to a ratio of IONP to TA: 2 x 10^{20} molecules / 25.37 x 10^{12} particles = 7.9 million ligands per NP.

4. Surface coverage of 10 mg IONPs with 10 mg, 100 mg and 500 mg tartaric acid

Average diameter of IONP determined by TEM in chapter 3: d = 8 nm so radius r = 4nm

Considering V = 4/3 π r^3 = 268.1 nm^3

The nanoparticle surface is then determined as S = 4 π r^2 = 201.1 nm^2

Considering the density of maghemite γFe_2O_3 is ρ(Fe_2O_3) = 4.9 g/cm^3 then the theoretical mass of one nanoparticle can be calculated as: m_{NP} = ρ(Fe_2O_3) x V = 98.54 x 10^{-17} g

So in 10 mg of nanoparticle powder, the theoretical amount of nanoparticles is:

n = m_{sample} / m_{NP} = 10 x 10^{-3} g / 98.54 x 10^{-17} g = 10.15 x 10^{12} particles. This divided by Avogadro's number = molarity of nanoparticles in the sample and as such: n = 10.15 x 10^{12} particles / 6.02 x 10^{23} = 1.69 x 10^{-11} mol

Considering M_{TA} = 150.087 g/mol, then in 10 mg there are n = 0.66 x 10^{-4} mol of ligand. In terms of number of molecules this is equivalent to: N = n x N_A = 0.66 x 10^{-4} x 6.02 x 10^{23} = 4 x 10^{19} molecules, thus corresponding to a ratio of IONP to TA: 4 x 10^{19} molecules / 10.15 x 10^{12} particles = 3.95 million ligands per NP.
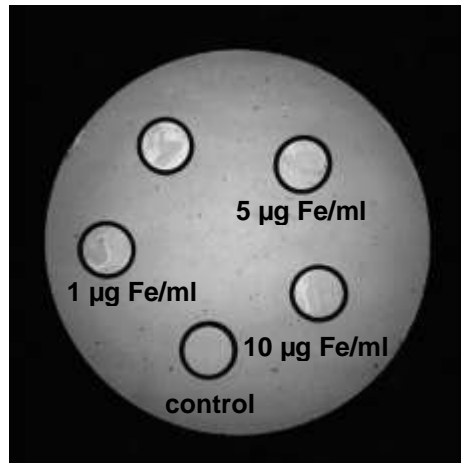
With 100 mg the ratio of IONP to TA will be increased to: 39.5 million ligands per NP.

With 500 mg the ratio of IONP to TA will be increased to: 197.5 million ligands per NP.
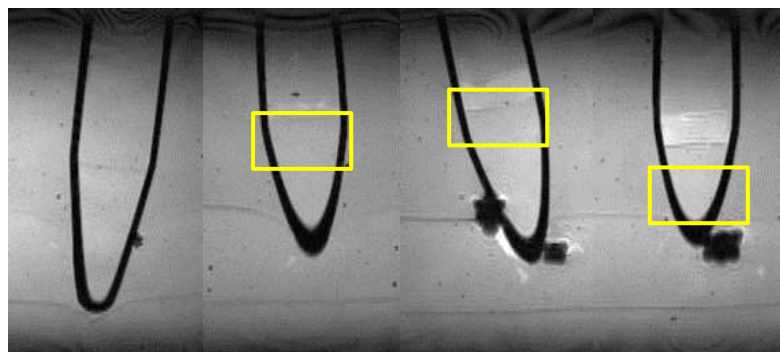
APPENDIX 4

In vitro MR image acquisition

Figure 111 Phantom homogeneity and positioning was assessed using FLASH 3D sequence (TE/TR: 15/200ms, matrix: 512x512x128, FOV: 60x60x30 mm, resolution: 0,117x0,117x0,234 mm). A: axial view of the phantom with samples containing 0, 1, 5 and 10 µg Fe/ml. Distance from the bottom of the phantom for each sample being respectively 21, 23, and 20 and 21 mm.
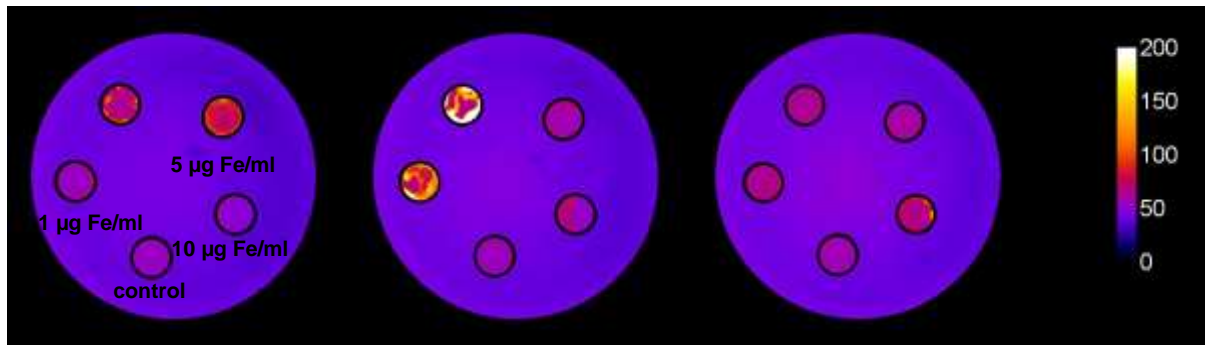
T₁ measurements
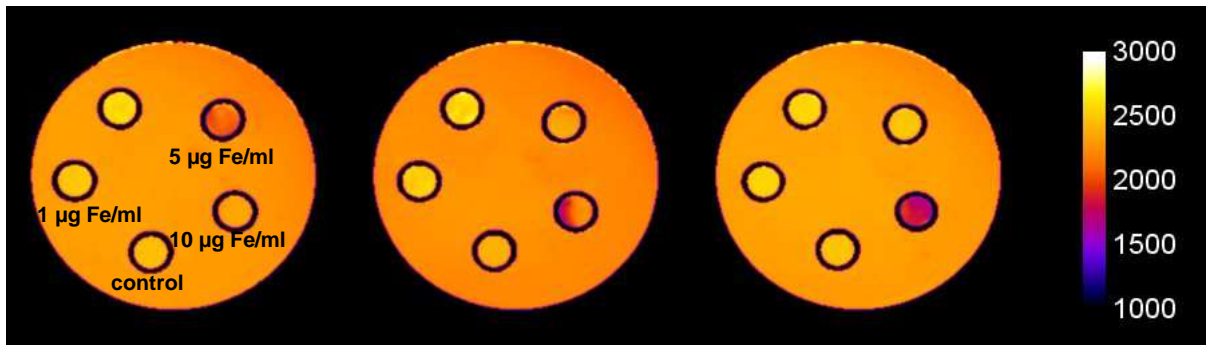
Fe concentration (µg/mL)	T₁ mean (ms)
0	2388 ± 19
1	2515 ± 27
5	2071 ± 60
10	1788 ± 92

Figure 21 Data were extracted from slices 2, 2, 1 and 3 for samples containing 0, 1, 5 and 10 µg Fe/ml respectively. Spin echo sequence with inversion preparation (TR: 10000 ms, TE: 5.67 ms, T₁: array of 12 Tis starting from 50 ms with regular increment of 500ms, FOV: 60 x 60 mm, matrix: 256 x 256, 5 slices of 1 mm thickness and 1 mm gap). Data were fitted to a mono-exponential recovery function and T₁ extracted (processing performed in PV5,1 using image sequence analysis tool.
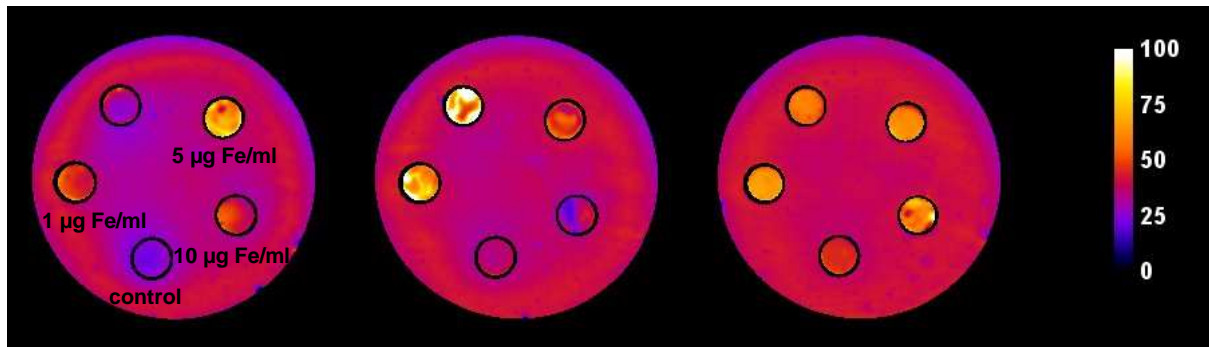
T_2 measurements

Fe concentration (µg/mL)	T_2 mean (ms)
0	54.5 ± 0.9
1	101 ± 29.9
5	80.9 ± 7.5
10	70.8 ± 10.8

Figure 22 Data were extracted from slices 2, 2, 1 and 3 for samples containing 0, 1, 5 and 10 µg Fe/ml respectively. Multi Spin Echo sequence (TR: 5000 ms, TE: 20 TEs equally spaced by 11.35 ms, FOV: 60 x 60 mm, matrix: 512 x 512, 5 slices of 1 mm thickness and 1 mm gap). Data were fitted to a mono-exponential and T_2 extracted (processing performed in ImageJ using the MRI processor plugin. T_2 maps were generated for pixels for which the R_2 of the fit was higher than 0.9 and capped at 1000 ms).

T$_2$* measurements

Fe concentration (µg/mL)	T$_2$* mean (ms)
0	35.2 ± 1.6
1	71.4 ± 17.4
5	64.5 ± 9.1
10	59.5 ± 10.7

Figure 23 Data were extracted from slices 2, 2, 1 and 3 for samples containing 0, 1, 5 and 10 µg Fe/ml respectively. Multi gradient echo sequence (TR: 5000 ms, TE: 14 Tes starting from 2.5ms with regular spacing of 4 ms, FOV: 60 x 60 mm, matrix: 256 x 256, 5 slices of 1 mm thickness and 1 mm gap). Data were fitted to a mono-exponential and T$_2$* extracted. Processing performed in ImageJ using the MRI processor plugin. T$_2$* maps were generated for pixels for which the R$_2$ of the fit was higher than 0.9 and capped at 200 ms).